Stochastic Modelling of the Cell Cycle

A thesis submitted in partial fulfilment of the requirements
for the degree of Doctor of Philosophy

Michaelmas Term 2011

Enuo He

Wolfson College
Supervisor: Professor Béla Novák

The Department of Biochemistry, University of Oxford

To my parents

Qinglai He & Chunmei Hu

Declaration

I, **Enuo He**, hereby declare that "Stochastic Modelling of the Cell Cycle" is my own original work. I have co-authored three publications during my D.Phil study:

- *Kapuy, O., He, E., López-Avilés, S., Uhlmann, F., Tyson, J. J., and Novák, B. (2009a). System-level feedbacks control cell cycle progression. FEBS Lett, 583 (24): 3992-3998.*

- *Kapuy, O., He, E., Uhlmann, F., and Novák, B. (2009b). Mitotic exit in mammalian cells. Mol Syst Biol, 5:324.*

- *He, E., Kapuy, O., Oliveira, R. A., Uhlmann, F., Tyson, J. J., and Novák, B. (2011). System-level feedbacks make the anaphase switch irreversible. Proc Natl Acad Sci U S A, 108 (24):10016-10021.*

With the permission from my supervisor Prof. Béla Novák and other coauthors, part of this published material is used in the thesis: part of Kapuy et al. (2009b) is used in Section1.3.1 in Chapter 1. Part of He et al. (2011) is used in Chapter 4. Part of Kapuy et al. (2009b) and Kapuy et al. (2009c) is used in Chapter 6 and Chapter 7.

All the other material (text and figures) that are used in this thesis, I have authored and produced myself. (Oxford, 13/03/2012)

Acknowledgements

I would like to express my heartfelt gratitude, appreciation and thanks to my supervisor Prof. Béla Novák for his effective supervision, scientific guidance and continuous support throughout my entire DPhil period. It enabled me to develop the understanding of the cell cycle subject and to extend the corresponding research skills. I am very thankful to my previous co-supervisor Dr. Andrew Dalby during the 1st year DPhil. I thank him for interviewing me and offering me such a great opportunity to study at the University of Oxford. I would also thank Dr. Andrew Phillips, my external advisor in the Microsoft Research Cambridge for scientific discussion and advice. My thanks go also to Prof. John J. Tyson for his suggestions and ideas regarding my projects. I would like to thank all the coauthors of my publications for their scientific suggestions and comments on my research.

The Dorothy Hodgkin Postgraduate Award (DHPA), provided by Microsoft Research and the Engineering and Physical Sciences Research Council, was essential in helping me focus on the research in the UK without too much financial worries.

A special thanks to Dr. Orsolya Kapuy for her support, extreme patience and a lot of encouragement. I would express my thankfulness to Dr. Bernhard Schmierer for the proofreading and for the day-to-day support (both scientific and non-scientific), I enjoyed our daily-coffee time in the past three years. Many thanks to all my colleagues Dr. Vinod P.K., Paula Freire, Yaseen Ladak, Dr. Ahmed Rattani, Maria Rosa Domingo Sananes, Oliver Britton, Dr. Elwy Okaz, Dr. Tongli Zhang, Dr. Anael Verdugo, Dr. Bence Melykuti, Guido Klingbeil and many, many friends who made my life in Oxford a unique and memorable experience.

ACKNOWLEDGEMENTS

I want to thank my examiners Prof. Philip K. Maini and Dr. Andrea Ciliberto for reading and assessing my thesis. Thanks for their scientific suggestions and comments on my research and my future career plan.

I want to address special thanks to Mr. Paul Collins, not only for his patiently proofreading my whole dissertation but also for his company and positive attitude about my ability.

Last but definitely not least, I would like to express my deepest thanks and my greatest love to my parents and brother, for their love, trust and support all through the years. Their kindness, openness, tolerance, generosity and love have made who I am.

Abstract

Precise regulation of cell cycle events by the Cdk-control network is essential for cell proliferation and the perpetuation of life. The unidirectionality of cell cycle progression is governed by several critical irreversible transitions: the G1-to-S transition, the G2-to-M transition, and the M-to-G1 transition. Recent experimental and theoretical evidence has pulled into question the consensus view that irreversible protein degradation causes the irreversibility of those transitions. A new view has started to emerge, which explains the irreversibility of cell cycle transitions as a consequence of systems-level feedback rather than of proteolysis.

This thesis applies mathematical modelling approaches to test this proposal for the M-to-G1 transition, which consists of two consecutive irreversible substeps: the metaphase-to-anaphase transition, and mitotic exit. The main objectives of the present work were: (i) to develop deterministic models to identify the essential molecular feedback loops and to examine their roles in the irreversibility of the M-to-G1 transition; (ii) to present a straightforward and reliable workflow to translate deterministic models of reaction networks into stochastic models; (iii) to explore the effects of noise on the cell cycle transitions using stochastic models, and to compare the deterministic and the stochastic approaches.

In the first part of this thesis, I constructed a simplified deterministic model of the metaphase-to-anaphase transition, which is mainly regulated by the spindle assembly checkpoint (the SAC). Based on the essential feedback loops causing the bistability of the transition, this deterministic model provides explanations for three open questions regarding the SAC: Why is the SAC not reactivated when the kinetochore tension decreases to zero at anaphase onset? How can a single unattached kinetochore keep the SAC active?

How is the synchronized and abrupt destruction of cohesin triggered?

This deterministic model was then translated into a stochastic model of the SAC by treating the kinetochore microtubule attachment at prometaphase as a noisy process. The stochastic model was analyzed and simulation results were compared to the experimental data, with the aim of explaining the mitotic timing regulation by the SAC. Our model works remarkably well in qualitatively explaining experimental key findings and also makes testable predictions for different cell lines with very different number of chromosomes. The noise generated from the chemical interactions was found to only perturb the transit timing of the mitotic events, but not their ultimate outcomes: all cells eventually undergo anaphase, however, the time required to satisfy the SAC differs between cells due to stochastic effects.

In the second part of the thesis, stochastic models of mitotic exit were created for two model organisms, budding yeast and mammalian cells. I analyzed the role of noise in mitotic exit at both the single-cell and the population level. Stochastic time series simulations of the models are able to explain the phenomenon of reversible mitotic exit, which is observed under specific experimental conditions in both model organisms. In spite of the fact that the detailed molecular networks of mitotic exit are very different in budding yeast and mammalian cells, their dynamic properties are similar. Importantly, bistability of the transitions is successfully captured also in the stochastic models.

This work strongly supports the hypothesis that uni-directional cell cycle progression is a consequence of systems-level feedback in the cell cycle control system. Systems-level feedback creates alternative steady states, which allows cells to accomplish irreversible transitions, such as the M-to-G1 transition studied here. We demonstrate that stochastic models can serve as powerful tools to capture and study the heterogeneity of dynamical features among individual cells. In this way, stochastic simulations not only complement the deterministic approach, but also help to obtain a better understanding of mechanistic aspects. We argue that the effects of noise and the potential needs for stochastic simulations should not be overlooked in studying dynamic features of biological systems.

Glossary

APC anaphase promoting complex/cyclosome

BNs Boolean networks

CAKs Cdk-activating kinases

CDK Cdk1/M-cyclins and Cdk1/S-cyclins activities

Cdk cyclin dependent kinase

Cdk1/CycB Cdk1 and Cyclin B complex

CHX cycloheximide

CI confidence intervals

CIN chromosomal instability

CKI Cyclin-Dependent Kinase Inhibitor

CLE Chemical Langevin Equation

CME chemical master equation

CPC chromosomal passenger complex

CTMC continuous-time Markov chain

CycB^M M cyclins

CycB^S S cyclins

EGFP enhanced green fluorescent protein

EP exit protein

FFL feed forward loop

G1 phase The gap phase one in the cell cycle

G2 phase the gap phase two in the cell cycle

GFP green fluorescent protein

Gillespie algorithm stochastic simulation algorithm (SSA)

GO Gene Ontology

HT hitting time

M phase mitotic phase in the cell cycle

MBF MCB binding factor

MCC mitotic checkpoint protein complex

MFPT mean first passage time

mitotic exit mitotic cell division and cell return to G1 phase

Mpf M phase promoting factor Cdk1/CycB

Mpfp phosphorylated form of Mpf

MTOC microtubule organizing center

NEBD nuclear envelope breakdown

ODEs ordinary differential equations

PBNs probabilistic Boolean networks

Ptk1 potoroo kidney cells

RNAi RNA interference

RRE reaction rate equation

S phase synthetic phase in the cell cycle

S.cerevisiae Saccharomyces cerevisiae

SAC spindle assembly checkpoint

SBF SCB binding factor

SCF Skp, Cullin, F-box containing complex

SEM standard error of the mean

SGD Saccharomyces Genome Database

SK starter kinases

SPB spindle pole body

SPNs stochastic petri nets

SRC signal response curves

SSA stochastic simulation algorithm

TEV tobacco etch virus

X.laevis Xenopus laevis

Contents

List of Figures

List of Tables

Chapter 1

Introduction

1.1 The Cell Cycle

Cell reproduction is the foundation of development and function of all life. The series of highly regulated events leading to cell duplication and division are referred to as the cell cycle. Cell division in simple unicellular organisms generates an entirely new organism and provides the mechanisms of repair and continual renewal of cells in multicellular organisms.

For the purposes of clarity and ease of understanding, the continuous eukaryotic cell cycle progression is commonly divided into two distinct and discrete periods: synthetic (S) phase and mitotic (M) phase (Fig. 1.1). Chromosomes are replicated during S phase which creates two identical copies of sister chromatids by the end of this stage. During M phase, sister chromatids are separated and equally distributed into two daughter nuclei. In addition to M phase and S phase, two temporal gap phases G1 and G2 exist in between (G1-S-G2-M-G1-etc.) (Alberts et al., 2008). Gap phases are usually much longer than M or S phase in order to provide additional time for cell growth. They also serve as important regulatory transition points, in which progression to the next cell cycle phase can be controlled by a variety of intracellular and extracellular signals.

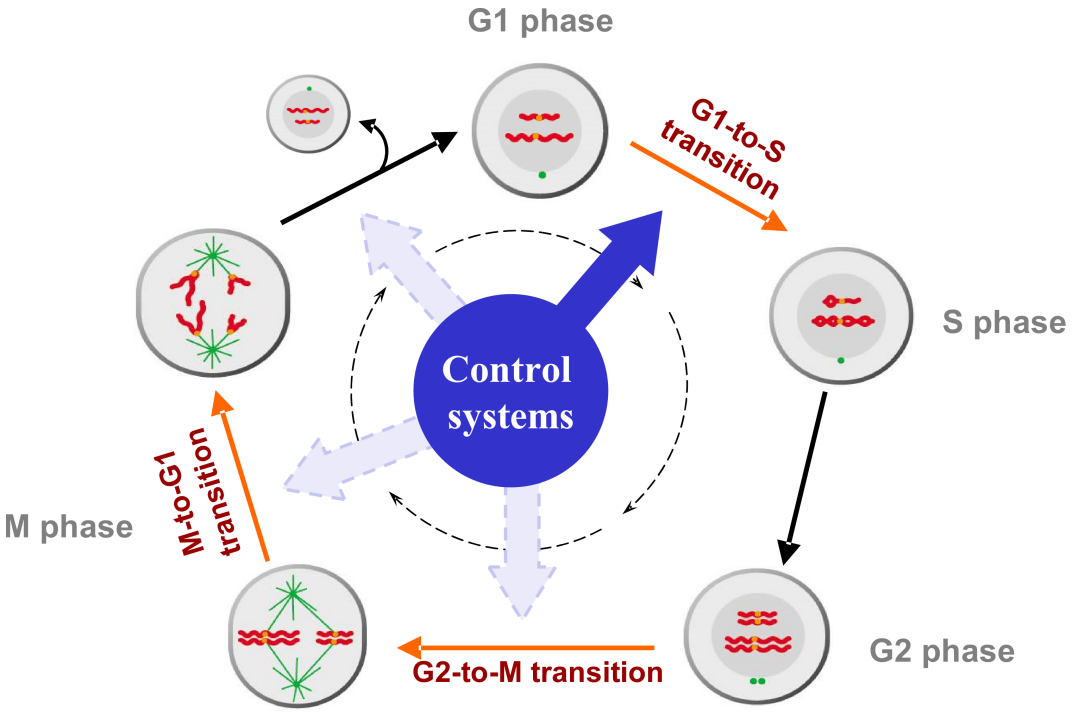

Figure 1.1: Cell phases and irreversible transitions in the cell cycle. The eukaryotic cell cycle can be divided into two periods: an S phase, in which chromosomes are replicated; and M phase, in which sister chromatids are separated and equally distributed into two daughter nuclei. Two gap phases (G1 and G2) are located in between. Cell cycle progression is characterized by the irreversible transitions: the G1-to-S transition, the G2-to-M transition and the M-to-G1 transition. The figure is adapted from Tyson and Novák (2001).

1.2 The Cell Cycle Control System

All types of living organisms, whether unicellular or multicellular, require a precise and reliable control mechanism to ensure the cell cycle progression continues over countless generations (Morgan, 2007; Alberts et al., 2008). The steadfastness of cell proliferation also depends on the regulatory mechanism that is able to guarantee the correct ordering of the cell cycle events. Once a cell is committed to enter a new cell cycle, it is crucial that it progresses uni-directionally through the entire cycle. A complex regulatory network called the "**cell cycle control system**", which exists in all eukaryotic cells, maintains the accuracy of cell cycle events. The cell cycle control system is a comprehensive cellular machinery consisting of hundreds of regulatory components that is responsible for switching the cell cycle events at the correct time and in the correct order.

Multiple checkpoints which assist to control the order and timings of cell cycle events have been identified (Fig. 1.1). They are the control mechanisms checking whether the

tasks of each phase have been properly accomplished before proceeding to the next phase. The G1-to-S transition (called "Start" in yeast and "restriction point" in higher eukaryotes), which defines the initiation of a new cell division cycle in late G1 phase; the G2-to-M transition, where the entry into mitosis is controlled; and the M-to-G1 transition, where the final events of mitosis take place. At each checkpoint, cells can be arrested at the particular stage of the cell cycle if certain requirements have not been fulfilled. Entry into mitosis is prevented, for example, when DNA replication is not completed, and chromosome separation in anaphase is delayed if chromosomes are not properly bioriented. The detailed irreversible regulatory mechanism of the checkpoints are explained in a later part of this chapter (Section 1.3.1).

1.2.1 Oscillations of Cdk/Cyclin activities

The most important core players of the cell cycle control system are cyclin-dependent kinases (Cdks). In budding yeast (*Saccharomyces cerevisiae*) and fission yeast (*Schizosaccharomyces pombe*), there is only one Cdk (called Cdk1) which is responsible for all major cell cycle events (Lee and Nurse, 1987; Nasmyth, 1993). Four different types of Cdks (Cdk1,2,4 and 6) are involved in animal cells. It is worth noting that there are additional Cdks, which do not have direct contributions to the cell cycle regulation (Morgan, 2007).

Cdks, as their name implies, require binding to their regulatory partners, cyclins, for protein kinase activity. Cdk levels are thought to be relatively constant and in excess over cyclin levels during the entire cell cycle. The oscillation of cyclin expression level results in the variation of Cdk/Cyclin complexes levels changing in a similar pattern throughout the cell cycle (Fig. 1.2). Cdks associate with different cyclins at different stages of the cell cycle to perform specific tasks (Evans et al., 1983).

Cyclins can be classified into four classes depending on the protein expression time and their corresponding cell-cycle regulatory function: G1 cyclins, G1/S cyclins, S cyclins and M cyclins (Morgan, 2007).

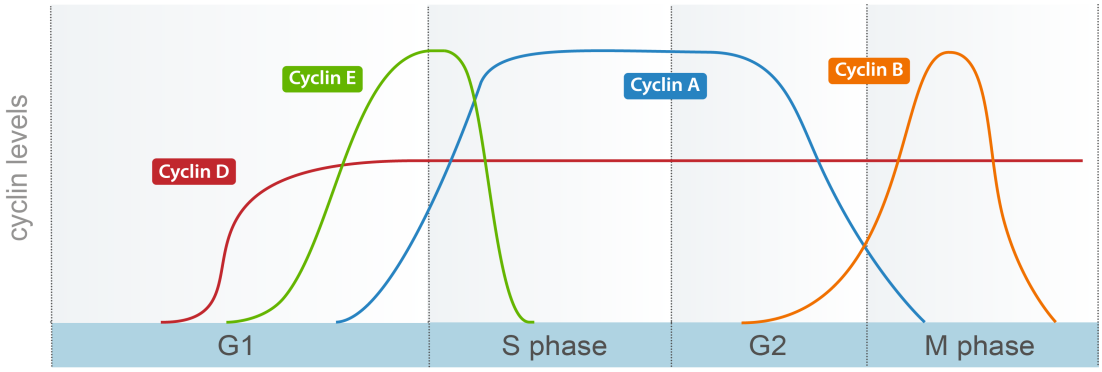

Figure 1.2: Vertebrate cyclin expression levels during one cell cycle. Cyclin D levels increase gradually from G1 and remain at a high level throughout the cell cycle. Cyclin E rises at late G1 and drops in the early S phase. Cyclin A starts to increase from late G1, holds steady at S and G2 phase, and it is finally degraded during early mitosis. Cyclin B levels increase at late G2, peaks in the mid of mitosis and eventually declines at the end of M phase.

- **G1 cyclins** (Cln3 in budding yeast, cyclin D in vertebrates): G1 cyclins are not directly involved in the control of cell cycle events and do not oscillate within a cell cycle. Instead, they help to coordinate cell growth and cell size control. They are also required at the G1-to-S transition to stimulate a new cell cycle in response to cell size, extracellular signals or growth-regulatory factors.

- **G1/S cyclins** (Cln1 and Cln2 in budding yeast, cyclin E in vertebrates): The primary function of G1/S cyclins is to assist the cell in passing the G1-to-S transition point and to stimulate the prior events prepared for S phase. G1/S cyclins levels start to increase in the late G1 phase and fall in the early S phase.

- **S cyclins** (Clb5 and Clb6 in budding yeast, cyclin A in vertebrates): S cyclins are directly responsible for triggering DNA replication in S phase. S cyclins rise from the late G1, stay high throughout the whole S phase and decrease at early M phase after promoting the events in early mitosis.

- **M cyclins** (Clb1, 2, 3, and 4 in budding yeast, cyclin B in vertebrates): The levels of M cyclins increase from late G2 and reach their peaks in M phase where the most striking cellular changes (e.g. spindle assembly, chromosome congression and segregation etc.) occur. The destruction of M cyclins starting from metaphase causes cells to exit from mitosis and to initiate cell divisions.

1.2.2 Regulation of Cdk/Cyclin activities

In addition to directly binding to cyclins, Cdk/Cyclin activity is regulated in multiple ways, including by periodic gene expression of its regulatory proteins (cyclins), by association with inhibiting proteins (CKIs), by post-translational modifications and by degradation of regulatory subunits, cyclins (Morgan, 2007). A schematic diagram of the multi-regulatory network that controls Cdk/Cyclin activity is shown in Figure 1.3.

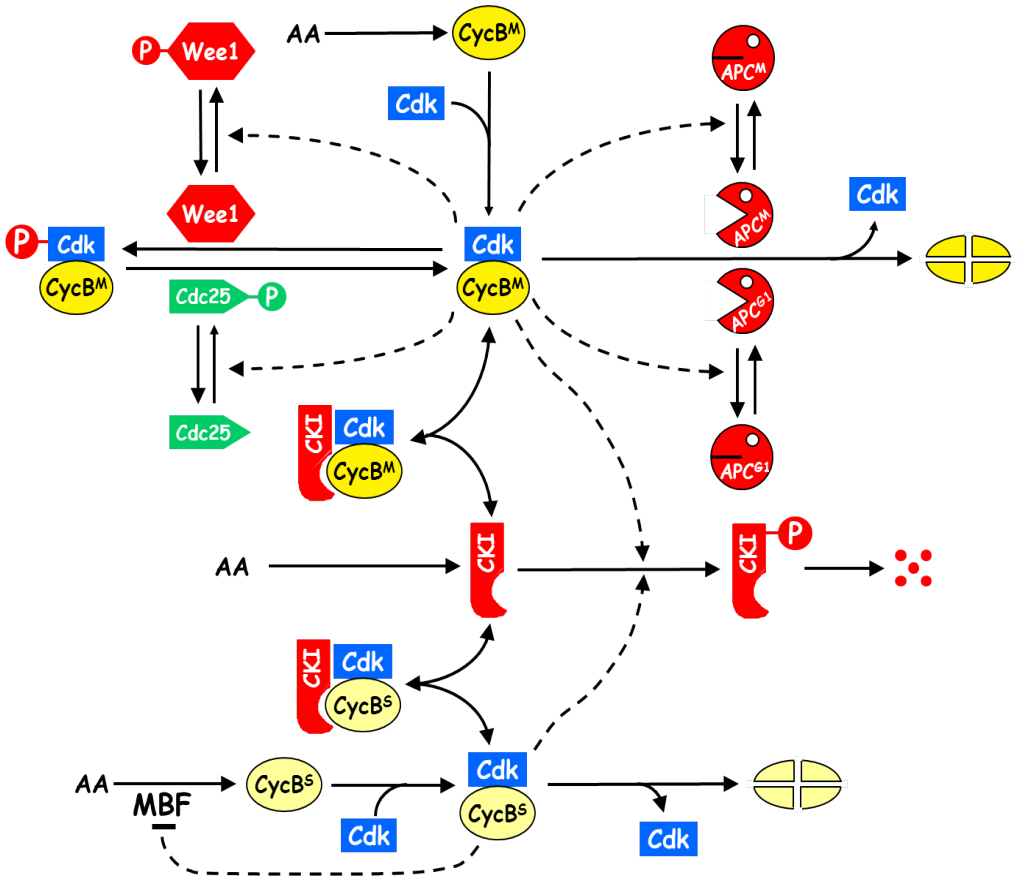

Figure 1.3: Multi-regulatory network of Cdk/Cyclin activities. Cdk activity is regulated in different ways including by sequential gene expression of regulatory proteins (e.g. synthesis of cyclin B), by association with inhibitory subunits (CKIs), by post-translational modifications (e.g. phosphorylation and dephosphorylation by Wee1 and Cdc25, respectively) and by degradation of control regulatory subunits (e.g. APC^{Cdh1}- and APC^{Cdc20}-dependent degradation of cyclin B). $CycB^{M}$ represents M cyclins; $CycB^{S}$ represents S cyclins; APC^{M} represents APC^{Cdc20} and APC^{G1} represents APC^{Cdh1}. 'AA' indicates amino acids. Solid lines refer to the biochemical reactions, and the dashed lines indicates regulatory interactions.

- **Regulation of Cdk/Cyclin kinase activity through gene transcription:** As mentioned earlier, cyclin levels oscillate throughout cell cycles and the synthesis of phase-specific cyclins is controlled by various transcription factors. For example, SCB-binding factor and MCB-binding factor, two transcription factors in budding

yeast, promote the transcription of the genes encoding the G1/S cyclin and S cyclins, respectively (Futcher, 2002; Lee et al., 2002). An Fkh2:Ndd1:Mcm1 complex is the transcription factor of Clb1, 2 and it activates the transcription of mitotic regulatory genes at the G2-to-M transition in budding yeast (Lydall et al., 1991).

- **Regulation of Cdk/Cyclin activity by stoichiometric inhibitors:** Cyclin dependent kinase inhibitors (CKIs) can bind to and inactivate Cdk/Cyclin complex. For example, stoichiometric inhibitors Sic1 in budding yeast and Rum1 in fission yeast play essential roles in promoting the M-to-G1 transition and stabilizing G1 state by suppressing Cdk1 activity. They are both potent inhibitors of Cdk1/$\mathrm{CycB^M}$ and Cdk1/$\mathrm{CycB^S}$, however, they have little inhibitory effect on Cdk1/G1-S-cyclins, whose activities raise from late G1 and promote the degradation of Sic1, Rum1 by phosphorylation (Sherr and Roberts, 1999). CKIs can be regulated by gene transcription as well. For instance, Swi5 is the transcription factor of Sic1 – a stoichiometric inhibitor of Cdk1/Clb2 – that activates the expression of genes at the M-to-G1 transition and in G1 phase (Moll et al., 1991).

- **Regulation of Cdk/Cyclin activity by post-translational modifications:** The activity of Cdk/Cyclin is also regulated through post-translational modifications, most commonly by phosphorylation and dephosphorylation. Phosphorylation at the tyrosine and another threonine residues on Cdks have the inhibitory effect on Cdk/$\mathrm{CycB^M}$ activity (Nurse, 1990; Nasmyth, 1993). Wee1 and Cdc25, the counteracting kinase and phosphatase, control this inhibitory process, and themselves are regulated by Cdk/$\mathrm{CycB^M}$ as well. Wee1 inhibits Cdk/$\mathrm{CycB^M}$ by phosphorylation and Cdc25 activates Cdk/$\mathrm{CycB^M}$ by removing the phosphor group. At the same time Cdk/$\mathrm{CycB^M}$ inactivates Wee1 and activates Cdc25 through its own kinase activity (Dunphy, 1994).

- **Regulation of Cdk/Cyclin activity by ubiquitin-dependent proteolysis:** Once the specific tasks in a certain phase of the cell cycle are completed, cyclins need to be targeted by ubiquitination for degradation. For example, anaphase promoting complex (APC), an E3 ubiquitin ligase, gets activated at the metaphase-to-

anaphase transition. APC together with its activator subunits Cdc20 and Cdh1, triggers ubiquitin-dependent proteolysis of $CycB^{M}$ and a large group of M phase substrates (Irniger, 2002; Futcher, 1996; Harper et al., 2002).

1.2.3 The major events of M phase in vertebrates

The mitotic phase of the cell cycle, where the most dramatic cellular changes occur, can be divided into successive steps according to the completion of specific morphologically distinct phases (Alberts et al., 2008): prophase, prometaphase, metaphase, anaphase and telophase (Fig. 1.4).

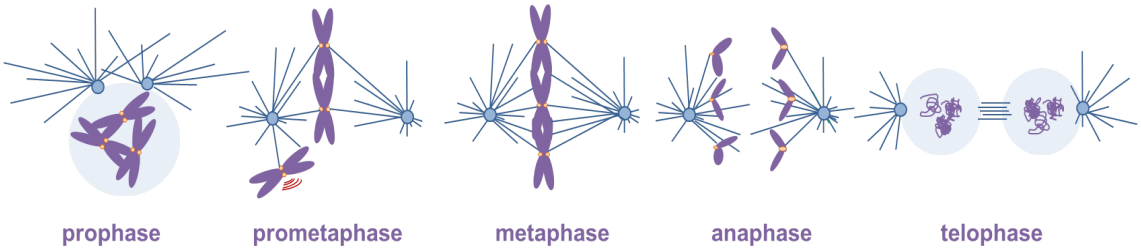

Figure 1.4: Major events of mitosis in a vertebrate cell. Mitosis can be divided into five different stages: prophase, prometaphase, metaphase, anaphase and telophase. In prophase, chromosomes undergo condensation. The nuclear envelope breaks down and chromosomes start to congress in prometaphase. Metaphase refers to the period when all the chromosomes have achieved biorientation. At anaphase onset, sister chromatids segregate and move to the opposite pole of the cell. Chromosomes are then decondensed, the spindle is disassembled and the nuclear envelope reforms in telophase. The figure is modified from Pines (2011).

• **Prophase:** In prophase, duplicated chromatins undergo condensation and are eventually packaged into compact condensed chromosomes, which is convenient for the chromosome separation in the later stage of mitosis (Morgan, 2007). At the same time, microtubule organizing centers (MTOCs), called “spindle pole bodies” (SPBs) in yeasts and “centrosomes” in animal cells, are separated and move to the opposite sides of the nucleus. The mitotic spindle starts to form by the bipolar microtubule array generated from both MTOCs.

• **Prometaphase:** In higher eukaryotes, nuclear envelope breaks down (NEBD) at the start of prometaphase and the nuclear barrier is removed to let microtubules from the opposite poles access the kinetochores on sister chromatids. The kinetochore is an as-

sembled multi-protein structure on the centromere of chromosomes serving as the major attachment platform for spindle microtubules. Unattached kinetochores send signals to prevent the next mitotic event, anaphase, taking place. The molecular framework of such a process is going to be introduced in detail in Section 1.2.4. Kinetochores are also responsible for monitoring chromosome movement, tension sensing and stabilization of microtubule-chromosome attachment in M phase (Morgan, 2007). Microtubules in mitosis are highly dynamic and they provide an efficient job to search and capture chromosomes by switching between states of growth and shrinkage (Maiato et al., 2004). Each pair of sister chromatids needs to be attached by the microtubules from both sides of the spindle respectively. The opposite pulling force by the microtubules is able to generate tension between sister kinetochores. Although the detailed tension sensing mechanism and signaling pathway still requires further study, it is widely accepted that tension is essential for proper chromosome biorientation and error correction mechanism (Clarke and Bachant, 2008).

• **Metaphase:** Metaphase defines the period when all the chromosomes have achieved biorientation and are locked at the metaphase plate, with sister chromatids attached to the opposite poles waiting for separation.

• **Anaphase:** At anaphase onset, a series of dramatic events such as sister chromatid segregation are triggered and drive cells to proceed from metaphase to anaphase. In early anaphase (**anaphase A**), sister chromatids are separated and move to the opposite poles of the cell. In late anaphase (**anaphase B**), segregated chromosomes move further apart from each other driven by an elongation of the mitotic spindle.

• **Telophase:** As the final step of mitosis, a series of reverse events of prometaphase and metaphase take place including chromosome decondensation, spindle disassembly and nuclear envelope reformation etc.

Cell division is completed by **cytokinesis** immediately after telophase, which responds for splitting the cytoplasm and form a pair of daughter cells.

1.2.4 The molecular framework of the spindle assembly checkpoint

The spindle assembly checkpoint (SAC) is a crucial regulatory machinery responsible for the successful metaphase-to-anaphase transition during mitosis. It makes sure all the previous activities have been completed and pre-requirements are satisfied before anaphase can occur. A simplified cartoon presented in Figure 1.5 is used to illustrate the mechanism of the SAC.

As previously discussed, cells enter prometaphase with highly dynamic spindle microtubules trying to search and capture chromosomes. Every chromosome must ultimately biorient at the metaphase plate with sister chromatids attached to the opposite poles (**amphitelic attachment**). Chromosome biorientation is ensured by an error-correction mechanism that is sensitive to the tension generated at kinetochores by the microtubules pulling force working against the resistance exerted by the cohesin rings. The error-correction mechanism destabilizes the attachment of spindle microtubules to kinetochores whenever the attachment is not under tension (Li and Nicklas, 1995). Common mis-attachments of microtubules and kinetochores are monotelic, syntelic and merotelic attachments (Walczak et al., 2010). **Monotelic attachment** denotes the kinetochore state that only has the microtubule from a single pole of the spindle attached. **Syntelic attachment** is the situation when both sister kinetochores are attached by the microtubules from the same pole, and **merotelic attachment** refers to the case where one kinetochore of a sister chromatid pair has microtubule attachment from both spindle poles (Fig. 1.5). These mis-attachments all lack of tension and are hence destabilized and corrected (Tanaka, 2010).

Aurora B kinase, a component of the chromosomal passenger complex (CPC), plays a central role in the error-correction process. The mis-attachments are thought to be unstable and such attachment can be weakened and reversed through phosphorylation by Aurora B located at the kinetochores (Lampson et al., 2004; Cheeseman et al., 2002; Iain M Cheeseman and Barnes, 2002). Bioriented chromosomes, in contrast, can be further stabilized and self-maintained (Westermann et al., 2006, 2005). Aurora B and its associated regulatory subunits will relocate to the middle of spindle during anaphase (Vázquez-

Novelle and Petronczki, 2010).

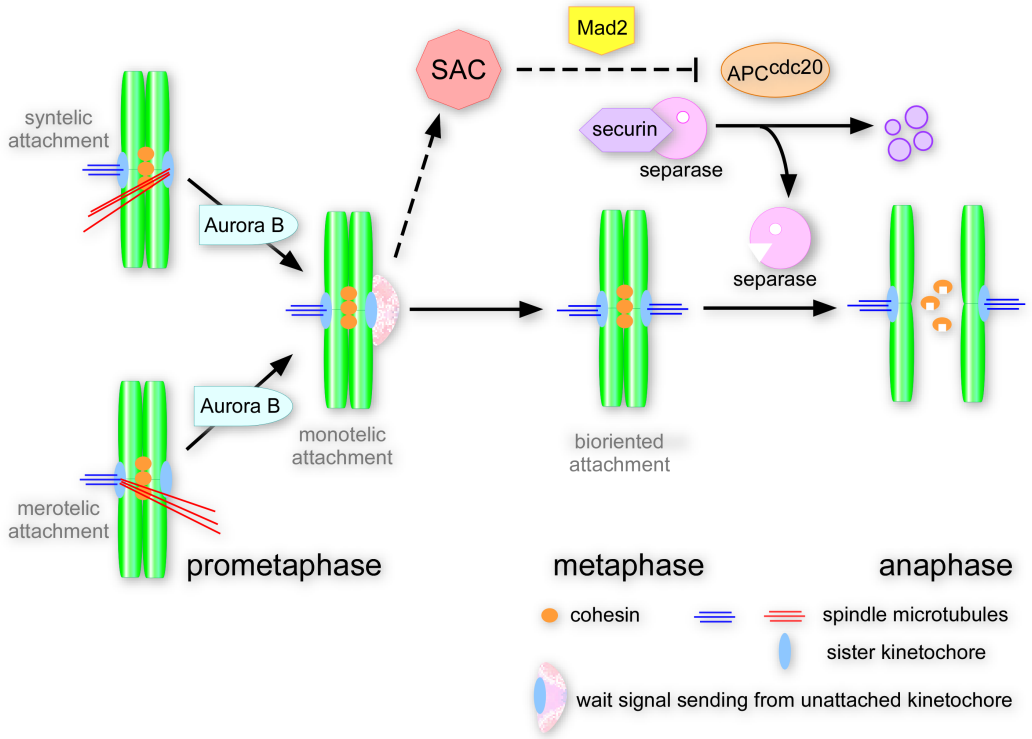

Figure 1.5: Molecular framework of the spindle assembly checkpoint. Cells enter M phase with replicated chromosomes, each containing a pair of sister chromatids held together by cohesin proteins. To ensure precise partitioning of the sister chromatids at anaphase onset, every chromosome must be bioriented. Chromosome biorientation is ensured by an error-correction mechanism that is sensitive to the tension generated at kinetochores by the spindle pulling force working against the resistance exerted by the cohesin rings. The error-correction mechanism destabilizes the microtubule-kinetochore mis-attachments if the chromosome is not under tension. Aurora-B kinase, a component of the chromosomal passenger complex, plays a central role in the error-correction process. In order to leave enough time to fix the mis-attachment, the SAC is activated by the unattached kinetochores to prevent the anaphase onset. The SAC acts through the spindle checkpoint proteins (e.g. Mad2) to sequester Cdc20, an activator of APC. Once all the chromosomes have properly bioriented on the metaphase plate, the SAC is inactive and Cdc20 is released. Active APC^{Cdc20} ubiquitinates securin, targeting it for destruction by the proteasome. Separase which is a protease inhibited by securin in turn can cleave the cohesive link between sister chromatids to trigger the anaphase.

Since chromosome biorientation and error correction require time, further progression of the cell cycle (i.e., cohesin cleavage at anaphase) needs to be prevented by the SAC. The SAC does so through the mitotic checkpoint complex (MCC) by inhibiting Cdc20, an activator of APC, thereby blocking the subsequent cell cycle events. Mad2, one of the best-understood components of MCC, can be used as an example to explain a potential mechanism of how the SAC works. Mad2 is found to exist at all the unattached kinetochores and shuttles back and forth between the unattached kinetochores and the cytoplasm (Howell et al., 2000; Simonetta et al., 2009). Structural and biochemical stud-

ies suggest that the unattached kinetochores serve as a catalytic platforms to modify the protein structure of Mad2, which accelerates its binding to and sequestering of Cdc20, resulting a positive feedback loop (Luo et al., 2004; Mapelli et al., 2007; Simonetta et al., 2009). This positive feedback on Mad2 activation can amplify the diffusible, inhibitory anaphase wait signal in cytoplasm when SAC is active. Mad2 disappears from the unattached kinetochores once the attachments have been completed. Thus the level of Mad2 at kinetochore is usually seen as an indicator of spindle assembly checkpoint activity (Morgan, 2007).

Several other checkpoint components are also involved in the SAC signaling pathway. Mps1, a protein kinase, its localization and kinase activity are required for the subsequent recruitment of other spindle checkpoint proteins (e.g. Mad1, Mad2, Bub1 and Bub2) on the unattached kinetochores (Zhao and Chen, 2006; Abrieu et al., 2001). Similar to Mad2, Mad1 is also found to accumulate at unattached kinetochores, it binds to Mad2 and helps it to form the complex formation of Mad2:Cdc20 (Antoni et al., 2005).

Once all the chromosomes have bioriented and are under tension, the SAC is almost immediately turned off. Cdc20 is released from MCC and active $\mathrm{APC}^{\mathrm{Cdc20}}$ ubiquitylates securin and cyclin B, targeting them for destruction by proteolysis. Separase, which is a protease inhibited by securin in turn can cleave the cohesin link between sister chromatids to trigger the anaphase. In vertebrate cells, separase activity is not only regulated through binding to securin but also inhibited by Cdk1 phosphorylation (Stemmann et al., 2001). APC-dependent degradation of both cyclin B and securin at metaphase will release separase inhibition in vertebrate cells.

1.3 Systems-level Feedback Controls Cell Cycle Progression

The cell cycle is an ordered sequence of events by which cells replicate their chromosomes and partition the identical sister chromatids to different daughter cells. All these

sophisticated events are precisely regulated by the cell cycle control system, which itself is a complicated molecular network machinery (Section 1.2). The system integration and coordination of multi-regulatory functions are realized through universal feedback loops embedded in the cell cycle control network (Pomerening, 2009). In a **positive (or double negative) feedback**, the output of a system has a positive effect on its own input. In a **negative feedback** by contrast, the output represses the input of the system (Tyson et al., 2003). The commonly used positive and negative feedback motifs in biological networks are shown in Figure 1.6. These feedback loops retain dynamic properties not evident in the individual components and execute crucial functions among the cell cycle transitions.

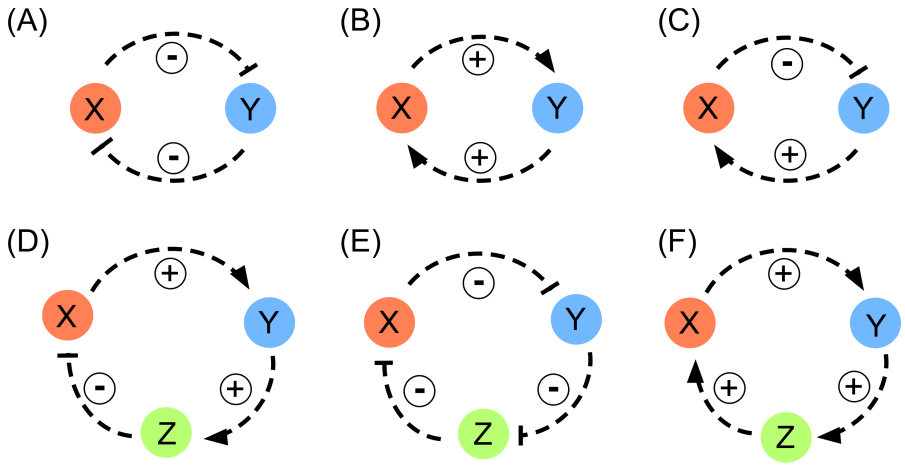

Figure 1.6: Positive and negative feedback motifs in biological networks. (A) Double-negative feedback loop between two components. (B) Positive feedback loop between two components. (C) Negative feedback loop between two components. (D) Negative feedback loop among three components. (E) Negative feedback loop among three components. (F) Positive feedback loop among three components. "⊕" presents the active effect, and "⊖" refers to the inhibitory effect.

1.3.1 Irreversible cell cycle transitions

Cell cycle progression is characterized by irreversible transitions: G1 to S phase (G1-to-S) transition, G2 to M phase (G2-to-M) transition and M to G1 phase (M-to-G1) transition (Fig. 1.1). Specific transient biochemical signals provoke these transitions, which are irreversible in the sense that, after the triggering signals disappear, the cell does not revert back to the previous cell-cycle phase but is continually ratcheted forward through the G1-S-G2-M sequence.

In Figure 1.7, a cartoon is used to illustrate the basic ideas of dynamic transitions in the different stages of the cell cycle. For simplification reasons, we use **CDK** to represent the collaborative activities of both Cdk1/M-cyclins and Cdk1/S-cyclins. The cell cycle is then split into two distinct states depending on CDK activity: a G1 state, where CDK activity is low and cells contain unreplicated chromosomes; and an S+G2+M state, where CDK activity is high and cells undergo chromosomes duplication, mitosis and cell division. At the boundaries between these two cell cycle states, two crucial transitions are defined: the G1-to-S transition and the M-to-G1 transition. Both G1 and S+G2+M states must be stable, and the two transitions between them need to be irreversible. An accidental transition from one state to the other will compromise the sequential order of cell cycle events. If, for example, a cell loses CDK activities before it has completed mitosis, then the next activation of CDK will trigger another round of genome replication and result in aneuploid cells (Broek et al., 1991). Hence, the underlying mechanisms that provide stability to the low- and high-CDK states and irreversibility to the transitions between these states are crucial for unidirectional progression through the cell cycle.

CDK activity is regulated by cyclin levels (through synthesis and degradation), by binding to CKIs, and by post-translational modifications (see Section 1.2.2). Many of the proteins regulating CDK activities are the phosphorylation targets by CDK as well. Feedback loops are therefore engaged in the CDK control network, and these feedbacks bring about dynamic attributes not exhibited in the individual components, i.e. "emergent properties" (Bruggeman et al., 2007; Alberghina et al., 2009). In the majority of cases, CDK down-regulates its inhibitory proteins, creating a double-negative (antagonistic) feedback loop. A positive feedback loop is established if CDK activates its own positive regulators. As introduced before, both of these network motifs can potentially create a bistable system with alternative stable steady states. Based on the experimental evidences and physiological arguments, Tyson and Novák (2008) have proposed that the CDK control network is a bistable system brought about by the regulatory feedback loops. The low- and high-activity states of CDK observed during the cell cycle are the two alternative stable steady states of this underlying control network (Novák et al., 2007; Tyson and Novák, 2008).

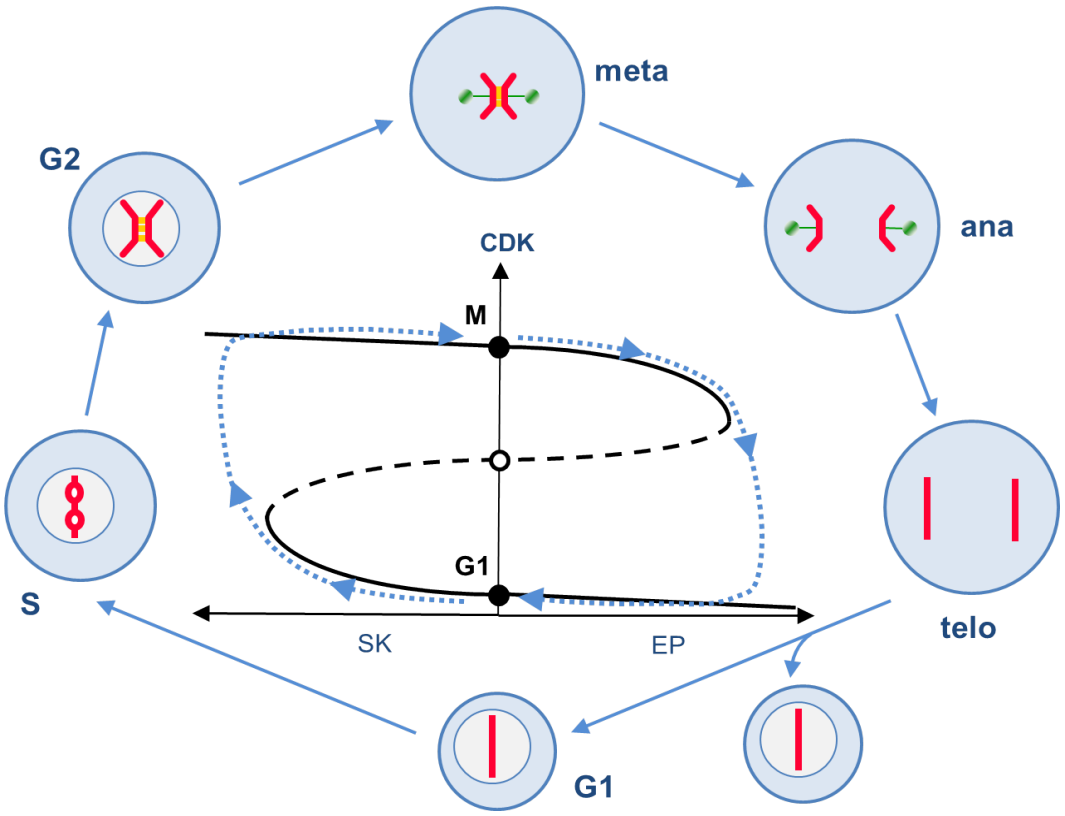

Figure 1.7: Alternative stable steady states of the eukaryotic cell cycle. Eukaryotic cell cycle can be divided into two stable steady states based on CDK activity: G1 state with low CDK activity, and S+G2+M state with high CDK activity. The two stable steady states are represented by continuous lines on the diagram, and they are separated by a locus of unstable steady states indicated by the dashed line. Each stable steady state is maintained by the specific positive (or double-negative) feedback loops that between CDK and its regulators. The transitions between the two stable states require 'helper proteins': Starter kinases (SKs) for the G1-to-S transition and Exit proteins (EPs) for the M-to-G1 transition. SKs destabilize the G1 state by inhibiting the inhibitor of CDK (and possibly by activating its activators). EPs have the opposite effect on the regulators of CDK, thereby promoting the system return to the G1 state. Eukaryotic cells move clockwise around this bistable switch, as indicated by the dashed blue trajectory (often referred to as a 'hysteresis loop') and the sequential order of cell cycle stages (G1-S-G2-metaphase-anaphase-telophase-G1) are surrounding the diagram. The figure is modified from Kapuy et al. (2009b).

Switching between the G1 and S+G2+M states is promoted by 'helper proteins'. Helper proteins are not integral components of the feedback loops that directly contribute to the bistability, but they provide driving force for cells progressing to one or the other direction. The helper proteins for the G1-to-S transition are 'Starter Kinases' (SKs) that downregulate the inhibitors of CDK (or activate its activators) and promote the entry into S phase. 'Exit Proteins' (EPs) work in the opposite way to destabilize the high CDK activity state through upregulation of CDK inhibitors, and thereby trigger the M-to-G1 transition (Fig. 1.7). Since the G1-to-S and M-to-G1 transitions flip the switch in opposite directions, the helper proteins for one transition often have inhibitory effect

on the other. Therefore, the corresponding helper proteins must only exist transiently during each transition. Otherwise cells would have to stuck at current stable steady state with constitutive impacts of the helper proteins. This transiency is usually achieved by negative feedback loops in the cell cycle control system. The SKs are downregulated by high CDK activities after the G1-to-S transition. By contrast, the EPs, whose activities are dependent on high CDK activity, are turn off after the M-to-G1 transition (Tyson and Novák, 2008; Kapuy et al., 2009b).

As a consequence of these negative feedback loops, after each transition a cycling cell returns to a neutral state of the control system (SKs = EPs = 0). In the neutral state, the control system is bistable. It locks into the high CDK activity state after the G1-to-S transition and into the low activity state after the M-to-G1 transition (Fig. 1.7). Consequently, this bistable switch with the negative feedback loops drives the cell cycle control system in a clockwise direction like a ratchet. This ratcheting effect ('hysteresis') ensures strict alternation between the low- and high-CDK activity states, thereby guaranteeing the correct order of cell cycle events.

Progression around this hysteresis loop is also monitored by checkpoint mechanisms. These surveillance mechanisms keep the control system in one of the stable states until certain conditions are satisfied. The spindle assembly checkpoint stabilizes the high CDK activity state by inhibiting the activation of EPs until all the chromosomes are properly attached to the bipolar spindle (Section 1.2.4). The G1 steady state is stabilized by a 'size control' mechanism which blocks the activation of SKs until cells grow to a critical size (Jorgensen and Tyers, 2004). This mechanism coordinates cell growth with DNA replication and mitosis – the events controlled by the bistable switching mechanism.

In the following subsections, the typical feedback loops and some experimental evidences of bistability in the irreversible cell cycle progression are specified and summarized to explain the systems-level feedback point of view in the cell cycle transition.

1.3.2 The G1-to-S transition

The transition from G1 phase to S phase is also a "point of no return", which not only defines the entry into S phase, but also makes the point at which a cell to divide (Reddy, 1994).

Take budding yeast as an example, starter kinase (Cdk1/Cln3), which only become active when cells grow to a critical size, triggers the gene expression of G1/S cyclins (Cln1,2) and $CycB^S$ (Clb5,6) at the G1-to-S transition (Start). Cdk1/$CycB^S$ immediately turns into an inactive form by binding to its stoichiometric inhibitor Sic1. Whereas, Cdk1/G1-S-cyclins, which are not inhibited by Sic1, are active and initiate the destruction of Sic1 through their kinase activities. Partial degradation of Sic1 results in releasing Cdk1/$CycB^S$ which again can phosphorylate Sic1 and accelerates its own activation (Verma et al., 1997). In this case, the stoichiometric inhibitors (CKIs) bind to and inhibit Cdk1/CycB in G1 phase. Degradation of CKIs is promoted by Cdk1/CycB phosphorylation at the G1-to-S transition. CKIs inactivate Cdk1/CycB and Cdk1/CycB promotes CKI destruction, thus a double-negative feedback loop is established (Fig. 1.8).

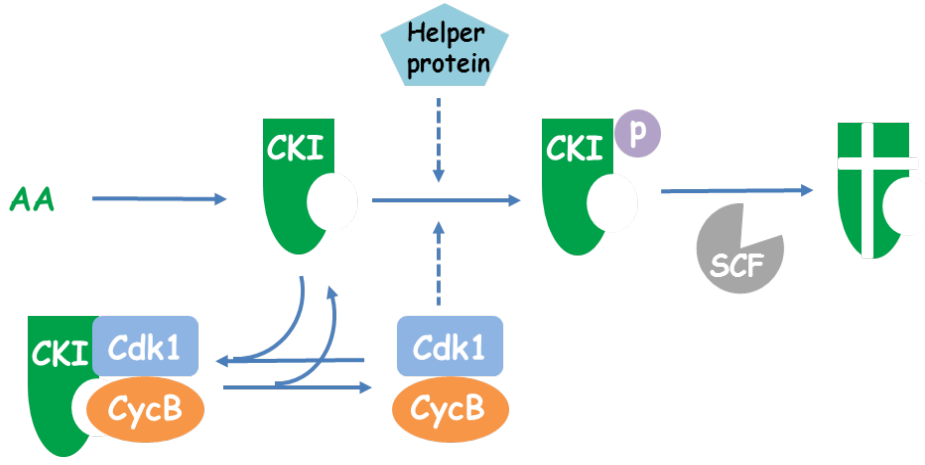

Figure 1.8: The underlying feedback loops governing the G1-to-S cell cycle transition. In G1 phase, Cdk1/CycB activity is inhibited through binding to its stoichiometric inhibitor CKI. At late G1, once Cdk1/CycB is activated and it will phosphorylate CKI to promote its degradation through ubiquitination by SCF, creating a double negative feedback. The activation of Cdk1/CycB is first initialized by the helper protein 'Starter kinase' which is often resistant to the inhibitory effect from CKI. The figure is modified from Novák et al. (2007).

The bistability of the G1-to-S transition has been experimentally tested and proved by Cross et al. (2002) in budding yeast. Cells were blocked in G1 phase with low CDK activity by depriving all the starter kinases (Cdk1/Cln), which are required for the G1-to-S transition. Blocked cells were then induced to synthesize one of the starter cyclins (Cln3) for different periods of time. At the end of this period, Cln3 synthesis was turned off and one of the EPs (Cdc14) was also inactivated to prevent mitotic exit. From the bistable point of view (Fig. 1.7): the system is initially blocked in the G1 stable steady state, and SK induction pushes the system transiently to the left, causing a rise of CDK activity once the SK activity exceeds the threshold. When SK induction and EP activity are turned off at the end of the treatment, the system moves to the right to the neutral position (SK = EP = 0) in Figure 1.7. In the neutral position the system must decide between the two alternative stable states. Which steady state wins depends on whether the system lands below or above the unstable steady state in the neutral position (the open circle in Fig. 1.7). Where it ends up will be determined by how much CDK activity can accumulate during the pulse of SK synthesis. As predicted, Cross et al. (2002) found that cell could exist either in G1 phase or in M phase, depending on the length of starter kinase treatment. In the experiment, a large majority of cells stayed unbudded, could not accumulate Clb2, and returned to the stable G1 phase after a short pulse of SK. While, after a longer pulse most of the cells moved to the stable mitotic state (Cross et al., 2002).

1.3.3 The G2-to-M transition

The G2-to-M transition is the process controlling the entry into mitosis. Mitosis will be prevented, for example, when DNA replication is not completed or chromosomes are damaged (Lukas et al., 2004). Cdk1/CycB is kept inactive by Wee1 phosphorylation in G2 phase and its activity is restored by the phosphatase Cdc25 at mitotic entry. Active Cdk1/CycB can both inactivate Wee1 and activate Cdc25 by phosphorylation, creating a double-negative and a positive feedback loops (Fig. 1.9). The double negative and positive feedback loops work cooperatively creating a robust bistable system with two stable steady states: a G2 state with inactive Cdk1/CycB, active Wee1 and inactive Cdc25;

and an M state with active Cdk1/CycB, active Cdc25 and inactive Wee1. The interlocking feedback loops cause abrupt activation of Cdk1/CycB at the G2-to-M transition (Solomon et al., 1990; Novák and Tyson, 1993; Pomerening et al., 2005).

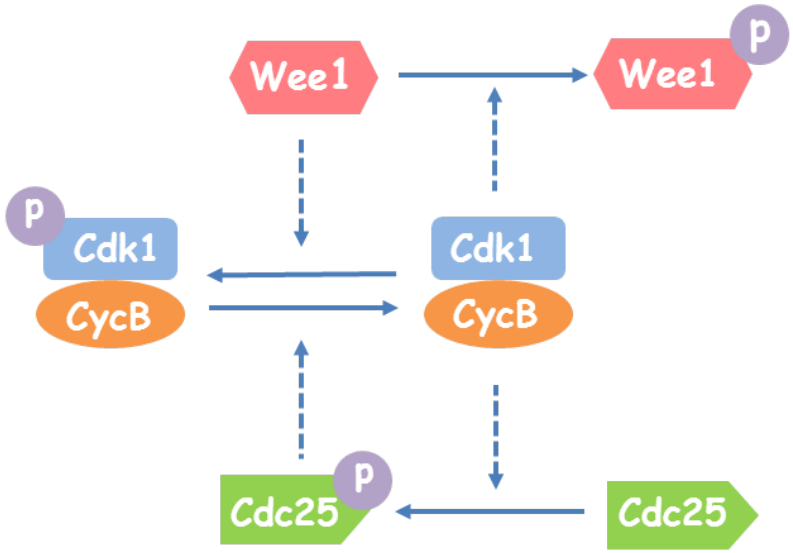

Figure 1.9: The underlying feedback loops governing the G2-to-M cell cycle transition. In G2 phase, kinase Wee1 is responsible for keeping Cdk1/CycB activity low by tyrosine-residue phosphorylation on Cdk1. At G2-to-M transition, phosphatase Cdc25 activates Cdk1/CycB by removing the phosphor group. The active Cdk1/CycB controls its regulators through inactivation Wee1 and activation Cdc25 creating a double negative and a positive feedback loop. The figure is modified from Novák et al. (2007).

The irreversible transition from G2 to M phase is achieved by a hysteretic response, a result from the bistability created by the positive/double-negative feedback loops arising from the phosphorylation and dephosphorylation of Wee1, Cdc25 and Cdk1/CycB. The **hysteretic response** in this context means that there are two distinct cyclin B level thresholds for the entry and the exit of the mitosis, respectively: T_a and T_i. The minimum cyclin B level that requires to maintain the mitotic state, T_i is remarkably lower than the maximum level of cyclin B required to enter the M phase, T_a. The existence of hysteresis has been experimentally proved using *Xenopus laevis* egg extracts (Sha et al., 2003). In the experiment, different amount of nondegradable cyclin B was added in *Xenopus* cell extract before it started the first mitotic cycle. The endogenous synthesis of cyclins was blocked by CHX (cycloheximide) either before or during the M phase of the first cell cycle. The measured activation threshold T_a for mitosis I is around $32 \sim 40$ nM and the inactivation threshold T_i is around $16 \sim 24$ nM. The intermediate concentrations between 24 and 32

nM are able to sustain either the G2 or the M state, depending on the start conditions, thus providing the further proof of the bistability of the G2-to-M transition (Sha et al., 2003).

1.3.4 The M-to-G1 transition

In this thesis, the term "**M-to-G1 transition**" is used for the cell cycle transition taking place after metaphase, and consists of two irreversible subsequent processes: **metaphase-to-anaphase transition**: partitioning of sister chromatids into daughter nuclei and **mitotic exit**: cell division and return to the G1 phase.

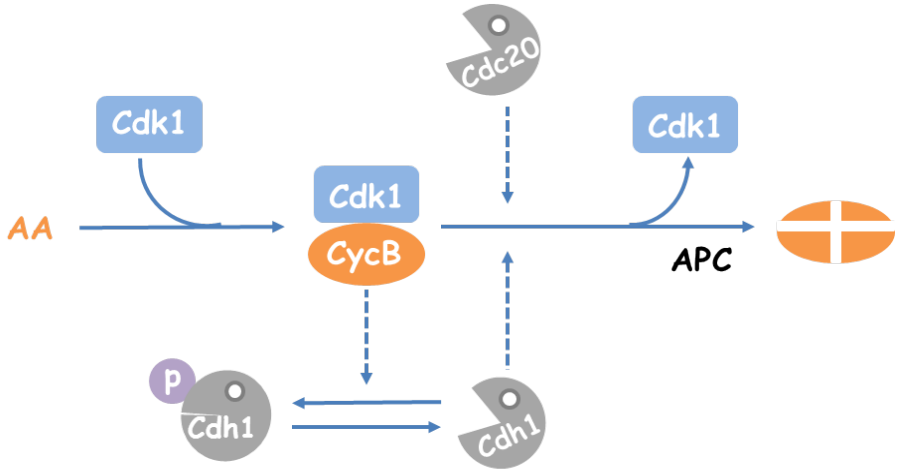

Figure 1.10: The underlying feedback loops governing the M-to-G1 cell cycle transition. Cyclin B proteolysis is promoted by $\mathrm{APC}^{\mathrm{Cdc20}}$ and $\mathrm{APC}^{\mathrm{Cdh1}}$. Cdh1 activity is also regulated by Cdk1/CycB phosphorylation: Cdh1 is only active in the dephosphorylated state, which is prevented by high Cdk1/CycB activity in M phase. Thus, a double-negative feedback is created between Cdk1/CycB and $\mathrm{APC}^{\mathrm{Cdh1}}$. The figure is modified from Novák et al. (2007).

For the M-to-G1 transition to occur, Cdk1/CycB activity needs to be downregulated and the previously phosphorylated Cdk1/CycB substrates need to be dephosphorylated. This process is initially triggered by $\mathrm{APC}^{\mathrm{Cdc20}}$, which targets cyclin B for degradation and thereby inhibits Cdk1/CycB activity. Cdh1, another activator of APC, is only active in the dephosphorylated form. When Cdk1/CycB activity is high in early mitosis, it phosphorylates Cdh1 and prevents it binding to the APC. At the end of M phase when Cdk1/CycB activity is decreasing, Cdh1 gets activated and $\mathrm{APC}^{\mathrm{Cdh1}}$ continues the destruction of mitotic regulatory proteins (Jaspersen et al., 1998). A double negative feedback is created between Cdk1/CycB and $\mathrm{APC}^{\mathrm{Cdh1}}$ (Fig. 1.10). $\mathrm{APC}^{\mathrm{Cdh1}}$ activity stays

high throughout the G1 phase in order to maintain the inhibitory effect on Cdk1/CycB.

López-Avilés et al. (2009) recently provided some experimental evidence for the irreversibility of mitotic exit in budding yeast. In the experiment, cells were arrested in mitosis with high Cdk1/CycB activity by Cdc20 depletion, then cyclin B degradation was turned on for different durations. Fifty minutes degradation of cyclin B promoted cell to exit from mitosis (assayed by spindle disassembly and some re-accumulation of CKI etc.). However, the termination of cyclin B degradation allowed itself to re-accumulate and pushed CKI down to the mitotic level through the feedback loops. By contrast, 10 minutes longer of cyclin B degradation was able to maintain the low Cdk1/CycB activity and kept the system in the G1 state (López-Avilés et al., 2009). The experiment suggests that cyclin degradation is not sufficient to make mitotic exit irreversible. Irreversibility of mitotic exit in this experimental condition, requires accumulation of CKI above a threshold rather than cyclin degradation per se.

Since studying the specific feedback loops and molecular networks underlying the M-to-G1 transition is a major focus of this work, we will re-investigate this experiment in more detail in later chapters.

1.4 Stochasticity in the Cell Cycle

Although the biological systems and their functions are highly regulated and cellular events occur in a precise and robust manner, noise and fluctuations are ubiquitous. There is growing empirical evidence for the effects of stochasticity on gene expression, cell proliferation, cell size control, cellular decision making, cell differentiation, cell cycle durations and cellular aging etc. (Novick and Weiner, 1957; Smith and Whitney, 1980; Sveiczer et al., 1996; McAdams and Arkin, 1999; Foo et al., 2011; Balzsi et al., 2011). In this section, the sources and the consequences of cellular stochasticity are going to be introduced, the functioning and regulation mechanism of noise are going to be reviewed and its effects on cell cycle will be discussed.

1.4.1 The origins and sources of noise

The cell is a noisy system with inevitable stochasticity due to the nature of chemical reactions, molecular number fluctuations and the random movement of molecules. The fundamental origins of stochasticity and heterogeneity are both temporal and spatial, and will become more significant for small molecule numbers (Kampen, 2007).

Temporal origin of noise: Temporal noise originates from the nature of the chemical reactions. The occurrence of each reaction has a certain probability and it changes over time. This interaction probability relies on the molecule number and the rate constant which follows a particular distribution (e.g. Poisson) depends on the system's properties. If there is only a limited number of reactant molecules, the probability of an interacting event is small and reaction arises rarely. The discrete steps of the reactions become obvious and therefore these temporal fluctuation will have a more pronounced effect and the system can be very noisy (Kuthan, 2005; Takahashi et al., 2010).

Spatial origin of noise: For a chemical reaction to occur, the reactant molecules first have to collide with each other. The cytoplasm or other organelles are heterogeneous environments with spatial difference in molecular concentration. Additionally, cellular compartments further cause subcellular localizations of biological entities and create spatial barriers for reactions to take place (Alberts et al., 2008). In prokaryotic cells, which have fewer membrane-bound compartments compared to the eukaryotes, molecular movements mainly depend on the diffusion process. In this case, the free diffusion can be rate-limiting and potentially introduces noise to the reactions. In eukaryotic cells, the trans-localization of molecules either by active or passive transport are also stochastic processes in nature. The spatial origin of noise can induce substantial stochastic effects on biological processes (Kaern et al., 2005; Dobrzynski et al., 2007; Takahashi et al., 2010)

The origins of noise and its consequences are commonly recognized and intensively studied in the context of the gene expression networks. According to the contributing factors to the fluctuations, the biological noise in gene regulatory circuits can be decom-

posed into two categories (Raser and O'Shea, 2005): intrinsic noise and extrinsic noise. **Intrinsic noise** refers to the inherent stochasticity within a single cell that directly causes variations in the expression of a particular gene, even though the genotype and the other intracellular conditions are identical. For instance, randomness of promoter binding and fluctuations in the copy number of messenger RNA in the process of gene transcription and translation contribute to the intrinsic noise. **Extrinsic noise** refers to the fluctuations in biomolecular levels, physiological conditions or biological processes due to cell-to-cell variation (e.g. various copy number of RNA polymerase, ribosomes) that indirectly contribute to the gene expression and overall cellular variations. These two noise sources have been characterized, distinguished and measured by a series of elegantly designed experiments (Swain et al., 2002; Elowitz et al., 2002; Blake et al., 2003; Raser and O'Shea, 2004; Newman et al., 2006).

The stochasticity of biological systems is the result of noise generated from multiple aspects. The different kinds of noise are interdependent at gene level, network level and organism level, and are often amplified or suppressed by the regulatory pathways (Kaern et al., 2005). It is arbitrary to attribute the observed fluctuations to a single origin. Examples have shown that different fluctuation patterns generated from the distinct noise sources could produce similar features as are observed in experiments and it is hard to differentiate and separate them (Paulsson, 2004; Pedraza and Paulsson, 2008). Huh and Paulsson propose that cell-to-cell heterogeneity is caused by the stochastic partitioning of molecules and segregation of cellular components at cell division rather than being caused by noise in gene expression (Huh and Paulsson, 2011).

1.4.2 Function and regulation of noise

Cells are intrinsically stochastic systems, however, cellular decisions and their corresponding outcomes are usually well-controlled and, to a large extent, demonstrate robustness and determination. It looks as though undesired molecular fluctuations are actively suppressed and that the key biological signals are properly stabilized, indicating that there must exist noise regulatory mechanisms to attenuate the non-operational noise (Brugge-

man et al., 2009). This section reviews the functions of noise and how noise is controlled and modified within the cell by biological processes.

Negative feedback loops are probably one of the most straightforward and commonly used approaches by living organisms to filter and reduce the noise level. The function of negative feedback loops in the cellular noise-attenuating mechanism has been experimentally confirmed (Austin et al., 2006; Yu et al., 2008). Becskei and Serrano constructed simple gene circuits to produce green fluorescent protein (EGFP) under the control of negative feedback loops in *Escherichia coli*. The detected distribution of fluorescent intensities of EGFP in the transcription network with the negative feedback is concentrated and bunched up, while the one without the negative feedback is more spread out and highly variable (Becskei and Serrano, 2000). This suggests that negative autoregulation helps the transcription network gain more stability.

Coherent feed-forward loops (Coherent FFLs), as a ubiquitous and highly conserved motif in transcription networks, have been shown both theoretically (Mangan and Alon, 2003; Ghosh et al., 2005) and experimentally (Mangan et al., 2003) to act as sign-sensitive delay elements that can efficiently filter noise and shorten the response time of gene transcription.

The stochasticity in a cell does not always exhibit disfavoured feature as its name implies, rather it sometimes derives and characterizes important biological operational functions (Rao et al., 2002; Kaern et al., 2005; Simpson et al., 2009). Physiological heterogeneity in a population resulting from fluctuations in gene expression provides a mechanism to increase the probability of survival rates in response to severe or unusual environmental conditions. Such population diversity generated without the requirement for gene mutation might be a very efficient adaptation of living organisms to respond to any sudden changes in environmental conditions (Balzsi et al., 2011). A well studied example of noise-induced population heterogeneity is the random switch between the lytic and the lysogenic pathways of phage lambda during infection. Pathway selection is made by competition of two independently synthesized regulatory proteins to control the pathway

switch point. Stochastic fluctuations can cause one pathway to be chosen over the other (Arkin et al., 1998).

While unwanted background noise must be attenuated and minimized, the operational noise needs to be amplified and exploited. Positive feedback loops in reaction networks can generate switch-like, bistable responses (Ferrell, 2002). They are frequently involved in gene expression and signalling pathways to enhance the effects of noise (Hasty et al., 2000; Rao et al., 2002; Wilkinson, 2009). Becskei et al. (2001) incorporated a positive feedback based on the tetracycline-controlled transactivator in a gene circuit of GFP in budding yeast. They discovered that the yeast cells with the positive feedback exhibited the binary response to the transcriptional activator. While only the graded responds were shown in the cells with constitutively expressed activator. They found that the noise in the gene expression network played a critical role in flipping the switch, partitioning the population into distinct subgroups. These results suggest that positive feedback loops can amplify noise and make its role more notable.

In summary, the studies of the functions and regulations of biological noise are never independent and should not be isolated from each other. The cellular noise control mechanism cannot be solely attributed to a single feedback loop or an elementary motif, instead it arises from multiple regulatory networks. The interplay between operational functionality and side effect of noise will become even more challenging in complex biological pathways (Waltermann and Klipp, 2011).

1.4.3 The cell cycle and noise

Although the cell cycle in general is stable and strictly controlled by multi-regulatory mechanism, many studies have shown that stochasticity and random events can have strong effects in different stages of the cell cycle (Steuer, 2004; Okabe and Sasai, 2007; Braunewell and Bornholdt, 2007; Kar et al., 2009). Cell cycle length is highly variable even among different cells of the same species (Smith and Martin, 1973). Fluctuations in the regulatory protein expression levels may cause this heterogeneous timing of the

cellular events.

Noise is also a key participant at the cellular decision making during differentiation and proliferation. An excellent review by Losick and Desplan (2008) describes the advantage and necessity of such a stochasticity when acquiring cell fate in development biology. Stochastic cell-to-cell variability has been found to have contribution to the activation of apoptosis signaling pathway response to the external death-inducing stimuli (Skommer et al., 2011). An example would be cells are usually arrested in mitosis and eventually trigger apoptosis when treated with anti-mitotic drug, however, many experiments have reported that there is small percentage of cells can escape from the apoptosis through the alternative mitotic slippage pathways (Brito and Rieder, 2006; Brito et al., 2008; Yang et al., 2009). A possible explanation for this phenomenon is that mitotic death and mitotic slippage are independent pathways stochastically compete with each other to determine a cell's fate (Huang et al., 2010).

Other than the negative feedback and the feed-forward loops (see Section 1.4.2), cell cycle checkpoints are recognized as another regulatory mechanism to control and suppress the significance of noise to ensure normal cell cycle progression (Hartwell and Weinert, 1989; Lew, 2000; Murakami and Nurse, 2000). The noise resistance of spindle assembly checkpoint has been researched both experimentally (Rieder et al., 1994) and theoretically (Doncic et al., 2006). If the spindle assembly checkpoint is dysfunctional and mitotic errors are not corrected, stochastic events can induce severe consequence, e.g. aneuploid cells, a potential cause of chromosomal instability (CIN), can be produced (Kops et al., 2005). Weakened or impaired mitotic checkpoint signals are observed in several tumor cell lines (Fang and Zhang, 2011).

The non-symmetrical division and randomness of molecular partitioning during cytokinesis of the cell cycle supplement the stochasticity of gene expression and can cause similar persistent fluctuations (Kar et al., 2009; Huh and Paulsson, 2011). However, the roles of stochasticity and its relationship with cell cycle are still unclear.

Chapter 2

Aim of the Thesis

The discovery of cyclin degradation has become a paradigm for the regulation of cell cycle progression (Evans et al., 1983), as many other cell cycle regulators were found to be abruptly degraded in specific phases of the cycle. Therefore, it is commonplace to explain irreversible cell cycle transitions by the irreversibility of protein degradation (Lodish et al., 2004). However, there is a flaw in this simple, appealing view: in a living cell, protein degradation is counteracted by protein synthesis. Consequently, although protein degradation is thermodynamically irreversible, the concentration of a cellular protein may rise or fall reversibly with the shifting kinetic balance between protein synthesis and degradation (Novák et al., 2007). As an alternative to the paradigm that protein degradation provides directionality to the cell cycle, Novák and Tyson have been arguing that the irreversibility of cell cycle transitions is an emergent property of feedback circuits in the molecular mechanism of Cdk/Cyclin control (Tyson et al., 1995; Novák and Tyson, 1997; Novák et al., 1998, 2007, 2010).

In particular, positive (and/or double negative) feedback circuits in these regulatory networks are thought to create one-way toggle switches with two alternative stable steady states: the pre-transition state and the post-transition state. The cell cycle checkpoints hold cells in the pre-transition state until a triggering signal is generated to induce a switch to the post-transition state. The switch is irreversible and the cell is locked in the post-transition state even after the inducing signal disappears. This systems view of

irreversibility was first proposed based on computational modelling (Novák and Tyson, 1993; Chen et al., 2004; Novák et al., 2007) and was later supported by experimental data (Cross et al., 2002; Pomerening et al., 2003; Sha et al., 2003) for both the G1-to-S and the G2-to-M cell cycle transitions.

Another important irreversible cell cycle progression, the M-to-G1 transition, consists of two subsequent irreversible processes: the metaphase-to-anaphase transition and mitotic exit. The irreversibility of metaphase-to-anaphase transition seems to be caused by thermodynamic reasons rather than network dynamic considerations: Sister chromatids are held together at metaphase by 'cohesin' rings that oppose the pulling forces of the mitotic spindle on the bioriented chromosomes. Anaphase is initiated by separase activation, which cleaves the cohesin rings, thereby allowing the sister chromatids to be pulled apart by the spindle forces. Cohesin cleavage by proteolysis is an irreversible process because the metaphase alignment of the chromosomes cannot be recreated simply by re-synthesizing cohesin proteins. Once the sister chromatids have been pulled apart by the shortening microtubules, they cannot come back together again spontaneously even if the inducing signal were removed and the cohesin rings were re-sealed. Thus, the separation of sister-chromatids at anaphase is an apparent exception to the feedback view of irreversible cell cycle transitions.

The irreversibility of mitotic exit has also been attributed to the degradation of M cyclins at the end of mitosis (Minshull et al., 1989; Lodish et al., 2004). Despite some experimental evidence in budding yeast suggests that mitotic exit is not only due to the proteolysis of cyclin B (López-Avilés et al., 2009), the whole issue of M-to-G1 transition seems to be more complicated and many details remain unclear. Here several key questions are raised that challenge the conventional view of the M-to-G1 irreversible transition.

Question I: Is the M-to-G1 transition irreversible because of systems-level feedback, as is the case for the G1-to-S and the G2-to-M transitions?

The irreversibility of M-to-G1 transition is the synergistic effect of two subsequent steps: metaphase-to-anaphase transition and mitotic exit. Each substep is an irreversible process itself and will be studied individually throughout this thesis. If it could be shown that both the metaphase-to-anaphase transition and mitotic exit are made irreversible by system-level feedback, this would directly lead to the second question.

Question II: What are the specific molecular feedback loops that create such one-way toggle switches in each individual process, i.e. the metaphase-to-anaphase transition and mitotic exit?

Feedback loops are the most common regulatory motifs which play various roles in the cell cycle control system. The essential feedback loops in the M-to-G1 transition will be examined and their importance and necessity in the irreversible cell cycle transitions will be evaluated.

As previously stated in Chapter 1, noise is ubiquitous in cells and can have crucial roles in the process of cellular decision making. There is growing experimental evidence for the heterogeneity in cell populations in response to perturbations in metaphase-to-anaphase transition and mitotic exit. Noise is a possible cause of this heterogeneous behaviour (Balzsi et al., 2011).

Question III: Will the system's bistability and dynamic behaviour be affected by the fluctuations in number of regulatory molecules? How stable and robust is the M-to-G1 transition against those noisy perturbations?

One objective of this work is to resolve the above biological questions with regard to the M-to-G1 transition. We propose that the molecular networks of both the metaphase-to-anaphase transition and mitotic exit are indeed bistable systems. Thus, we explain the irreversibility of these transitions as a consequence of system-level feedback rather than a consequence of the proteolysis of single regulatory proteins (e.g. cyclin B, cohesin). In particular, I am going to illustrate these arguments within a stochastic framework. De-

terministic and stochastic models of the cell cycle are developed and numerical analyses are applied to help us understand the experimental data and to provide a more convincing interpretation of the two irreversible transitions in M-to-G1: the metaphase-to-anaphase transition and the mitotic exit. **The second objective** of the work is to develop a reasonable approximation to convert a deterministic model to a stochastic model, to present a work flow to transform the reaction network into stochastic model, and finally to identify a strategy to quantitatively compare features of noisy dynamics, as well as similarities and differences between stochastic and deterministic approaches.

According to the sequential order of addressing the questions raised for the M-to-G1 transition, the whole dissertation is divided into two main parts:

Part One describes stochastic modelling of the spindle assembly checkpoint. First of all, I constructed a simplified deterministic model that focus on the underlying regulatory feedback loops causing the bistability of the anaphase switch (Chapter 4). Subsequently, the stochastic model was build by integrating noise, fine tuning all the numerical parameters and modifying other computational aspects of the model. The stochastic model is further used to explain the sensitivity and the robustness of the spindle assembly checkpoint. The model is able to reproduce a significant number of experimental observations and the population heterogeneity found in cells (Chapter 5).

Part Two is the stochastic modelling of the mitotic exit. One goal was to identify the specific feedback loops that have major contributions to the irreversibility of the mitotic exit in different species. Two model organisms, budding yeast (Chapter 6) and mammalian cells (Chapter 7), are studied. In spite of the fact that the detailed molecular networks of mitotic exit are very different in budding yeast and mammalian cells, the dynamic properties are similar. The bistability of the transitions are both confirmed and successfully reproduced using the stochastic simulation.

Chapter 3

Computational Modelling, Methods and Software

Cell cycle regulation mechanisms have been intensively studied by biochemical, cell biological and molecular biological methods (Schafer, 1998). Many existing experimental data and hypotheses await further validation, and traditional wet-lab experiments often are insufficient for a thorough understanding of complex biological systems. Therefore, a large number of mathematical and computational methods have been developed. Mathematical modeling and control analysis of dynamic systems have become widely used approaches in helping biologists to make more reasonable and more convincing interpretations of their experimental observations (Alves et al., 2006; Beard, 2011).

This chapter first gives a brief introduction into one of the most commonly used deterministic modelling methods, ordinary differential equations (ODEs) and its related analytical approaches, such as phase plane analysis, bifurcation analysis and rate plot. The importance and benefits of stochastic modelling have gradually been recognized because of the increasing evidence of stochasticity in cells and its effects on cellular decision making during cell cycle transitions (see Chapter1). The next part of the chapter introduces and compares two stochastic algorithms: the Gillespie algorithm and the chemical Langevin equation, which are both intensively used throughout this thesis. The software packages and computational tools used for conducting the studies in this work are listed

at the end of this chapter.

3.1 Deterministic Modelling

Mathematical models have become necessary and invaluable tools to quantitatively study the dynamic behaviour of biological systems. Deterministic modelling is a long-standing approach to describe the systems dynamics in cell cycle control networks (Tyson et al., 2001; Sible and Tyson, 2007). The solutions of any deterministic models, as implied by its name, are predetermined and predictable whenever the equations and the initial conditions are given (Robinson, 2004; Wilkinson, 2009).

3.1.1 Ordinary differential equations

One of the most widely used deterministic approaches is to describe a dynamic system by a set of ordinary differential equations and calculate the time evolutions of the state variables in the system. $\mathbf{C}_j(t)$ is the concentration of a species j at time t and $R(\mathbf{C}_j) = R_j$ denotes the reaction rate law, which describes the reaction chemical kinetics. A typical reaction rate equation (RRE) which expresses the rate of concentration change of a chemical species $\mathbf{C}_j$ is presented in Equation 3.1. A collection of ODEs that characterizes a biological network is usually a nonlinear dynamic system and cannot be solved explicitly, except in special cases. Computer simulations are therefore required to find the approximate numerical solutions. A common way to visualize the solutions is to plot a time course $\mathbf{C}_j(t)$ against t.

$$\frac{d\,\mathbf{C}_j(t)}{dt} = R(\mathbf{C}_j) = V_{synthesis} + V_{activation} - V_{degradation} - V_{inactivation} \tag{3.1}$$

ODEs are suitable for modelling systems that are well mixed and perfectly homogeneous, with a sufficiently large number of each chemical component. All possible reactions take place continuously and simultaneously. These assumptions hold approximately true in a lot of biological systems (Alves et al., 2006; Resat et al., 2009).

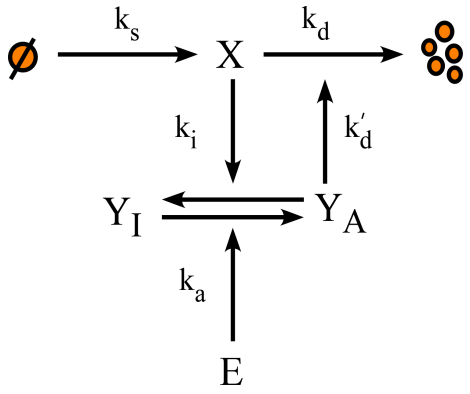

Figure 3.1: Example of formulating ODEs for the chemical species with mass action and Michaelis-Menten kinetics. The detailed explanation of the figure please see the main text (Section 3.1.1). The parameter values used for simulation and numerical analysis are listed in the following: the dimensionless constants are $E = 1$, $Y_T = 1$, $K_a^m = 0.05$, $K_i^m = 0.08$, and the rate constants are $k_s = 0.04\ min^{-1}$, $k_d = 0.04\ min^{-1}$, $k'_d = 1\ min^{-1}$, $k_a = 1\ min^{-1}$ and $k_i = 8\ min^{-1}$. The example is modified from Fall et al. (2002).

As an example, the simple biochemical reaction network in Figure 3.1 is introduced to illustrate different mathematical modelling techniques. The interactions can be described by a pair of ODEs (Eqs. 3.2 - 3.3).

$$\frac{d\,[X]}{dt} = k_s - k_d \cdot X - k'_d \cdot X \cdot Y_A \tag{3.2}$$

$$\frac{d\,[Y_A]}{dt} = k_a \cdot \frac{E \cdot (Y_T - Y_A)}{K_a^m + (Y_T - Y_A)} - k_i \cdot \frac{X \cdot Y_A}{K_i^m + Y_A} \tag{3.3}$$

Chemical components X and Y mutually inhibit each other. Species X has a constant zero-order synthesis rate k_s and it can be degraded either spontaneously with rate $k_d X$ or Y_A-dependently with rate $k'_d X Y_A$. Species Y exists in two forms: an active form Y_A and an inactive form Y_I. We assume that the total concentration of Y is constant, i.e. $Y_T = Y_I + Y_A$. The two forms can be transformed into each other based on Michaelis-Menten kinetics with V_{max} equal to $k_i X$ and $k_a E$, respectively. Y_A also promotes degradation of X with a rate constant k'_d. The synthesis and degradation reactions of X are modelled using the law of mass action. The **law of mass action** kinetics states that "the rate of an elementary reaction (a reaction that proceeds through a single transition state and one mechanistic step) is proportional to the product of the quantitative level of the participating molecules" (Lund, 1965). The activation and inactivation of Y are catalyzed by extra molecules and are formulated with **Michaelis-Menten equations**, where

K_a^m and K_i^m are the Michaelis constants. Michaelis-Menten kinetics is used to describe enzyme catalyzed reactions, where an intermediate step of forming a complex between an enzyme and a substrate is required before a product can be generated. For more details please see Johnson and Goody (2011), a new translation of the original paper from Michaelis and Menten (1913).

When the chemical switches between Y_A and Y_I are both governed by Michaelis-Menten kinetics, the equilibrium solution of Y can be obtained by the **Goldbeter-Koshland equation** (Goldbeter and Koshland, 1981). The Goldbeter-Koshland equation is often used to generate switch-like (ultrasensitive) behaviour in modelling biological systems (Tyson et al., 2003).

3.1.2 Methods to analyse deterministic dynamical systems

The well-established theories of nonlinear dynamics are widely applied in the numerical analysis of biological systems (Strogatz, 1994; Tyson et al., 2003). The explicit numerical solutions are not always necessary, as qualitative behaviour of the dynamical system is often able to provide sufficient information. In these cases, rate plot, bifurcation analysis and phase plane analysis can be applied. These methodologies are going to be illustrated using the same toy model given in Figure 3.1 and by Equations. 3.2 - 3.3.

Rate plot: A rate plot illustrates the rate changes of the forward and reverse reactions of a specific dynamic variable. Taking Equation 3.3 as an example, its right-hand side can be separated into two parts: the activation rate $V_{Y_A}^+$ (Eq. 3.4) and the inactivation rate $V_{Y_A}^-$ (Eq. 3.5).

$$V_{Y_A}^+ = k_a \cdot \frac{E \cdot (Y_T - Y_A)}{K_a^m + (Y_T - Y_A)} \tag{3.4}$$

$$V_{Y_A}^- = k_i \cdot \frac{X \cdot Y_A}{K_i^m + Y_A} \tag{3.5}$$

If we assume that X is already at steady state, then X can be presented as $k_s/(k_d +$

$k'_d \cdot Y_A)$ and replace X in Equation 3.5. The function of $V^-_{Y_A}$ can be written in the form of Equation 3.6.

$$V^-_{Y_A} = \frac{k_i \cdot k_s \cdot Y_A}{(K_i^m + Y_A) \cdot (k_d + k'_d \cdot Y_A)} \tag{3.6}$$

The activation ($V^+_{Y_A}$) and inactivation ($V^-_{Y_A}$) rates of Y_A are plotted using Equation 3.4 and Equation 3.6, as shown in Figure 3.2. $V^+_{Y_A}$ (yellow) and $V^-_{Y_A}$ (green) rates are drawn for the increasing values of Y_A from 0 to 1. Both are nonlinear curves. The points of intersections for the two curves are the steady states of Y_A where $V^+_{Y_A} = V^-_{Y_A}$. P1 and P3 are the stable steady states and P2 is the unstable steady state. The slope difference between these two curves also give intuitive information about how fast (or slow) the system will move to or from the steady states. The greater the difference in slope, the faster the dynamic variable changes (Tyson et al., 2003).

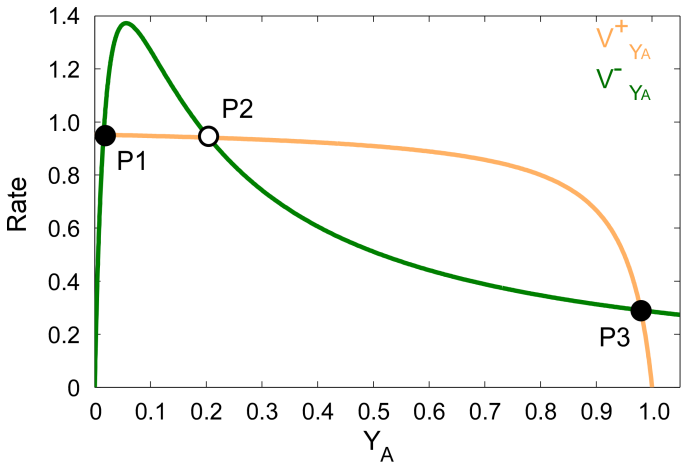

Figure 3.2: Activation and inactivation rates of Y_A calculated from Equation 3.4 and Equation 3.6. Activation rate $V^+_{Y_A}$ and inactivation rate $V^-_{Y_A}$ of Y_A are drawn for the increasing values of Y_A from 0 to 1 with orange and green curves respectively. The intersections of the two curves are the steady states of Y_A where $V^+_{Y_A} = V^-_{Y_A}$. P1 and P3 are the stable steady states and P2 is the unstable steady state. Parameter values are the same as given in Figure 3.1.

Bifurcation analysis: Parameters in a ODE model characterize specific biological processes and represent different cellular functions, changing or adjusting the parameter values mimic cells response to stimuli (e.g. protein deletion or over-expression). Bifurcation diagrams (more commonly referred to as "signal-response curves" by biologists) are used to calculate the steady state responses to specific parameters with varying values in particular ranges (Tyson et al., 2003). The appealing feature of the bifurcation plot is that

a small smooth parameter value shift can lead to a dramatic change of the long-term response, usually the stability of the system. In the bifurcation diagram the stable solutions are presented using solid lines while the unstable solutions are plotted as dotted lines.

An example of bifurcation diagram generated from the toy model is given in Figure 3.3. Continuously varying parameter E creates the discontinuous response of X. The solid lines show how the stable steady states depend on the value of E and the intermediate dotted line traces the unstable steady states. The system is bistable (i.e. has two stable steady states) between two critical points ($E1$, $E2$). $E1$ and $E2$ are the points where the system has sudden qualitative behaviour change, called **saddle node bifurcation point** (Robinson, 2004).

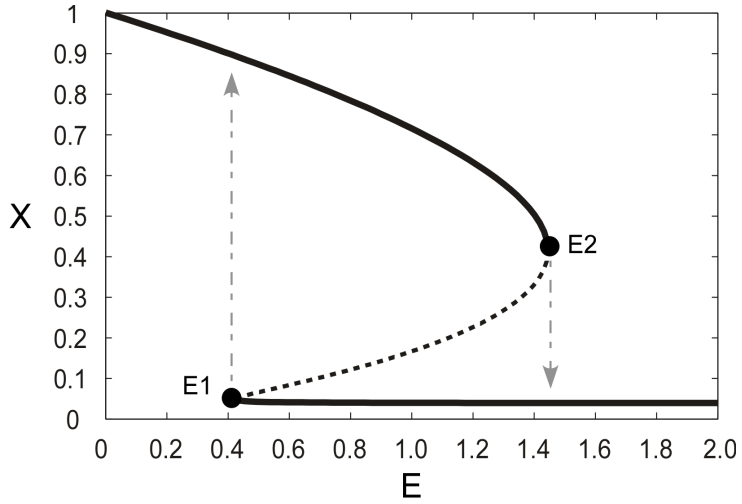

Figure 3.3: Bifurcation diagram of X responds to E for Equation 3.2 and Equation 3.3. The steady state concentration of X is plotted as a function of the bifurcation parameter E. The saddle node bifurcations occur at $E1$ = 0.43 and $E2$ = 1.45. For the intermediate values of E ($0.43 < E < 1.45$), Equation 3.2 and Equation 3.3 have three steady states. Parameter values are given in Figure 3.1.

Phase plane analysis: Phase space defines all the possible states of all the variables in a dynamical system (Strogatz, 1994). For a system containing n components, its corresponding phase space is n-dimensional. Since it is impossible to visualize a phase space which has more than three dimensions, two-dimensional phase spaces (also called a phase plane) is frequently used. Given any initial conditions (x_0, y_0) on the phase plane, there are trajectories ($x(\Delta t)$, $y(\Delta t)$) describing in which direction and how fast the variables move in the next small time interval Δt. However, there is no further information about where

the system will eventually settle within the phase plane as $t \to \infty$. In this case, nullclines, where the change of the variables equals zero, can be plotted to display the steady state solutions of the state variables. The phase plane portrait calculated from Equations 3.7 and 3.8 is plotted in Figure 3.4. The orange curve represents the X nullcline ($\dot{X} = 0$) and the blue curve is the Y_A nullcline ($\dot{Y_A} = 0$), where the two curves intersect, both $\dot{X} = 0$ and $\dot{Y_A} = 0$. These are the steady states of the system and can be further divided into two different categories depending on the stability: **stable steady states** (the solid circles) are when small perturbation away from these points will attract back to the original states along time; while small disturbances from the **unstable steady states** (the empty circle) will grow in time and repel the trajectories (Tyson et al., 2001).

$$X\ nullcline : 0 = k_s - k_d \cdot X - k'_d \cdot X \cdot Y_A \tag{3.7}$$

$$Y_A\ nullcline : 0 = k_a \cdot \frac{E \cdot (Y_T - Y_A)}{K_a^m + (Y_T - Y_A)} - k_i \cdot \frac{X \cdot Y_A}{K_i^m + Y_A} \tag{3.8}$$

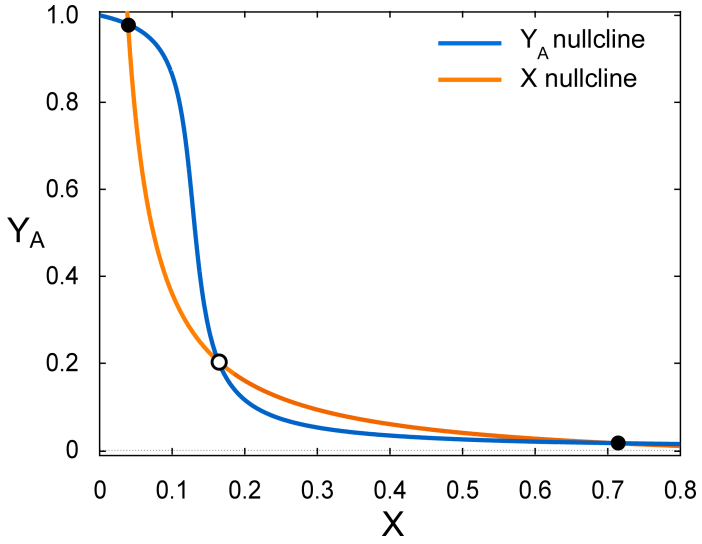

Figure 3.4: Phase plane portrait of the toy model by Equation 3.2 and Equation 3.3. The orange curve represents X nullcline ($\dot{X} = 0$) plotted from Equation 3.7 and the blue curve is Y_A nullcline ($\dot{Y_A} = 0$) plotted from Equation 3.8. The points where the two curves intersect are called steady states. This system has three steady states: stable steady states (the solid circles) and unstable steady states (the empty circle). Parameter values are the same as given in Figure 3.1.

Rate plot, bifurcation diagram and phase plane are all closely connected concepts. They each provide different visual displays of dynamical systems and supply qualitative inform-

ation about the molecular network. The choice of these approaches depends upon the nature of the problems and these methodologies will be applied in the following chapters.

3.2 Stochastic Modelling

Deterministic approaches are powerful in modelling of dynamic systems only if the molecular abundance is high and the dynamic behaviour of the system is definite and predictable. There are two situations where a deterministic approach often encounters difficulties or failure: when low copy number of molecules has important influence on the system or when stochastic fluctuation induces multiple outcomes. In both circumstances, the underlying deterministic formulation of the chemical kinetics are unrealistic and consequently the predictions are unreliable (Rao et al., 2002). It is commonly accepted that stochastic modelling is necessary to capture certain biological systems in a realistic and proper way (Wilkinson., 2006; Wilkinson, 2009).

In contrast to deterministic methods, stochastic approaches are implemented within a likelihood framework and assign specific probabilities to chemical interactions. The interactive reactants are visualized as individual particles and reactions take place in a discrete, step-wise manner. Several classic stochastic algorithms are going to be introduced in the following sections.

3.2.1 Chemical master equations

Let us consider a system that contains the mixture of N chemical species $\{S_1, ..., S_N\}$, which interact through M chemical reactions $\{R_1, ..., R_M\}$. $X_i(t)$ denotes the number of molecules of species S_i in the system at time t. The probability for a reaction R_j to take place in the next infinitesimal time interval dt is given by $a_j(\mathbf{x})dt$, where $a_j(\mathbf{x})$ is the propensity function (Eq. 3.9). The state-change vector is represented by $\mathbf{v}_j$, where v_{ji} is the molecular number change in S_i caused by reaction R_j, so the system will jump from state $\mathbf{x}$ to state $\mathbf{x} + \mathbf{v}_j$.

$$a_j(\mathbf{x})dt \stackrel{\text{def}}{=} Prob\,\{R_j\ occurs\ in\ [\ t, t+dt\ ) \mid \mathbf{X}(t) = \mathbf{x}\} \tag{3.9}$$

Define $P(\mathbf{x}, t\,|\mathbf{x}_0, t_0)$ as the probability of a chemical system existing in the state $\mathbf{X}(t)$ at time t given the initial condition as $\mathbf{X}(t_0) = \mathbf{x}_0$ (Eq. 3.10).

$$P(\mathbf{x}, t \mid \mathbf{x}_0, t_0) \stackrel{\text{def}}{=} Prob\,\{\mathbf{X}(t) = \mathrm{x},\ given\ \mathbf{X}(t_0) = \mathbf{x}_0\} \tag{3.10}$$

$P(\mathbf{x}, t+dt \mid \mathbf{x}_0, t_0)$, the probability of achieving the current state covers two situations: one situation is that the system moves from state $(\mathbf{x} - \mathbf{v_j})$ to the current state $\mathbf{x}$ provided that the reaction R_j takes place, and the second possibility is that the system has already been under the molecular distribution $\mathbf{x}$ at time t and in order to remain in the current state requires no reactions can happen in the time interval dt. The sum of the probabilities of these two situations bring about the format in Equation 3.11.

$$\begin{aligned} P(\mathbf{x}, t+dt \mid \mathbf{x}_0, t_0) = &\sum_{j=1}^{M} P(\mathbf{x} - \mathbf{v}_j, t \mid \mathbf{x}_0, t_0) \cdot [a_j(\mathbf{x} - \mathbf{v_j})dt] \\ &+\ P(\mathbf{x}, t\,|\mathbf{x}_0, t_0) \cdot [1 - \sum_{j=1}^{M} a_j(\mathbf{x})dt] \end{aligned} \tag{3.11}$$

We may reformulate the above equation into Equation 3.12 by giving it the common format of the Chemical Master Equation (CME). The CME is the time derivative equation that describes the probability that each species will have a specific molecular population at a given time (McQuarrie, 1967; Gillespie, 1992).

$$\frac{\partial P(\mathbf{x}, t \mid \mathbf{x}_0, t_0)}{\partial t} = \sum_{j=1}^{M} [a_j(\mathbf{x} - \mathbf{v_j}) \cdot P(\mathbf{x} - \mathbf{v}_j, t \mid \mathbf{x}_0, t_0) - a_j(\mathbf{x}) \cdot P(\mathbf{x}, t \mid \mathbf{x}_0, t_0)] \tag{3.12}$$

The chemical master equation includes the sum of all possible states and transitions of the system to achieve the current state $\mathbf{X}(t)$. With the exception of a few simple and specific cases, where it can be solved analytically (McQuarrie, 1967), it is almost impossible to explicitly derive the solutions from the CME due to its large number of

possible combinations of reactant molecules for a realistic biological network.

3.2.2 The Gillespie algorithm

In 1976, Daniel T. Gillespie developed the **Stochastic Simulation Algorithm (SSA)**, also widely known as the **Gillespie algorithm**, which offers a computational simulation to numerically generate time trajectories of the molecular populations in exact accordance with the CME (Gillespie, 1976, 1977).

The SSA considers a chemical system that is in thermal equilibrium at a constant temperature, so the positions of the molecules become randomized throughout the system volume V. Only the events that could potentially change the population levels of chemical species are taken into account, while the nonreactive molecular collisions are ignored. At each step of the SSA, it explicitly simulates every chemical interacting event by deciding which reaction will occur and at what time. Given a current state of the system, the next state only depends on this current state, hence, $(\mathbf{X}(t))_{t\geq 0}$ is a continuous-time Markov chain (CTMC). The Gillespie algorithm uses a Monte Carlo procedure for numerically generating time trajectories of CTMC in terms of propensity functions (the Monte Carlo is going to be explained in Section 3.2.5). The goal is to estimate the state vector $\mathbf{X}(t) \equiv (X_1(t), ..., X_N(t))$ given that the system was in state $\mathbf{X}(t_0) = \mathbf{x}_0$ at the initial time t_0. The discrete event simulation of the SSA is implemented by the following essential steps:

Step 1. Initialization: set the initial number of molecules for each species in the system $\mathbf{x} = \mathbf{x}_0$ and set the simulation start time $t = t_0$.

Step 2. Calculation of propensity functions: on the basis of the current molecular abundance, calculate the propensity function $a_j(\mathbf{x})$ for each reaction and their sum $a_0(\mathbf{x}) = \sum_{j=1}^{M} a_j(\mathbf{x})$.

Step 3. Generate the time τ to the next reaction: $\tau = \frac{1}{a_0(\mathbf{x})} \ln\left(\frac{1}{r_1}\right)$, where r_1 is a uniformly distributed random number from the unit interval [0, 1].

Step 4. Choose the next reaction: pick up an integer j from the reaction index satisfying $\sum_{j'=1}^{j} a_{j'}(\mathbf{x}) \geq r_2 \cdot a_0(\mathbf{x}) > \sum_{j'=1}^{j-1} a_{j'}(\mathbf{x})$, where r_2 is also a random number from the uniform distribution in the unit interval [0, 1].

Step 5. Update and Iteration: update $t = t+\tau$ and $\mathbf{x} = \mathbf{x}+\mathbf{v}_{ij}$ accordingly. Record the new state and simulation time $(\mathbf{x}, t)$. If $t < t_{end}$, the simulation is not yet finished, return to Step 2; else end the simulation.

The outputs generated from the SSA are time course trajectories of the dynamic system in the form of molecular abundance as a function of time. Given the same initial condition, each simulation is independent and different from the others. They are 'exact' in the sense that every realization obtained from the SSA is based on the probability distribution solution deduced from the CME at any time point. The SSA provides an alternative simulation approach to gain new perception of the stochastic features of the system without the necessity of solving the CME.

The fundamental assumption of the Gillespie algorithm is that all the reactions have to take place in a homogeneous system in a way that positions and velocities of the individual molecules do not matter, only a minority of reactions occur among the overwhelming number of molecular collisions. This assumption is justified for two reasons: most elastic collisions will not cause a chemical reaction and will not change the population of molecules; secondly, well-mixed gas-phase systems are more or less well stirred as described in the assumptions. However, this may not be true in living cells where molecules locate in different compartments such as nucleus and cytoplasm. Spatial stochastic influence on biological system is more complicated and less well understood than the non-spatial stochastic effects (Shanbhag and Rao, 2003). Grima and Schnell (2008) suggest that

when consider both spatial and internal interaction noise effects can induce a quantitatively different physiological predictions compared with the stochasticity in homogeneous environment alone.

The problem with the Gillespie approach compared to the deterministic methods is that it requires prohibitive computational time, especially when models become complex and more components and reactions are involved. Therefore many extensions have been developed to improve the efficiency and speed of the SSA. For example, Gibson and Bruck reformulated the SSA into "next-reaction method", which greatly increases the speed by pre-computing the index queue of propensity functions and storing in a special designed memory structure (Gibson and Bruck, 2000). The tau-leaping method that simulates the reacting system using a Poisson approximation to take time steps that leap over many reaction events (Cao et al., 2006). A detailed review of the SSA, its improvements and approximations can be found in Gillespie (2007).

3.2.3 Chemical Langevin equations

Although it is simple and straightforward to implement, the SSA can be impractically slow because it keeps on tracking every individual reaction event. In this case, the chemical Langevin equation (CLE), another commonly used stochastic simulation method, is usually chosen when the computational capacity for the SSA becomes a challenge. However, the CLE calculates the approximate solution of the CME where certain requirements need to be satisfied (Gillespie, 2000; Coffey et al., 2004).

Let $F_j(\mathbf{x}_t, \Delta t)$ denote the number of reactions R_j that occur in the time interval $[t, t + \Delta t]$, then the state change of species S_i during that time is $\sum_{j=1}^{M} F_j(\mathbf{x}_t, \Delta t) v_{ji}$. Thus an alternate way to characterize the dynamic evolution of particle number X_i in the stochastic system is shown in Equation 3.13.

$$X_i(t + \Delta t) = X_i(t) + \sum_{j=1}^{M} v_{ji} \cdot F_j(\mathbf{x}_t, \Delta t) \quad (i = 1, ..., N) \tag{3.13}$$

Directly solving $F_j(\mathbf{x}_t, \Delta t)$ is no easier than solving the CME, however, Equation 3.13 can be reformulated and simplified under two reasonable conditions.

- **Condition (i)**: If Δt is small so that the new propensity function $a_j(\mathbf{x_t})$ evaluated at $t + \Delta t$ is not distinguishable from its original value $a_j(\mathbf{x_t})$, then the number of reactions R_j occurring in the time interval $[t, t + \Delta t]$ become independent events with the average probability $a_j(\mathbf{x_t})$. As a consequence of condition (i), $F_j(\mathbf{x}_t, \Delta t)$ can be approximated by a Poisson random variable $\mathcal{P}_j(a_j(\mathbf{x_t}), \Delta t)$ and Equation 3.13 can be rewritten into Equation 3.14.

$$X_i(t + \Delta t) = X_i(t) + \sum_{j=1}^{M} v_{ji} \cdot \mathcal{P}_j(a_j(\mathbf{x}_t), \Delta t) \quad (i = 1, ..., N) \tag{3.14}$$

- **Condition (ii)**: If Δt is large enough that many reactions are expected to take place within the time interval $[t, t + \Delta t]$, then the expected value of $\mathcal{P}_j(a_j(x_t), \Delta t)$ is much larger than 1 (Eq. 3.15).

$$E[\mathcal{P}_j(a_j(x_t), \Delta t)] = a_j(\mathbf{x}_t)\Delta t \gg 1, \quad j \in [1, M] \tag{3.15}$$

  With condition (ii) being satisfied, the Poisson random variable $\mathcal{P}_j(a_j(\mathbf{x}_t), \Delta t)$ can be further approximated into a normal random variable N_j with both mean and variance equal to $a_j(\mathbf{x}_t)\Delta t$ and Equation 3.14 is further approximated into the form of Equation 3.16.

$$X_i(t + \Delta t) = X_i(t) + \sum_{j=1}^{M} v_{ji} \cdot N_j(a_j(\mathbf{x}_t)\Delta t, a_j(\mathbf{x}_t)\Delta t) \tag{3.16}$$

Substitute the normal random variable $N_j(a_j(\mathbf{x}_t)\Delta t, a_j(\mathbf{x}_t)\Delta t)$ by a standard normal random variable $N_j(0, 1)$ using linear combinations, then $N_j(a_j(\mathbf{x}_t)\Delta t, a_j(\mathbf{x}_t)\Delta t) = a_j(\mathbf{x}_t)\Delta t + N_j(0, 1) \cdot \sqrt{a_j(\mathbf{x}_t)\Delta t}$. Equation 3.16 can be rearranged into the following

form:

$$\begin{aligned} X_i(t+\Delta t) - X_i(t) &= \sum_{j=1}^{M} v_{ji} \cdot (a_j(\mathbf{x}_t)\Delta t + \sqrt{a_j(\mathbf{x}_t)\Delta t} \cdot N_j(0,1)) \\ &= \sum_{j=1}^{M} v_{ji} \cdot a_j(\mathbf{x}_t)\Delta t + \sum_{j=1}^{M} v_{ji} \cdot \sqrt{a_j(\mathbf{x}_t)} \cdot \frac{N_j(0,1)\cdot \Delta t}{\sqrt{\Delta t}} \end{aligned} \tag{3.17}$$

Assume Δt in both conditions is infinitesimal and replaced by dt. $N_j(0,1)\cdot\Delta t$ can be substituted by the Gaussian white noise $W_j(t)$ with definition $W_j(t) = \lim_{dt\to 0} N(0, 1/dt)$. The chemical Langevin equation can be derived (Eq. 3.18).

$$\begin{aligned} \frac{X_i(t+\Delta t) - X_i(t)}{\Delta t} &= \sum_{j=1}^{M} v_{ji} \cdot a_j(\mathbf{x}_t) + \sum_{j=1}^{M} v_{ji} \cdot \sqrt{a_j(\mathbf{x}_t)} \cdot \frac{N_j(0,1)}{\sqrt{\Delta t}} \\ \frac{d\, X_i(t)}{dt} &= \sum_{j=1}^{M} v_{ji} a_j(\mathbf{x}_t) + \sum_{j=1}^{M} v_{ji} \sqrt{a_j(\mathbf{x}_t)}\, W_j(t) \quad (i = 1, ..., N) \end{aligned} \tag{3.18}$$

The condition (i) and (ii) appear to contradict each other; however both requirements can be fulfilled simultaneously when the reactant molecules are sufficiently large. The detailed proof and discussion of the circumstances of existence can be found in Gillespie (2000, 2009).

During the process of approximation, discrete non-negative integer of species in the CME is approximated as a continuous stochastic random variable in CLE. As a type of stochastic differential equations (SDEs), the CLE in Equation 3.18 is presented in a form which contains a deterministic part $\sum_{j=1}^{M} v_{ji} a_j(\mathbf{x}_t)$, and an additional random effect term $\sum_{j=1}^{M} v_{ji} \sqrt{a_j(\mathbf{x}_t)}\, W_j(t)$. The resulting solutions of the CLE are stochastic processes (Oksendal, 2007). The stochastic term is neglectable compared to the deterministic term under the "thermodynamic limit" when $X_i \to \infty$, $V \to \infty$ and $X_i/V = constant$, thus the CLE is abbreviated into the RRE with deterministic and continuous kinetics.

As an intermediate approach from the SSA to the RRE, the CLE plays the trade offs between accuracy and efficiency. The advantage of the CLE method is that its inclusion

of stochastic elements in the operation of dynamical systems, and the computation is performed in a relatively fast manner compared to the SSA approach. However, the CLE method may generate undesired solutions (e.g. negative or unrealistic values for the concentration) for modelling the biological systems if no attention is paid to the selection of the value for the parameters.

3.2.4 Other stochastic modelling approaches

In addition to the SSA and the CLE approaches, a number of stochastic modeling techniques have been applied to model biological phenomena (Wilkinson, 2009). Recently, various applications of Stochastic Petri Nets (SPNs) have become popular tools used in stochastic modelling (Goss and Peccoud, 1998; Mura and Csiksz-Nagy, 2008; Toni et al., 2011; Csiksz-Nagy and Mura, 2011). The SPNs not only provide a graphical representation of the reacting components but they also capture the dynamics of the stochastic molecular processes in a system (Marsan, 1989; Haas, 2010). SPNs consist of four different building blocks based on the description of a discrete-event system: "places" which represent different chemical species and biological entities; "tokens" which indicate the molecular quantities of each species within places; "transitions" which describe the interactions among the species and "arcs" which serve as a connection between reactants and products via transitions (Wilkinson., 2006).

Probabilistic Boolean Networks (PBNs) incorporate the uncertainty (noise) into the deterministic Boolean networks (BNs) and assign the transition probabilities between different states (Shmulevich et al., 2002). The dynamic evolution of PBNs also follows the properties of Markov Chain (Wilkinson., 2006). The structural properties and the steady-state probability distribution of the PBNs can provide an insight of robustness and sensitivity of the modelled pathways (Li et al., 2004; Yuping et al., 2006; Zhang et al., 2007).

The hybrid simulation method partitions fast and slow reactions of a system into different subsets. It approximates the fast reactions as a continuous process and describes

the slow dynamics using the stochastic simulation algorithm (Salis and Kaznessis, 2005). The hybrid stochastic methods can significantly speed up the simulations, especially in the systems including reactions that take place in different time scales (Cao et al., 2006).

These stochastic modelling approaches have been intensively studied in recent decades and have become a popular area of research (Wilkinson, 2009). Each individual method has its own distinct advantages and weaknesses, the selection of a specific algorithm needs to be justified according to the biological problems and the particular research questions. Modelers should take various factors into account and assure that the results are best interpreted by the selected methods. It is important to acknowledge that certain stochastic effect may have an impact on the results, and as such, it is important for modelers to study both deterministic and stochastic approaches in order to address different aspects of the experiments. There are many theoretical derivations and proofs of modelling algorithms based on the mathematical and computational analysis available in the literature (Chatterjee et al., 2005; Cao et al., 2005; Macnamara et al., 2008). However, the detailed computer implementation of the stochastic algorithms is not the research focus in this thesis; the stochastic approaches are only used to study their biological applications and assess the ability to explain the experimental observations.

3.2.5 Monte Carlo Simulation

Stochastic simulation, unlike deterministic approaches, does not produce an exact and unique solution of a model due to the nature of the algorithm. The reaction kinetics of a stochastic model is not described by fixed unique values, rather it is derived from the probability distributions given by the CME and updated throughout the simulations (Section 3.2.1). Hence each stochastic realization varies and is unpredictable even the system and the initial conditions stay the same. It is meaningless to make any interpretations of a stochastic system based on a single simulation. Monte Carlo strategy, as an estimation procedure, is used in these situations to repeatedly sample from the distributions to obtain the average dynamic behaviour of a stochastic system (Wilkinson., 2006; Dirk P. Kroese and Botev, 2011). In order to resemble the possible realities and get a more complete

picture of a stochastic system, sufficient number of simulations need to be conducted and statistics analysis are usually required (Tom and Schulman, 1997).

3.3 Software Packages and Databases

All the numerical simulations and phase plane analysis of the deterministic models in this thesis were performed using the computer programs XPPAUT and WINPP. XPPAUT was used to formulate and conduct most of the stochastic simulations (both the CLE and the SSA) unless otherwise stated. The programs can be freely downloaded from G. Bard Ermentrout's personal webpage: `http://www.math.pitt.edu/~bard/xpp/xpp.html`. The detailed implementation of the stochastic simulation algorithm and examples can be found in his book titled "Simulating, analyzing, and animating dynamical systems: a guide to XPPAUT for researchers and students" (Ermentrout, 2002). The parameter bifurcation analysis of the presented models were conducted using Oscill8 (`http://oscill8.sourceforge.net/`), a free software for analyzing ODE based dynamical systems.

The analysis and plot of the simulation data were performed using MATLAB® R2008b and SimBiology 3.0 toolbox. MATLAB® is a high-level language and interactive environment that has the capabilities to perform computationally intensive tasks (`http://www.mathworks.com/products/matlab/`). SimBiology is a graphical and programmatic tool for modeling, simulation and analyzing biological systems (`http://www.mathworks.co.uk/products/simbiology/`). It has built-in stochastic and deterministic solvers allowing the users to simulate the model as well (Ullah et al., 2006).

The major public resources and freely available biological databases that were mainly used to annotate the components of the models in the thesis are: ChEBI, Gene Ontology (GO), SGD and UniProt. ChEBI (`http://www.ebi.ac.uk/chebi/`) is a widely used database collecting small chemical compounds. It includes the chemical structures, information on their biological activities and cross reference to other database (Degt-

yarenko et al., 2008). Gene Ontology (`http://www.geneontology.org/`) is an ontology database providing controlled vocabulary to annotate genes, gene products and the corresponding biological processes (Ashburner et al., 2000). Cellular component, molecular function and biological process are the three domains defined by GO term. Saccharomyces Genome Database (SGD) (`http://www.yeastgenome.org/`) is a scientific database with comprehensive data of the molecular components, biochemical reactions and biological pathways of the yeast *Saccharomyces cerevisiae* (Cherry et al., 1997, 1998). UniProt (`http://www.uniprot.org/`), the shortened form for 'Universal Protein Resource', is a knowledge base with a comprehensive collection of protein sequence, structure and the relevant functional information data with quality of annotations (Apweiler et al., 2004).

Chapter 4

A Deterministic Model of the Anaphase Switch

The anaphase switch (also referred to as the metaphase-to-anaphase transition) is controlled by the spindle assembly checkpoint (SAC), which is a surveillance mechanism of regulating the timing and the quality of mitosis. As previously described in the Introduction (Chapter 1), the SAC inhibits cohesin cleavage through blocking $\mathrm{APC}^{\mathrm{Cdc20}}$ activity until all the chromosomes are bioriented and kinetochore tension has been generated. It is well known and experimentally proven that a single unattached kinetochore is sufficient to prevent the anaphase onset (Rieder et al., 1994, 1995). As soon as all the chromosomes are properly aligned on the metaphase plate, the checkpoint is almost immediately silenced and triggers a series of events (e.g. $\mathrm{APC}^{\mathrm{Cdc20}}$ activation, cyclin B degradation, separase activation, cohesin cleavage, sister chromatid segregation, etc) which drive cells to proceed from metaphase to anaphase.

The segregation of sister chromatids is triggered by the proteolysis of cohesins via separase activity. The separated chromosomes quickly move apart from each other after cohesin cleavage, thus the previous metaphase state can not be recreated simply by resynthesis more cohesin protein. It seems conceivable that the irreversibility of the metaphase-to-anaphase transition is caused by thermodynamic reason? If this is the case, is the anaphase switch an exception to our systems-level view of the irreversible cell cycle

transitions? In addition to this important question (see also **Question I** in Chapter 2), there are several unresolved problems regarding the SAC as well: • Why is it that, before the metaphase-to-anaphase transition, the absence of tension prevents cell cycle progression into anaphase and stabilizes metaphase, but after the transition, when tension is lost due to the destruction of cohesin rings, the control network is locked in a post-transitional anaphase state and does not revert to the pre-transitional metaphase state? • How is it that a single unattached kinetochore is sufficient to block the metaphase-to-anaphase transition? • How is it that even a weak signal can keep the SAC active, and yet once the signal disappears, the SAC is rapidly disengaged?

This chapter will address and suggest solutions for these unresolved questions based on the proposal that the SAC network is indeed a one-way toggle switch.

4.1 Experimental Evidence for the Anaphase Switch

The detailed biomolecular regulation network and the working mechanism of the spindle assembly checkpoint during the metaphase-to-anaphase transition have already been introduced in Chapter 1. In this section we will focus on the experimental evidences provided by recent publications, which have addressed the long standing gaps in our understanding of the anaphase switch.

Several papers come to the conclusion that the drop of Cdk1/CycB activity during the metaphase-to-anaphase transition is responsible for blocking the reactivation of the error-correction mechanism and the spindle assembly checkpoint (Mirchenko and Uhlmann, 2010; Oliveira et al., 2010; Vázquez-Novelle and Petronczki, 2010). *Drosophila* embryos (Oliveira et al., 2010) and budding yeast cells (Mirchenko and Uhlmann, 2010) expressing cohesins engineered to contain tobacco etch virus (TEV) protease cleavage sites were arrested in metaphase by $\mathrm{APC}^{\mathrm{Cdc20}}$ inactivation. Experimental induction of the TEV protease in these metaphase arrested cells triggered cohesin cleavage and anaphase onset in a separase-independent manner. Initially, the separation of the sister chromatids appeared to be normal, but problems soon arose: microtubule-kinetochore attachments

were destabilized in the fruit fly embryo (Oliveira et al., 2010), and the checkpoint protein Bub1 was reactivated in budding yeast cells (Mirchenko and Uhlmann, 2010). Why are the error-correction and the checkpoint mechanisms reactivated under these conditions? Since $\mathrm{APC}^{\mathrm{Cdc20}}$ was kept inactive in those experiments, neither securin nor cyclin B could be degraded; hence separase activity was kept low and Cdk1/CycB activity remained high. The early anaphase activation of Cdc14, a Cdk1/CycB-counteracting phosphatase in budding yeast, was blocked because of the low separase activity (Sullivan and Uhlmann, 2003). TEV-induced anaphase happened in a situation where Cdk1/CycB was active and Cdc14 was inactive, indicating that Cdk1/CycB dependent phosphorylation might be responsible for the reactivation of the error-correction and the SAC machinery.

An earlier paper came to a similar conclusion from *Drosophila* embryos, suggesting that expression of nondegradable cyclin B caused the reactivation of the error-correction mechanism during anaphase (Parry et al., 2003). Furthermore, negative regulation of Cdk1-dependent phosphorylation during TEV-induced anaphase by the Cdk inhibitor p27 in fly embryos (Oliveira et al., 2010) or by overexpression of Cdc14 phosphatase in yeast cells (Mirchenko and Uhlmann, 2010) blocked the SAC reactivation during sister chromatid separation. Similar effects observed in yeast, fly and mammalian cells (Vázquez-Novelle and Petronczki, 2010) have confirmed the role of Cdk1/CycB in blocking the SAC reactivation and suggest that this silencing mechanism may be universal among all eukaryotes.

4.2 A Conceptual Model with Essential Feedback Loops

The experimental results mentioned above indicate that loss of tension at anaphase onset has the potential to reactivate the SAC, but it is strictly prohibited during the normal metaphase-to-anaphase transition, when Cdk1/CycB activity is downregulated at the same time. Despite the fact that sister chromatids segregation is a morphologically irreversible process, we propose that, like many cell cycle transition processes, the underlying regulatory network of the anaphase switch is still a bistable system thus reversible.

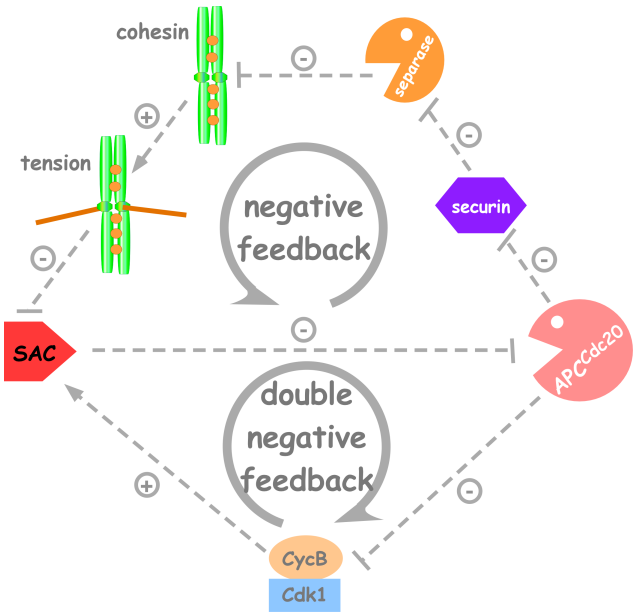

Figure 4.1: Essential feedback loops governing the anaphase switch. $\mathrm{APC}^{\mathrm{Cdc20}}$ has two main substrates during the metaphase-to-anaphase transition: cyclin B and securin. Negative feedback loop (the upper branch): $\mathrm{APC}^{\mathrm{Cdc20}}$ promotes securin degradation to release separase from the inactive complexed form. Activated separase cleaves cohesin and makes the kinetochore tensionless which could reactivate the SAC to inhibit $\mathrm{APC}^{\mathrm{Cdc20}}$. Double negative feedback loop (the lower branch): Cdk1/CycB indirectly inhibits $\mathrm{APC}^{\mathrm{Cdc20}}$ through the SAC, and $\mathrm{APC}^{\mathrm{Cdc20}}$ downregulates Cdk1/CycB activity by degradation of cyclin B.

A bistable switch at the metaphase-to-anaphase transition could be based on the molecular interactions proposed in Figure 4.1. $\mathrm{APC}^{\mathrm{Cdc20}}$ promotes securin degradation and helps to release separase from the inactive complex form. Activated separase cleaves the cohesin and leaves the kinetochore tensionless, which could reactivate the SAC and re-block $\mathrm{APC}^{\mathrm{Cdc20}}$, thus creating a negative feedback loop. Cdk1/CycB and $\mathrm{APC}^{\mathrm{Cdc20}}$ are locked in a feedback loop of mutual inhibition. Cdk1/CycB inhibits $\mathrm{APC}^{\mathrm{Cdc20}}$ indirectly by promoting the checkpoint signals from unaligned chromosomes to activate Mad2, which subsequently inactivates $\mathrm{APC}^{\mathrm{Cdc20}}$. However, active $\mathrm{APC}^{\mathrm{Cdc20}}$ destroys Cdk1/CycB activity by degradation of cyclin B. The double negative feedback loops of this sort are excellent candidates for creating one-way toggle switches (Tyson et al., 2003). The essential role of this bistable switch is to suppress the potential dangerous negative feedback loop which could reactivate the checkpoint during the anaphase switch.

Figure 4.1 is expanded into a more detailed molecular network suitable for constructing a mathematical model (Fig. 4.2). Two different classes of chromosomes are distinguished: the bioriented chromosomes that are under tension ($\mathrm{N}_{\mathrm{tens}}$) and those not under

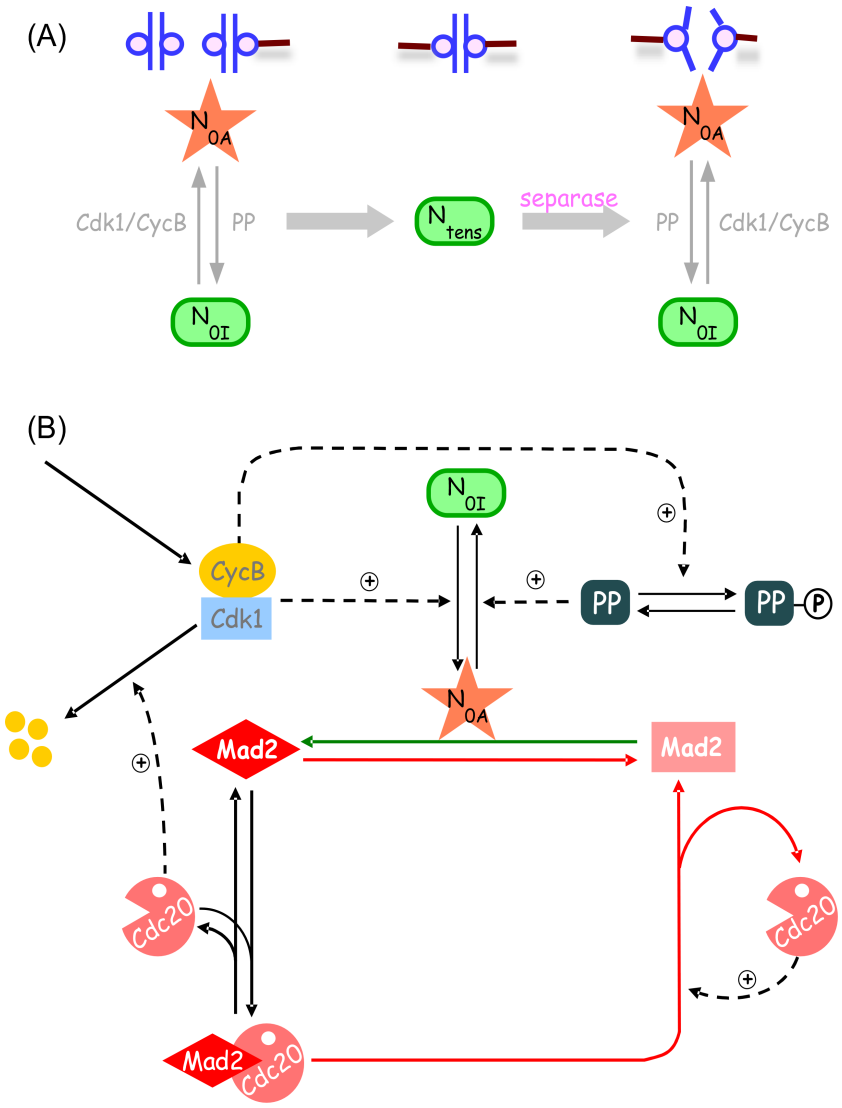

Figure 4.2: The molecular network controlling the metaphase-to-anaphase transition. (A) Different N forms represent different states of chromosomes during metaphase-to-anaphase transition. N_{0A}, N_{0I}: chromosomes that are not under tension; N_{tens}: chromosomes that have bipolar microtubules attachment and tension has been generated. The red Ns can activate the SAC, whereas the green ones cannot. The total number of chromosomes $N_T = N_{0A} + N_{0I} + N_{tens}$. (B) Molecular network of the anaphase switch. The mitotic checkpoint protein Mad2 is activated by the active tensionless chromosomes N_{0A}. Active Mad2 (red diamond) binds to and inactivates Cdc20. Active Cdc20 (pacman) combined with APC degrades cyclin B. Active Cdc20 also promotes the dissociation of Mad2:Cdc20 complex into active Cdc20 and inactive Mad2 (pink rectangle). The interconversion between tensionless chromosomes is regulated by Cdk1/CycB and an unspecified protein phosphatase PP. Figure (B) is modified from He et al. (2011).

tension (N_0). Tensionless chromosomes are further divided into the active (N_{0A}) and inactive (N_{0I}) forms which are interconverted by Cdk1/CycB and an unspecified protein phosphatase PP (Fig. 4.2A). It is assumed that only the phosphorylated forms (N_{0A}) can activate the error correction and the checkpoint, reflecting the finding that phosphorylation of the chromosomal passenger complex is required for its kinetochore localization (Vader et al., 2008; Vázquez-Novelle and Petronczki, 2010). Cyclin B is synthesized

at a constant rate and degraded by $\mathrm{APC}^{\mathrm{Cdc20}}$-dependent ubiquitination. The activity of the Cdk1/CycB complex is determined by the level of cyclin B. An additional positive feedback loop of Cdc20 accelerates its own release from the mitotic checkpoint protein complex (MCC) is incorporated into the model which provides a means to speed up the activation of $\mathrm{APC}^{\mathrm{Cdc20}}$ at the anaphase onset (Fig. 4.2B). Ubiquitination of Cdc20 by APC causes the disruption of MCC and releases Cdc20 from the complex, which could provide a possible molecular explanation for this feedback (Reddy et al., 2007). Another alternative mechanism for quickening the activation of Cdc20 during anaphase is suggested by the role of Cdc20 phosphorylation in MCC formation (D'Angiolella et al., 2003) This will be described later in the alternative model of the anaphase switch (see Section 4.3).

The dynamics of the model can be expressed in terms of five ODEs and two conservation equations (Eq.4.1 - Eq.4.6).

$$\frac{d\,[\mathrm{CycB}]}{dt} = k_{scyc} - (k_{dcyc} + k'_{dcyc} \cdot [\mathrm{Cdc20}]) \cdot [\mathrm{CycB}] \tag{4.1}$$

$$\frac{d\,\mathrm{X_{0A}}}{dt} = k_{ax,cyc} \cdot [\mathrm{CycB}] \cdot (1 - \mathrm{X_{tens}} - \mathrm{X_{0A}}) - k_{ix,pp} \cdot [\mathrm{PP}] \cdot \mathrm{X_{0A}} \tag{4.2}$$

$$\frac{d\,[\mathrm{PP}]}{dt} = k_{app} \cdot ([\mathrm{PPT}] - [\mathrm{PP}]) - k_{ipp} \cdot [\mathrm{CycB}] \cdot [\mathrm{PP}] \tag{4.3}$$

$$\begin{aligned}\frac{d\,[\mathrm{Mad2AT}]}{dt} &= k_{amad} \cdot \mathrm{X_{0A}} \cdot ([\mathrm{Mad2T}] - [\mathrm{Mad2AT}]) - k_{imad} \cdot [\mathrm{Mad2AT}] \\ &\quad - k'_{imad} \cdot [\mathrm{Cdc20}] \cdot [\mathrm{MCC}]\end{aligned} \tag{4.4}$$

$$\begin{aligned}\frac{d\,[\mathrm{MCC}]}{dt} &= k_{asmcc} \cdot [\mathrm{Cdc20}] \cdot [\mathrm{Mad2AF}] - k'_{imad} \cdot [\mathrm{Cdc20}] \cdot [\mathrm{MCC}] \\ &\quad - (k_{dimcc} + k_{imad}) \cdot [\mathrm{MCC}]\end{aligned} \tag{4.5}$$

$$[\mathrm{Cdc20}] = [\mathrm{Cdc20T}] - [\mathrm{MCC}], \qquad [\mathrm{Mad2AF}] = [\mathrm{Mad2AT}] - [\mathrm{MCC}] \tag{4.6}$$

First, we assumed the following values for the rate constants in the above ODEs and we will explore the ranges of the parameter choices using two-parameter bifurcation analysis later in Section 4.2.4.

$k_{dcyc} = 0.001\ min^{-1}$, $k_{scyc} = 0.001 \cdot [CycBM]\ min^{-1}$, $k'_{dcyc} \cdot [Cdc20T] = 0.1\ min^{-1}$, $k_{ax,cyc} = k_{ix,pp} = 1\ nM^{-1}\ min^{-1}$, $k_{amad} \cdot N_T = 10\ min^{-1}$, $k_{imad} = 0.1\ min^{-1}$, $k'_{imad} \cdot$

$[Cdc20T] = 10\ min^{-1}$, $k_{asmcc} \cdot [Cdc20T] = 400\ min^{-1}$, $k_{dimcc} = 1\ min^{-1}$, $k_{app} = 0.1\ min^{-1}$, $k_{ipp} \cdot [CycBM] = 1\ min^{-1}$ and $[CycBM] = k_{scyc}/k_{dcyc}$.

The active tensionless chromosomes $\mathrm{N_{0A}}$, described by the differential equation $\frac{d\ \mathrm{N_{0A}}}{dt} = k_{an,cyc} \cdot [\mathrm{CycB}] \cdot (\mathrm{N_T} - \mathrm{N_{tens}} - \mathrm{N_{0A}}) - k_{in,pp} \cdot [\mathrm{PP}] \cdot \mathrm{N_{0A}}$, is normalized by total number of chromosomes $\mathrm{N_T}$. Therefore $\mathrm{X_{0A}}$ in Equation 4.2 represents the fraction of active tensionless chromosomes. $\mathrm{X_{tens}}$ is treated as an adjustable parameter. During prometaphase, $\mathrm{X_{tens}}$ increases steadily from 0 to 1 as chromosomes are bioriented, and in anaphase $\mathrm{X_{tens}}$ decreases abruptly from 1 to 0 upon cleavage of cohesins. Checkpoint activity is described by an equation for Mad2, which is activated at a rate proportional to $\mathrm{X_{0A}}$ and inactivated by a first-order process (Eq. 4.4). Active Mad2 binds reversibly to active Cdc20 and forms an inactive complex Mad2A:Cdc20 (the MCC). The MCC will dissociate if the bound Mad2 molecule undergoes spontaneous inactivation (Eq. 4.5).

The Cdk-counteracting phosphatase in budding yeast is Cdc14, which is activated during anaphase after degradation of securin by separase (Sullivan and Uhlmann, 2003; Queralt et al., 2006). Since securin and separase are not presented as differential equations for simplification reasons, securin level changes are inferred in parallel to cyclin B (i.e., high CycB $\rightarrow$ high securin $\rightarrow$ low separase $\rightarrow$ low Cdc14). This chain of relationships formally suggests that Cdk1/CycB suppresses the activity of Cdk1-counteracting phosphatase (PP). This scheme is also compatible with higher eukaryotes, where PP is also inhibited by high Cdk1/CycB activity (Mochida et al., 2009). Based on these findings, the model assumes that the Cdk1/CycB-counteracting phosphatase PP is inhibited by Cdk1/CycB-dependent phosphorylation (Fig. 4.2B). This assumption creates a coherent feed-forward loop of Cdk1/CycB on the activation of tensionless kinetochores and makes the bistability of the system more robust.

4.2.1 Bistability of the anaphase switch

To demonstrate the properties of the bistable anaphase switch, a one-parameter bifurcation diagram is plotted in Figure 4.3 to investigate how the steady states of a specific dynamic

variable (e.g. X_{0A}, MCC, CycB) change as a function of the fraction of chromosomes under tension (X_{tens}). The bifurcation parameter X_{tens} increases from zero to one as chromosomes line up at the metaphase plate during prometaphase, and the dynamical variable (the response) shows the state of the control system. All the plots in Figure 4.3 have the same qualitative features, namely two branches of stable steady states (the SAC active and inactive states; solid lines) separated by an intermediate branch of unstable steady states (dashed lines).

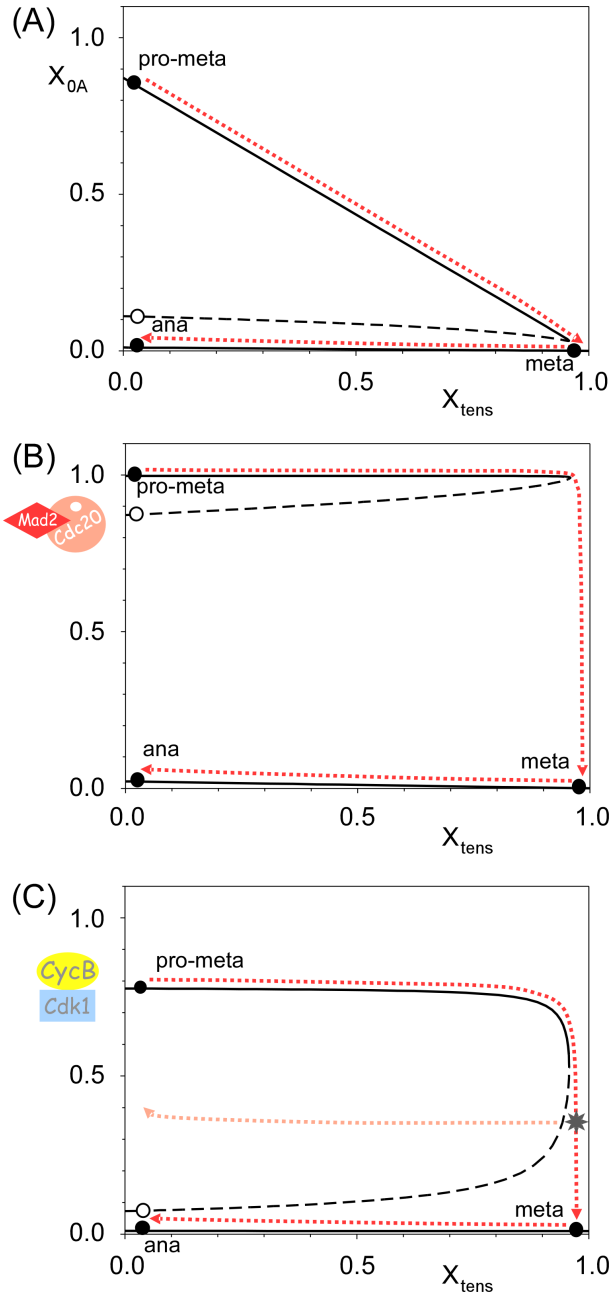

Figure 4.3: Bifurcation analysis of the irreversible anaphase switch. Bifurcation diagrams of three dynamic variables are plotted as functions of X_{tens}: (A) Fraction of active tensionless chromosomes X_{0A}, (B) Mad2:Cdc20 (MCC) complex, and (C) Cdk1/CycB. The regulatory network of anaphase switch is bistable with two alternative stable steady states (black circles): a SAC active state (high level of MCC, active Cdk1/CycB, large percent of X_{0A}) and a SAC inactive state (low level of MCC, inactive Cdk1/CycB, small percent of X_{0A}). The unstable steady states are presented by white circles. The red dashed lines indicate the cell progression from prometaphase to metaphase to anaphase. In prometaphase, the chromosomes are gradually aligning on the metaphase plate (i.e., X_{tens} is steadily increasing to one). Once all the chromosomes have bioriented ($X_{tens} \sim 1$), the SAC switches from the active state to the inactive state. At anaphase onset, X_{tens} level quickly drops because of the cohesin cleavage; however the SAC will not revert back to the prometaphase active state because its lower steady state is stable for all values of X_{tens} between one and zero. The asterisk and the dotted trajectory back to the prometaphase state are used to illustrate the point of no return, which is explained in Section 4.2.2. The simulations were generated using the ODEs and parameters listed in Section 4.2. These figures are modified from He et al. (2011).

To mathematically illustrate the change of X_{0A} (fraction of active tensionless chromosomes) undergoing the process of the metaphase-to-anaphase transition, X_{0A} is represented by Equation 4.7, which is derived from the steady-state solution of Equation 4.2:

$$X_{0A} = \frac{\theta}{\theta + ([PP]/[CycB])}(1 - X_{tens}), \qquad \text{where } \theta = \frac{k_{ax,cyc}}{k_{ix,pp}} \tag{4.7}$$

In prometaphase, cells in the upper branch of the curve with X_{tens} close to zero when phosphatase to kinase ratio is low ([PP]/[CycB] $\ll \theta$) and X_{0A} approximately equals to 1 - X_{tens} (Fig. 4.3A). As individual chromosomes become bioriented, X_{tens} increases in small steps, and the state of the control system moves slowly to the right on the bifurcation diagram. This causes a decrease in the fraction of active, tensionless chromosomes (X_{0A}) according to Equation 4.7. Although X_{0A} is decreasing, the SAC is still active, Mad2:Cdc20 level is high and Cdk1/CycB stays active. The system cannot overcome the checkpoint until X_{tens} exceeds the bifurcation point, which is very close to one. Once X_{tens} becomes larger than the bifurcation point, the SAC is bypassed, Cdc20 is activated and cyclin B begins to degradate (Figs. 4.3B,C). Although tension is lost on the kinetochores, the control system is now on the lower branch of stable steady states on the bifurcation diagram with small X_{0A} and large X_{0I} (Fig. 4.3A).

The MCC dissociation and the SAC inactivation at metaphase will push the system to the lower branch of stable steady states. Because cyclin B and securin levels decrease simultaneously during the metaphase-to-anaphase transition, separase gets activated and starts to cleave cohesins. Loss of sister chromatid cohesion causes a decrease of X_{tens}, but only after some time of APC^{Cdc20} activation, because securin degradation and cohesin cleavage are not instantaneous. Therefore, the SAC is inactivated first and then the control system starts traveling to the left along the lower branch of stable steady states. Once all the sister chromatids are segregated, X_{tens} is again close to zero, which it was at the beginning of mitosis. Along the lower branch of stable steady states, X_{0A} remains close to zero even as X_{tens} drops to zero because [PP]/[CycB] $\gg \theta$. Therefore, Mad2 is not reactivated and the spindle assembly checkpoint stays inactive (Fig. 4.3B).

The double negative feedback between Cdk1/CycB and $\mathrm{APC}^{\mathrm{Cdc20}}$ creates a bistable switch which blocks the reactivation of the spindle assembly checkpoint in anaphase.

4.2.2 Reversible Anaphase Switch

The transition between two stable steady states of a bistable system is a cooperative (autocatalytic) process with a point of no return. If the transition is disturbed before the point of no return, the bistable switch will return to the initial state; if the transition is disturbed after the point of no return, it will proceed to the final state. Furthermore, by breaking the positive feedback loop (the mutual antagonism between Cdk1/CycB and $\mathrm{APC}^{\mathrm{Cdc20}}$), it should be possible to abolish bistability of the anaphase switch and observe reactivation of the error-correction/checkpoint mechanism during anaphase.

A reversible anaphase switch has been observed in the experiments by Clute and Pines (1999) and Hagting et al. (2002). Using live-cell imaging, their studies showed that both securin and cyclin B are degraded during metaphase in mammalian cells. The addition of a microtubule-stabilizing drug taxol halfway through the degradation of these $\mathrm{APC}^{\mathrm{Cdc20}}$ substrates blocked further degradation of securin and cyclin B. This suggested that the SAC was reimposed and $\mathrm{APC}^{\mathrm{Cdc20}}$ was reactivated. The result can be interpreted by the same bifurcation of Cdk1/CycB (Fig. 4.3C). During a normal metaphase-to-anaphase transition, cyclin B is degraded all the way down to the lower stable steady state, but in response to taxol treatment halfway through the process, active kinetochores start signaling again ($\mathrm{X}_{0\mathrm{A}}$ reincreases and $\mathrm{X}_{\mathrm{tens}}$ drops), $\mathrm{APC}^{\mathrm{Cdc20}}$ is inactivated, cyclin B degradation is halted and the spindle checkpoint is reactivated.

Reactivation of the SAC is also observed when cohesin cleavage is carried out by TEV in the absence of $\mathrm{APC}^{\mathrm{Cdc20}}$ activity (Mirchenko and Uhlmann, 2010; Oliveira et al., 2010). When the activity of $\mathrm{APC}^{\mathrm{Cdc20}}$ is blocked, cyclin B levels stay high throughout the process and the SAC control system loses the bistability (Fig. 4.4). With only the prometaphase (upper) stable steady state remaining, cohesin cleavage by TEV protease ($\mathrm{X}_{\mathrm{tens}}$ decreases to zero) only reverts the system back to a pseudo-anaphase with active

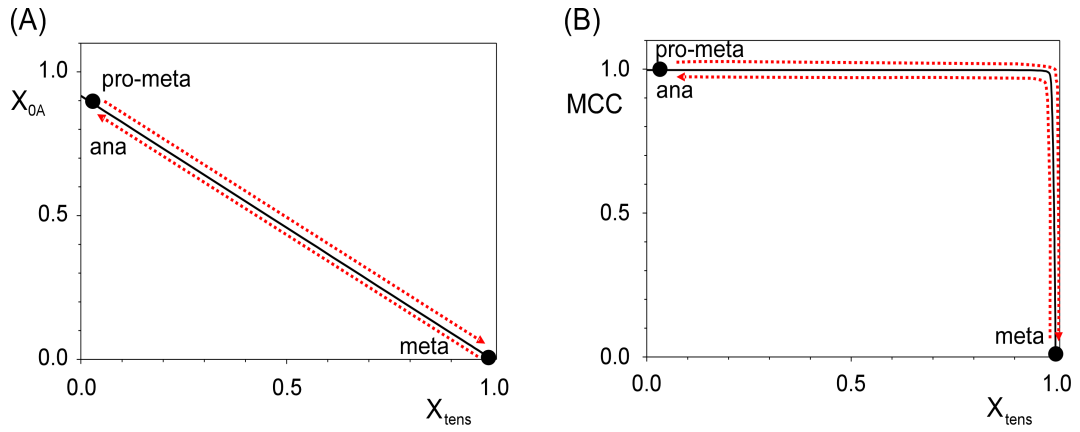

Figure 4.4: Signal response curves for TEV-induced anaphase switch. (A) Fraction of active tensionless chromosomes (X_{0A}) is plotted as a function of X_{tens}. (B) Mad2:Cdc20 complex (MCC) is plotted as a function of X_{tens}. The scaled model was used for the numerical analysis. The same parameter values were used as in Figure 4.3, except that APC^{Cdc20} activity was set to zero ($k'_{dcyc} = k'_{imad} = 0$). Bistability is lost because the double negative feedback between APC^{Cdc20} and Cdk1/CycB is comprised. Therefore, TEV-induced cohesin cleavage pushes the system backward along the same path. The figure is modified from He et al. (2011).

Cdk1/CycB and active SAC. This is an abnormal anaphase state which is similar to the initial prometaphase, however without tension (Fig. 4.4).

4.2.3 Sensitivity of the spindle assembly checkpoint for a single unattached kinetochore

The conceptual model in Figure 4.2B has two positive feedback loops: (i) the mutual inhibition between Cdk1/CycB and APC^{Cdc20} creating a bistable switch and (ii) a self-activation loop, whereby APC^{Cdc20} accelerates its own activation by disrupting the MCC (Reddy et al., 2007). These two positive feedback loops work synergistically to ensure that a single unaligned chromosome can keep the SAC active in prometaphase and yet the SAC can be rapidly disengaged after the metaphase-to-anaphase transition once the kinetochore tension is achieved (Rieder et al., 1995).

To illustrate how these positive feedback loops work together, the rates of activation and inactivation of Mad2 are plotted as a function of total active Mad2 in Figure 4.5. From the differential equation of Mad2AT (Eq. 4.4), the activation (V^+) and inactivation

(V^-) rates of Mad2 are presented as follows (Eqs. 4.8 - 4.9):

$$V^+ = k_{amad} \cdot X_{0A} \cdot ([Mad2T] - [Mad2AT]) \tag{4.8}$$

$$V^- = k_{imad} \cdot [Mad2AT] + k'_{imad} \cdot [Cdc20] \cdot [MCC] \tag{4.9}$$

If assume PP, CycB and X_{0A} are in the steady states, then the corresponding steady-state solutions (Eqs. 4.10 - 4.12) can be derived from their ODEs (Eqs. 4.1 - 4.3):

$$[PP] = \frac{k_{app} \cdot [PPT]}{k_{app} + k_{ipp} \cdot [CycB]} \tag{4.10}$$

$$[CycB] = \frac{k_{scyc}}{k_{dcyc} + k'_{dcyc} \cdot [Cdc20]} \tag{4.11}$$

$$X_{0A} = (1 - X_{tens}) \cdot \frac{k_{ax,cyc} \cdot [CycB]}{k_{ax,cyc} \cdot [CycB] + k_{ix,pp} \cdot [PP]} \tag{4.12}$$

Replacing Cdc20 and Mad2AF with [Cdc20] = [Cdc20T] - [MCC] and [Mad2AF] = [Mad2AT] - [MCC] respectively in Equation 4.13, the steady-state solution of MCC is then calculated from its pseudo-steady state approximation (i.e. $\frac{d[MCC]}{dt} = 0$).

$$[MCC] = \frac{2 \cdot [Mad2AT] \cdot [Cdc20T]}{BB + \sqrt{BB^2 - 4 \cdot (1 + \frac{k'_{imad}}{k_{asmcc}}) \cdot [Mad2AT] \cdot [Cdc20T]}}, \tag{4.13}$$

$$\text{where} \quad BB = [Mad2T] + [Cdc20T] + \frac{k_{dimcc} + k_{imad} + k'_{imad} \cdot [Cdc20T]}{k_{asmcc}}$$

Substitute X_{0A} in Equation 4.8 with Equation 4.12 for V^+ and substitute MCC in Equation 4.9 with Equation 4.13 for V^-. Hence, the analytical solutions can be readily deduced.

Since the activation rate of Mad2 is dependent on the signaling state of chromosomes, it is plotted for different values of X_{tens}. Without the feedback loops, both rate curves would be straight lines: the inactivation rate of Mad2A would increase directly proportional to the level of total active Mad2 ([Mad2AT]), while the activation rate would have a negative slope because it is proportional to the concentration of inactive Mad2 ([Mad2T]

- [Mad2AT]). Because of the feedback loops, both rate curves are non-monotonic, with distinct maxima (Fig. 4.5A). Wherever the two rate curves intersect, [Mad2AT] is unchanged, and therefore the system has a steady state. For most values of $\mathrm{X_{tens}}$, the two rate curves intersect at three points (two stable steady states separated by an unstable steady state). The left and right stable states represent the SAC inactive and active states respectively. As $\mathrm{X_{tens}}$ increases, the unstable steady state and the SAC active state come closer together and fuse when $\mathrm{X_{tens}}$ reaches the saddle-node bifurcation point ($\mathrm{X_{tens}}$ = $\mathrm{X_{SN_{off}}}$ = 0.958). For $\mathrm{X_{tens}} > \mathrm{X_{SN_{off}}}$, the only remaining steady state is the checkpoint inactive state, and the system moves in that direction. The fact that the bifurcation happens at a value of $\mathrm{X_{tens}}$ close to one is a consequence of the slow Mad2 inactivation rate (k_{imad}) at high Mad2 values (greater than one). However, at low Mad2 values (less than one), Mad2 is rapidly inactivated because of our assumption that $\mathrm{APC^{Cdc20}}$ catalyzes the inactivation of Mad2. If Mad2 inactivation is not catalyzed by $\mathrm{APC^{Cdc20}}$, the inactivation rate curve of Mad2 would be a straight line and the silencing of the checkpoint would happen too slowly (Fig. 4.5B).

To explicitly demonstrate our argument that the spindle assembly checkpoint can be quickly turned off with the help of Cdc20 autocatalysis. We further plotted the temporal simulation of the model with and without Cdc20 positive feedback in Figure 4.6. With Cdc20 autoactivation, the SAC quickly disengaged and cyclin B degradation starts soon after the last chromosome is aligned (Fig. 4.6A). The disengagement of the spindle checkpoint is compromised, and cyclin B degradation requires much longer time without Cdc20 autoactivation (Fig. 4.6B).

4.2.4 Robustness analysis of anaphase switch

The features of the spindle assembly checkpoint must be also the robust properties of the model, i.e. they must be exhibited not only for specific parameter values as illustrated in Figures 4.3 and 4.5, but over a broad range of reasonable parameter values. For a single unattached chromosome to keep the checkpoint active, the termination point of the upper branch of stable steady states must lie in the interval $(\mathrm{N_T} - 1)/\mathrm{N_T} < \mathrm{X_{SN_{off}}} < 1$, where

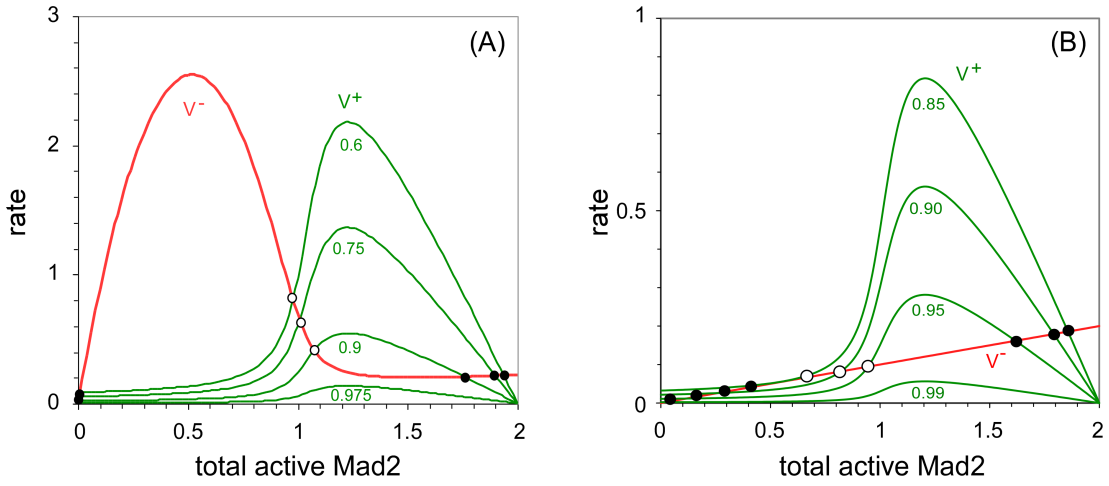

Figure 4.5: Positive feedback loops make the irreversible anaphase switch robust. (A) The rate plot of the model with both positive and double-negative feedbacks. The double-negative and the positive feedback influence the Mad2 activation (V^+, green) and inactivation (V^-, red) rate respectively. Both rate curves are sharply peaked because of the feedback loops in the reaction network (Fig. 4.2). The activation rate curve is drawn for increasing values of $\mathrm{X_{tens}}$ from 0.6 to 0.975. Points of intersection (circles) of the green and red curves are steady states of Mad2 activity (black circles are stable steady states; white circles are unstable steady states). In prometaphase, Mad2 is active (black circles on the right), but as the last chromosome comes into alignment on the metaphase plate (as $\mathrm{X_{tens}}$ increases above ~ 0.95, the active stable steady state disappears by coalescing with the unstable saddle point. The SAC must now switch to the Mad2-inactive steady state (black circles on the left). It does so quickly, because the inactivation rate constant increases as Mad2 activity drops. (B) $\mathrm{APC^{Cdc20}}$ autoactivation is responsible for rapid disengagement of the SAC at the metaphase-to-anaphase transition. The rates of Mad2 activation (V^+, green) and inactivation (V^-, red) are plotted as functions of active Mad2 in the absence of Cdc20 autoactivation (k'_{imad}[Cdc20T] = 0). The activation rate curve is drawn for increasing values of $\mathrm{X_{tens}}$ from 0.85 to 0.99 and they have the same shape as in Figure (A). However, the inactivation curve is simply a straight line because there is no autoactivation of Cdc20. The transition of the SAC to the Mad2-inactive steady state (black circles on the left) happens more slowly, because the inactivation rate is low at small levels of active Mad2. The rate plots were generated using the parameter values given in Section 4.2. These figures were first published in He et al. (2011).

$\mathrm{N_T}$ is the total number of chromosomes in the cell. For the checkpoint not to reactivate during anaphase, the SAC must be bistable for $\mathrm{X_{tens}} < 0$ (i.e., termination point of the lower branch of stable steady states, $\mathrm{X_{SN_{on}}}$ must be a negative number). In this section we are going to show that these two requirements are indeed robust properties of our model.

Firstly, dimensionless values of all of the concentration variables in the original ODEs (Eqs. 4.1 - 4.6) are introduced by the following definitions:

$$C_{\mathrm{cycB}} = \frac{[\mathrm{CycB}]}{[\mathrm{CycBM}]}, \quad C_{\mathrm{Mad2AT}} = \frac{[\mathrm{Mad2AT}]}{[\mathrm{Cdc20T}]}, \quad C_{\mathrm{MCC}} = \frac{[\mathrm{MCC}]}{[\mathrm{Cdc20T}]},$$
$$C_{\mathrm{PP}} = \frac{[\mathrm{PP}]}{[\mathrm{PPT}]}, \quad C_{\mathrm{Cdc20}} = \frac{[\mathrm{Cdc20}]}{[\mathrm{Cdc20T}]}, \quad X_{tens} = \frac{N_{tens}}{N_T},$$
$$X_{0A} = \frac{N_{0A}}{N_T}, \quad X_{0I} = \frac{N_{0I}}{N_T}.$$

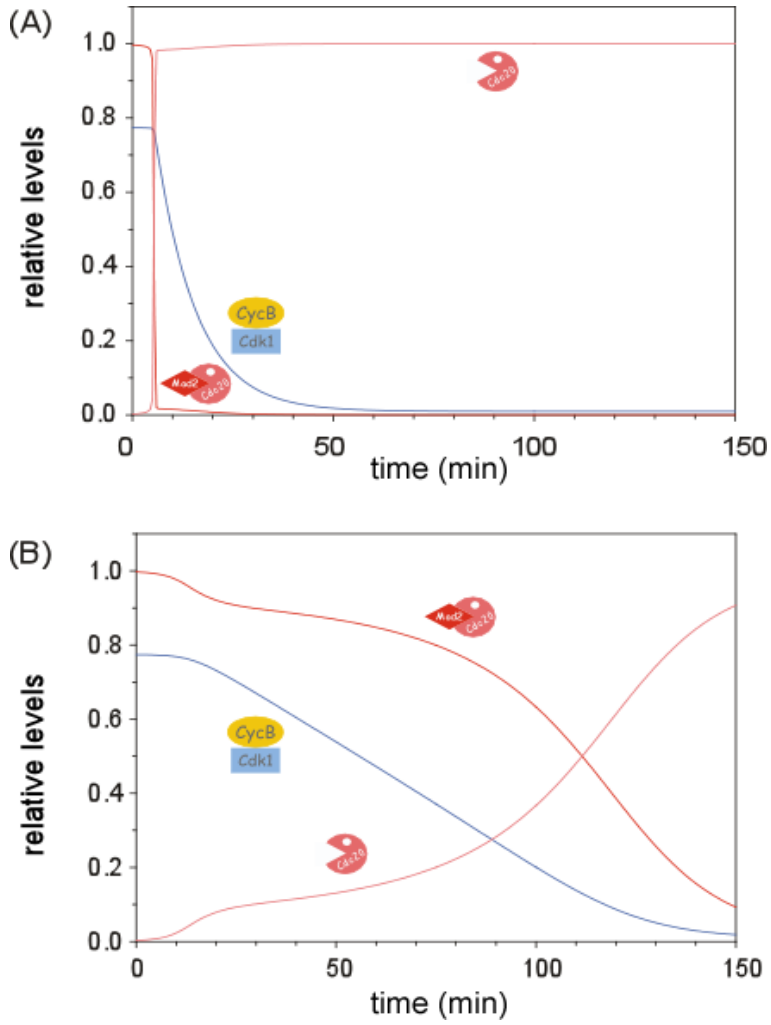

Figure 4.6: Time series simulation of mitotic checkpoint disengagement after the last chromosome is aligned. Simulations were performed using the ODEs and parameters given in Section 4.2. The initial conditions are corresponding to the high CDK steady state at X_{tens} = 0. At time 0, set X_{tens} value to 0.99, which mimics biorientation of all chromosomes. (A) With Cdc20 autoactivation ($k'_{imad}[Cdc20T]$ = 10), the checkpoint quickly disengaged and cyclin B degradation starts soon after the last chromosome is aligned. (B) The disengagement of the spindle checkpoint is compromised, and cyclin B degradation requires much longer time without Cdc20 autoactivation ($k'_{imad}[Cdc20T]$ = 0). The figures were first published in He et al. (2011).

In these definitions, [CycBM] = k_{scyc}/k_{dcyc} is the concentration of Cdk1 / CycB complex in mitosis. PP in our model is an unspecified protein phosphatase that gets activated after the metaphase-to-anaphase transition and counteracts Cdk1 / CycB activity. Hence, it is a reasonable assumption that the activity of total PP ([PPT]) is able to balance the activity of mitotic Cdk1 / CycB ([CycBM]) and that the two antagonistic activities are of a similar strength. We assume, without loss of generality, that [PPT] = [CycBM]. In addition, we assume that [Mad2T]/[Cdc20T] = 2 and the consequence of this assumption will be discussed later in this section. In terms of these variables, the system of ODEs can be displayed as in Equations 4.14 - 4.19.

$$\tau_{\mathrm{cyc}} \cdot \frac{d\, C_{cycB}}{dt} = 1 - (1 + \beta \cdot C_{\mathrm{Cdc20}}) \cdot C_{\mathrm{CycB}} \tag{4.14}$$

$$\tau_{\mathrm{x}} \cdot \frac{d\, X_{0A}}{dt} = \theta \cdot C_{\mathrm{CycB}} \cdot (1 - X_{tens} - X_{0A}) - C_{\mathrm{PP}} \cdot X_{0A} \tag{4.15}$$

$$\tau_{\mathrm{mad}} \cdot \frac{d\, C_{\mathrm{Mad2AT}}}{dt} = \gamma \cdot X_{0A} \cdot (\psi - C_{\mathrm{Mad2AT}}) - C_{\mathrm{Mad2AT}} - \delta \cdot C_{\mathrm{Cdc20}} \cdot C_{\mathrm{MCC}} \tag{4.16}$$

$$\tau_{\mathrm{mcc}} \cdot \frac{d\, C_{\mathrm{MCC}}}{dt} = \lambda \cdot C_{\mathrm{Cdc20}} \cdot C_{\mathrm{Mad2AF}} - (1 + \kappa \cdot (1 + \delta \cdot C_{\mathrm{Cdc20}})) \cdot C_{\mathrm{MCC}} \tag{4.17}$$

$$\tau_{\mathrm{pp}} \cdot \frac{d\, C_{\mathrm{PP}}}{dt} = (1 - C_{\mathrm{PP}}) - \eta \cdot C_{\mathrm{CycB}} \cdot C_{\mathrm{PP}} \tag{4.18}$$

$$C_{\mathrm{Cdc20}} = 1 - C_{\mathrm{MCC}}, \quad C_{\mathrm{Mad2AF}} = C_{\mathrm{Mad2AT}} - C_{\mathrm{MCC}} \tag{4.19}$$

In these dimensionless ODEs, the time constants are $\tau_{\mathrm{cyc}} = 1/k_{dcyc}$, $\tau_{\mathrm{x}} = 1/(k_{in,pp} \cdot [\mathrm{PPT}])$, $\tau_{\mathrm{mad}} = 1/k_{imad}$, $\tau_{\mathrm{mcc}} = 1/k_{dimcc}$ and $\tau_{\mathrm{pp}} = 1/k_{app}$. The dimensionless parameters are

$$\beta = \frac{k'_{dcyc} \cdot [\mathrm{Cdc20T}]}{k_{dcyc}} = 100, \quad \gamma = \frac{k_{amad} \cdot N_T}{k_{imad}} = 100, \quad \delta = \frac{k'_{imad} \cdot [\mathrm{Cdc20T}]}{k_{imad}} = 100,$$
$$\lambda = \frac{k_{asmcc} \cdot [\mathrm{Cdc20T}]}{k_{dimcc}} = 400, \quad \kappa = \frac{k_{imad}}{k_{dimcc}} = 0.1, \quad \eta = \frac{k_{ipp} \cdot [\mathrm{CycBM}]}{k_{app}} = 10,$$
$$\theta = \frac{k_{an,cyc} \cdot [\mathrm{CycBM}]}{k_{in,pp} \cdot [\mathrm{PPT}]} = 1, \quad \psi = \frac{[\mathrm{Mad2T}]}{[\mathrm{Cdc20T}]} = 2.$$

Numerical values are assigned to these dimensionless parameters based on the assumed values of the rate constants in Equations 4.1 - 4.6. Note that we are looking for the

steady states by setting the left-hand side of the equations to zero, thus the steady-state solutions of the ODEs depend only on these eight dimensionless ratios of parameters and not on the timescale constants (τ values).

$\mathrm{X_{tens}}$ is considered as an adjustable parameter in the model. During prometaphase, chromosomes come into alignment on the metaphase plate and $\mathrm{X_{tens}}$ increases stepwise: 0, 1/N_T, 2/N_T,..., (N_T - 1)/N_T, 1. At the metaphase-to-anaphase transition, $\mathrm{X_{tens}}$ drops rapidly from one to zero due to cohesin cleavage. The model has shown bistability for $X_{SN_{on}} \leq X_{tens} \leq X_{SN_{off}}$ and the desired saddle-node bifurcation points have to satisfy: **condition (i)**: $(N_T - 1)/N_T < X_{SN_{off}} < 1$ and **condition (ii)**: $X_{SN_{on}} < 0$.

To visualize how these dimensionless parameters can affect the steady-state solutions ($\mathrm{X_{SN_{on}}}$, $\mathrm{X_{SN_{off}}}$) of the model, two-parameter bifurcation diagrams are employed (Fig. 4.7). Bifurcation analysis demonstrates that **condition (i)** can be satisfied over a very broad range of parameter values: $\beta < 500,\ \gamma > 50,\ \delta < 400,\ \eta > 0,\ \kappa < 1,\ \lambda > 200,\ \theta > 1,\ \psi > 2$. This confirms that the SAC is active for $0 < \mathrm{X_{tens}} < (\mathrm{N_T} - 1)/\mathrm{N_T}$ and inactive for $(\mathrm{N_T} - 1)/\mathrm{N_T} < \mathrm{X_{tens}} < 1$ is truly a robust property of this model. In addition, the two-parameter bifurcation diagrams also show that **condition (ii)**, the SAC remains inactive in anaphase and telophase when $\mathrm{X_{tens}}$ drops to zero, is satisfied as long as the parameters fall within these boundaries: $\beta > 15,\ \gamma < 800,\ \delta > 10,\ \eta < 650,\ \theta < 9.5,\ \psi < 14$.

In summary, when both **conditions(i)** and **(ii)** are fulfilled, the dimensionless parameters are limited by the following boundaries (Fig. 4.7): $15 < \beta < 500$; $50 < \gamma < 800$; $10 < \delta < 400$; $0 < \eta < 650$; $1 < \theta < 9.5$; $2 < \psi < 14$. These boundary conditions are not too restrictive and they can be easily fulfilled with a wide range of parameter values.

The biological implications of the above boundary restrictions can be interpreted as follows:

- Total active Mad2 levels should be in excess in order to be able to inactivate all

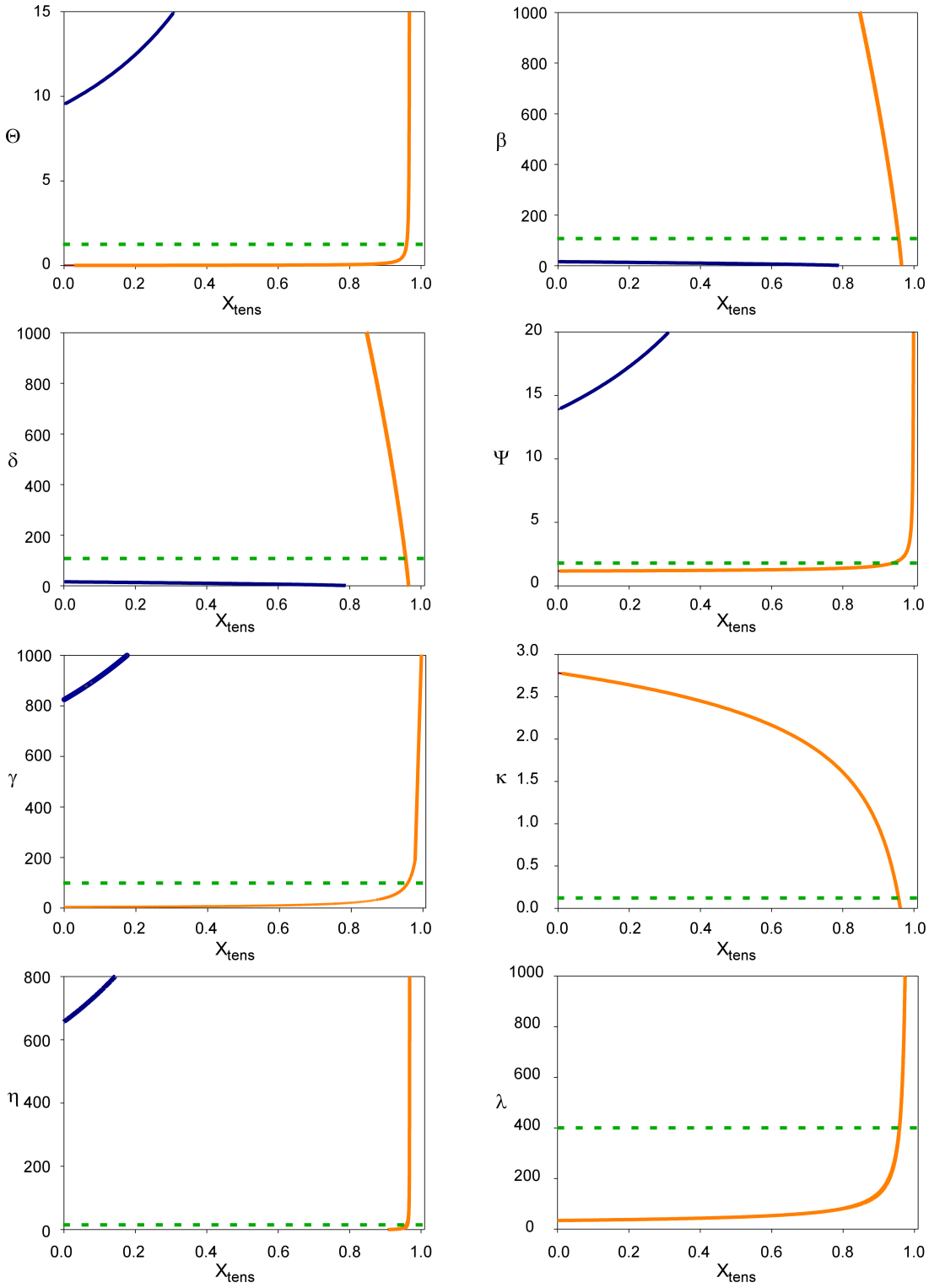

Figure 4.7: The robustness analysis of the anaphase switch. The figures represent two-parameter bifurcation diagrams, where the x-axis is the first parameter X_{tens}, while the parameters of y-axis are θ, β, ψ, λ, κ, η and γ respectively. The scaled model was used for the calculations. The orange line determines the upper saddle node points ($X_{SN_{off}}$); while the dark blue line defines the lower ($X_{SN_{on}}$) boundaries of bistable regime. Green dashed lines show the parameter values as used for one-parameter bifurcation diagrams in Figure 4.3. These figures are modified from He et al. (2011).

Cdc20 molecules in prometaphase but not as many as to reactivate the SAC in telophase: $2 \cdot [\text{Cdc20T}] < [\text{Mad2T}] < 14 \cdot [\text{Cdc20T}]$. Mad2 has been shown to

stoichiometrically binds to Cdc20 and forms protein complex (MCC) to inhibit the activity of APC (Fang et al., 1998; Sironi et al., 2001; Luo et al., 2002). As a stoichiometric inhibitor, Mad2 level needs to be in excess compared to Cdc20, and/or it should bind to Cdc20 with high affinity. The total concentrations of BubR1, Mad2 and Cdc20 in mitotic HeLa cells were estimated around 90 nM, 120 nM, 100 nM, respectively based on quantitative immunoblotting (Tang et al., 2001). The Mad2 in the model represents the total activity of mitotic checkpoint proteins which could potentially inhibit Cdc20 before the anaphase onset. Lumping the concentration of BubR1 and Mad2 together (around 210 nM) is already twice as much as Cdc20 level (100 nM), consisting with our calculation.

- There is a strong binding affinity between Mad2 and Cdc20: $k_{asmcc} \cdot [\mathrm{Cdc20T}] > 200 \cdot k_{dimcc}$. Using isothermal titration calorimetry, a high affinity binding of the closed form of Mad2 to Cdc20 has been demonstrated (dissociation constant K_d=0.1 μM, at least in vitro) (Sironi et al., 2002; Lad et al., 2009).

- The activation rate of Mad2 by a single unaligned chromosome is larger than the background inactivation rate of Mad2: $k_{imad} \cdot (50/N_T) < k_{amad} < k_{imad} \cdot (800/N_T)$. The background inactivation of Mad2 in the model only severs as the initial force to trigger the positive feedback of Cdc20-dependent Mad2 inactivation. This background inactivation acts against the activation of the spindle assembly checkpoint and is constantly present in the system even in prometaphase. Hence the activation rate of Mad2 by one unattached kinetochore should be larger than the background inactivation in order for a single unaligned chromosome to keep the checkpoint active (Rieder et al., 1994).

- The effects of $\mathrm{APC}^{\mathrm{Cdc20}}$-dependent degradation of cyclin B and Cdc20-dependent inactivation of Mad2 are neither too strong nor too weak: $15 \cdot k_{dcyc} < k'_{dcyc} \cdot [\mathrm{Cdc20T}] < 500 \cdot k_{dcyc}$ and $10 \cdot k_{imad} < k'_{imad} \cdot [\mathrm{Cdc20T}] < 400 \cdot k_{imad}$.

- The activation rate of tensionless chromosomes promoted by Cdk1 / CycB is greater than their inactivation rate by PP: $k_{in,pp} < k_{an,cyc} < 9.5 \cdot k_{in,pp}$.

- The inhibition effect of Cdk1/CycB on the phosphatase PP is not too strong: $k_{ipp} \cdot [\mathrm{CycBM}] < 650 \cdot k_{app}$. Since the identity of PP remains unclear, further experimental data is needed to confirm or refute the validity of this assumption..

- The background inactivation rate of Mad2 is smaller than the dissociation rate of MCC: $k_{dimcc} > k_{imad}$.

Although the boundaries for $\psi = [\mathrm{Mad2T}]/[\mathrm{Cdc20T}]$ are tight, the condition that $2 <$ [Mad2T]/[Cdc20T] < 14 is reasonable in light of our strong requirements on the saddle-node bifurcation points. As mentioned previously, the concentration of Mad2 ([Mad2T]), a stoichiometric inhibitor of Cdc20, needs to be greater than the total amount of Cdc20 ([Cdc20T]) in order to fully inhibit $\mathrm{APC}^{\mathrm{Cdc20}}$ activity (Fang et al., 1998). An experiment shows that maximal inhibition of Cdc20 requires a 12-fold excess of Mad2 over Cdc20 (Fang, 2002). This [Mad2T]/[Cdc20T] ratio reported in the literature falls into the range calculated from our two-parameter bifurcation analysis. On the other hand, Mad2 level must not be too high, as overexpression of Mad2 will block cells in metaphase and prevent the cell's exit from mitosis (Sotillo et al., 2007). The other set of tight bounds on the ratio $\theta = k_{an,cyc}/k_{in,pp}$ is also a consequence of how the spindle checkpoint works. As explained earlier in Section 4.2.3, [PP]/[CycB] $\ll \theta$ in prometaphase, and in telophase [PP]/[CycB] $\gg \theta$. Using Equations 4.14 - 4.19, we can estimate that in prometaphase [PP]/[CycB] = $1/(1+\eta) = 0.09$ and in telophase [PP]/[CycB] = $(1+\beta)^2/(1+\eta+\beta)$ = 92. Hence, the tight bounds on θ are imposed by the conditions that $0.1 \ll \theta \ll 90$.

4.3 An Alternative Model of the Anaphase Switch

The model in Section 4.2 assumed that Cdc20 directly promotes its own dissociation from the MCC (see Fig. 4.2). Presumably, active $\mathrm{APC}^{\mathrm{Cdc20}}$ ubiquitinates some components of the MCC, which leads to its dissociation and the inactivation of Mad2. The target of APC-dependent ubiquitination could possibly be Cdc20 or Mad2 (Reddy et al., 2007). However, we are not certain about the molecular mechanism of the self-activation loop. As has been suggested by D'Angiolella et al. (2003), another possibility is that the phos-

phorylation of Cdc20 by Cdk1/CycB is required to stabilize the MCC. More specifically, APC^{Cdc20}-dependent ubiquitination and subsequent degradation of cyclin B might account for dissociation of the MCC.

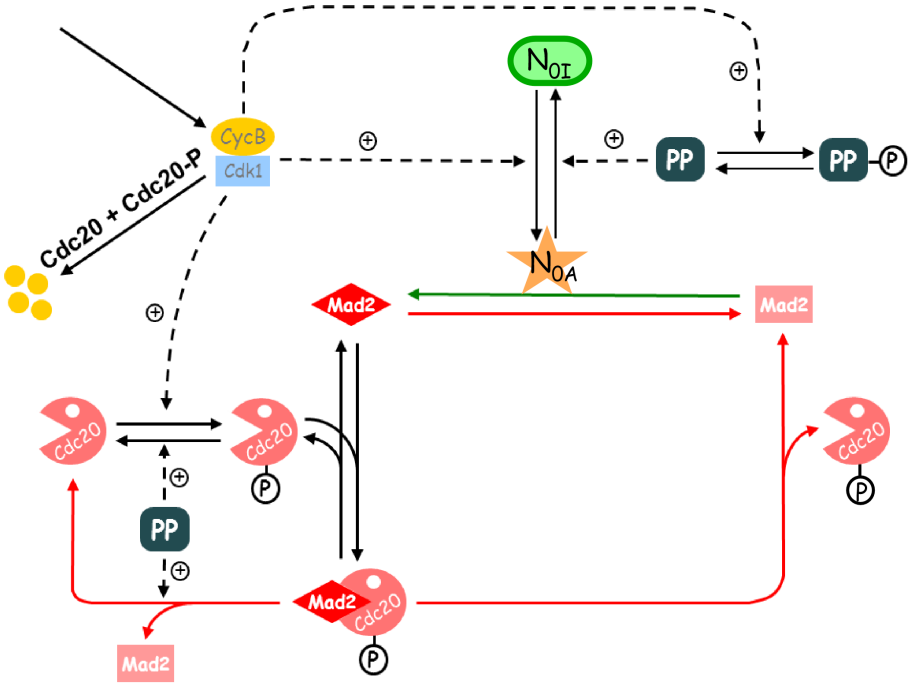

Figure 4.8: The alternative model of anaphase switch based on Cdc20 phosphorylation by Cdk1/CycB. In this model Cdc20 is phosphorylated by Cdk1/CycB and dephosphorylated by PP. Only the phosphorylated Cdc20 can bind to Mad2 creating an alternative positive feedback on Cdc20 activation. The dephosphorylation of Cdc20 promotes its release from its inhibitory complex Mad2:Cdc20. The APC^{Cdc20}-dependent Mad2 inactivation is not taken into account by this model. The figure is modified from He et al. (2011).

In this section, an alternative model of the SAC is developed based on this proposed mechanism and the schematic diagram is shown in Figure 4.8. Cdc20 is phosphorylated by Cdk1/CycB and dephosphorylated by an unspecified phosphatase PP. Only the phosphorylated form of Cdc20 (Cdc20P) can bind to Mad2 and form the MCC complex. In prometaphase, when Cdk1/CycB activity is high, nearly all Cdc20 is phosphorylated and sequestered by Mad2 in the complex form. Once all the chromosomes have bioriented, Cdc20P dissociates from the MCC and triggers the destruction of cyclin B due to the inactivation of Mad2. It is assumed in the model that both Cdc20 and Cdc20P promote cyclin B degradation with the same efficiency. This further downregulates Cdk1/CycB activity and leads to more Cdc20 release, creating an alternative positive feedback on Cdc20 activation. Apart from these modifications, the regulatory network of the model remained

unchanged as in the original (Fig. 4.2). The alternative model of the anaphase switch is described by a set of ODEs (Eqs. 4.20 - 4.26).

$$\frac{d\,[\mathrm{CycB}]}{dt} = k_{scyc} - (k_{dcyc} + k'_{dcyc} \cdot ([\mathrm{Cdc20}] + [\mathrm{Cdc20P}])) \cdot [\mathrm{CycB}] \tag{4.20}$$

$$\frac{d\,\mathrm{N_{0A}}}{dt} = k_{an,cyc} \cdot [\mathrm{CycB}] \cdot (\mathrm{N_T} - \mathrm{N_{tens}} - \mathrm{N_{0A}}) - k_{in,pp} \cdot [\mathrm{PP}] \cdot \mathrm{N_{0A}} \tag{4.21}$$

$$\frac{d\,[\mathrm{PP}]}{dt} = k_{app} \cdot ([\mathrm{PPT}] - [\mathrm{PP}]) - k_{ipp} \cdot [\mathrm{CycB}] \cdot [\mathrm{PP}] \tag{4.22}$$

$$\frac{d\,[\mathrm{Mad2AT}]}{dt} = k_{amad} \cdot \mathrm{N_{0A}} \cdot ([\mathrm{Mad2T}] - [\mathrm{Mad2AT}]) - k_{imad} \cdot [\mathrm{Mad2AT}] \tag{4.23}$$

$$- k_{ac20,pp} \cdot [\mathrm{PP}] \cdot [\mathrm{MCC}]$$

$$\frac{d\,[\mathrm{MCC}]}{dt} = k_{asmcc} \cdot [\mathrm{Cdc20P}] \cdot [\mathrm{Mad2AF}] - k_{ac20,pp} \cdot [\mathrm{PP}] \cdot [\mathrm{MCC}] \tag{4.24}$$

$$- (k_{dimcc} + k_{imad}) \cdot [\mathrm{MCC}]$$

$$\frac{d\,[\mathrm{Cdc20P}]}{dt} = k_{ic20} \cdot [CycB] \cdot [\mathrm{Cdc20}] + (k_{dimcc} + k_{imad}) \cdot [\mathrm{MCC}] - k_{ac20} \cdot [\mathrm{PP}] \cdot [\mathrm{Cdc20P}] \tag{4.25}$$

$$- k_{asmcc} \cdot [\mathrm{Cdc20P}] \cdot ([\mathrm{Mad2AT}] - [\mathrm{MCC}])$$

$$[\mathrm{Cdc20}] = [\mathrm{Cdc20T}] - [\mathrm{MCC}] - [\mathrm{Cdc20P}], \qquad [\mathrm{Mad2AF}] = [\mathrm{Mad2AT}] - [\mathrm{MCC}] \tag{4.26}$$

The bifurcation analysis and rate plots were performed on the system of the ODEs. As shown from the bifurcation diagram, the alternative model maintains the bistability, and the dynamic variables (e.g. $\mathrm{X_{0A}}$, Mad2:Cdc20, Cdk1 / CycB) follow similar trajectories to the original model as the system undergoes the anaphase switch (Fig. 4.9). The activation and inactivation rate plots of total active Mad2 are not significantly different either (Fig. 4.10). The time series simulation of the metaphase-to anaphase transition is shown in Figure 4.11. It can be seen from the figure, with the help of the positive feedback, once all the chromosomes are bioriented at time zero (by setting $\mathrm{X_{tens}}$=1), Mad2 is quickly inactivated, MCC dissociates, Cdc20 gets activated and CycB is quickly degraded, that eventually leads cell to exit from mitosis.

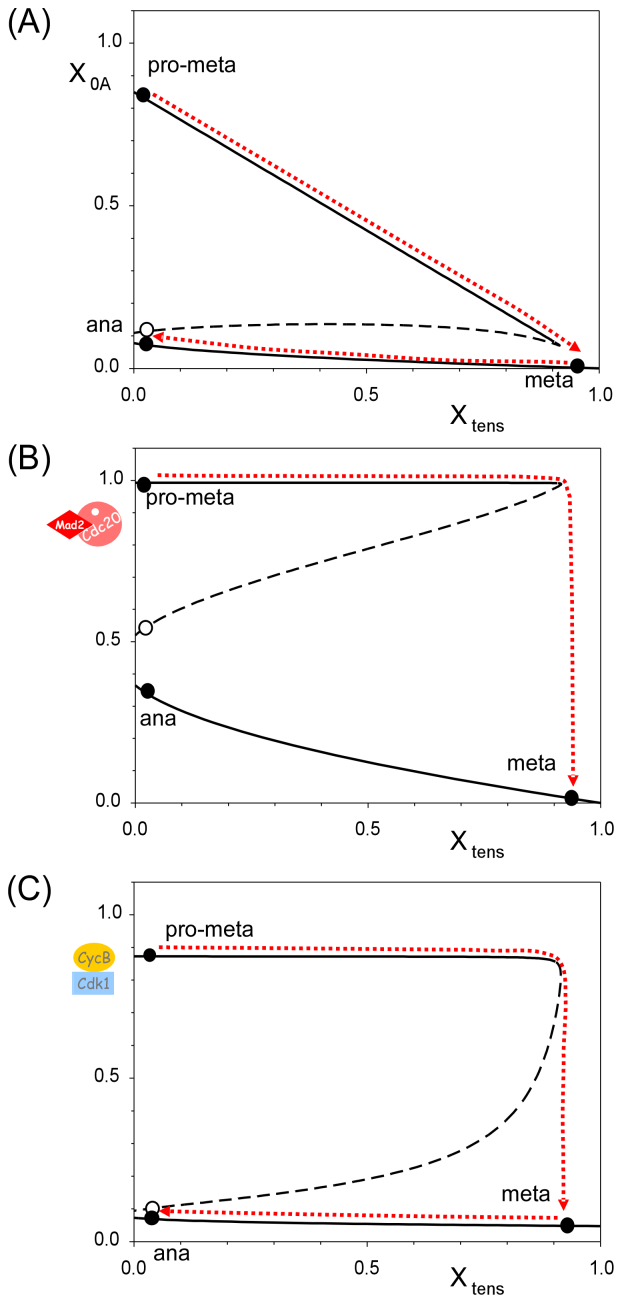

Figure 4.9: Bifurcation diagram of the alternative model of the anaphase switch. Three dynamical variables: (A) fraction of active tensionless chromosomes X_{0A}, (B) Mad2:Cdc20 complex, and (C) Cdk1/CycB were plotted as functions of X_{tens} (fraction of chromosomes under tension). The bistable behavior of the network is similar to the original model of the anaphase switch (see Fig. 4.3). The bifurcation analysis was conducted using the following initial conditions and parameter values: $[CycB] = 0.8725$, $[Mad2AT] = 1.9257$, $[MCC] = 0.9927$, $N_{0A} = 0.8498$, $[PP] = 0.1028$, $[Cdc20P] = 0.0003$, $N_{tens} = 0$, $[Cdc20T] = 1$, $[Mad2T] = 2$, NT=1, $[PPT] = 1$, $k_{scyc} = 0.1$, $k_{dcyc} = 0.1$, $k'_{dcyc} = 2$, $k_{amad} = 1$, $k_{imad} = 0.001$, $k_{ic20} = 10$, $k_{ac20} = 0.6$, $k_{asmcc} = 4000$, $k_{dimcc} = 1$, $k_{app} = 0.1$, $k_{ipp} = 1$, $k_{an,cyc} = 1$ and $k_{in,pp} = 1.5$. The units of the parameters depend on the reaction order: $M \cdot min^{-1}$ for zero order, min^{-1} for first order and $M^{-1} \cdot min^{-1}$ for second order reactions. These figures were first published in He et al. (2011).

4.4 Summary

Several recent experiments have implied that loss of tension at anaphase onset has the potential to reactivate the spindle assembly checkpoint, but that this is usually prevented in a normal mitotic cell cycle progression (Clute and Pines, 1999; Mirchenko and Uhlmann, 2010; Vázquez-Novelle and Petronczki, 2010; Oliveira et al., 2010). According to the experimental evidence, a deterministic model of the metaphase-to-anaphase transition based on a bistable switch has been presented in this work. The model simulations and numerical studies suggest that the metaphase-to-anaphase transition is indeed governed

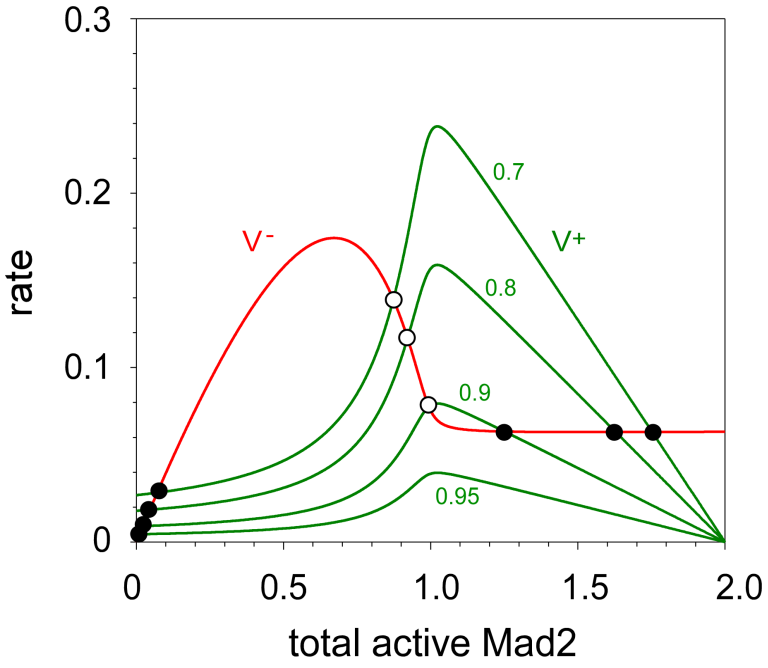

Figure 4.10: Rate plots from the alternative model of the anaphase switch. Rates of Mad2 activation (V^+, green) and inactivation (V^-, red) as functions of total active Mad2. This calculation was done with the alternative model for the anaphase switch based on Cdc20 phosphorylation by Cdk1/CycB. The activation rate curves were drawn from increasing values of X_{tens} from 0.7 to 0.95, and they had the same shape as in Figure 4.5A. The intersections represent steady states of Mad2 activity (black circle is the stable steady state; white circle is the unstable steady state). The parameter values are given in the caption of Figure 4.9. The figure was first published in He et al. (2011).

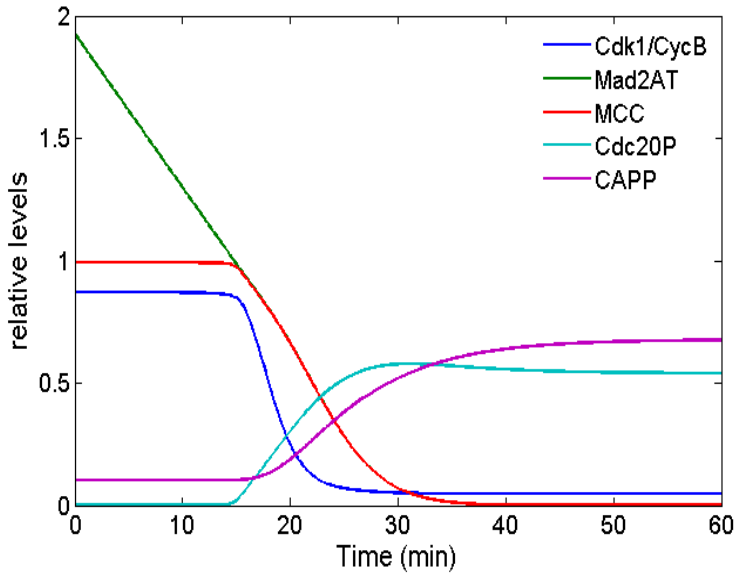

Figure 4.11: Temporal simulation of mitotic checkpoint disengagement after the last chromosome is aligned using the alternative model. Simulation was performed with the alternative mode with initial conditions corresponding to the high Cdk1/CycB steady state at X_{tens}=0. At time 0, increase X_{tens} to 1 and set X_{0A} to 0, which mimics biorientation of all chromosomes. The parameter values are given in the caption of Figure 4.9.

by a one-way toggle switch, just as the other irreversible cell cycle transitions. Bistability arises from the mutual inhibition between Cdk1/CycB and $\text{APC}^{\text{Cdc20}}$. As a consequence

of the bistability, the mitotic control network has two stable steady states in the absence of kinetochore tension: prometaphase with active SAC and anaphase with inactive SAC.

We have addressed, from a systems-level's point of view, three open questions regarding the spindle assembly checkpoint (SAC): • Why is the SAC not reactivated when tension decreases to zero at anaphase onset? • Why is a single unattached kinetochore able to keep the SAC active? • How is the synchronized and abrupt destruction of cohesin triggered? The steady state analysis from the model provides a plausible mechanism and suggests solutions for these unresolved questions: As illustrated in the bifurcation diagram (Fig. 4.3), the mitotic control system remains in a bistable region when $\mathrm{N_{tens}}$ (the number of chromosomes under tension) increases from zero to $N_T - 1$. However, down-regulation of Cdk1/CycB activity during the metaphase to anaphase transition prevents the reactivation of the SAC at anaphase onset even though kinetochore tension again decreases to zero (Fig. 4.3). Additionally, the fact that the saddle node point of the switch robustly lies between $N_T - 1$ and N_T, recapitulates the biological requirement for the metaphase-to-anaphase transition to only occur until the last chromosome is bioriented (Fig. 4.3). The autocatalytic activation of Cdc20 upon its disassembly from the mitotic checkpoint complex MCC (Mad2:Cdc20) significantly accelerates the SAC disengagement and triggers the synchronized events at anaphase onset. The importance of the autocatalytic effect for abrupt silencing of the checkpoint becomes apparent from the rate plots for Mad2 activity (Fig. 4.5)

In summary, the model provides a unique interpretation of the irreversible metaphase-to-anaphase transition in terms of systems-level feedback. It proposes novel explanations for several long-standing gaps in our understanding of the spindle assembly checkpoint, and correctly recapitulates all important features of the SAC, in agreement with the experiments from *Drosophila*, *Saccharomyces cerevisiae* and *Homo sapiens*.

Chapter 5

A Stochastic Model of the Anaphase Switch

Chapter 4 has described the construction of a simplified deterministic model of the anaphase switch to address several long-standing puzzles in the spindle assembly checkpoint. The deterministic model confirmed that metaphase-to-anaphase transition is governed by a bistable toggle switch, similarly to other irreversible cell cycle transitions (e.g. G1-to-S transition, G2-to-M transition).

The working mechanism of the spindle assembly checkpoint provides a precise timing regulatory machinery for the anaphase switch, given that events such as sister chromatid biorientation are stochastic processes due to the low copy number of chromosomes. These low copy numbers are in stark contrast to the large quantities of the other regulatory components involved in the metaphase-to-anaphase transition (Howell et al., 2000; Frisa and Jacobberger, 2009). The discrepancy may cause some special dynamic features of the cell cycle control system that are worth exploring further (Doncic et al., 2006).

In this chapter we will study the effect of biological noise on the anaphase switch using stochastic approaches. Treating the kinetochore-microtubule attachment at prometaphase as a noisy process, a simple stochastic model with sufficient complexity will be developed. Stochastic simulations will then be applied to explain how the spindle assembly checkpoint is able to detect mono-oriented chromosomes; how stochastic processes can

influence the duration of mitotic progression and how to interpret the timing relationship between prometaphase and metaphase in different model organisms. The model will also be used to reproduce and explain a group of important and classical experimental observations.

5.1 Stochastic Model Construction

The stochastic model is developed based on the deterministic model in Chapter 4 and the modifications that have been made are detailed in the following sections:

In the previous deterministic model, the number of bioriented chromosomes (N_{tens}) was expressed as a normalized parameter X_{tens}, denoting the fraction of chromosomes under tension (see Eq.4.2 in Section 4.2). Its value ranged between zero and one. For the purpose of conducting the stochastic simulation, N_{tens} is presented as a dynamic variable. The switches between different states of the chromosomes are shown in Figure 5.1. In addition to the bioriented chromosomes N_{tens}, the tensionless chromosomes are denoted by N_0. Depending on the ability to activate the spindle assembly checkpoint, N_0 is further subdivided into the active (N_{0A}) and inactive (N_{0I}) forms, whose interconversion is regulated by Cdk1/CycB and an unspecified protein phosphatase (PP).

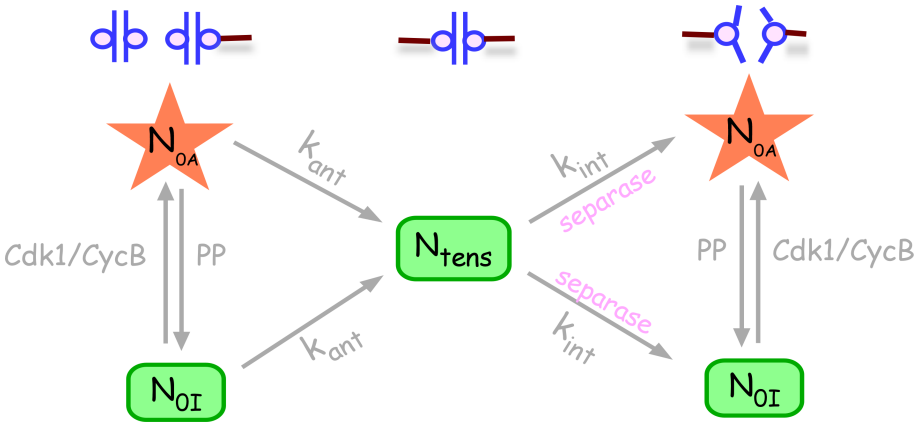

Figure 5.1: Different forms of chromosomes and their interconversion. N_{tens} and N_0 represent chromosomes with or without tension, respectively. Tensionless chromosomes (N_0) are further divided into an activate form (N_{0A}) and an inactive form (N_{0I}). The red Ns can activate the SAC, whereas the green ones cannot. The interconversion between N_{0A} and N_{0I} is regulated by Cdk1/CycB and its counteracting phosphatase PP. Reactions $N_0 \xrightarrow{k_{ant}} N_{tens}$ and $N_{tens} \xrightarrow{k_{int}} N_0$ characterize the chromosome congression and sister chromatid segregation procedure accordingly.

In prometaphase, chromosome congression (characterized by the reactions $N_{0A} \rightarrow N_{tens}$ and $N_{0I} \rightarrow N_{tens}$ with rate constant k_{ant}) requires spindle microtubules from both cell poles to search and capture unattached kinetochores. Since this process is stochastic, it takes various lengths of time for all the chromosomes to ultimately become bioriented on the metaphase plate (Lew and Burke, 2003). Sister chromatid segregation at anaphase onset by contrast, which is characterized by the reactions $N_{tens} \rightarrow N_{0A}$ and $N_{tens} \rightarrow N_{0I}$ with rate constant k_{int}, takes place in a rapid, synchronized manner (Meraldi et al., 2004). This indicates that the reactions of anaphase onset are much faster than the reactions representing chromosome congression, i.e. $k_{ant} \ll k_{int}$ (Reactions 11-14 in Table 5.1).

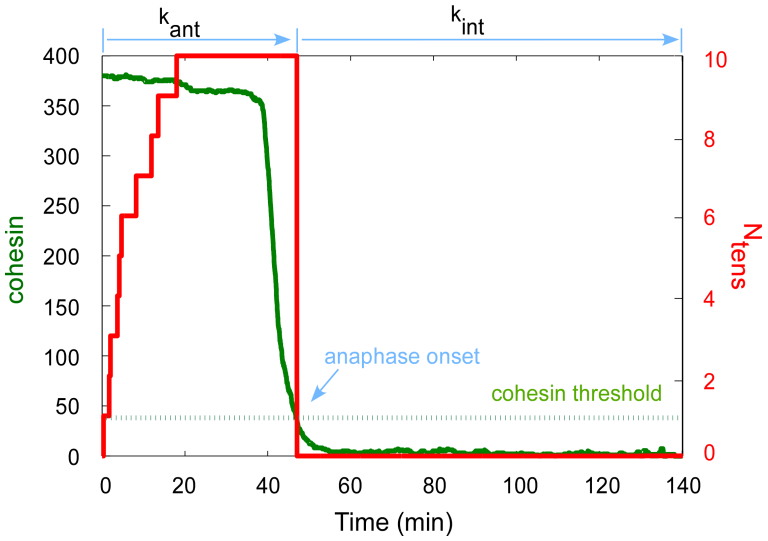

Figure 5.2: Modelling the successive steps of the mitotic progression with Heaviside function. In the stochastic model, $\mathrm{N_{tens}}$ is modelled as a dynamic variable with the activation rate k_{ant} and the inactivation rate k_{int}. The generation and release of tension take place at different time scales. In order to let the system's dynamic follow the unidirectional sequence of the mitotic progression, Heaviside step function is introduced. $Heav(cohesin - threshold) = 1$ if cohesin $\geq$ threshold, otherwise $Heav(cohesin - threshold) = 0$. Only when the cohesin level decreases below the threshold, anaphase can take place. Cohesin level (green curve) is labeled on the left y-axis and $\mathrm{N_{tens}}$ (red curve) is labeled on the right y-axis. Total number of chromosomes $\mathrm{N_T}$ = 10, total number of cohesin Cohe = 380 and cohesion threshold thre = 38.

Since the chromosome segregation ($N_{tens} \rightarrow N_0$) happens abruptly and requires separase activity, a new component 'cohesin protein'– serving as a timer to control the anaphase onset – is introduced into the model. Cohesin is synthesized at a constant rate and degraded in a separase-dependent manner (Reactions 7,8 in Table 5.1). Only when the cohesin level drops below a certain threshold (set arbitrarily to 10% of its total level) can reactions $N_{tens} \rightarrow N_{0A}$ and $N_{tens} \rightarrow N_{0I}$ occur.

According to the temporal order of the cell cycle events, tension generation ($N_0 \rightarrow N_{tens}$) and tension release ($N_{tens} \rightarrow N_0$) must occur successively. Therefore, the Heaviside step function is employed to mimic the successive procedures of tension generation and chromosome segregation (see the propensity function of v_{11}, v_{12}, v_{13}, v_{14} in Table 5.1 caption). Figure 5.2 demonstrates the working mechanism of the Heaviside function to ensure the correct order of the mitotic progression in the model. In prometaphase, cells have none bioriented chromosomes ($\mathrm{N_{tens}}$ = 0) and a large amount of intact cohesin (Cohe = 380); only reaction $N_0 \rightarrow N_{tens}$ takes place because cohesin $\geq$ threshold and $Heav(cohesin - threshold) = 1$. When all the chromosomes are bioriented ($\mathrm{N_{tens}} = \mathrm{N_T}$), the SAC is inactivated and separase is activated to promote cohesin destruction. Once the cohesin levels decrease below the threshold (38 number of molecules), the Heavside function will switch to zero and allows the reaction $N_{tens} \rightarrow N_0$ to occur (Fig. 5.2).

The deterministic model does not explicitly include securin and separase, however in the stochastic model both species are modelled as dynamic variables. Moreover, the complex formation of separase and securin is assumed to be at equilibrium, as shown in Equation 5.1. The same applies for the complex of Mad2 and Cdc20 (Eq. 5.2). Additionally, there are three conservation relations $PPT = PP + PP_i$, $SepT = Sep + SepSec$ and $Mad2T = Mad2 + Mad2AT$ for total phosphatase (PPT), total separase (SepT) and total Mad2 (Mad2T), respectively. All the elementary reactions of the stochastic model are listed in Table 5.1.

$$SepSec = \frac{2 \cdot Sect \cdot SepT}{SS + \sqrt{SS^2 - 4 \cdot SepT \cdot Sect}}, \tag{5.1}$$

$$where, \quad SS = Sect + SepT + \frac{ldss + (kdsec' + kdsec \cdot Cdc20)}{lass}.$$

$$MCC = \frac{2 \cdot Mad2AT \cdot Cdc20T}{BB + \sqrt{BB^2 - 4 \cdot Mad2AT \cdot Cdc20T \cdot (1 + \frac{kimad}{lamcc})}}, \tag{5.2}$$

$$where, \quad BB = Cdc20T + Mad2AT + \frac{ldmcc + kimad' + kimad \cdot Cdc20T}{lamcc}$$

No.	*Paramete*	*Values*	*Reactions*	*Description*
1	*kscyc*	*10*	$\emptyset \rightarrow CycB$	*cyclin B synthesis*
2	*kdcyc'*	*0.01*	$CycB \rightarrow \emptyset$	*cyclin B degradation*
3	*kdcyc*	*0.001*	$CycB \xrightarrow{Cdc20} \emptyset$	*APC^{Cdc20}-dependent cyclin B degradation*
4	*kssec*	*10*	$\emptyset \rightarrow Sect$	*securin synthesis*
5	*kdsec'*	*0.01*	$Sect \rightarrow \emptyset$	*securin degradation*
6	*kdsec*	*0.001*	$Sect \xrightarrow{Cdc20} \emptyset$	*APC^{Cdc20}-dependent securin degradation*
7	*ksc*	*1*	$\emptyset \rightarrow Cohe$	*cohesin synthesis*
8	*kdc*	*0.0006*	$Cohe \xrightarrow{Sep} \emptyset$	*cohesin cleavage by separase*
9	*kan*	*0.1*	$N_{0I} \xrightarrow{CycB} N_{0A}$	*Cdk1/CycB-dependent transformation from N_{0I} to N_{0A}*
10	*kin*	*0.1*	$N_{0A} \xrightarrow{PP} N_{0I}$	*PP-dependent transformation from N_{0A} to N_{0I}*
11	*kant*	*0.12*	$N_{0A} \rightarrow N_{tens}$	*biorientation of an active tensionless chromosome*
12	*kant*	*0.12*	$N_{0I} \rightarrow N_{tens}$	*biorientation of an inactive tensionless chromosome*
13	*kint*	*1*	$N_{tens} \rightarrow N_{0A}$	*chromosome segregation yielding an active chromosome*
14	*kint*	*1*	$N_{tens} \rightarrow N_{0I}$	*chromosome segregation yielding an inactive chromosome*
15	*kamad*	*0.2*	$Mad2 \xrightarrow{N_{0A}} Mad2AT$	*tensionless active chromosomes activate Mad2*
16	*kimad'*	*0.02*	$Mad2AT \rightarrow Mad2$	*background inactivation of Mad2*
17	*kimad*	*0.002*	$MCC \xrightarrow{Cdc20} Mad2$	*Cdc20 promotes MCC dissociation*
18	*kapp*	*0.1*	$PP_i \rightarrow PP$	*phosphatase activation*
19	*kipp*	*0.001*	$PP \xrightarrow{CycB} PP_i$	*Cdk1/CycB-dependent phosphatase inactivation*

Table 5.1: Elementary reactions in the stochastic model of the anaphase switch. The initial values (number of molecules) of the species are: $Sect = 758$, $Mad2AT = 1976$, $CycB = 849$, $PP = 130$, $N_{0A} = 10$, $N_{0I} = 0$, $Cohe = 380$, $Cdc20T = 1000$, $SepT = 500$, $Mad2T = 2000$, $N_T = 10$, $PPT = 1000$, $V = 1000$. The units of the parameter depend on the reaction order: $molecule \cdot min^{-1}$ for zero order, min^{-1} for first order and $molecule^{-1} \cdot min^{-1}$ for second order reactions. The propensity functions of Reactions 11-14 include the Heaviside function: $\mathrm{v}_{11} = \mathrm{kant} \cdot \mathrm{N_{0A}} \cdot \mathrm{heav(Cohe - thre)}$, $\mathrm{v}_{12} = \mathrm{kant} \cdot \mathrm{N_{0I}} \cdot \mathrm{heav(Cohe - thre)}$, $\mathrm{v}_{13} = \mathrm{kint} \cdot \mathrm{N_{tens}} \cdot \mathrm{heav(thre - Cohe)} \cdot \frac{\mathrm{kan \cdot CycB}}{\mathrm{kan \cdot CycB + kin \cdot PP}}$ and $\mathrm{v}_{14} = \mathrm{kint} \cdot \mathrm{N_{tens}} \cdot \mathrm{heav(thre - Cohe)} \cdot \frac{\mathrm{kin \cdot PP}}{\mathrm{kan \cdot CycB + kin \cdot PP}}$. $Heav(Cohe - thre) = 1$ if Cohe $\geq$ thre, otherwise $Heav(Cohe - thre) = 0$. The threshold of the cohesin $thre = 38$, set as 10% of the total cohesin level.

5.2 Analysis of Mitotic Timing in PtK1 Cells

Conly L. Rieder and colleagues filmed 126 PtK1 cells and monitored the length of each phase in mitosis (Rieder et al., 1994). They discovered that the time taken from the

nuclear envelope breakdown (NEBD) to anaphase onset has a strong linear correlation with the duration of prometaphase, suggesting that prometaphase is likely to be the most time-consuming step in the mitotic progression before anaphase. They provided evidence that the working function of the spindle assembly checkpoint is to detect kinetochore-microtubule attachments and even a single unattached kinetochore is able to delay anaphase onset. They have also found that anaphase initiation takes place at a fixed time, approx 23 minutes after the completion of chromosome congression (Rieder et al., 1994). This section will study and revisit the findings of these classic experiments using the stochastic model (Table 5.1).

The question as to how a single unattached kinetochore is sufficient to block the metaphase to anaphase transition has already been investigated by bifurcation analyses (Fig. 4.3) and rate plots (Fig. 4.5) using the deterministic model in Chapter 4. Here, this question will be re-examined by the stochastic time course simulations. In total ten pairs of sister chromatids ($\mathrm{N_T}$ = 10) are considered in the model, which corresponds to the experimental model system, PtK1 cell. The simulation starts from prometaphase with high Cdk1/CycB activity, active Mad2, inactive separase, intact cohesion and the absence of bioriented chromosomes ($\mathrm{N_{tens}}$ = 0). Unless otherwise stated, the stochastic simulations are carried out using the parameter set and initial conditions listed in Table 5.1. In the time course simulation of a normal metaphase-to-anaphase transition, anaphase only occurs after all the chromosomes have bioriented and are under tension ($\mathrm{N_{tens}}$ = $\mathrm{N_T}$ = 10), as shown in Figures 5.3A,B. In the simulation of nocodazole blocked cells by contrast, even if 9 out of 10 chromosomes are under tension ($\mathrm{N_{0A}}$ = 1, $\mathrm{N_{tens}}$ = 9), anaphase is still prevented, because the SAC remains active (Figs. 5.3C,D). From a dynamical systems properties, the reason that the system is completely blocked in metaphase is that the saddle node lies between 9/10 and 1 (see Fig. 4.3 in the deterministic model of the SAC). Thus, the stochastic simulation confirms the sensitivity of the spindle assembly checkpoint to a single unattached kinetochore even in a noisy environment (Rieder et al., 1994).

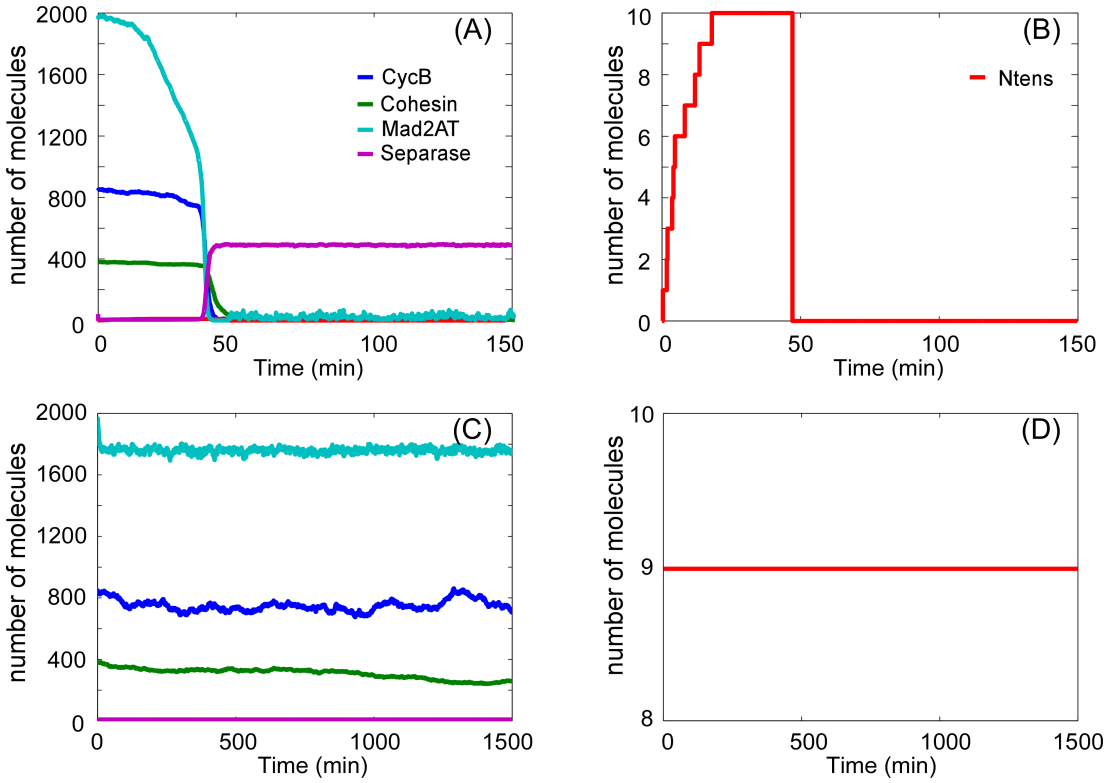

Figure 5.3: Stochastic simulations provide further proof of the robustness of the anaphase switch. (A, B) Normal metaphase-to-anaphase transition in PtK1 cells. The transition occurs once cohesin levels have decreased below a threshold. (C, D) In nocodazole blocked cells, the SAC is kept active by a single unattached kinetochore and anaphase onset is prevented. Mad2AT levels are used as a readout for the SAC activity. The computer code of the SSA simulations can be found in Appendix B.1 using the parameters sets and variable initial values listed in Table 5.1. Following parameters need to be changed to simulate the nocodazole block condition: k_{ant} = 0, $\mathrm{N_{0A}}$ = 1, $\mathrm{N_{tens}}$ = 9.

Following the experimental protocol of Rieder et al. (1994), a group of 126 independent stochastic simulations were conducted. Compared to Figure 5.4 from the experiment, the computed outcomes match the experimental data remarkably well. The histogram plot generated from batch simulations shows the time intervals from NEBD to anaphase onset vary substantially (ranging from 20 mins to 100 mins) between individuals in a population of PtK1 cells (Fig. 5.5A). The timing of mitotic events in the simulations are defined as follows: NEBD is set as time zero; the initiation of metaphase is determined when $\mathrm{N_{tens}}$ = $\mathrm{N_T}$ for the first time, i.e. all chromosomes are bioriented and under tension; anaphase onset is defined by the time when cohesin levels decreasing below the threshold for the first time (Fig. 5.3). The strong linear correlation between the duration from NEBD to anaphase onset and the length of prometaphase was observed experimentally (Fig. 5.4B) and is captured successfully by the model simulations (Fig. 5.5B). It confirms the experimental finding that the dominant contributing factor to the variable

duration of mitotic progression is prometaphase, more specifically the stochastic process of kinetochore-microtubule attachment. Cells are divided into four groups based on the lengths for holding mono-oriented chromosomes relative to NEBD. The average time of anaphase onset is then calculated for each group. The simulations reveal that the longer a cell has mono-oriented chromosomes, the longer anaphase onset is delayed in accordance with the experiments (Fig. 5.5C).

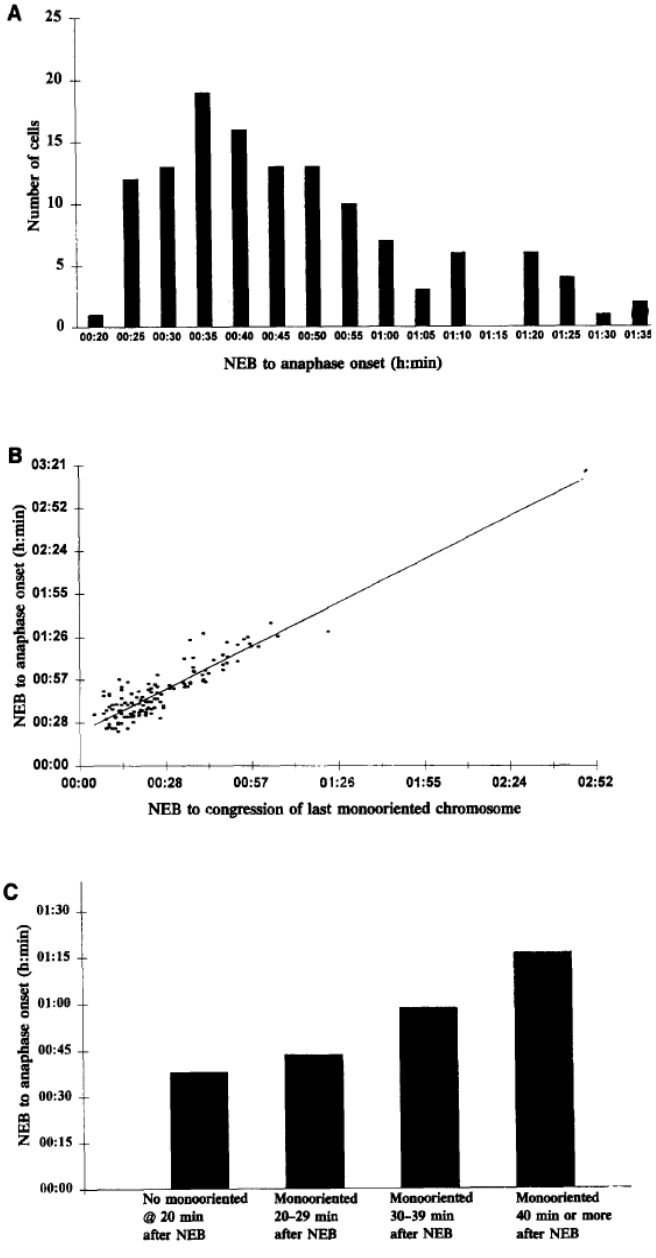

Figure 5.4: Timing variations of the mitotic events at anaphase switch in a population of cells in the experiment of Rieder et al. (1994). (A) Histogram plotting the number of cells versus the duration of spindle formation (NEB to anaphase onset) rounded to the nearest 5 min. This plot does not include a single cell that took over 3 h to complete spindle formation. Note that the duration from NEB to anaphase onset in PtK is highly variable. (B) Scatter plot in which the duration of spindle formation is plotted against the time it takes for the last monooriented chromosome in the cell to biorient relative to NEB. Note the strong positive linear relationship ($r^2 = 0.85$) between these two variables. (C) The average duration between NEB and anaphase onset versus the time the last monooriented chromosome initiates congression relative to NEB. Note that the longer the cell has monooriented chromosomes the longer anaphase onset is delayed relative to NEB. The plots and the caption are taken from Figure 3 in Rieder et al. 1994.

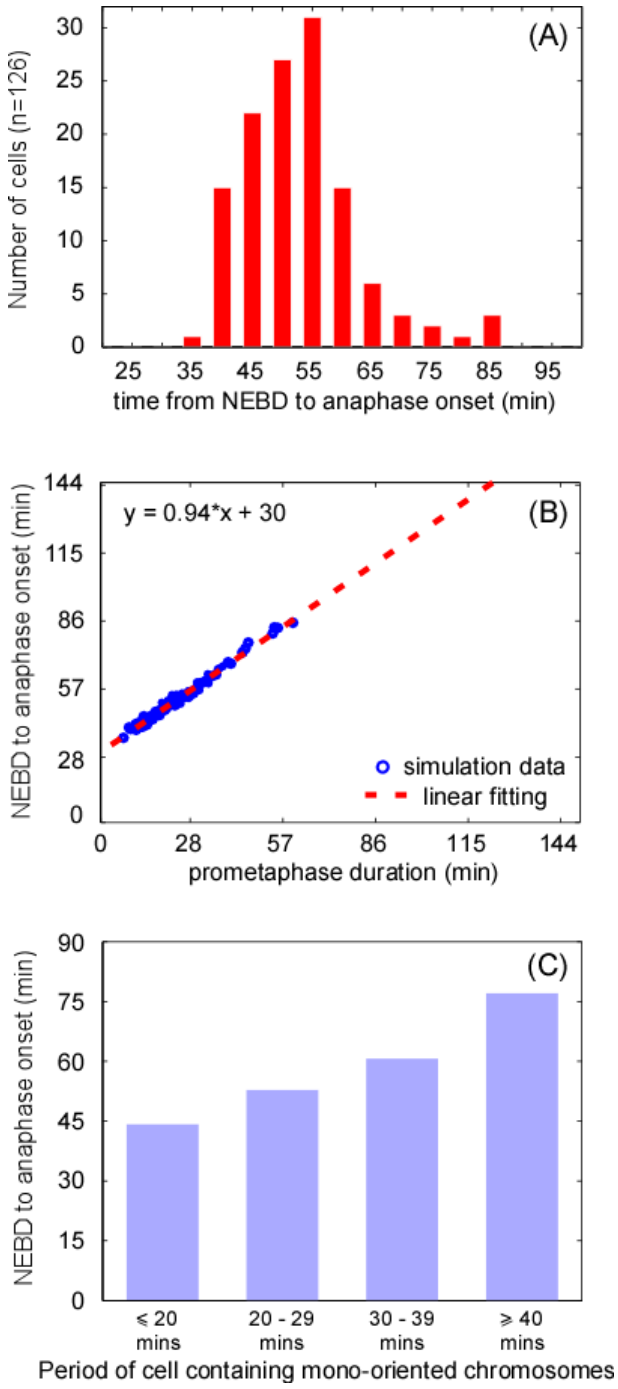

Figure 5.5: Timing variations of the mitotic events at anaphase switch in a population of cells. A group of 126 stochastic simulations was conducted and plotted the same way as Figure 3 in Rieder et al. (1994). NEBD is defined at time zero; the initiation of metaphase is defined when the first time N_{tens} equals the total number of chromosomes N_T; and anaphase onset is denoted when cohesin level decreases below the threshold (10% of total number of cohesin) for the first time as explained in Figure 5.3. (A) Histogram plot with the number of cells versus the durations from NEBD to anphase onset. As can be seen from the figure, the durations from NEBD to anaphase onset are highly variable (from 20 mins to 100 mins). The time is rounded to the nearest 5 min. (B) Scatter plot in which the durations from NEBD to anaphase onset are plotted against the lengths of prometaphase. There is a strong positive linear relationship between the two variables. The linear regression curve was plotted in a red dashed line. (C) The average length of time intervals between NEBD and anaphase onset versus the time of cell containing monooriented chromosomes. The time durations from NEBD to the initiation of metaphase is classified into four different groups and the average length of time from NEBD to anaphase onset for each group is calculated. The longer the cell has monooriented chromosomes the longer anaphase onset is delayed relative to NEBD.

5.3 Timing Relationship between Prometaphase and Metaphase

Meraldi et al. (2004) studied the mitotic progression in HeLa cells following the similar experimental protocol of Rieder et al. (1994) and found a biphasic timing relationship between prometaphase and metaphase. This relation was not seen in Rieder's experiment (1994) and in our corresponding simulations (Fig. 5.5B), most likely because they mainly

focused on the relationship between prometaphase length and the time of anaphase onset relative to NEBD. The way they plotted the figure could easily obscure the timing correlation between prometaphase and metaphase that was observed in the experiment of Meraldi et al (1994).

Therefore, further analysis was performed to investigate if a similar relationship between prometaphase and metaphase can be seen from our simulations as shown in Meraldi et al. (2004). Using the same dataset generated from the previous study (Fig. 5.5B), the simulation outcomes were split into two groups according to the prometaphase lengths. One group contains the simulations with prometaphase shorter than 35 mins and the other group has prometaphase longer than 35 mins. A plot of the metaphase time against the duration of prometaphase for each simulation was generated (Fig. 5.6). A biphasic relationship can indeed be seen between the two time intervals by linear regression. If the length of prometaphase is shorter than 35 mins, metaphase is longer; but the sum of the two durations (i.e. the duration from NEBD to anaphase onset) is approximately constant (around 50 mins). If the length of prometaphase is longer than 35 mins then the metaphase duration remains the same (around 27 mins) regardless of the prometaphase lengths. In this case, anaphase onset relative to NEBD will be longer than 50 mins.

One of the crucial assumptions in the deterministic model was that the total level of active Mad2 (Mad2AT) exceeds the total level of Cdc20 (Cdc20T). This is a reasonable assumption because an excess of the inhibitor Mad2 will guarantee that Cdc20 is kept fully inactive in prometaphase (for details, see Chapter 4). This assumption is going to be revisited in the following sections using the stochastic model.

To investigate the role of Mad2AT in regulating the timing of prometaphase and metaphase, four independent stochastic simulations of normal metaphase-to-anaphase transition were performed and the Mad2AT level was plotted as a function of time (Fig. 5.7). The level of Mad2AT appears correlated with the lengths of both prometaphase and metaphase. In the two simulations where prometaphase durations are shorter (red and green curves), the corresponding metaphases take relatively longer. Whereas, for the other two

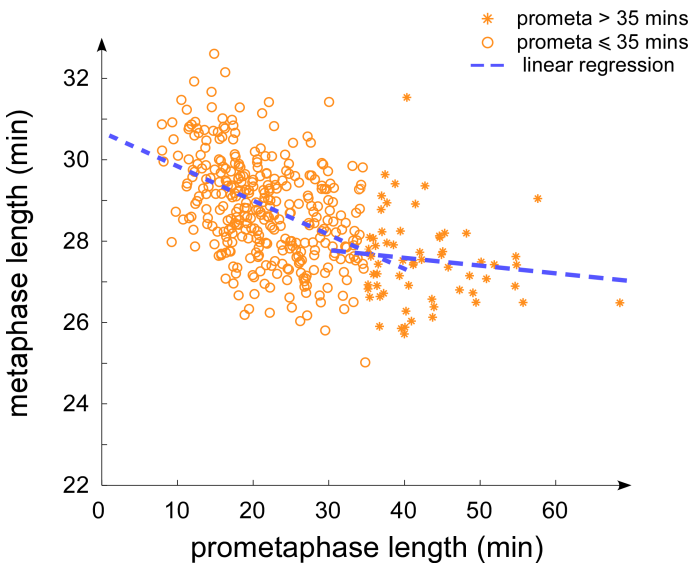

Figure 5.6: Scatter plot of prometaphase length versus metaphase length in PtK1 cells generated from the stochastic simulations. Simulations were divided into two groups according to their prometaphase durations and plotted separately. The system whose prometaphase is longer than 35 mins (plotted as '$*$') has a constant metaphase length of about 27 mins. However, when the system with prometaphase shorter than 35 mins (plotted as '$\circ$'), the metaphase becomes steadily longer. The linear regression lines for each subpopulation are indicated by the red dashed lines.

cases with longer prometaphases (blue and purple curves), their metaphase durations are approximately constant (Fig. 5.7).

We explain this by the fact that Mad2AT inactivation is not instantaneous but requires a certain amount of time. In a mitotic cell with fast chromosome biorientation (i.e. a cell with a short prometaphase), after completion of chromosome congression, additional time is needed to bring down Mad2AT levels to trigger anaphase onset. By contrast, in cells with longer prometaphase, Mad2AT inactivation takes place alongside the slower chromosome alignment. In this case, Mad2AT levels have already reached the lowest possible level ($\sim$ 1800 molecules in the model simulation) that still keeps the SAC active at the time when the last chromosome becomes bioriented. The time interval from this point to anaphase onset, i.e. the duration of metaphase, is then roughly constant, as it takes approximately the same time to inactivate equivalent amounts of active Mad2 (Fig. 5.7).

If the interpretation from the individual simulations is correct, we would expect biphasic relationship between Mad2AT level and prometaphase length similar to Figure 5.6. This

cell cycle stages (min)	red	green	blue	magenta
prometaphase	10	15	46	55
metaphase	29	30	27	27

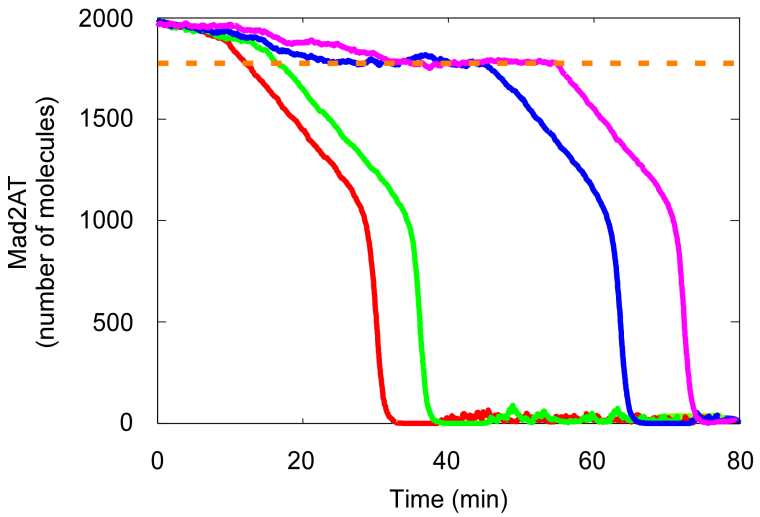

Figure 5.7: The timing of prometaphase and metaphase is dependent on the total level of active Mad2. Four stochastic time course simulations of Mad2AT and their corresponding prometaphase durations are plotted. The durations of metaphase and prometaphase were calculated separately as described in Section 5.2. The table shows the calculated the prometaphase and metaphase lengths from the simulations. 1) Red curve: prometaphase = 10 mins, metaphase = 29 mins; 2) Green curve: prometaphase = 15 mins, metaphase = 30 mins; 3) Blue curve: prometaphase = 46 mins, metaphase = 27 mins; 4) Magenta curve: prometaphase = 55 mins, metaphase = 27 mins. Both prometaphase and prometaphase are longer than the threshold 35 mins, so they have a relatively constant metaphase length approx 27 mins. The orange dashed line represents the minimal level of Mad2AT before metaphase onset.

hypothesis is confirmed when plotting these two variables in Figure 5.8. If prometaphase is shorter than $\sim$ 35 mins, Mad2AT levels are higher than 1800 molecules at the end of prometaphase and metaphase length is inversely correlated with the duration of prometaphase. However if prometaphase is longer than $\sim$ 35 mins, Mad2AT has already reached the lowest level required to maintain the active state of the SAC before chromosome congression is completed. Hence it takes the same time to inactivate Mad2AT and the duration of metaphase becomes constant (Fig. 5.8A). A linear relationship can be further revealed when plotting the metaphase length and Mad2AT level at the congression of the last monooriented chromosome: the metaphase duration depends on the Mad2AT level at the beginning of metaphase (Fig. 5.8B).

This finding supports the initial modelling assumption that Mad2 is in excess over Cdc20: inactivation of excess active Mad2 provides a delay in cells where prometaphase

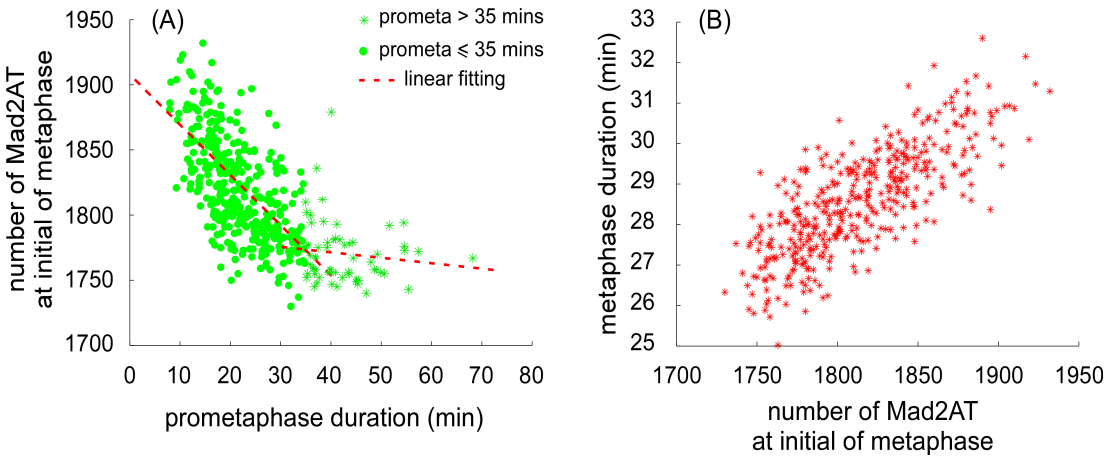

Figure 5.8: The timing of prometaphase and metaphase are related to the total level of active Mad2. A batch of 400 independent stochastic simulations was conducted. (A) Scatter plot in which the Mad2AT level at the congression of the last monooriented chromosome is plotted against the duration of prometaphase. The shorter the prometaphase length, the greater amount of Mad2AT at the initiation of metaphase and the longer it takes for cells to complete metaphase. The simulations with prometaphase shorter than 35 mins are plotted as '$\circ$' and the simulations with prometaphase longer than 35 mins are plotted using '$*$'. The red lines are the linear regression for the simulation data. (B) Scatter plot in which the duration of metaphase is plotted against the level of Mad2AT at congression of the last monooriented chromosome, recreating a positive linear correlation.

is short, thus preserving the accurate timing of anaphase onset and preventing potential errors in the chromosome segregation process (Meraldi et al., 2004).

5.4 Analysis of Mitotic Timing in HeLa Cells

As an important spindle assembly checkpoint protein, Mad2 has a significant role in regulating the timing of mitotic events by inhibiting the APC activator Cdc20 (see Section 1.2.4 in Chapter 1). Partial down-regulation of Mad2 has been shown to cause premature chromosome segregation (Kienitz et al., 2005).

Meraldi et al. (2004) used RNA interference (RNAi) and time-lapse imaging to study the effect of mitotic checkpoint proteins depletion on the chromosome dynamics and mitotic events in HeLa cells. They followed the experimental protocol of Rieder et al. (1994) and monitored the timing of mitotic progression in control and Mad2 RNAi conditions. They discovered that in HeLa cells with depleted Mad2 the time from NEBD to anaphase onset was significantly shorter than in control cells and Mad2 depletion induced enormous errors in sister chromatid separation. Among these Mad2 RNAi cells, 95% showed

premature anaphase onset, regardless of the presence of lagging or monooriented chromosomes (Meraldi et al., 2004; Held et al., 2010). This live-cell imaging experiments provide data with sufficient resolution for the stochastic model to quantitatively reproduce the results.

To simulate the experiments, the same stochastic model in Section 5.1 was used and parameter values were modified. In total, 50 pairs of sister chromatids ($\mathrm{N_T}$ = 50) are considered for Hela cells in the model. The parameters which differ from those in Table 5.1 are given in the caption of Figure 5.9. According to the experiments by Meraldi et al. (2004), 376 and 127 independent stochastic simulations were conducted for the control and Mad2-depletion conditions, respectively.

The stochastic simulations successfully capture the dynamics of the mitotic events for both control and Mad2 RNAi cells (Fig. 5.9). 20 simulations of mitotic progression in control cells were selected randomly and shown in Figure 5.9A. Note that the model only considers the events from NEBD to anaphase onset. It is thus impossible to simulate the anaphase durations as described in the original paper (Meraldi et al., 2004). Nevertheless, the average lengths of prometaphase (25 mins) and metaphase (10 mins) can be calculated from the simulations. In contrast to the control, a majority of Mad2 RNAi simulations have relatively shorter prometaphase ($\sim$ 20 mins) and lost the entire metaphase (Fig. 5.9B). For the Mad2 RNAi condition, if anaphase onset takes place prematurely, metaphase duration is set as zero and the time of anaphase onset is denoted by the time when cohesin levels decrease below the threshold, regardless of unaligned chromosomes. The time distributions and cumulative functions of anaphase onset for the control and Mad2 RNAi conditions were calculated and plotted respectively (Figs. 5.9C,D). As shown in the figure, the average duration from NEBD to the anaphase initiation in Mad2 knockdown cell is reduced to 12 mins compared to 34 mins in control cells. The number of bioriented chromosomes at anaphase onset was recorded from the simulations and the distributions were plotted as histograms (Figs. 5.9E,F). Contrary to the control, in which 99$\%$ of cells with all the chromosomes have bioriented before anaphase onset (Fig.

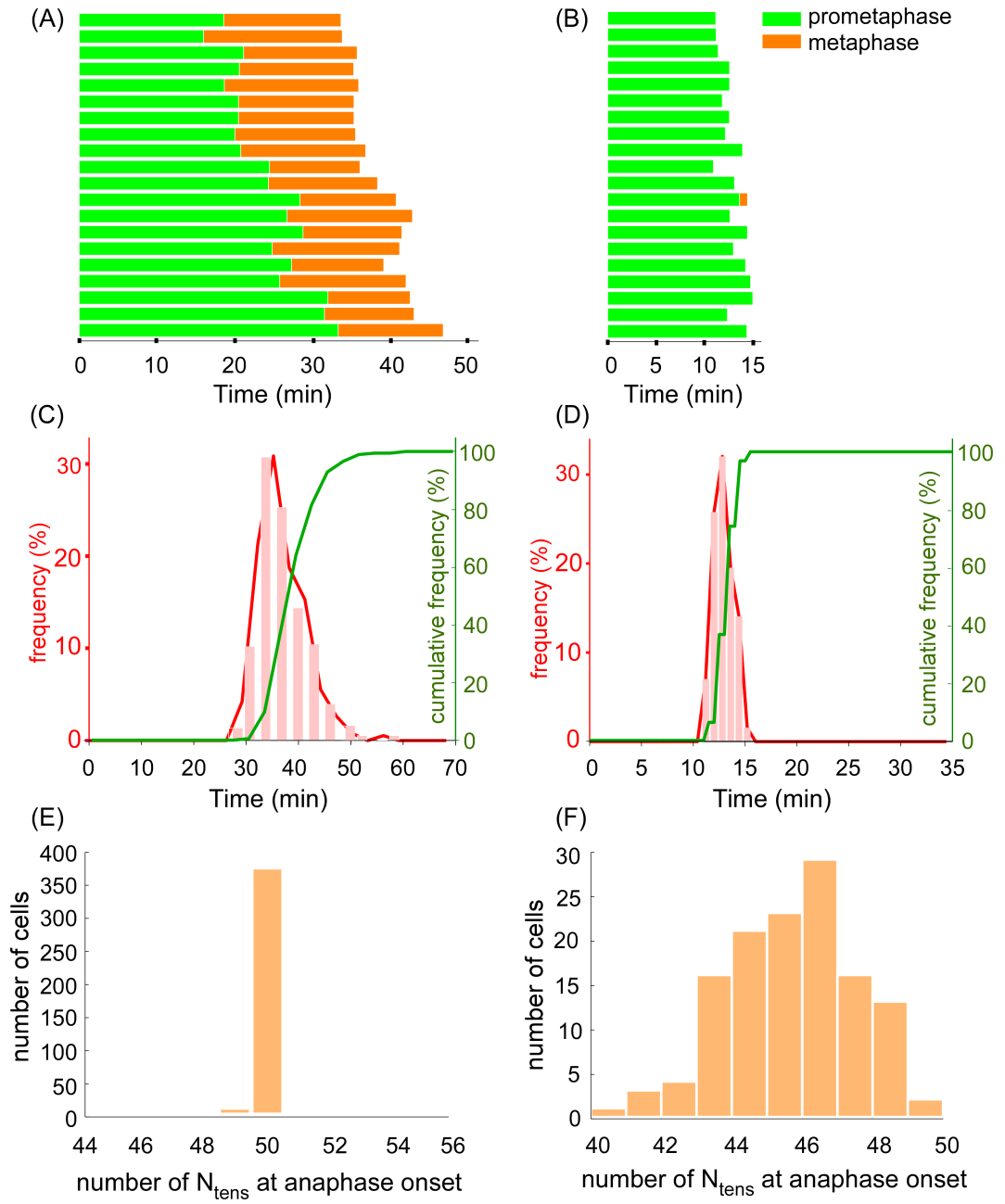

Figure 5.9: Stochastic simulations of the mitotic progression in HeLa cells. Following the experiments in Meraldi et al. (2004), 376 independent stochastic simulations were performed for control cells and 127 for Mad2-depletion cells. Simulation results were plotted in the same way as Figure 1 in Meraldi et al. (2004). 20 simulations of normal mitotic progressions selected at random for control cells (A) and Mad2 depleted cells (B). Timing from NEBD to anaphase onset in a population of control cells (C) and Mad2-depletion cells (D). The histogram distribution (red) and cumulative frequency (green) of the durations from NEBD to anaphase onset were plotted. The cumulative function of anaphase onset at each time point is shown on the green y-axis. Number of bioriented sister-chromatids at anaphase onset for the control (E) and Mad2-depletion cells (F) plotted as histograms. The parameters which differ from Table 5.1 are: kint = 1, kant = 0.2, kan = kin = 20, cohesin = 300, cohesin threshold = 30, N_T = 50, Mad2AT = 1200, Mad2T = 1200 for Mad2 RNAi condition.

5.9E), Mad2-depletion cells initiate anaphase with lagging chromosomes, and the number of bioriented chromosomes at anaphase onset is much smaller than the total number of chromosomes in a cell (Fig. 5.9F).

5.5 Summary

In this chapter the stochastic model has been developed to study how stochastic processes can influence the metaphase-to-anaphase transition in vertebrate cells. Microtubules searching and capturing chromosomes during prometaphase is likely to be a major source of noise. The varied durations of prometaphase and metaphase which are controlled by the spindle assembly checkpoint have been examined under a wide range of perturbations.

Despite its simplicity, the stochastic model demonstrates a striking ability in reproducing a group of important and classic experimental observations. The model not only captures the stochastic dynamics of the chromosome congression, but also gives a convincing interpretation of the sensitivity and robustness of the anaphase switch. The role of noise in the anaphase switch has been explored at both the single-cell and cell-population level. For the spindle assembly checkpoint, the noise generated from the chemical interactions seems to only perturb the transit timing of the mitotic events, but not their ultimate outcomes. More specifically, under normal conditions, the onset of anaphase in each individual cell will always take place once the prerequisite is satisfied, although the waiting time may be heterogeneous across the population. Such robustness is a desired feature for all the cell-cycle checkpoints to maintain accurate cell proliferation (Tighe et al., 2001; Musacchio and Salmon, 2007).

Cells are sensitive to the number of tensionless chromosomes, revealing a strong timing correlation between prometaphase and the time interval from NEBD to anaphase onset (Fig. 5.3). This work reinforces the experimental findings that the inherently diverse timing of anaphase onset relative to NEBD arises primarily in early mitosis, i.e. prometaphase, as shown in Figure 5.5 (Rieder et al., 1994; Meraldi et al., 2004). Furthermore, the stochastic model has also been applied to analyze new datasets not used in model construction, and it performs well. Not only did the model confirm the idea that the total amount of checkpoint protein Mad2 should be in excess compared to the APC activator,

Cdc20, but it also gives a novel interpretation to the timing regulation mechanism of the spindle assembly checkpoint. The stochastic model supplements the deterministic approach and offers a direct solution to mimic the cell-to-cell heterogeneity in population behaviour in response to perturbations (e.g. Mad2 knockdown).

Several kinetic models of the spindle assembly checkpoint have been published, each focusing on different aspects of the system (Doncic et al., 2006; Sear and Howard, 2006; Okabe and Sasai, 2007; Ibrahim et al., 2007, 2008; Mistry et al., 2008; Doncic et al., 2009; Simonetta et al., 2009). A deterministic spindle assembly checkpoint model was built by Ibrahim et al. (2008) based on the template model (Antoni et al., 2005) with realistic kinetic constants from the experiments. However, the kinetochore-microtubule attachment process is represented as a binary parameter rather than a proper dynamical variable. The same paper also describes a stochastic version using stochastic differential equations focused on the segregation surveillance process. The similar conclusion is drawn from their simulation that the noise seems not disturb the spindle assembly checkpoint function within a wide range of physiological parameter values (Ibrahim et al., 2007).

Chapter 6

Modelling Mitotic Exit in Budding Yeast

The mitotic state (M phase) in eukaryotes is brought about by activation of Cdk1/CycB in conjunction with other mitotic kinases (e.g. members of the Polo and Aurora families). Vice versa, mitotic exit is characterized by downregulation of Cdk1/CycB activity in response to cyclin B proteolysis (Sullivan and Morgan, 2007; Rieder, 2010). The transition of mitotic exit in normal cells should always be an irreversible process to guarantee the unidirectional progression of the cell cycle, i.e. cells should never revert back into M phase once exit.

Based on the physiological properties of mitotic cell divisions, Novák and Tyson have proposed that the irreversible mitotic exit is a bistable switch created by systems-level feedback underlying the Cdk-control network (Novák et al., 2007). Very recently, this theoretical scenario has been supported experimentally in budding yeast by López-Avilés et al. (2009). Although the deterministic model included in that paper sheds light on the importance of feedback loops and gives a qualitative explanation of the experimental data at the population level, the cell-to-cell heterogeneity concurrently found in the experiment was not taken into account in the model (López-Avilés et al., 2009). In contrast to the population-averaged behavior, cells showed varied responses in the same experimental setup that could not be explained or reproduced by the deterministic model. In this chapter, the original deterministic model is modified and converted into a stochastic model. Stochastic simulations are conducted and compared with the experimental results

in order to investigate noise effects and to study the variability of mitotic exit.

6.1 López-Avilés's Original Model

Our starting point is the original deterministic model developed in the paper of López-Avilés et al (2009). The López-Avilés's model was constructed containing 9 ODEs to complement the experimental work and examine how the systems-level feedback work together to proceed the unidirectional mitotic exit in the budding yeast cell cycle.

Figure 6.1 shows the interaction network in the yeast strain used to experimentally analyze the irreversibility of mitotic exit. In wild type cells, Cdk1/Clb2 phosphorylates and activates its own transcription factor Mcm1 (short form for Fkh2:Ndd1:Mcm1 complex). Unphosphorylated Cdh1 in complex with APC ($\mathrm{APC}^{\mathrm{Cdh1}}$) promotes Clb2 degradation, while Cdk1/Clb2 inhibits $\mathrm{APC}^{\mathrm{Cdh1}}$ activity by phosphorylation, creating a double negative feedback loop. Degradation of Clb5, an S-phase cyclin, is regulated in the same way as the degradation of Clb2 in the model. Sic1, a cyclin dependent kinase inhibitor, stoichiometrically binds to Cdk1/Clb2 and Cdk1/Clb5 to form the inactive complexes Trim2 and Trim5, respectively. Sic1 can also be phosphorylated by Cdk1/Clb2 or Cdk1/Clb5, which triggers its proteolysis. Swi5, a transcription factor of Sic1, is not able to enter the cell nucleus once it is phosphorylated by Cdk1/Clb2 (Moll et al., 1991). Thus Cdk1/Clb2 inhibits the synthesis and promotes the degradation of Sic1. Phosphorylation of Swi5 is reversed by the phosphatase Cdc14.

It is worth noting that the Cdh1 overexpressed in the experimental setup has eleven Cdk phosphorylation sites mutated (called Cdh1m11 in the model). The protein is constitutively active and can activate APC irrespective of Cdk1/Clb2 activity (Zachariae et al., 1998; Jaspersen et al., 1999; Visintin et al., 1998; López-Avilés et al., 2009). Without the inhibitory effect from Cdk1/Clb2, the constitutively active Cdh1m11 acts like an "exit protein" rather than a feedback component (Section 1.3.1). In the experiment, cells were arrested in M phase by Cdc20 depletion and the budding yeast strain carried a temperature sensitive APC mutation, which allowed the termination of $\mathrm{APC}^{\mathrm{Cdh1m11}}$-

dependent cyclin degradation by shifting to the restrictive temperature (López-Avilés et al., 2009). In the absence of $\mathrm{APC}^{\mathrm{Cdc20}}$, mitotic exit of budding yeast cells can be artificially induced by induction of $\mathrm{APC}^{\mathrm{Cdh1m11}}$.

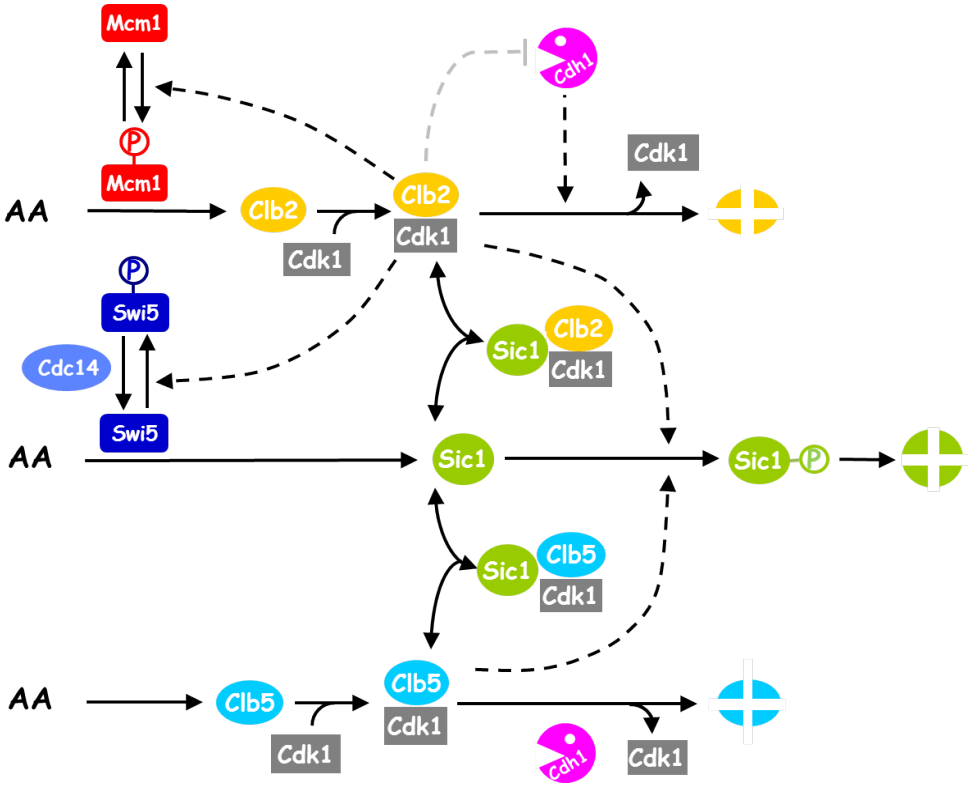

Figure 6.1: The molecular network controlling mitotic exit in budding yeast. Mcm1 and Swi5 are the transcription factors of Clb2 and Sic1, respectively. Cdh1m11, a constitutively active variant of Cdh1 can activate APC irrespective of Cdk activity. APC is not explicitly presented in the model, and instead its activity is incorporated into constitutively active Cdh1m11 under inducible control. Clb2 and Clb5 represent their respective complexes with the Cdk1 subunit that is neglected from the equations (Eqs. 6.1-6.15) of the model because they are not rate limiting. The gray dashed line represents the inhibitory effect of Cdk1/Clb2 on Cdh1. In the experiments, this regulation does not occur, because of the overexpression of Cdh1m11. For simplicity reasons, the endogenous Cdh1 is not included in the model. The figure is adapted from Supplementary Figure 6 in López-Avilés et al. (2009).

All numerical simulations of López-Avilés's model start from a stable steady state representing metaphase arrested cells (high Cdk1/Clb2 activity, low Sic1 and inactive Swi5). The initial level of Clb2 is twice that of Clb5, the estimation based on their abundance in asynchronous cultures, and their pattern of accumulation (Schwob and Nasmyth, 1993; Spellman et al., 1998). In the experiment, there was little release of Cdc14 from its inhibition in the nucleolus as separase could not be activated when $\mathrm{APC}^{\mathrm{Cdc20}}$ activity was blocked (Sullivan and Uhlmann, 2003). Therefore, a constant low Cdc14 activity is as-

sumed, representing the free form of the phosphatase which is not bound to its inhibitor Net1/Cfi1 (Visintin et al., 1999). The detailed explanations of the original model and the simulation results can be found in the paper and its supplementary information (López-Avilés et al., 2009).

6.2 A Modified Deterministic Model based on the Law of Mass Action

The López-Avilés's model cannot be directly used for the stochastic simulation since it includes non-elementary reactions, and hence reformulating the reactions using mass action kinetics is required (Salwinski and Eisenberg, 2004).

The interconversion of the phosphorylated and unphosphorylated forms of Swi5 was modelled using Goldbeter-Koshland kinetics in the original model (for details, see the Supplementary Information in López-Avilés et al., 2009). It has been shown that the Goldbeter-Koshland equation can be replaced by a multi-phosphorylation mechanism without losing the non-linearity of the system (Kapuy et al., 2009a). Accordingly, Swi5 is described using a distributive, ordered multi-phosphorylation mechanism (Fig. 6.2). Three serine residues of Swi5 regulated by Cdk1/Clb2 phosphorylation are identified as essential for its intracellular localization (Moll et al., 1991). Therefore three phosphorylation sites of Swi5 are considered in the modified model. Swi5, Swi5p and Swi5pp are regarded as the fully active forms, meaning that they are equally efficient in activating the transcription of Sic1. The total activity of Swi5 is the sum of all three active forms (Fig. 6.2).

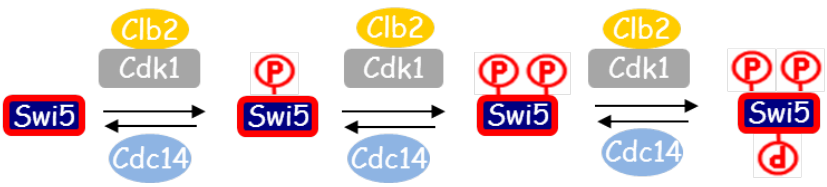

Figure 6.2: Distributive, ordered multi-phosphorylation of Swi5. Swi5 has three phosphorylation sites that can be phosphorylated and dephosphorylated by the kinase Cdk1/Clb2 and the phosphatase Cdc14 respectively.

In addition to the modification of Swi5, for simplification purposes, endogenous Cdh1 is neglected in the model because it does not play an important role under the experimental conditions. The modified model (Eq. 6.1 - Eq. 6.15) only contains the law of mass action and it serves as an intermediate model that can be readily converted into the stochastic model later.

$$\frac{d\,[\text{Clb2T}]}{dt} = ksclb2' + ksclb2 \cdot [\text{Mcm1p}] - (kdclb2' + kdclb2 \cdot [\text{Cdh1m11}]) \cdot [\text{Clb2T}] \tag{6.1}$$

$$\frac{d\,[\text{Clb5T}]}{dt} = ksclb5 - (kdclb5' + kdclb5 \cdot [\text{Cdh1m11}]) \cdot [\text{Clb5T}] \tag{6.2}$$

$$\frac{d\,[\text{Mcm1p}]}{dt} = (kamcm1' + kamcm1 \cdot [\text{Clb2}]) \cdot ([\text{Mcm1T}] - [\text{Mcm1p}]) - kimcm1 \cdot [\text{Mcm1p}] \tag{6.3}$$

$$\frac{d\,[\text{Cdh1m11}]}{dt} = kscdh1 - kdcdh1 \cdot [\text{Cdh1m11}] \tag{6.4}$$

$$\begin{aligned}\frac{d\,[\text{Trim2}]}{dt} &= kas2 \cdot [\text{Clb2}] \cdot [\text{Sic1}] - kds2 \cdot [\text{Trim2}] - (kdclb2' + kdclb2 \cdot [\text{Cdh1m11}]) \cdot [\text{Trim2}] \\ &\quad - (kdsic1' + kdsic1'' \cdot [\text{Clb5}] + kdsic1 \cdot [\text{Clb2}]) \cdot [\text{Trim2}]\end{aligned} \tag{6.5}$$

$$\begin{aligned}\frac{d\,[\text{Trim5}]}{dt} &= kas5 \cdot [\text{Clb5}] \cdot [\text{Sic1}] - kds5 \cdot [\text{Trim5}] - (kdclb5' + kdclb5 \cdot [\text{Cdh1m11}]) \cdot [\text{Trim5}] \\ &\quad - (kdsic1' + kdsic1'' \cdot [\text{Clb5}] + kdsic1 \cdot [\text{Clb2}]) \cdot [\text{Trim5}]\end{aligned} \tag{6.6}$$

$$\frac{d\,[\text{Sic1T}]}{dt} = kssic1' + kssic1 \cdot [\text{Swi5ac}] - (kdsic1' + kdsic1'' \cdot [\text{Clb5}] + kdsic1 \cdot [\text{Clb2}]) \cdot [\text{Sic1T}] \tag{6.7}$$

$$\begin{aligned}\frac{d\,[\text{Swi5pp}]}{dt} &= (kaswi5 + kaswi5' \cdot [\text{Cdc14}]) \cdot [\text{Swi5ppp}] + (kiswi5 + kiswi5' \cdot [\text{Clb2}]) \cdot [\text{Swi5p}] \\ &\quad - (kiswi5 + kiswi5' \cdot [\text{Clb2}]) \cdot [\text{Swi5pp}] - (kaswi5 + kaswi5' \cdot [\text{Cdc14}]) \cdot [\text{Swi5pp}]\end{aligned} \tag{6.8}$$

$$\begin{aligned}\frac{d\,[\text{Swi5p}]}{dt} &= (kaswi5 + kaswi5' \cdot [\text{Cdc14}]) \cdot [\text{Swi5pp}] - (kiswi5 + kiswi5' \cdot [\text{Clb2}] \cdot [\text{Swi5p}] \\ &\quad - (kaswi5 + kaswi5' \cdot [\text{Cdc14} \cdot [\text{Swi5p}] + (kiswi5 + kiswi5' \cdot [\text{Clb2}]) \cdot [\text{Swi5}]\end{aligned} \tag{6.9}$$

$$\frac{d\,[\text{Swi5}]}{dt} = (kaswi5 + kaswi5' \cdot [\text{Cdc14}]) \cdot [\text{Swi5p}] - (kiswi5 + kiswi5' \cdot [\text{Clb2}]) \cdot [\text{Swi5}] \tag{6.10}$$

$$[\text{Clb2}] = [\text{Clb2T}] - [\text{Trim2}] \tag{6.11}$$

$$[\text{Clb5}] = [\text{Clb5T}] - [\text{Trim5}] \tag{6.12}$$

$$[\text{Sic1}] = [\text{Sic1T}] - [\text{Trim2}] - [\text{Trim5}] \tag{6.13}$$

$$[\text{Swi5ac}] = [\text{Swi5}] + [\text{Swi5p}] + [\text{Swi5pp}] \tag{6.14}$$

$$[\text{Swi5T}] = [\text{Swi5}] + [\text{Swi5p}] + [\text{Swi5pp}] + [\text{Swi5ppp}] \tag{6.15}$$

6.2.1 Essential feedback loops engaged in the process of mitotic exit

The bistability of the mitotic exit relies on the essential feedback loops regulating the activity of Cdk1/Clb2 (Fig. 6.3). Sic1 binds to and inhibits Cdk1/Clb2; and moreover Cdk1/Clb2 promotes Sic1 degradation through phosphorylation creating a double negative feedback loop. The mutual inhibition between Cdk1/Clb2 and Sic1 is strengthened by Cdk1/Clb2 inhibition of Swi5. Cdk1/Clb2 also positively regulates its own synthesis via its kinase activity, establishing an additional positive feedback loop (Fig. 6.3).

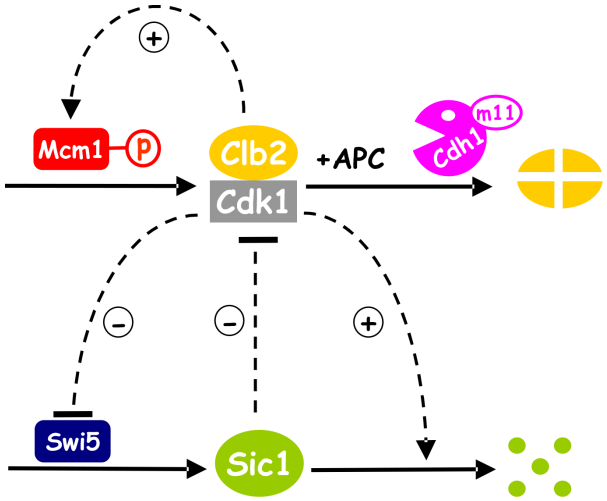

Figure 6.3: The underlying key feedback loops drive the mitotic exit progression in budding yeast. Positive feedback loops: Cdk1/Clb2 activates its own synthesis by phosphorylation of its own transcription factor Mcm1. Double negative feedback loop: Sic1 binds to Cdk1/Clb2 and forms the inactive complex; Cdk1/Clb2 not only promotes Sic1 degradation but also inhibits Swi5, a transcription factor of Sic1.

As introduced in Chapter 3, phase plane analysis allows us to assess the bistability of a system and provides an intuitive understanding of the mitotic exit process. By taking Cdh1m11 as a parameter and by assuming that other species in the model (e.g. Clb5T, Mcm1p, Swi5, Trim2, Trim5 etc.) are in pseudo-steady state, the control system can be simplified into two dimensions with Clb2T and Sic1T as dynamical variables. Clb2T represents the total level of Cdk1/Clb2 complexes, including inactive complexes bound to Sic1 (Eq. 6.11). Sic1T represents the total level of Sic1, including the free form of Sic1, and the complexes Trim2 and Trim5 (Eq. 6.13). The WinPP file used to plot the nullclines for Clb2T and Sic1T in Figure 6.4 can be found in Appendix C.2.

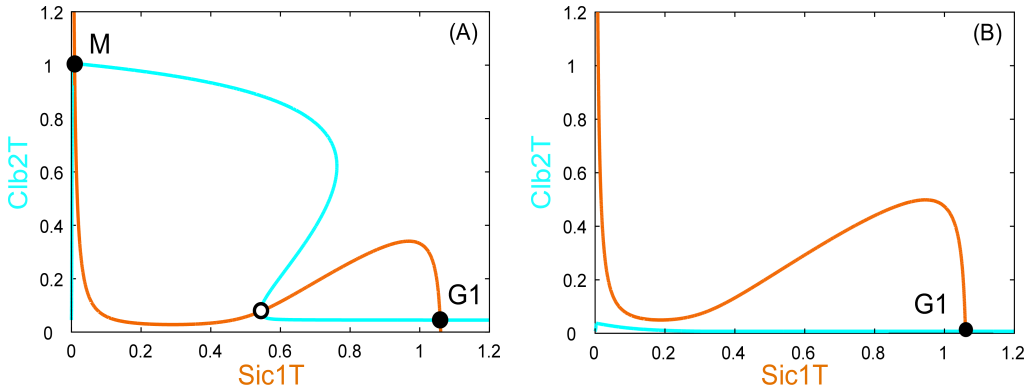

Figure 6.4: Alternative steady states of Clb2T and Sic1T on the phase plane of mitotic exit in budding yeast cells. (A) Three steady states are shown on the phase plane for the mitotic exit cell without Cdh1m11 induction (Cdh1m11 = 0). The two stable steady states correspond to M phase and G1 phase. When cells are blocked in metaphase by Cdc20 deprivation, the system settles in the M stable steady state. (B) Cdh1m11 induction demolishes M stable steady state and pushes the system to the G1 stable steady state (Cdh1m11 = 0.3). If Clb2 degradation is terminated before the system reaches G1, the system can recreate bistability. Cell can either go to M phase or G1 phase depending on the current regulatory protein levels. The WinPP file used to generate the figure can be found in Appendix C.2.

Normal cells have two stable steady states: M phase and G1 phase represented by the black dots at the intersections of the two nullclines (Fig. 6.4A). Cells that are blocked in M phase by Cdc20 deprivation reside in the M stable steady state. Induction of Cdh1m11 pushes the Clb2T balance curve down and the M stable steady state disappears (Fig. 6.4B). The system is moving toward the G1 stable steady state, first by a drop in Clb2T level, then followed by Sic1T accumulation at low Cdk1 / Clb2 activity levels (Fig. 6.4B). If $\mathrm{APC}^{\mathrm{Cdh1m11}}$ is inactivated during this process, the nullclines are restored as in Figure 6.4A. The subsequent evolution of the control system depends on how much Sic1T has accumulated in the meantime. If the level of Sic1T is already sufficient to keep Clb2T inactive when Clb2 degradation has ceased, the cell can successfully exit from mitosis and enter the G1 phase (i.e. 'irreversible mitotic exit'). Otherwise, the cell has to go back to M phase (i.e. 'reversible mitotic exit').

6.2.2 Deterministic simulation of mitotic exit

This phase plane analysis gives us a preliminary idea about how the system behaves in different experimental conditions; however time series simulations are essential for further insight and understanding.

Deterministic time course simulations of the reversible and irreversible mitotic exit are shown in Figure 6.5. The time profiles of Clb2 and other regulated proteins are consistent with López-Avilés's model and agree with experimental observations from the western blot (López-Avilés et al., 2009). Within 60 minutes induction of Cdh1m11, Clb2 is degraded to undetectable levels and the system completes the process of mitotic exit (Fig 6.5A). However, Figure 6.5B shows that if the length of $\mathrm{APC}^{\mathrm{Cdh1m11}}$ treatment is 10 minutes shorter (i.e. 50 minutes), the exit becomes reversible because Clb2 is able to re-accumulate and pushes Sic1 back to its low mitotic level through the positive and double-negative feedback loops. There is a critical threshold of Sic1 level required to maintain the low Cdk1/Clb2 activity and to keep the system in the G1 state. The system will always return back to its mitotic state in the Sic1 depletion condition (Fig. 6.5C). To the contrary, Sic1 overexpression is able to secure the irreversibility of mitotic exit of the system (Fig. 6.5D).

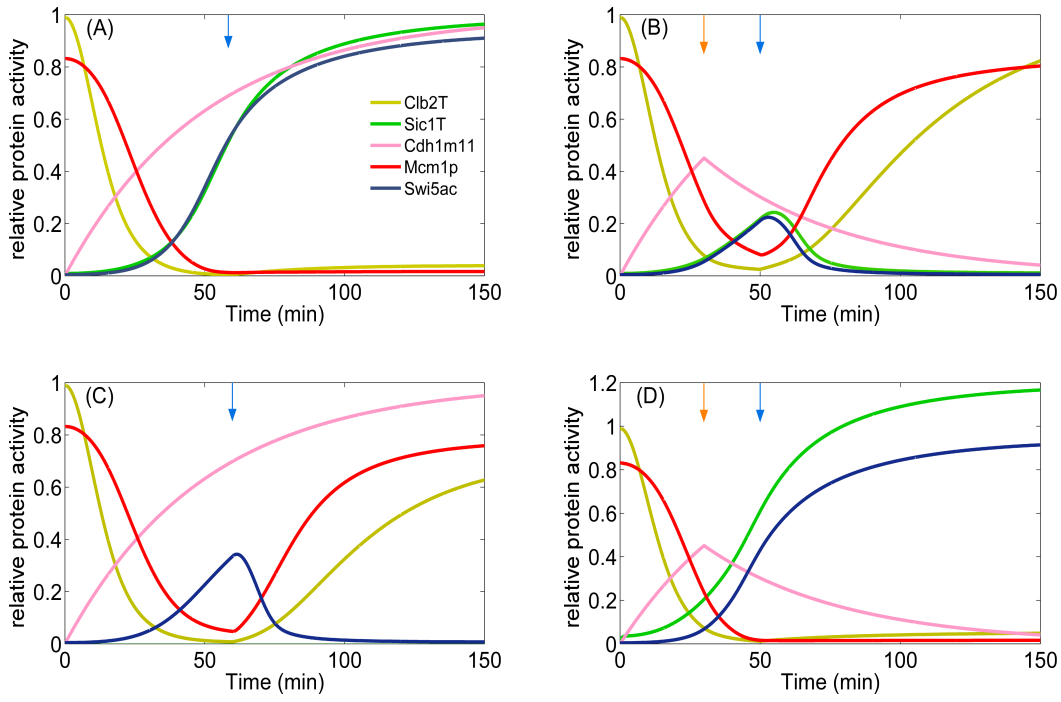

Figure 6.5: Deterministic simulations of Cdh1m11 induced mitotic exit using the modified model. Swi5ac is the active form of the Sic1 transcription factors which includes Swi5, Swi5p and Swi5pp. In the irreversible exit (A) and the Sic1Δ conditions (C), $\mathrm{APC}^{\mathrm{Cdh1m11}}$ activity lasts for 60 mins. In the reversible exit (B) and the Sic1 overexpression conditions (D), Cdh1m11 and APC activities are inactivated at 30 mins and 50 mins respectively. The time points to terminate Cdh1m11 and APC are presented with orange and blue arrows in the figure. Table 6.2 lists the initial conditions and the parameter values of the deterministic model. The parameters that need to be changed in the simulation of the different experimental conditions can be found in Table 8.1 in Appendix C.

6.3 Stochastic Model of Mitotic Exit

All the reactions presented in the above modified model used only mass action kinetics. Therefore, it is straightforward to reformulate the deterministic model and simulate it using the Gillespie algorithm. In addition to the change in the kinetic mechanism of Swi5 phosphorylation and dephosphorylation, several supplementary conversions have been made so that the model can be readily adapted to the stochastic simulation: (i) the original rate constants are scaled into the propensity functions; (ii) the concentration of each component is converted into number of molecules by introducing the cell volume V; (iii) realistic numbers of molecular abundance for Mcm1 and Swi5 in the model were taken from the literature (Ghaemmaghami et al., 2003). The reformulated stochastic model includes 13 chemical species, 45 elementary reactions and 27 parameters (see the computer code in Appendix C.4.2). Model components, their initial values and corresponding annotations are shown in Table 6.1. The reactions, kinetic parameters and biological explanations are listed in Table 6.2.

Name	***Description***	***SGD ID***	***Initial Value***†
Sic1	*inhibitor of Cdk1/Clb kinase complexes*	*S000004069*	*0*
Clb2	*M-cyclin*	*S000006323*	*2000*
Clb5	*S-cyclin*	*S000006324*	*1000*
Trim2	*trimeric complex of Cdk1/Clb2 and Sic1*		*0*
Trim5	*trimeric complex of Cdk1/Clb5 and Sic1*		*0*
Mcm1	*transcription factor of Clb2*	*S000004646*	*3400*
Mcm1p	*phosphorylated form of Mcm1*	*S000004646*	*16600*
Swi5	*transcription factor of Sic1*	*S000002553*	*0*
Swi5p	*single phosphorylated form of Swi5*	*S000002553*	*0*
Swi5pp	*double phosphorylated form of Swi5*	*S000002553*	*0*
Swi5ppp	*triple phosphorylated form of Swi5*	*S000002553*	*1400*
Cdh1m11	*a variant of Cdh1 in which 11 Cdk phosphorylation sites have been mutated and cannot be phosphorylated by the Cdk1/Clb complex*	*S000002971*	*0*
Cdc14	*protein phosphatase*	*S000001924*	*40*

Table 6.1: Molecular components in the stochastic model of mitotic exit in budding yeast. The biological definition, annotations and initial values of each component in the stochastic model are described in the table. SGD^{TM} (`http://www.yeastgenome.org/`) is a scientific database of the molecular biology and genetics of the yeast *Saccharomyces cerevisiae* (Cherry et al., 1997). † The unit of the initial condition for each species is number of molecules.

No.	*Par*	*Value*	*Reactions*	*Description*
1	*kamcm1'*	*0.01*	$Mcm1 \rightarrow Mcm1p$	*Mcm1 phosphorylation*
2	*kamcm1*	*0.0025*	$Mcm1 \xrightarrow{Clb2} Mcm1p$	*Clb2-dependent phosphorylation of Mcm1*
3	*kimcm1*	*1*	$Mcm1p \rightarrow Mcm1$	*Mcm1p dephosphorylation*
4	*kscdh1*	*40*	$\emptyset \rightarrow Cdh1m11$	*Cdh1m11 background synthesis*
5	*kdcdh1*	*0.02*	$Cdh1m11 \rightarrow \emptyset$	*Cdh1m11 background degradation*
6	*kiswi5'*	*0.007*	$Swi5 \xrightarrow{Clb2} Swi5p$	*Clb2-dependent Swi5 phosphorylation*
7			$Swi5p \xrightarrow{Clb2} Swi5pp$	*Clb2-dependent Swi5p phosphorylation*
8			$Swi5pp \xrightarrow{Clb2} Swi5ppp$	*Clb2-dependent Swi5pp phosphorylation*
9	*kiswi5*	*0.01*	$Swi5 \rightarrow Swi5p$	*Swi5 phosphorylation*
10			$Swi5p \rightarrow Swi5pp$	*Swi5p phosphorylation*
11			$Swi5pp \rightarrow Swi5ppp$	*Swi5pp phosphorylation*
12	*kaswi5'*	*0.001*	$Swi5p \xrightarrow{Cdc14} Swi5$	*Cdc14-dependent Swi5p dephosphorylation*
13			$Swi5pp \xrightarrow{Cdc14} Swi5p$	*Cdc14-dependent Swi5pp dephosphorylation*
14			$Swi5ppp \xrightarrow{Cdc14} Swi5pp$	*Cdc14-dependent Swi5ppp dephosphorylation*
15	*kaswi5*	*0.01*	$Swi5p \rightarrow Swi5$	*Swi5p dephosphorylation*
16			$Swi5pp \rightarrow Swi5p$	*Swi5pp dephosphorylation*
17			$Swi5ppp \rightarrow Swi5pp$	*Swi5ppp dephosphorylation*
18	*kas5*	*0.01*	$Sic1 + Clb5 \rightarrow Trim5$	*Sic1 binding to Clb5*
19	*kds5*	*0.01*	$Trim5 \rightarrow Sic1 + Clb5$	*Trim5 dissociation*
20	*kdclb5*	2.5×10^{-5}	$Trim5 \xrightarrow{Cdh1m11} Sic1$	$APC^{Cdh1m11}$*-dependent degradation of Clb5 from Trim5*
21	*kdsic1'*	*0.3*	$Trim5 \rightarrow Clb5$	*Sic1 degradation from Trim5*
22	*kdclb5'*	*0.02*	$Trim5 \rightarrow Sic1$	*Clb5 degradation from Trim5*
23	*kdsic1"*	2.5×10^{-5}	$Trim5 \xrightarrow{Clb5} Clb5$	*Clb5-dependent degradation of Sic1 from Trim5*

Continued on next page

No.	*Par*	*Value*	*Reactions*	*Description*
24	*kdsic1*	*0.001*	*Trim5* $\xrightarrow{Clb2}$ *Clb5*	*Clb2-dependent degradation of Sic1 from Trim5*
25	*ksclb2'*	*2*	$\emptyset \rightarrow$ *Clb2*	*Clb2 background synthesis*
26	*ksclb2*	*0.0035*	$\emptyset \xrightarrow{Mcm1p}$ *Clb2*	*Mcm1p-dependent Clb2 synthesis*
27	*kdclb2'*	*0.03*	*Clb2* $\rightarrow \emptyset$	*Clb2 background degradation*
28	*kdclb2*	*0.00025*	*Clb2* $\xrightarrow{Cdh1m11} \emptyset$	$APC^{Cdh1m11}$*-dependent Clb2 degradation*
29	*ksclb5*	*20*	$\emptyset \rightarrow$ *Clb5*	*Clb5 background synthesis*
30	*kdclb5'*	*0.02*	*Clb5* $\rightarrow \emptyset$	*Clb5 background degradation*
31	*kdclb5*	2.5×10^{-5}	*Clb5* $\xrightarrow{Cdh1m11} \emptyset$	$APC^{Cdh1m11}$*-dependent Clb5 degradation*
32	*kssic1'*	*40*	$\emptyset \rightarrow$ *Sic1*	*Sic1 background synthesis*
33	*kdsic1'*	*0.3*	*Sic1* $\rightarrow \emptyset$	*Sic1 background degradation*
34	*kssic1*	*0.429*	$\emptyset \xrightarrow{Swi5}$ *Sic1*	*Swi5-dependent Sic1 synthesis*
35			$\emptyset \xrightarrow{Swi5p}$ *Sic1*	*Swi5p-dependent Sic1 synthesis*
36			$\emptyset \xrightarrow{Swi5pp}$ *Sic1*	*Swi5pp-dependent Sic1 synthesis*
37	*kdsic1"*	2.5×10^{-5}	*Sic1* $\xrightarrow{Clb5} \emptyset$	*Clb5-dependent Sic1 degradation*
38	*kdsic1*	*0.001*	*Sic1* $\xrightarrow{Clb2} \emptyset$	*Clb2-dependent Sic1 degradation*
39	*kas2*	*0.01*	*Sic1 + Clb2* $\rightarrow$ *Trim2*	*Sic1 binding to Clb2*
40	*kds2*	*0.01*	*Trim2* $\rightarrow$ *Sic1 + Clb2*	*Trim2 dissociation*
41	*kdclb2'*	*0.03*	*Trim2* $\rightarrow$ *Sic1*	*Clb2 degradation from Trim2*
42	*kdsic1'*	*0.3*	*Trim2* $\rightarrow$ *Clb2*	*Sic1 degradation from Trim2*
43	*kdclb2*	*0.00025*	*Trim2* $\xrightarrow{Cdh1m11}$ *Sic1*	$APC^{Cdh1m11}$*-dependent degradation of Clb2 from Trim2*
44	*kdsic1"*	2.5×10^{-5}	*Trim2* $\xrightarrow{Clb5}$ *Clb2*	*Clb5-dependent degradation of Sic1 from Trim2*
45	*kdsic1*	*0.001*	*Trim2* $\xrightarrow{Clb2}$ *Clb2*	*Clb2-dependent degradation of Sic1 from Trim2*

Table 6.2: Elementary reactions in the stochastic model of mitotic exit in budding yeast. For enzymatic reactions, the enzymes are written above the arrow. The parameter values used in the stochastic model are scaled from the deterministic model. The units of the parameter depend on the reaction order: $molecule \cdot min^{-1}$ for zero order, min^{-1} for first order and $molecule^{-1} \cdot min^{-1}$ for second order reactions.

6.3.1 Stochastic simulation of mitotic exit in a single cell

The stochastic simulations are started from M phase with high level of Cdk1/Clb2, active Mcm1, low Sic1 level and inactive Swi5. $\mathrm{APC^{Cdh1m11}}$ is introduced at time 0 and

removed at different time according to the experimental protocols (see Section 6.2.2). The stochastic realization for each experimental condition is selected and presented in Figure 6.6. Although the time course plots show fluctuations for individual protein levels in these examples, the reversible and irreversible behaviors are still preserved due to the fundamentally robust characteristics of the cell cycle (Fig. 6.5).

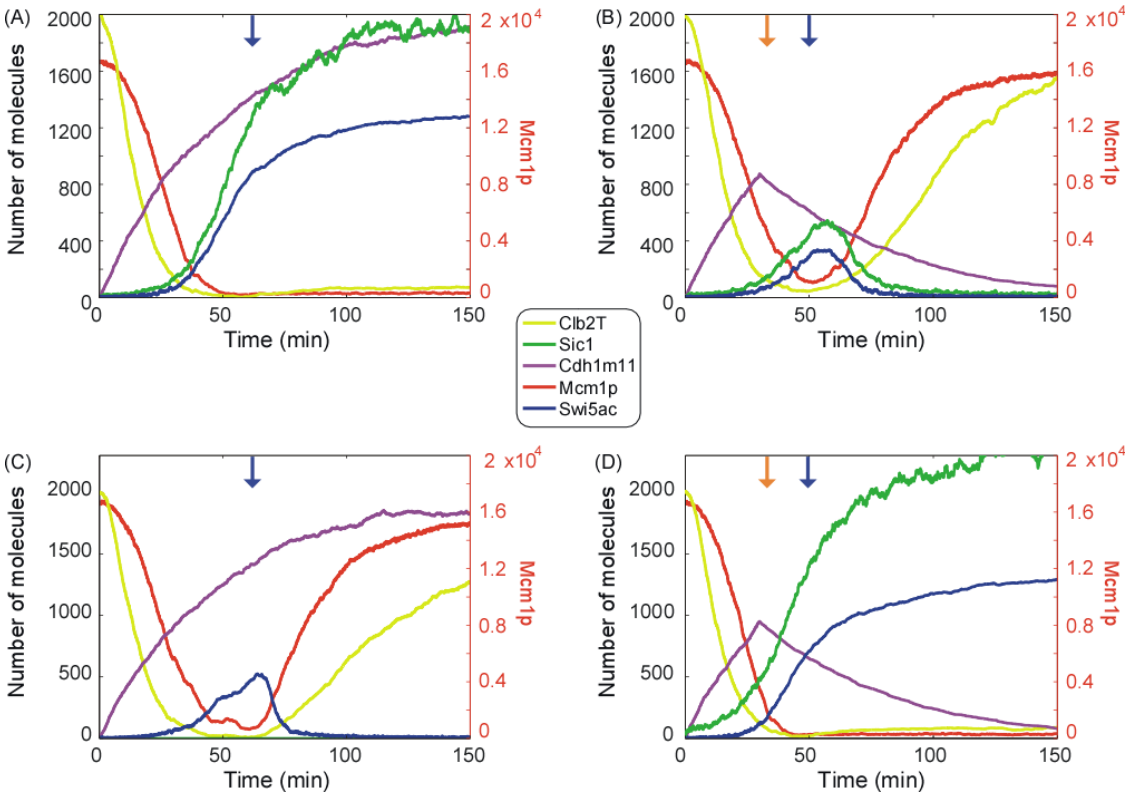

Figure 6.6: Stochastic simulations of reversible and irreversible mitotic exit in single budding yeast cells. The simulation conditions are the same as in Figure 6.5. An example is given for each situation: (A) The irreversible mitotic exit, (B) the reversible mitotic exit, (C) Sic1 deletion and (D) Sic1 overexpression. The time points to turn off Cdh1m11 and APC are indicated with orange and blue arrows. The curves of the Mcm1p are scaled according to the right y-axis. Numerical simulations and data analysis were conducted in MATLAB 7.6 and the SimBiology 3.0 toolbox using Gillespie's algorithm (Appendix C.4.2).

However this does not always hold true for every single stochastic simulation. Irreversible mitotic exit requires Sic1 level to rise above a critical threshold to prevent Clb2 re-accumulation. If the time point of termination for the Clb2 degradation is close to the time that Sic1 crosses its threshold, the noise will drive the system into one of the two possible outcomes. Because Sic1 levels vary for each stochastic simulation, in some cases it might be able to jump above the critical threshold. Consequently, the cells will exit from M phase even in the reversible protocol under this circumstances (Fig. 6.7).

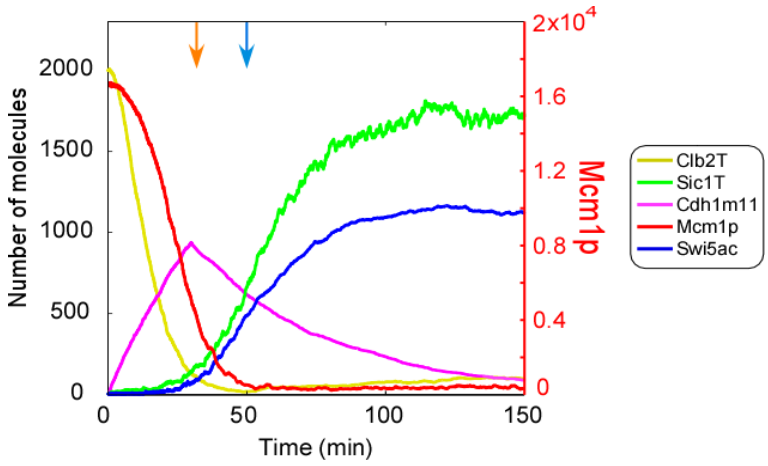

Figure 6.7: Irreversible mitotic exit in the reversible protocol. An example of irreversible mitotic exit under the reversible experimental conditions due to the molecular fluctuation in the stochastic simulation. The curves of the Mcm1p are scaled according to the right y-axis. The time points to terminate Cdh1m11 and APC are presented with orange and blue arrows in the figure.

6.3.2 Stochastic simulation of a population of cells

By carrying out the above procedure one possible realization of the mitotic exit is obtained from Figure 6.7; but the outcome is only predictable for a perfectly deterministic system. In living cells with molecular noise arising from small numbers of molecules, the outcome is less predictable. To illustrate this point, one-hundred independent stochastic simulations were carried out under conditions which led to a reversible mitotic exit in the deterministic system. The average behaviour of the batch simulations was calculated. In contrast to the single simulation results under the reversible conditions (Figs. 6.5B, 6.6B), the average pattern changes from the data were very interesting. After turning off $\mathrm{APC}^{\mathrm{Cdh1m11}}$-dependent Clb2 degradation, Sic1T and Swi5ac activities decrease and stay at a certain level instead of returning to zero (Fig. 6.9). This phenomenon is experimentally observed when the measurements are taken for a population of cells rather than individual cells (see Fig. 2c in López-Avilés et al., 2009). In order to get a more complete picture of the temporal evolution of the system, more simulations were performed and different outcomes were recorded. After running 1350 stochastic simulations of the reversible condition, 91.93% cases were reversible and 8.07% cases were irreversible. The reversibility of mitotic exit was monitored through the level of Sic1T at the end of the simulation (t = 150 min). This result is also in accord with the experimental data given in Figure 6.9, in which around 80% of the cells returned to M phase and 20% exited (see

Supplementary Fig. 3a in López-Avilés et al., 2009).

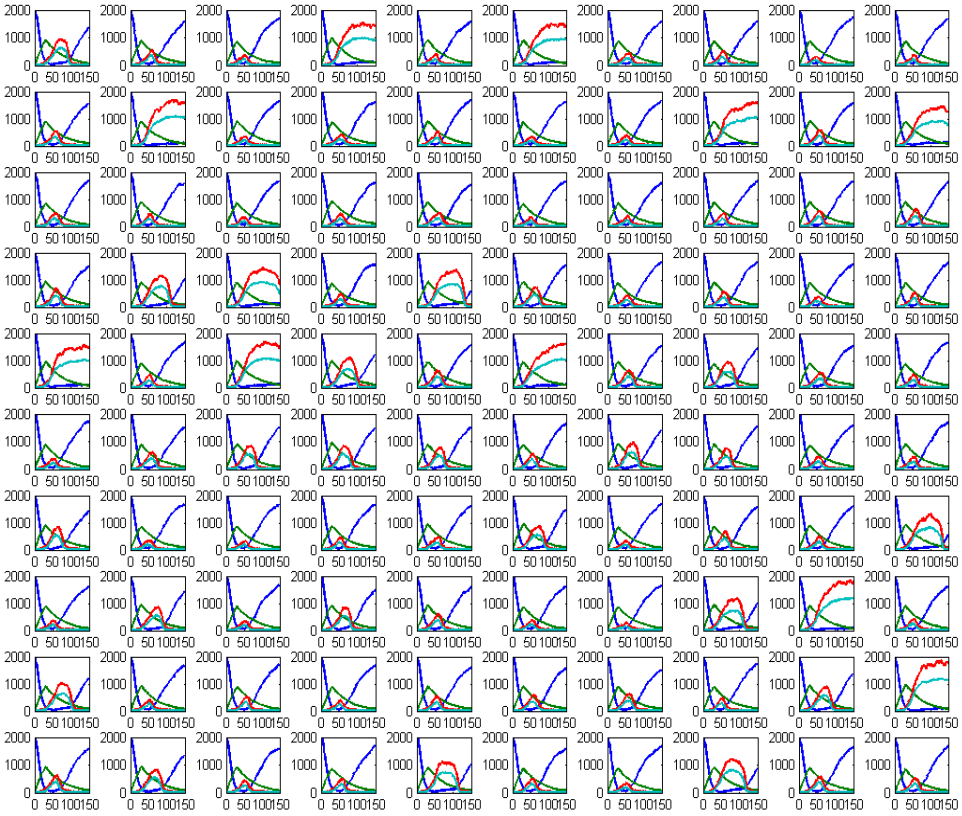

Figure 6.8: A sample plot of 100 stochastic simulations under the reversible experimental conditions. Clb2T, Cdh1m11, Sic1T and Swi5ac are plotted in blue, green, red and light blue separately. Mcm1p is not shown in the figure. Because of the molecular fluctuation, cells are not necessarily following the same reversible behaviours as in the deterministic model. Among these 100 independent simulations, 11 cases are irreversible and 89 cases are reversible. The x-axis is the time and y-axis is number of molecules.

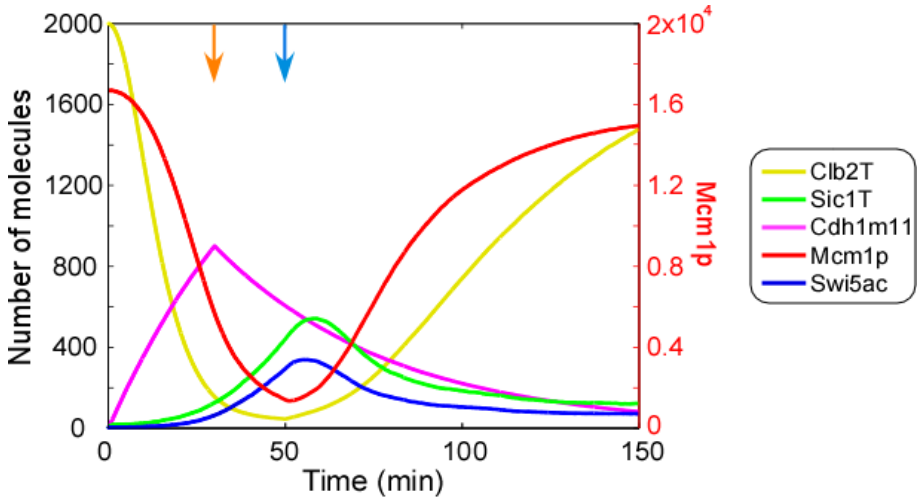

Figure 6.9: The averaged behaviour of a population of yeast cells under the reversible mitotic exit condition. In contrast to the individual single cell level (see Fig. 6.6B), the activity of Sic1T in the population-averaged measurements is consistent with the experimental data in the western blot analysis.

To further investigate the distinct outcomes, molecular distributions were calculated at each time point for one hundred simulations under the condition of the reversible mitotic exit protocol. This is presented as a 3D plot in Figure 6.10. A majority of cells resynthesize Clb2 and downregulate Sic1 level after inactivation of APC at 50 minutes, whereas others escape to the G1 state. The splitting behavior in the population of cells is because of the timing of APC inactivation is close to the time when Sic1 reaches its threshold. The 3D histograms of Clb2T, Mcm1p, Sic1T and Swi5 that are projected to 2D histograms also exhibit similar trends (Fig. 6.11). As a consequence of 'dividing of the ways' behavior the distribution of these regulatory components are bimodal at the end of the experiments. This demonstrates that the inclusion of stochasticity is in good agreement with recent mitotic exit experimental findings in budding yeast (López-Avilés et al., 2009).

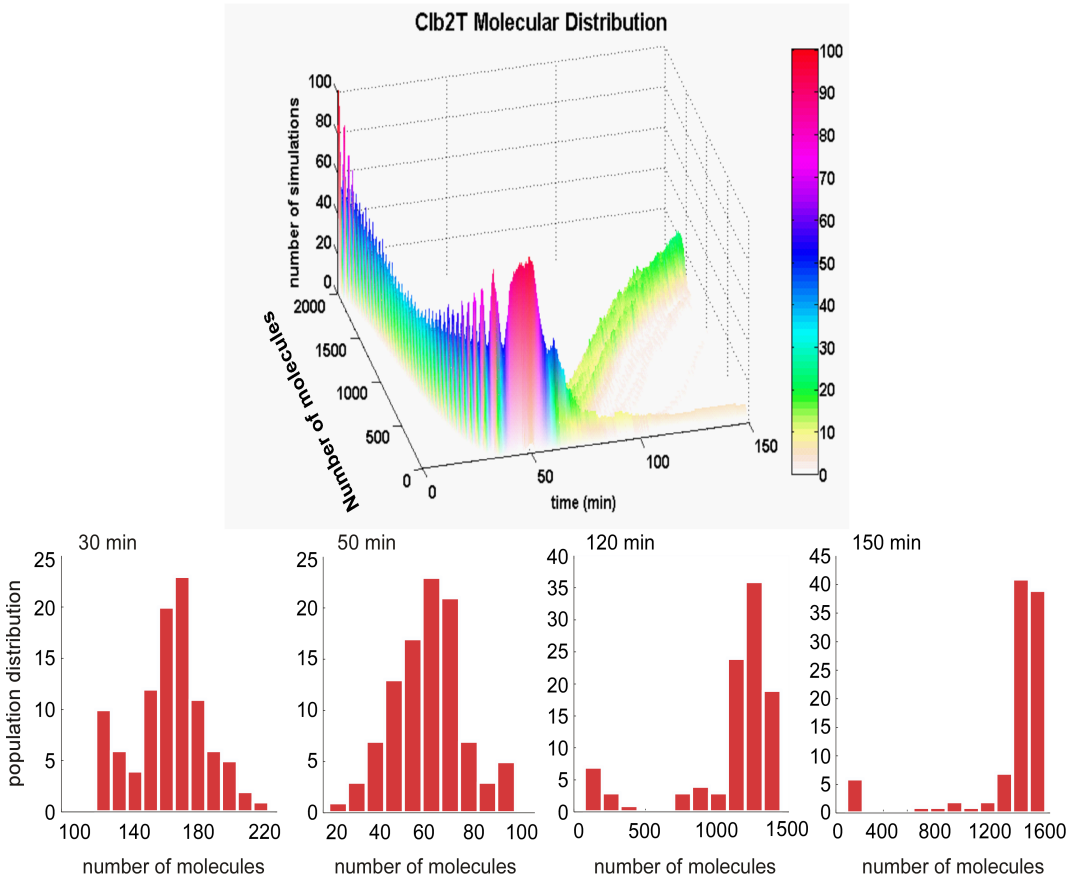

Figure 6.10: 3D presentation of Clb2T molecular distribution under the reversible mitotic exit conditions. Data was generated from 100 stochastic simulations as described in Figure 6.6B. The time series data was interpolated according to the same time vector. Histograms were calculated at each time point for the whole length of the simulation. Four histogram examples are given at 30 mins, 50 mins, 120 mins and 150 mins. From time 0 to 50 mins, Clb2T levels follow the normal distribution; after turning off the $APC^{Cdh1m11}$-dependent Clb2 degradation at 50 mins, two major distributions appear: reversible and irreversible. The z-axis of the plot represents the number of simulations fall that into different outcomes.

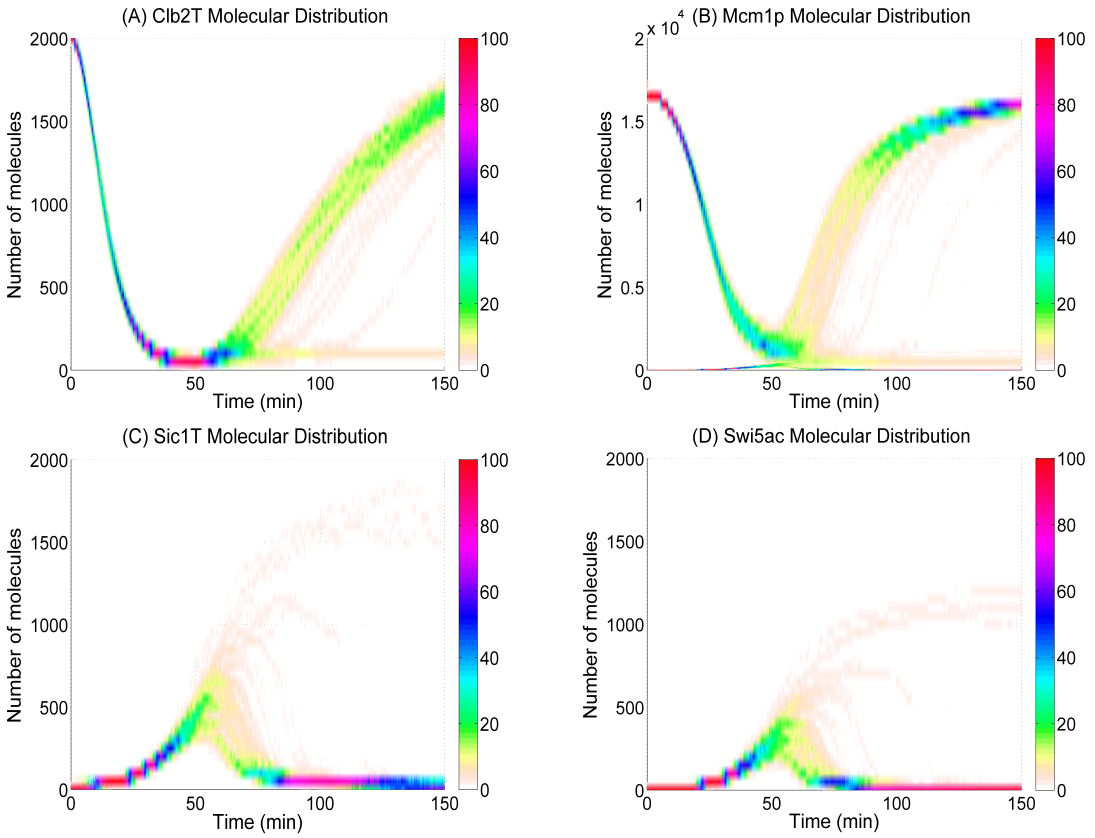

Figure 6.11: The molecular distribution as a 2D presentation under the reversible mitotic exit protocol. 3D molecular distributions of Clb2T (A), Mcm1p (B), Sic1T (C) and Swi5ac (D) were generated as in Figure 6.10, then projected onto the 2D plane. In the deterministic simulation, only one outcome can be produced, but in the stochastic simulation, different outcomes can happen.

6.4 Summary

With the highly regulated cell cycle control system, cells complete mitosis and proceed into G1 phase in a precise unidirectional manner. The data presented in López-Avilés et al. (2009) has suggested that the mitotic exit transition can be a reversible process in budding yeast under particular experimental conditions: Even if cells that have already exited from mitosis, that transition will become dynamically reversible once cyclin B degradation is terminated. We propose that mitotic exit will remain reversible until the essential feedback signals that create a bistable switch are sufficiently engaged.

In order to illustrate this argument, both deterministic and stochastic models are presented based on the key molecular feedback loops controlling the mitotic exit cell cycle transition in budding yeast. The time series simulations are able to reproduce the ex-

perimental observations and the steady state phase plane analysis has provided a better understanding of the essential feedback loops operation within the network. The mutual antagonism between Cdk1/Clb2 and Sic1 creates a bistable switch during the process of mitotic exit. Our simulations further confirm the notion that proteolysis of mitotic cyclins (e.g. Clb2) alone is neither sufficient nor necessary to ensure the irreversible mitotic exit transition (López-Avilés et al., 2009). Instead, all regulatory molecular components act with system-level feedback to generate and maintain the cell cycle unidirectionality.

In addition, a simple one-to-one conversion from the ODE model into the SSA model has been presented through the model definition process. We have demonstrated the straightforward workflow which generates an intermediate deterministic model that can be easily converted into a stochastic model, which ultimately facilitates the construction process. The validation of the model demonstrated a general agreement between the results of the deterministic and stochastic methods. However, the stochastic version provides a better picture of the population-averaged measurement and deeper insights into the heterogeneous response to a similar stimulus of a cell population. This is because it allows independent outcomes from different simulations. In some circumstances, for instance when the population of cells varies, the stochastic model can reproduce the experimental observation with greater accuracy. It is worth noting that some other important proteins and regulators (e.g. Cdc14, Net1, APC, Cdc20, Cdh1, Cdc5) are omitted from the model for simplification. Still, despite the real mitotic exit regulatory network is far more complicated, our models provide significant insights to illustrate the fundamental ideas.

Chapter 7

Modelling Mitotic Exit in Mammalian Cells

In Chapter 6 mathematical models have been developed to explain the irreversible mitotic exit in budding yeast. The models also capture yeast cells reversibly exiting from mitosis when the essential feedback loops were disrupted under a specific experimental condition (López-Avilés et al., 2009). However, the cell cycle control network in budding yeast is different from that of higher eukaryotes in several aspects (Herskowitz, 1988). Therefore, we must ask how relevant are our conclusions from budding yeast for higher eukaryotes? In particular, are irreversible transitions in the replication-division cycles of mammalian cells caused by protein degradation or by systems-level feedback loops (Kapuy et al., 2009b)? Recent experimental studies by Potapova et al. (2006, 2009) suggest that double-negative (or positive) feedback is required for accomplishment of irreversible mitotic exit not only in yeast but also in mammalian cells . Otherwise, mitotic exit in mammalian cells could be reversible if transiently inhibited Cdk1/CycB activity in the presence of proteasome inhibitors (Potapova et al., 2009).

We argue that the fundamental mechanism of irreversible mitotic exit in mammalian cells is very similar to that in budding yeast, which is due to system-level feedback (Kapuy et al., 2009c,b). However the underlying molecular network that creates such a bistable switch differs in these model organisms. In this chapter the specific regulatory network

of mitotic exit in mammalian cells will be studied at a detailed level and mathematical modelling approaches will be applied to illustrate our argument.

7.1 Experimental Evidence of Reversible Mitotic Exit

Experimental support for reversible mitotic exit in mammalian cells was recently provided by Potapova et al. (2006, 2009). Cells were blocked in metaphase by treatment with the microtubule-depolymerizing agent nocodazole. This agent disrupts the formation of the mitotic spindle and consequently activates the spindle assembly checkpoint. The active spindle assembly checkpoint blocks the degradation of securin and cyclin B, but the destruction of cyclin A takes place normally (Fry and Yamano, 2006; van Leuken et al., 2008; van Zon and Wolthuis, 2010). In the nocodazole arrested cells, mitotic exit could be induced by chemical inhibition of Cdk1/CycB with flavopiridol and simultaneous inhibition of proteasome activity with MG132 – similar to what is observed after cyclin degradation in normal mitotic exit. Inhibition of Cdk1/CycB activity, as assayed by phosphorylation of nucleolin, induced mitotic exit as indicated by chromosome decondensation, nuclear envelope reformation, early stages of cytokinesis and dephosphorylation of Cdk1/CycB substrates (Potapova et al., 2006). However, removal of Cdk1/CycB inhibition by washing out flavopiridol but keeping MG132 after 30 minutes permitted a recovery of Cdk1/CycB activity and rephosphorylation of the Cdk1/CycB substrates, resulting in a majority of cells returning to mitosis, i.e. mitotic exit was reversible. Re-entry into mitosis after flavopiridol wash out was judged by the following criteria in the experiment: chromosomes recondensed and realigned on the metaphase plate, midbody and cytokinetic furrow disappeared, the mitotic spindle reassembled, and the newly formed nuclear envelope dissolved (Potapova et al., 2006). By contrast, when cyclin proteolysis was allowed to proceed in a parallel experiment, the mitotic exit became irreversible (Potapova et al., 2006).

After a longer period of Cdk1/CycB inhibition (around 60 minutes), the mitotic state could not be reestablished even after flavopiridol was removed. This is because the re-

activation of Cdk1/CycB was fully blocked and cells have irreversibly exited from M phase and entered into G1 phase. The authors found that the block of Cdk1/CycB reactivation required the inhibitory phosphorylation of Cdk1/CycB by the kinases Wee1 and Myt1. Their experiments suggest that after a transient inhibition of Cdk1 activity, metaphase arrested mammalian cells could settle in either an M- or a G1-like state, indicating that the mammalian cell cycle control system has at least two alternative steady states (i.e. it is bistable). Moreover the results suggest that the bistable behaviour is caused by the mechanism of reversible Cdk1/CycB inhibitory phosphorylation. The finding is consistent with an earlier study that mitotic exit was compromised in cells expressing non-phosphorylatable, constitutively active Cdk1 (Pomerening, 2008).

7.2 Reconstructing the Molecular Network of Mammalian Mitotic Exit

The activation of Cdk1/CycB at mitotic entry is triggered by removing the inhibitory phosphate groups on Thr-14 and Tyr-15 residues from Cdk1 (Nurse, 1990; Dunphy, 1994) (see Chapter 1). The experiment of Potapova et al. (2009) indicates that Cdk1/CycB needs to be phosphorylated and inactivated for cells to exit from mitosis.

The major components of the mammalian molecular network that controls the activity of Cdk1/CycB through phosphorylation and dephosphorylation during mitotic exit are presented in Figure 7.1. The unphosphorylated, active kinase Wee1 (and also Myt1, not shown) inactivates Cdk1/CycB which can be reversed by the phosphorylated, active phosphatase Cdc25. The unphosphorylated active form of Cdk1/CycB controls its regulators through inactivation of Wee1 and activation of Cdc25. Phosphorylation-dependent inhibition of Wee1 by Cdk1/CycB itself creates a double negative feedback loop; while the activation of Cdc25 by Cdk1/CycB defines a positive feedback loop. The two network motifs act in synergy and both create bistability if their reaction kinetics have certain nonlinear features (Tyson et al., 2003; Ferrell, 2008). We also assume a Cdk counteracting phosphatase (PP) in the model to be inhibited by Cdk1/CycB, as shown in Figure

7.1. Although the identity of the phosphatase remains to be ascertained, experimental evidence is consistent with this requirement (Mochida and Hunt, 2007; Wu et al., 2009). An additional and reasonable assumption of PP is that the phosphatase autocatalytically activates itself (Wu et al., 2009). It is worth pointing out that the phosphatase regulation is not essential to create the alternative steady states of Cdk1/CycB phosphorylation but strengthens its bistability (Kapuy et al., 2009c).

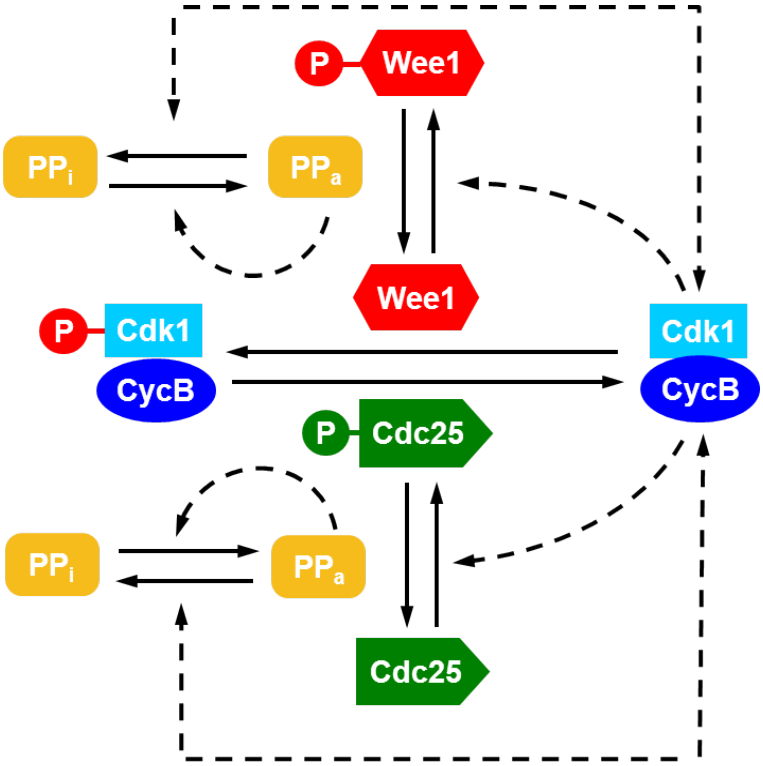

Figure 7.1: The molecular feedback loops of mitotic exit in mammalian cells. Cdk1/CycB (called Mpf in the model) is active in the dephosphorylated form and inactive in the phosphorylated form. The active form controls its regulators through inactivation of the kinase Wee1 and activation of the phosphatase Cdc25, creating a double negative feedback loop and a positive feedback loop. PP represents a phosphatase that activates Wee1 and inactivates Cdc25, thus inactivates Cdk1/CycB activity. PP is autocatalytic itself and inactivated by Cdk1/CycB-dependent phosphorylation. The figure is modified from Kapuy et al. (2009c).

The molecular components and the detailed elementary reactions that quantitatively represent the above mitotic exit regulatory network are listed in Table 7.1 and Table 7.2. A simple mathematical model that incorporates the reactions has subsequently been created for showing the bistable mitotic exit in the specific experimental conditions (Potapova et al., 2009). The basic structure of the presented model describing the switch of the Cdk1/CycB activity by phosphorylation is similar to the formerly published model

by Novák and Tyson (1993). While the previous model used Goldbeter-Koshland kinetics for Wee1 and Cdc25 regulation (Novák and Tyson, 1993), a Cdk regulated phosphatase PP counteracting Cdk1/CycB activity and mass action kinetics are used for all the interactions in the reconstructed model. Mpf and Mpfp denote the active and inactive forms of Cdk1/CycB respectively. Proteolysis is blocked using the proteasome inhibitor MG132 in the experiment (Potapova et al., 2009), therefore the synthesis and degradation of all the proteins in the model are ignored and the total amount of each species is assumed constant (Kapuy et al., 2009c).

Name	***Description***	***Initial Value***†
Mpfp	*inactive, phosphorylated Cdk1/CycB*	*108*
Mpf	*active, dephosphorylated Cdk1/CycB*	*892*
$\boldsymbol{PP_a}$	*unknown phosphatase counteracting Cdk1/CycB phosphorylation*	*0*
$\boldsymbol{PP_i}$	*inactive form of PP*	*1000*
Wee1	*protein kinase that inhibits Mpf by phosphorylating a tyrosine residue in the Cdk active site*	*0*
Wee1p	*inactive, phosphorylated form of Wee1*	*1000*
Cdc25p	*protein phosphatase that actives Mpf by removing phosphate from specific residues in the Cdk active site*	*1000*
Cdc25	*inactive, dephosphorylated Cdc25*	*0*
CycB	*sum of Mpf and Mpfp*	*1000*
I	*Cdk1 inhibitor*	*0*

Table 7.1: Molecular components in the stochastic model of mitotic exit in mammalian cells. † The unit of the initial condition for each species is number of molecules.

Since there are cell-to-cell variations in the reversible and irreversible exits from mitosis in response to the Cdk inhibition (Potapova et al., 2009), stochastic simulations are used to characterize the dynamics of the mitotic exit in the experiments. In the following sections the model will be simulated by both the CLE and SSA approaches. The noise influence on the choice of steady states by the bistable system will be tested using statistical analysis.

No.	*Par*	*Value*	*GO Term*	*Reactions*	*Description*
1	*kwee″*	*25*	*GO:0016310*	*Mpf* $\xrightarrow{Wee1}$ *Mpfp*	*Wee1-dependent Mpf phosphorylation*
2	*kwee′*	*0.5*	*GO:0016310*	*Mpf* $\xrightarrow{Wee1p}$ *Mpfp*	*Wee1p-dependent Mpf phosphorylation*
3	*k25′*	*0.03*	*GO:0016791*	*Mpfp* $\xrightarrow{Cdc25}$ *Mpf*	*Cdc25-dependent Mpfp dephosphorylation*
4	*k25″*	*0.03*	*GO:0016791*	*Mpfp* $\xrightarrow{Cdc25p}$ *Mpf*	*Cdc25p-dependent Mpfp dephosphorylation*
5	*kai*	*1000*	*GO:0004861*	*Mpf + I* $\rightarrow$ *IMpf*	*Inhibitor I binding to Mpf*
6	*kai*	*1000*	*GO:0004861*	*Mpfp + I* $\rightarrow$ *IMpfp*	*Inhibitor I binding to Mpfp*
7	*kdi*	*1000*	*GO:0043241*	*IMpf* $\rightarrow$ *Mpf + I*	*IMpf dissociation*
8	*kdi*	*1000*	*GO:0043241*	*IMpfp* $\rightarrow$ *Mpfp + I*	*IMpfp dissociation*
9	*kwee″*	*25*	*GO:0016301*	*IMpf* $\xrightarrow{Wee1}$ *IMpfp*	*Wee1-dependent IMpf phosphorylation*
10	*kwee′*	*0.5*	*GO:0016301*	*IMpf* $\xrightarrow{Wee1p}$ *IMpfp*	*Wee1p-dependent IMpf phosphorylation*
11	*k25″*	*5*	*GO:0016791*	*IMpfp* $\xrightarrow{Cdc25}$ *IMpf*	*Cdc25-dependent IMpfp dephosphorylation*
12	*k25′*	*0.03*	*GO:0016791*	*IMpfp* $\xrightarrow{Cdc25p}$ *IMpf*	*Cdc25p-dependent IMpfp dephosphorylation*
13	*Va25*	*0.01*	*GO:0016310*	*Cdc25* $\rightarrow$ *Cdc25p*	*background Cdc25 phosphorylation*
14	*Va25′*	*0.3*	*GO:0004693*	*Cdc25* $\xrightarrow{Mpf}$ *Cdc25p*	*Mpf-dependent Cdc25 phosphorylation*
15	*Vi25*	*1*	*GO:0016791*	*Cdc25p* $\xrightarrow{PP_a}$ *Cdc25*	PP_a*-dependent Cdc25p dephosphorylation*
16	*Viwee′*	*0.3*	*GO:0004693*	*Wee1* $\xrightarrow{Mpf}$ *Wee1p*	*Mpf-dependent Wee1 phosphorylation*
17	*Viwee*	*0.01*	*GO:0016310*	*Wee1* $\rightarrow$ *Wee1p*	*background Wee1 phosphorylation*
18	*Vawee*	*1*	*GO:0016791*	*Wee1p* $\xrightarrow{PP_a}$ *Wee1*	PP_a*-dependent Wee1p dephosphorylation*
19	*kapp*	*0.003*	*GO:0016311*	$PP_i \rightarrow PP_a$	PP_i *background activation*
20	*kapp′*	*0.05*	*GO:0016791*	$PP_i \xrightarrow{PP_a} PP_a$	*PP autocatalytic activation*
21	*kipp′*	*3*	*GO:0004693*	$PP_a \xrightarrow{Mpf} PP_i$	*Mpf-dependent* PP_a *inactivation*
22	*ktr*	*0.5*	*GO:0006412*	$I_0 \rightarrow I$	*Inhibitor synthesis*

Continued on the next page

No.	*Par*	*Value*	*GO Term*	*Reactions*	*Description*
23	*ktr*	*0.5*	*GO:0051603*	$I \rightarrow \emptyset$	*Inhibitor degradation*

Table 7.2: Elementary reactions with corresponding Gene Ontology annotations and parameter values in the mammalian mitotic exit model. For enzyme catalytic reactions, enzymes are written above the arrows. These reaction sets can be formulated and simulated using both the deterministic or the stochastic approaches. * The rate constant values (k) listed in the table need to be scaled for the CLE and the SSA models. The details can be found in Appendixes D.1, D.4.

7.3 The Chemical Langevin Equation Version

The Chemical Langevin Equation (CLE) version of the model is expressed in terms of five stochastic differential equations. Each equation is supplemented with a noise term which is proportional to the square root of the individual rate expressions (Table 7.3). The CLE model was implemented and numerically simulated using the computer program XPPAUT (see Appendix D.1).

Following the experimental protocol, numerical simulations are started from metaphase with high Mpf, active Cdc25, inactive Wee1 and inactive PP. The Cdk inhibitor flavopiridol is introduced at 10 fold of its IC_{50} at time zero and removed subsequently at different time points. The inhibitor binds reversibly to both Mpf and Mpfp, causing an abrupt drop in Mpf activity, which causes the activation of Wee1 and PP_{a} followed by the dephosphorylation of Cdc25p. If Cdk inhibition is terminated after 30 minutes, all these changes are reversible and the cell goes back to M phase as shown in Figure 7.2A. If flavopiridol is removed after 60 minutes, the inhibitory phosphorylation of Mpf remains inactive even in the absence of flavopiridol and the cell maintains the G1 stage (Fig. 7.2B). After 45 minutes Cdk1/CycB inhibition, both reversible and irreversible outcomes can be generated for mitotic exits. Two distinct representative simulations are plotted in Figures 7.2C,D. The molecular fluctuation during the transition process is a great contributor to bring about these two distinguished outcomes of the bistable system (Kapuy et al., 2009c).

Each stochastic simulation corresponds to the behavior of an individual cell, therefore two-hundred simulations were performed for each experimental condition (i.e. duration

Protein	**Activation flux** $f^+_{i(x)}$	**Inactivation flux** $f^-_{i(x)}$
MpfT	$k25' \cdot Cdc25p \cdot MpfpT + \sigma^+_{mpf(i)}$ $k25'' \cdot Cdc25 \cdot MpfpT + \sigma^+_{mpf(i)}$	$kwee' \cdot Wee1p \cdot MpfT + \sigma^-_{mpf(i)}$ $kwee'' \cdot Wee1 \cdot MpfT + \sigma^-_{mpf(i)}$
Cdc25p	$V_{a25} \cdot Cdc25 + \sigma^+_{cdc25(i)}$ $V'_{a25} \cdot Mpf \cdot Cdc25 + \sigma^+_{cdc25(i)}$	$V_{i25} \cdot PP_a \cdot Cdc25p + \sigma^-_{cdc25(i)}$
Wee1	$V_{awee} \cdot PP_a \cdot Wee1p + \sigma^+_{wee1(i)}$	$V_{iwee} \cdot Wee1 + \sigma^-_{wee1(i)}$ $V'_{iwee} \cdot Mpf \cdot Wee1 + \sigma^-_{wee1(i)}$
PP_a	$kapp' \cdot PP_a \cdot PP_i + \sigma^+_{pp(i)}$ $kapp \cdot PP_i + \sigma^+_{pp(i)}$	$kipp' \cdot Mpf \cdot PP_a + \sigma^-_{pp(i)}$
I	$ktr \cdot I_0$	$ktr \cdot I$

The conservation of mass equation	**Equilibrium assumption**
$\mathrm{Cdc25} = \mathrm{Cdc25_{tot}} - \mathrm{Cdc25p}$ $\mathrm{Wee1p} = \mathrm{Wee1_{tot}} - \mathrm{Wee1}$ $\mathrm{MpfpT} = \mathrm{CycB_{tot}} - \mathrm{MpfT}$ $\mathrm{PP_i} = \mathrm{PP_{tot}} - \mathrm{PP_a}$	$\mathrm{Mpf} = \mathrm{MpfT} \cdot \frac{\mathrm{K_d}}{\mathrm{K_d}+\mathrm{I}}$

Table 7.3: Mathematical representation of the reaction fluxes in the CLE model of mitotic exit in mammalian cells. They are derived from the reaction mechanism in the wiring diagram in Figure 7.1. The CLE of each species is formulated as activation flux minus inactivation flux ($\sum f^+_{i(x)} - \sum f^-_{i(x)}$) and the equations are supplemented with a noise term σ_i, which is proportional to the square root of individual rate expressions. For simplicity, the synthesis and degradation of all proteins are ignored and their total level is assumed constant. Mpf and Mpfp in the equations represent active and inactive Cdk1/CycB respectively. Mpf is calculated by an algebraic equation based on the assumption of fast and reversible binding of inhibitor (I). We assume that there is no stochasticity for the inhibitor flavopiridol treatment.

of the Cdk inhibition) and the ratio of reversible to irreversible mitotic exit events was recorded (Fig. 7.6B). The criterion of reversibility was the Mpf level at 60 minutes after removing flavopiridol as described in the experimental protocol (Potapova et al., 2009). The threshold is defined as 50% of the Mpf level at mitotic steady state, and if the value is larger than the threshold, mitotic exit is considered reversible. As shown in Figure 7.6B, if the inhibitor flavopiridol is washed out at any time earlier than 30 minutes, almost all the cells will homogeneously re-enter into M phase. The completely opposite behaviour, i.e. successful exit from M phase, is observed if the inhibitor flavopiridol is removed at any time after 70 minutes. Between 30 minutes and 70 minutes, there we find a transition window in which cells almost randomly choose between G1 and M phase. The two out-

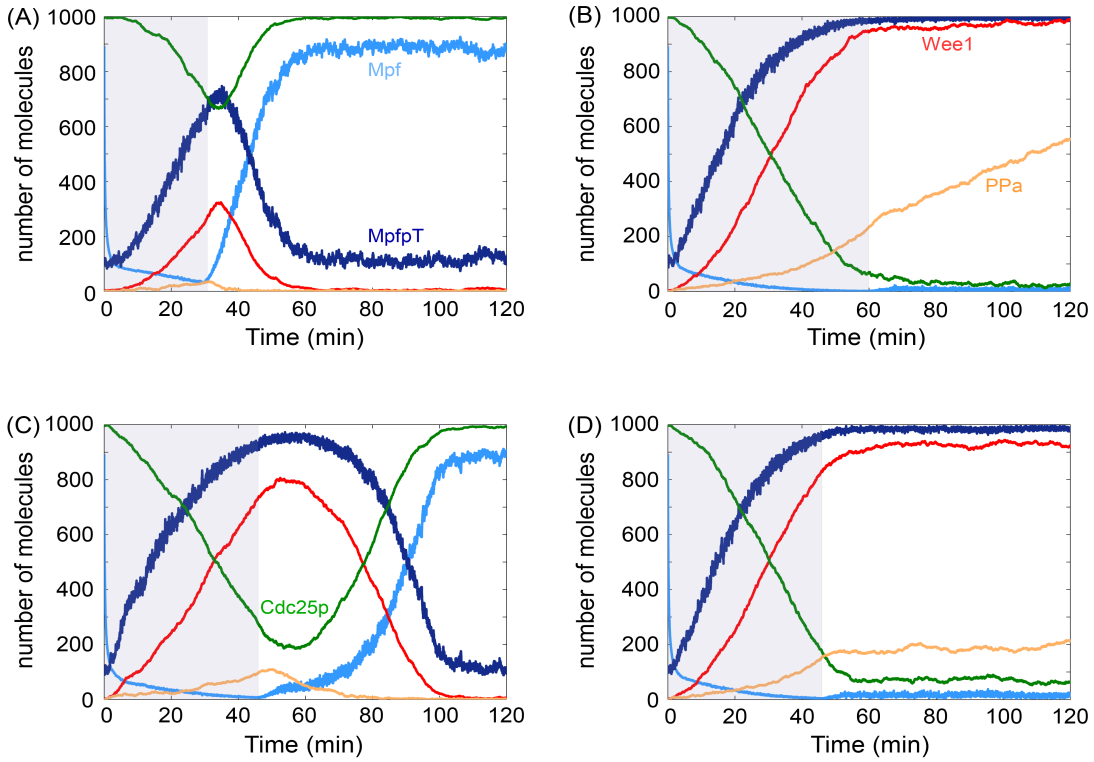

Figure 7.2: Stochastic simulations of the mitotic exit in single cells using the CLE model. The active forms of enzymes Wee1, Cdc25 and PP are plotted. (A) When flavopiridol is removed at 30 mins, the cell goes back to M phase because of the low level of Wee1. The active Mpf (light blue curve) is able to rephosphorylate Wee1 and Cdc25, thereby reactivating the inhibited forms of Mpfp (dark blue curve). (B) When the inhibitor flavopiridol is removed at 60 mins, the cell maintains the G1 state. This is because the inhibitory phosphorylation of Mpf is kept inactive. (C) and (D) In the middle of the transition period (45 mins), the cell switches almost randomly between G1 and M phases. The inhibitory treatment period is shaded in a gray color in each plot. The XPP file for the SSA simulation can be found in Appendix D.4.

comes of this transition period were captured well by the simulation: the model predicts that the probability for an irreversible mitotic exit gradually increases with time between 30 minutes and 70 minutes during flavopiridol treatment (Fig. 7.6B).

7.3.1 Stochastic effects on the bistable switch

The stochastic time series simulations successfully reproduce the experimental results and suggest that a metaphase arrested mammalian cell is indeed a bistable system with two alternative steady states (Novák et al., 2007; Kapuy et al., 2009b). Cells enter into mitosis when Cdk1 activity is high and only the mitotic stable steady state should exist. As a helper molecule for mitotic entry, cyclin A is degraded in early mitosis (Devault et al., 1992). Therefore, we propose that metaphase cells only become bistable compared to the prometaphase cells because of the degradation of cyclin A. In order to further reveal the

bistable features of such a process, a signal response curve (SRC) (see Chapter 3) is used to plot the steady state level of Mpf as a function of total cyclin B ($\mathrm{CycB_{tot}}$) in Figure 7.3. In the absence of inhibitory phosphorylation the SRC would be a straight line with a slope of one (not shown), because all the Cdk1/CycB dimers are active. These could also be the cases when Cdk1 is non-phosphorylatable or in the absence of Cdk1/CycB counteracting phosphatase. Once the feedback signals are present in the system, the response curve becomes 'S' shaped with overlapping low and high Cdk1 kinase activity states in the middle. The SRC defines two fundamental stable steady states: a low Cdk1/CycB activity state with active Wee1 and inactive Cdc25 (red branch); and a high Cdk1/CycB activity state with inactive Wee1 and active Cdc25 (green branch) (Fig. 7.3A).

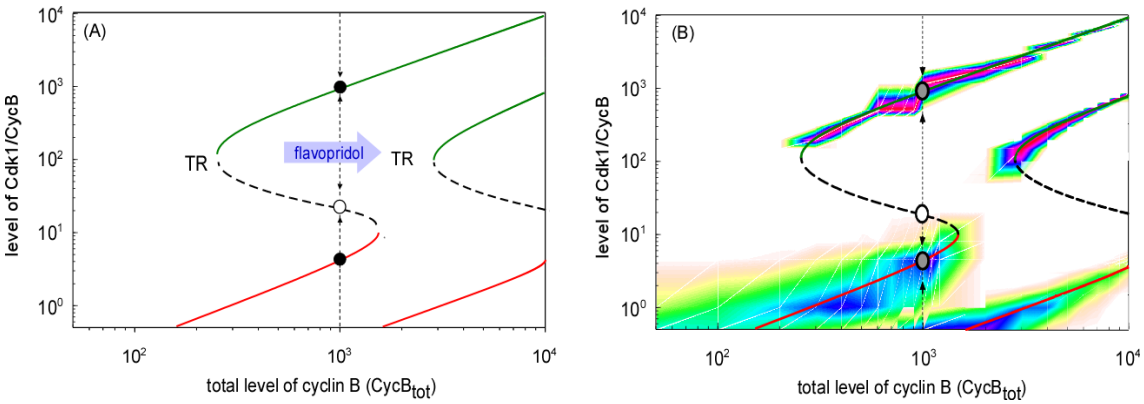

Figure 7.3: Bistability analysis of the mitotic exit in mammalian cells. (A) One parameter bifurcation diagram calculated from the deterministic ODE with (right curve) or without (left curve) inhibitor flavopiridol. The characteristic transition points (TRs) represent the mitotic exit transitions during the cell cycle. (B) Simulated steady states responding to different levels of $\mathrm{CycB_{tot}}$ using the CLE model. The distributions of Mpf abundance generated from 200 stochastic simulations were assembled and plotted as a function of $\mathrm{CycB_{tot}}$ on top of the SRCs from the deterministic model. The dependence of active Cdk1/CycB on $\mathrm{CycB_{tot}}$ levels follows an S-shaped curve characteristic for bistable systems. At intermediate $\mathrm{CycB_{tot}}$, there are two stable steady states (filled circles) along the high (green) and low (red) branches of the S-shaped curve, corresponding to the M and G1 states. The unstable steady state (open circle) along the middle branch (black dashed lines) of the curve divides the trajectories of chemical kinase inhibition at constant $\mathrm{CycB_{tot}}$ (dotted arrows). The unstable steady states in the bifurcation diagram cannot be observed in stochastic temporal simulation. When the system comes across the intermediates region, the stochasticity plays an important role in pushing the system to one of its alternative stable steady states. The XPP file for plotting the bifurcation diagram can be found in Appendix D.2.

The experimental observations from the paper can also be interpreted using an SRC plot. Metaphase arrested mammalian cells are on the SRC upper branch where Cdk1/CycB is fully active (Fig. 7.3). Using flavopiridol to chemically inhibit Cdk1/CycB activity has a dramatic effect on the SRC by extending the lower Cdk1/CycB activity stable steady

state towards a higher $\mathrm{CycB_{tot}}$ level and correspondingly both cyclin B switch thresholds are increased. Therefore cells treated with flavopiridol tend to lose their stable mitotic states and move vertically down in the direction of a lower stable steady state: a new G1 state (the right curve in Fig. 7.3A). If flavopiridol were not removed, cells would reach the low Cdk1/CycB activity state and would eventually stay in the G1 stable steady state. However, reaching the lower Cdk1/CycB activity stable steady state requires additional time, since the enzymes (e.g. PP, Wee1 and Cdc25) that regulate the inhibitory phosphorylation of Cdk1 need to be dephosphorylated first. If Cdk1 inhibition is terminated during the experiment, the SRC will attempt to revert back to its original position and the final outcome of such an experiment is determined by the state of the system at the time of flavopiridol removal. The unstable steady states are the boundaries of the two distinct modes of behaviours, while the position of the system is determined by the extent to which the enzymes (Wee1 and Cdc25) responsible for Cdk1 inhibitory phosphorylation have been dephosphorylated. If flavopiridol is removed shortly after its addition, the system remains in the mitotic attraction zone, because the inhibitory phosphorylation is not strong enough to keep Cdk1/CycB inactive. As opposed to the above situation, after a longer Cdk inhibition, the system is attracted by the low Cdk1/CycB activity steady state (G1 phase), where the inhibitory phosphorylation effect is already able to maintain Cdk1 inactivation even in the absence of flavopiridol. Although the unstable steady states cannot be normally observed, they play important parts in the experiments of Potapova et al. (2009) as shown by the distinct outcomes in the stochastic simulations in Figures 7.2C,D.

In order to resemble the Mpf response to the change of $\mathrm{CycB_{tot}}$ as shown from the SRCs in the deterministic simulations, batch stochastic simulations were performed using the CLE model with different levels of $\mathrm{CycB_{tot}}$: simulations were run until the levels of all the species stayed relatively stable. The molecular distribution of Mpf at the end of each simulation was calculated and plotted as a function of $\mathrm{CycB_{tot}}$ in Figure 7.3B. The assembled histograms from the stochastic simulations are consistent with the SRC from the ODE model (where the noise term is set to zero). However, the unstable branch of

the SRC in the deterministic model could not be captured by time series simulation in the stochastic model, because the system cannot settle down in the intermediate steady state in the bistable regime.

7.3.2 Mean first passage time of the mitotic exit

In the last section, the bistability of mitotic exit has been shown in the presented model in both a deterministic and stochastic context (Fig. 7.3). In order to further quantitatively analyze the stochastic effect during the transition from M to G1, the mean first passage time (MFPT) of mitotic exit is calculated from the stochastic simulations using the CLE model. In this specific context, MFPT refers to the average time that a cell spends in the M state until it jumps to the G1 state for the first time. MFPT can be directly monitored and measured from the numerical simulation and strongly depends on Cdk1/CycB activity. Each stochastic simulation starts with a different level of $\mathrm{CycB_{tot}}$, with or without the Cdk inhibitor flavopiridol, and it continues until Cdk1/CycB reaches its lower steady state for the first time. The waiting time for this event to take place is recorded as MFPT.

A series of independent stochastic simulations were conducted, from which the mean and the standard deviation of MFPT are plotted in Figure 7.4. As can be seen from the figure, the larger $\mathrm{CycB_{tot}}$, the larger MFPT, meaning that cells spend more time in M phase if $\mathrm{CycB_{tot}}$ is high. In the presence of flavopiridol, it takes less time for cells to exit from M to G1 at the identical level of $\mathrm{CycB_{tot}}$. If $\mathrm{CycB_{tot}}$ level exceeds a certain threshold (thres), MFPT become infinite, i.e. the cells remain in M phase indefinitely and do not exit. For the flavopiridol treatment condition, the $\mathrm{CycB_{tot}}$ threshold ($\mathrm{thres_{in}}$) is around 280 molecules and for the condition without flavopiridol, the threshold ($\mathrm{thres_{noi}}$) is around 3000 molecules.

The MFPT also reflects the pattern of the signal response curve (Fig. 7.3). The $\mathrm{CycB_{tot}}$ threshold level corresponds to the upper saddle node of the M-phase steady states in the bifurcation plot (Fig. 7.3A). For $\mathrm{CycB_{tot}} < \mathrm{thres}$, the $\mathrm{CycB_{tot}}$ level is not high enough to keep the system in the mitotic steady state and it almost immediately jumps to the

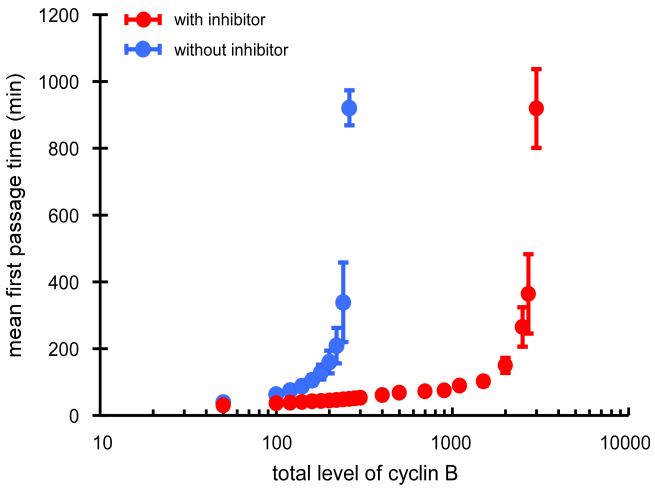

Figure 7.4: The mean and the standard deviation of MFPT simulated from the CLE model. MFPT is recorded from 200 simulations each at different $\mathrm{CycB_{tot}}$ levels with (red dots) or without (blue dots) the Cdk1 inhibitor flavopiridol. The error bars indicate the standard deviations. Note the logarithmic scale of the x-axis.

G1 steady state. With increasing $\mathrm{CycB_{tot}}$ levels, it takes longer for the system to jump down. There is a small range of thres where the system may or may not jump within the limited simulation length due to stochasticity. For $\mathrm{CycB_{tot}} > \mathrm{Thres}$, the $\mathrm{CycB_{tot}}$ level is sufficient to maintain the mitotic stage and the MFPT curve gradually turns into a vertical line. In the presence of flavopiridol, the MFPT line shifts to a larger $\mathrm{CycB_{tot}}$ value similar to the pattern change of the SRC.

7.4 The SSA Version of the Model

Since all the reactions presented in this regulatory network are using mass-action kinetics (Table 7.2), the model can also be readily simulated by the SSA algorithm (Chapter 3). The first attempt to directly implement the SSA suffers from computational inefficiency because the model spends inordinate amounts of time on the association and dissociation reactions between the inhibitor flavopiridol (called "I" in the model) and Mpf. This effect can be observed more clearly in Figure 8.1 in Appendix D.3. In order to improve the efficiency of the SSA simulation, a quasi-equilibrium assumption is used to express the analytical solution of Mpf and this solution is the same as the equilibrium approximation that is given in Table 7.3. After integration of the quasi-equilibrium assumption the computational ability of the SSA model is much improved. Single simulation results appear

similar to the ones generated by the CLE approach (Fig. 7.5).

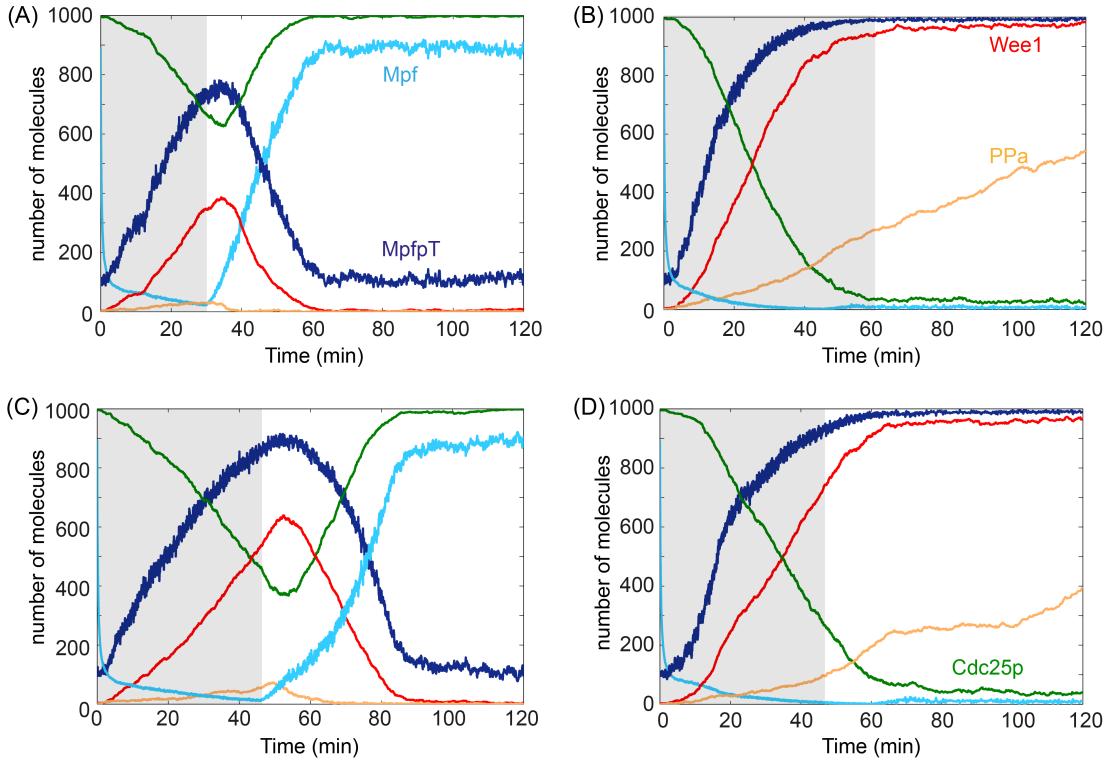

Figure 7.5: Stochastic simulations of mitotic exit in single cells using the SSA model. The same simulations as described in Figure 7.2 but generated from the SSA model. The active forms of the enzymes Wee1, Cdc25 and PP are plotted. The Cdk1 inhibitor flavopiridol is added at time zero with a level 10-fold higher than its IC_{50} value and is thought to bind reversibly to both phosphorylated and unphosphorylated Mpf. (A) Flavopiridol is removed at 30 mins and the cell reverts back to the mitotic state. (B) The cell is able to secure the G1 state if the flavopiridol is removed at 60 mins. (C) and (D) There are two distinguished outcomes if the flavopiridol is removed anytime between 30 mins and 60 mins.

7.5 Comparison between the SSA and the CLE using the Mammalian Mitotic Exit Model

Because of the features of the stochastic method, it is meaningless to compare single realizations from stochastic simulations. Instead, the mean and the standard deviation from the batch simulations are often used to characterize the behavior of stochastic models. In this section, statistical approaches are going to be employed to quantitatively analyze and compare the results from SSA and CLE simulations for the mitotic exit model.

Two hundred cells were simulated using either the SSA or the CLE approaches for different Cdk inhibition conditions. The percentage of the reversible and irreversible mitotic

exit outcomes were counted and plotted as functions of different Cdk1 inhibition durations (Figs. 7.6A,B). The probabilities of reversible mitotic exit in different simulations are plotted in Figure 7.6C. The CLE and the SSA version both predict the heterogeneous response to Cdk inhibition of cell populations. Both curves are almost identical (Fig. 7.6C). By contrast, in the deterministic model there is only one threshold (around 49.3 minutes); before and after the threshold cells show an all-or-none pattern (i.e. all exit or all reverse).

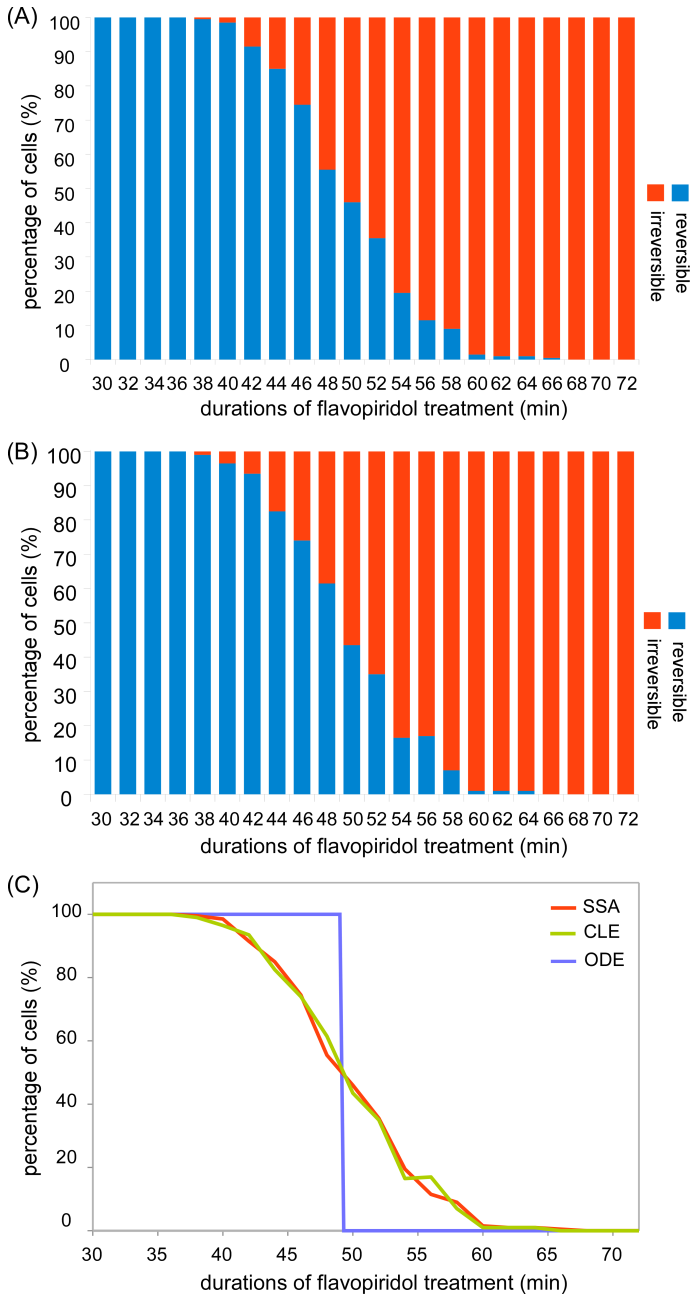

Figure 7.6: Probability distributions of the reversible and irreversible mitotic exit in cell populations. Two hundred simulations were conducted with different durations of the Cdk inhibition using the SSA approach (A) and the CLE approach (B) to mimic the heterogeneity of population responses. Percentages of the reversible of mitotic exit are calculated and plotted as histograms. (C) Comparison of the reversible probability among the SSA, the CLE and the ODE models. By setting the noise term to zero, the CLE equations in Table 7.3 become normal ODEs so that they can be simulated deterministically.

An alternative standard comparison of the batch stochastic simulations is to compare the arithmetic mean of the simulations. The average values of the time series are calculated for different durations of Cdk inhibition (Fig. 7.7). If the inhibitor is washed out at 30 mins or 60 mins outside the time window (36 mins $\sim$ 64 mins in Fig. 7.6), both the ODE and the CLE approaches are as good as the SSA version (Figs. 7.7A,C). However, the average values of the time trajectories diverge and each takes its own path when the Cdk inhibitor flavopiridol is removed at 50 mins. The stochasticity is responsible for leading cells to distinct outcomes. Whereas the deterministic model always produces the same solutions and completely fails to capture the noise, the CLE version works as well as the SSA model despite the mean value being slightly different (Fig. 7.7B).

The sample mean ($\bar{x}$) calculated from a limited number of stochastic simulations can be different from the real mean of the population, therefore the sample standard error of the mean (SEM) is used to estimate the population means. It is calculated from the equation $SEM = s/\sqrt{n}$, where s is the sample standard deviation and n is the sample size. Confidence intervals at 95% of the mean are computed based on the formula $\bar{x} \pm 1.96 \cdot SEM$.

The upper ($\bar{x} + 1.96 \cdot SEM$) and lower boundaries ($\bar{x} - 1.96 \cdot SEM$) of Mpf from the SSA and the CLE time series simulations are calculated and three examples of the Cdk1 / CycB inhibitory treatment with different lengths are shown in Figure 7.8. The areas between the boundaries are shaded with different colours for different methods, where blue is for the CLE and red is for the SSA. In the 50 minutes case, the reversible and the irreversible outcomes are divided from each other and plotted separately (Fig. 7.8B). The shaded regions of the two approaches almost completely overlap for all three conditions. Again this demonstrates that the CLE approach is as precise as the SSA approach. It also shows a narrow confidence range for the 30 mins and the 72 mins cases (Figs. 7.8A,C), implying high precision and an adequate sample size with 200 simulations. Compared with the other two situations, the 95% confidence interval for the intermediate inhibitory treatment duration is slightly wider (Fig. 7.8B).

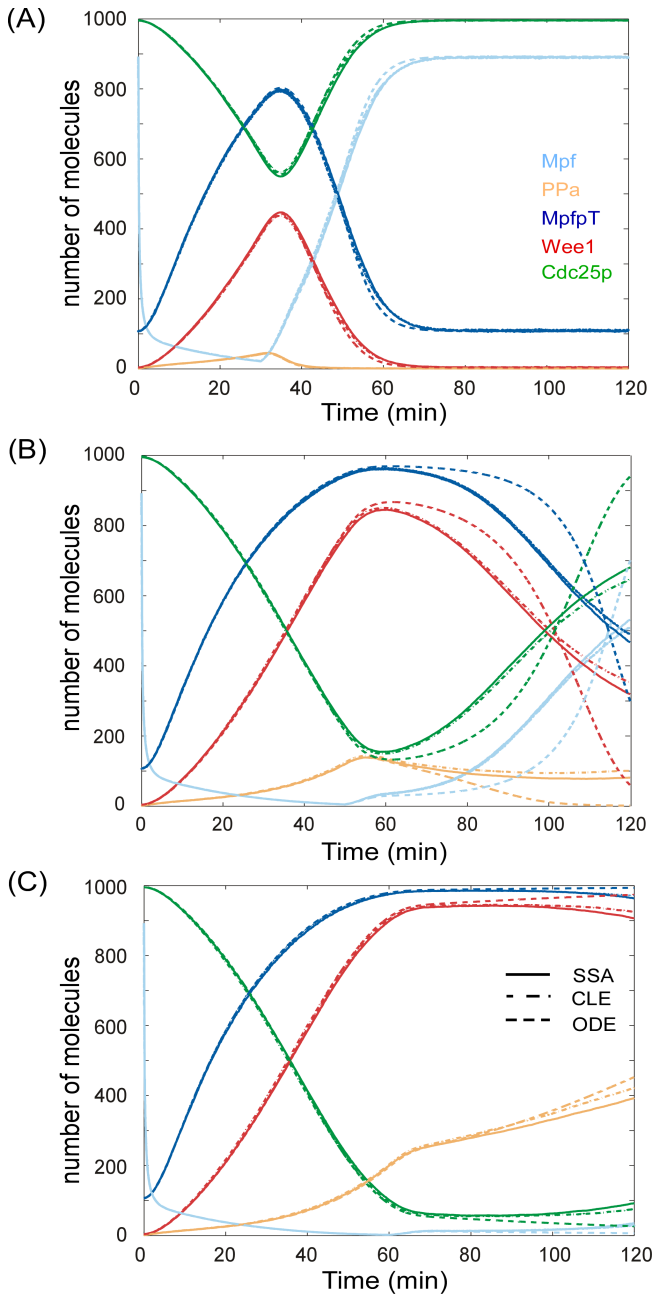

Figure 7.7: Comparison of the time course simulations from the ODE and the CLE with the SSA model. The mean of batch stochastic simulations from the SSA (solid line) and the CLE models (dashed dotted line) are calculated and plotted together with the deterministic ones (dashed line). The Cdk inhibitory treatment lasts (A) 30 mins (B) 50 mins and (C) 60 mins respectively. The active forms of the enzymes Wee1, Cdc25 and PP are also plotted in the figure.

To further compare bistable features between the CLE and the SSA, the difference and coefficient of variation of the MFPT with or without the inhibitor are displayed in Figure 7.9. The mean first passage times from the SSA always take longer than those of the CLE (Figs. 7.9A,B). In the absence of flavopiridol, the MFPT has a greater dispersion in the CLE version compared to that of the SSA (Fig. 7.9C), but the dispersion difference is not so obvious in the presence of flavopiridol (Fig. 7.9D).

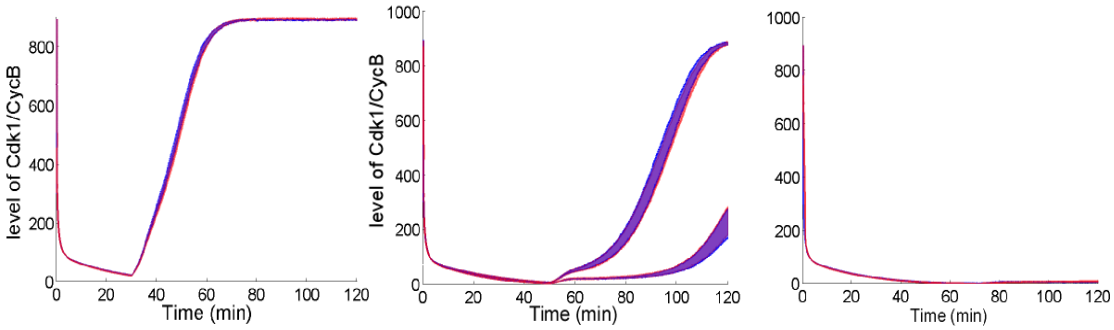

Figure 7.8: Confidence intervals comparison of Mpf between the SSA and the CLE methods. With 95% confidence interval, upper and lower boundaries of Mpf in the stochastic simulations were calculated using the equation $\bar{x} \pm 1.96 \times \text{SEM}$. Three examples from different lengths of Cdk inhibiton are shown: (A) 30 mins, (B) 50 mins and (C) 72 mins. Curves of CLE are shaded using blue colour and the ones from the SSA are shaded in red colour. For the 50 mins case, the reversible and the irreversible outcomes are divided and plotted separately.

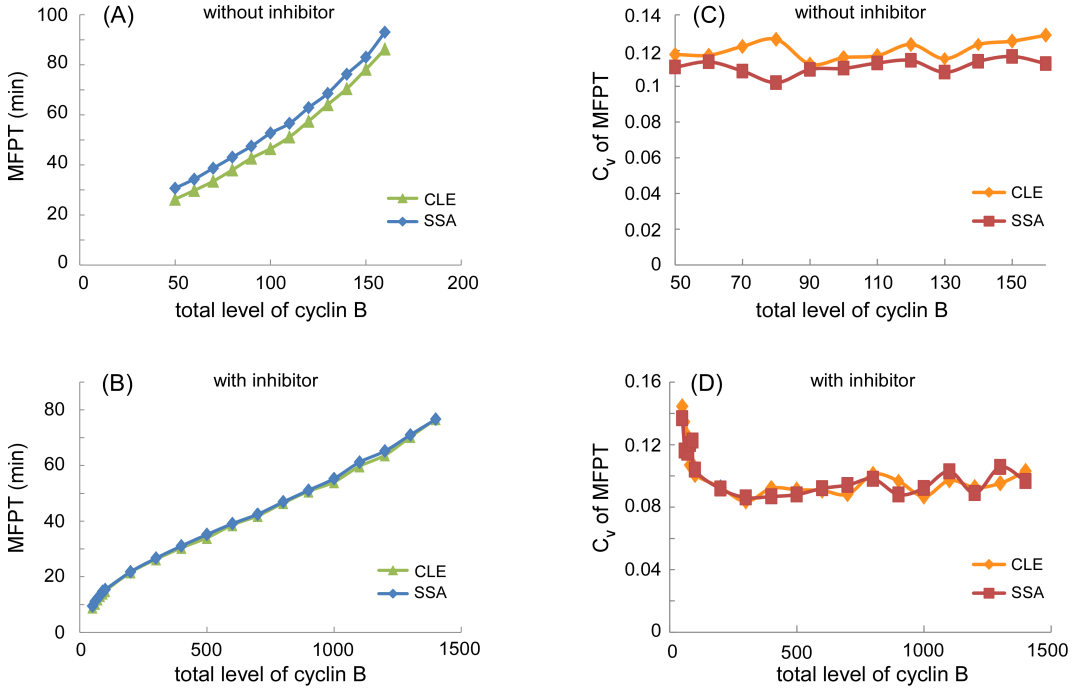

Figure 7.9: Compare the mean and the coefficients of variation of the first passage time between the SSA and the CLE approaches. (A) Comparison of MFPT for the CLE (green) and the SSA (blue) in the absence of flavopiridol. (B) Comparison of MFPT for the CLE and the SSA in the presence of flavopiridol. (C) Comparison the coefficient of variation (C_v) of MFPT between the SSA (red) and the CLE (orange) without flavopiridol. (D) Comparison the coefficient of variation (C_v) of MFPT for the CLE and the SSA with flavopiridol during the whole simulation. The coefficient of variation (C_v) at different levels of CycB_{tot} for both approaches are calculated using the formula $C_v = s/\bar{x}$, where s is the standard deviation and $\bar{x}$ is the mean.

7.6 Summary

One of the generic features of mitotic exit in eukaryotes is the proteolytic degradation of the Cdk1 regulatory subunit cyclin B (Morgan, 1997). In contrast to the conven-

tional proposition that cyclin degradation makes the mitotic exit irreversible in eukaryotes (Lodish et al., 2004), we propose that it only provides a driving force and that the sustaining of irreversibility of mitotic exit requires a ratcheting mechanism (Novák et al., 2007). This ratcheting mechanism works through systems-level feedback, which locks the cell cycle machinery in the G1 state after exiting from mitosis. A proof of principle experiment in budding yeast shows that cyclin degradation does not make mitotic exit irreversible (López-Avilés et al., 2009). The experiment also shows that yeast cells get locked in the G1 phase by up-regulation of the Cdk1/CycB inhibitor Sic1, which interacts in a double negative feedback loop with Cdk1/CycB. Recent experiments with mammalian cells conducted by Potapova et al. (2009) and the presented analysis in this chapter strongly suggests that mammalian cells also possess a ratcheting mechanism that provides the irreversible mitotic exit in the absence of cyclin degradation. Depending on the duration of Cdk1/CycB inhibition, the mitotic kinase can return to an active, non-phosphorylated state, or remains inactive and phosphorylated. The inhibitory phosphorylation of Cdk1/CycB by kinase Wee1 and phosphatase Cdc25 is responsible for the irreversible mitotic exit in mammalian cells under the specific experimental conditions (Potapova et al., 2009) as explained in this chapter. Although the molecular details are different, the underlying principles are the same from yeast to humans: systems-level double negative and positive feedbacks are required to secure the irreversible cell cycle transitions.

The CLE model of mitotic exit in mammalian cells illustrates the bistability and suggests an explanation of the reversible mitotic exit observed by Potapova et al. (2006, 2009). Our work shows that mitotic cells have M and G1 as two alternative steady states and that mitotic exit remains reversible until the feedback loops are sufficiently engaged. Molecular noise in the biochemical systems has an influence on the choice of the steady state by the bistable system, and a stochastic model can thus provide more comprehensive descriptions of the observations. The model successfully reproduces the time series data for both single cells and cell populations, and the simulations are consistent with the experimental findings. The model further predicts a gradual increase in the probability

of irreversible mitotic exit in conjunction with the time of Cdk inhibition. The steady state analysis using the stochastic simulation with different total cyclin B initial conditions recreates and extends the signal response curves (SRCs) that are calculated from the deterministic model. This supports the conventional bifurcation diagram and provides insight into the bistability of the stochastic system.

The model is then simulated using the Stochastic Simulation Algorithm (SSA). The comparison between the CLE and the SSA is done using the mammalian mitotic exit model as a test case. The features that have been examined and compared are single / batch time series simulations, the mean, the standard deviation and coefficient of variation of the mean first passage time (MFPT). Histograms of the reversible and irreversible mitotic exit outcomes from two algorithms show a strong agreement with experimental results (Potapova et al., 2009). Statistically, the MFPT calculated by the SSA is larger than that calculated from the CLE. However, the comparisons have shown that, for this particular test case, the CLE approach is roughly equivalent to the SSA for the following reasons: (1) the cell volume and the molecular abundance used in this model fall within a range where the CLE is still a good approximation of SSA (details see Section 3.2.3 in Chapter 3); (2) the stochasticity in the model is assumed to be only generated from internal noise (e.g. no temporal correlations of perturbations or spatial anisotropies etc.); (3) the experimental data sets are qualitative and do not have sufficient quantitative accuracy to distinguish between the two stochastic methods; (4) since the test case is a simplified model with only 10 species and 23 elementary reactions, the advantage of the CLE in terms of simulation efficiency is marginal.

Chapter 8

Conclusions

Metaphase-to-anaphase transition and mitotic exit, two successive irreversible processes that contribute to the irreversibility of M-to-G1 transition, have been theoretically studied in the presented work. Based on the latest experimental findings, mathematical models have been established. The questions that were raised at the beginning of the thesis have been addressed and the results are summarized as follows.

Question I: Is the M-to-G1 transition irreversible because of systems-level feedback, as is the case for the G1-to-S and the G2-to-M transitions?

Our models provide strong evidence that both the metaphase-to-anaphase transition and mitotic exit are functioning as bistable systems. Additionally, the models support the idea that they are each controlled by a one-way toggle switch similar to the other irreversible cell cycle transitions. Although the specific regulatory molecular networks differ between different species, the fundamental working mechanisms share the same dynamical principles i.e. systems-level feedback is in operation. Positive and/or double-negative feedback loops create the bistability which allows cells to accomplish the irreversible M-to-G1 transition.

Question II: What are the specific molecular feedback loops that create such one-way toggle switches in each individual process, i.e. metaphase-to-anaphase transition and mitotic exit?

The specific feedback loops that establish a one-way toggle switch for each individual process during the M-to-G1 transition have been identified and analyzed by simulation studies. We attribute the bistable switch of the metaphase-to-anaphase transition to the double-negative feedback between Cdk1/CycB and $\mathrm{APC}^{\mathrm{Cdc20}}$. For mitotic exit, the antagonistic relationship between Cdk1/Clb2 and its stoichiometric inhibitor Sic1 reinforces the bistable switch of mitotic exit in budding yeast. Likewise, the same irreversible process in mammalian cell requires the inhibitory phosphorylation of Cdk1/CycB by the kinase Wee1 and the phosphatase Cdc25. Both irreversible metaphase-to-anaphase transition and mitotic exit are dependent on these feedback loops that create a bistable system with hysteresis.

Question III: Is the system's bistability and dynamic behaviour affected by fluctuations in the number of regulatory molecules? How stable and robust is the M-to-G1 transition against those noisy perturbations?

The stochastic simulations of the metaphase-to-anaphase transition and of mitotic exit in the modeled organisms support the claim that cell cycle transitions are resistant to molecular noise as long as the essential feedback loops are in place and the molecular numbers of the participating species are above a critical threshold (Cross et al., 2002; Ghaemmaghami et al., 2003; Bruggeman et al., 2009; Kapuy et al., 2009b). The system's robustness is compromised if the critical feedback loops are disrupted. In this case, cells cannot be locked in the post-transition state and the transitions become reversible (Potapova et al., 2006, 2009; López-Avilés et al., 2009; Oliveira et al., 2010; Mirchenko and Uhlmann, 2010). For mitotic exit if the system is approaching the transition point, stochastic molecular fluctuations can play an important role in determining exactly at what time a cell makes the transition and thus introduce the variability of the cell-cycle progression observed between individual cells of a cell population.

In conclusion, the presented work has analyzed the irreversible M-to-G1 cell cycle transition from a dynamic systems view of the molecular regulatory networks. System-level feedback, bistability and irreversible transitions are all intimately connected con-

cepts (Novák et al., 2007; Kapuy et al., 2009b). The significance of feedback loops in creating alternative stable steady states and in reinforcing the irreversible cell cycle progression is gaining increasing recognition in cell cycle studies (Murray, 1992; Ciliberto et al., 2005; Holt et al., 2008; Ferrell, 2008; Pomerening, 2009; Novák et al., 2010). Systems-level feedbacks and potential bistability should be considered in modelling of any biological system, as these features are found in the molecular control systems of many cellular functions (Davidson and Surette, 2008; Veening et al., 2008; Mitrophanov and Groisman, 2008; Pomerening, 2008; Sauro, 2009).

A methodical focus of this work was the development of a straightforward procedure of mapping deterministic models into stochastic models. With such a procedure now at hand, this work provides a guideline of how to efficiently convert an ODE model into an SSA model, how to study the relationship between deterministic and stochastic models, and how to compare different simulation outcomes.

We also demonstrated that stochastic models are necessary and serve as powerful tools to illustrate and analyze the heterogeneity between individual cells. Stochastic simulation results not only complement the deterministic approaches, but can also contribute to a more realistic understanding of processes such as the M-to-G1 transition. The effects of noise and the potential need for stochastic simulations should not be overlooked in studying dynamic features of cells or biological systems.

All the models developed in this work have been deliberately kept simple, yet include all the necessary information to highlight the proposed ideas. In practice, the models work remarkably well in qualitatively explaining significant experimental findings and also make interesting predictions. These models can be updated into more comprehensive versions once more quantitative experimental data become available in the future and will be able to provide additional quantitative predictions that can then be compared with the experiments. Alternatively, these simple models can serve as templates and can be potentially extended by incorporating more biological features to avoid the repetitive task of reconstructing similar models from scratch.

Finally, the models proposed in this work aim to show how mathematical approaches, specifically stochastic simulations, can aid biologists or biochemists to interpret experimental findings and assist future experimental design. The application of mathematical and computational modelling to quantitatively describe and evaluate biological systems is an appealing and promising methodology, as it is able to provide an integrative systems view. Theoretical and experimental studies need to complement each other and only the joint effort of both will further benefit the scientific community.

Appendices

The computer codes for simulating the deterministic and stochastic models presented in the thesis are included in the Appendix. The plain text format of the file containing the equations, initial conditions and parameter values for the models need to be saved as .ODE file. The XPP and Winpp .ODE file can then be executed by the freely available software package XPPAUT and WINPP respectively. The publications related to this D.Phil thesis are attached at the end of the Appendix.

A Deterministic Model of the Anaphase Switch

A.1 XPP file for the conceptual deterministic model

```
# Xppaut file for anaphase switch
init CycB=0.773, Mad2aT=1.96, MCC=1, CAPP=0.114, N0A=1
CycB' = kscyc - (kdcyc' + kdcyc*Cdc20)*CycB
Mad2aT' = kamad*N0A*(Mad2T - Mad2aT) - kimad'*Mad2aT - kimad*Cdc20*MCC
MCC' = kasmcc*(Cdc20T-MCC)*(Mad2aT-MCC)-(kdimcc+kimad'+kimad*Cdc20)*MCC
CAPP' = kacapp*(CAPPT - CAPP) - kicapp*CycB*CAPP
N0A' = kan*CycB*(NT - Ntens - N0A) - kin*CAPP*N0A
Cdc20 = Cdc20T - MCC
aux Cdc20 = Cdc20
p Ntens=0, Cdc20T=1, NT=1, CAPPT=1, Mad2T=2
p kscyc=0.01, kdcyc'=0.01, kdcyc=1
p kamad=1, kimad'=0.01, kimad=1
p kan=1, kin=1, kasmcc=40, kdimcc=0.1
p kacapp=0.1, kicapp=1
# numerical method
@ meth=stiff
done
```

A.2 XPP file for the dimensionless model of anaphase switch

```
# The XPPaut file of the Model of anaphase switch with scalled parameters
# The file can be used for both one and two parameters bifurcation plot
Cdc20 = 1 - MCC
CycB' = 1- (1 + beta*Cdc20)*CycB
Mad2AT' = gamma*X0A*(PSI - Mad2AT)-Mad2AT-delta*Cdc20*MCC
MCC' = lambda*(1 - MCC)*(Mad2AT-MCC)-(1 + kappa*(1+delta*Cdc20))*MCC
PP' = 1-PP - eta*CycB*PP
X0A' = (1 - Xtens - X0A)* THETA *CycB - PP*X0A
p Xtens=0, PSI=2, THETA=1
p beta=100, gamma=100, delta=100
```

```
p lambda=400, kappa=0.1, eta=10
i CycB=0.776380, Mad2AT=1.974064, MCC=0.997120, PP=0.114106, X0A=0.871861
done
```

B Stochastic Model of the Anaphase Switch

B.1 Xpp file of the stochastic model

```
init tr=0, Sect=758, Mad2at=1976, CycB=849, PP=130, Na=10
init Ni=0, Cohe=380, Ntens=0, ther=38
p Cdc20T=1000, SepT=500, Mad2T=2000, NT=10, PPT=1000, V=1000, kdc=0.6
p kscyc=0.01, kdcyc'=0.01, kdcyc=1, kssec=0.01, kdsec'=0.01, kdsec=1
p kapp=0.1, kipp=1, ksc=0.001, kant=0.12, kint=1, lamcc=400, ldmcc=1
p kamad=200, kimad=2, kimad'=0.02, lass=40, ldss=0.1, kan=100, kin=100

v1 = kscyc*V
v2 = v1 + kdcyc'*CycB
v3 = v2 + kdcyc*CycB*Cdc20/V
v4 = v3 + kssec*V
v5 = v4 + kdsec'*Sect
v6 = v5 + kdsec*Sect*Cdc20/V
v7 = v6 + ksc*V
v8 = v7 + kdc*Cohe*Sep/V
v9 = v8 + kan*Ni*CycB/V
v10 = v9 + kin*Na*PP/V
v11 = v10 + kant*Na*heav(Cohe-ther)
v12 = v11 + kant*Ni*heav(Cohe-ther)
v13 = v12 + kint*Ntens*heav(ther-Cohe)*kan*CycB/(kan*CycB + kin*PP)
v14 = v13 + kint*Ntens*heav(ther-Cohe)*kin*PP/(kan*CycB + kin*PP)
v15 = v14 + kamad*Mad2*Na/V
v16 = v15 + kimad'*Mad2at
v17 = v16 + kimad*MCC*Cdc20/V
v18 = v17 + kapp*(PPT-PP)
v19 = v18 + kipp*PP*CycB/V

s=ran(1)*v19
z1=(s<v1)
z2=(s<v2)&(s>=v1)
z3=(s<v3)&(s>=v2)
z4=(s<v4)&(s>=v3)
z5=(s<v5)&(s>=v4)
z6=(s<v6)&(s>=v5)
z7=(s<v7)&(s>=v6)
z8=(s<v8)&(s>=v7)
z9=(s<v9)&(s>=v8)
z10=(s<v10)&(s>=v9)
z11=(s<v11)&(s>=v10)
z12=(s<v12)&(s>=v11)
z13=(s<v13)&(s>=v12)
z14=(s<v14)&(s>=v13)
z15=(s<v15)&(s>=v14)
z16=(s<v16)&(s>=v15)
z17=(s<v17)&(s>=v16)
z18=(s<v18)&(s>=v17)
z19=(s>=v18)

ther' = ther
```

```
tr'= tr-log(ran(1))/v19
CycB' = CycB + z1 - z2 - z3
Sect' = Sect + z4 - z5 - z6
Cohe' = Cohe + z7 - z8
Na'= Na + z9 + z13 - z10 - z11
Ni' = Ni + z10 + z14 - z9 - z12
Ntens' = Ntens + z11 + z12 - z13 - z14
Mad2at' = Mad2at + z15 - z16 - z17
PP'= PP + z18 - z19

SS = Sect + SepT + (ldss*V + (kdsec'*V + kdsec*Cdc20))/lass
SepSec = 2*Sect*SepT/(SS + sqrt(SS^2 - 4*SepT*Sect))
Sep = SepT - SepSec
aux Sep = Sep
BB = Cdc20T + Mad2at + (ldmcc*V + kimad'*V + kimad*Cdc20T)/lamcc
MCC = 2*Mad2at*Cdc20T/(BB + sqrt(BB^2 - 4*Mad2at*Cdc20T*(1 + kimad/lamcc)))
aux MCC = MCC
Cdc20 = Cdc20T - MCC
aux Cdc20 = Cdc20
Mad2 = Mad2T - Mad2at
aux Mad2 = Mad2
# Cohesion that has been destroyed
y = 380 - Cohe
aux y = y
global +1 {y - 342} {ther=1e7}

@ bound=100000000,meth=discrete,total=50000,njmp=25, seed=2173592
@ maxstor=5000000
@ nplot=5, xp=tr, yp=CycB, xp2=tr, yp2=Ntens, xp3=tr, yp3=MCC
@ xp4=tr, yp4=Cohe, xp5=tr, yp5=Mad2aT
done
```

C Mitotic Exit in Budding Yeast

C.1 The ODE file for the modified deterministic model of mitotic exit in budding yeast

```
# initial conditions
init Clb2T=0.99, Clb5T=1, Mcm1P=0.83, APC=1, kscdh1=0.02
# differential equations
Clb2T' = ksclb2' + ksclb2*Mcm1P - Vdclb2*Clb2T
Clb5T' = ksclb5 - Vdclb5*Clb5T
Sic1T' = kssic1' + kssic1*Swi5ac - Vdsic1*Sic1T
Trim2' = kas2*(Clb2T-Trim2)*(Sic1T-Trim2-Trim5)-kds2*Trim2-(Vdclb2+Vdsic1)*Trim2
Trim5' = kas5*(Clb5T-Trim5)*(Sic1T-Trim2-Trim5)-kds5*Trim5-(Vdclb5+Vdsic1)*Trim5
Cdh1m11'= kscdh1 - kdcdh1*Cdh1m11
Mcm1P' = (kamcm1' + kamcm1*Clb2)*(1 - Mcm1P) - kimcm1*Mcm1P
Swi5' = (kaswi5 + kaswi5'*Cdc14)*Swi5P - (kiswi5 + kiswi5'*Clb2)*Swi5
Swi5P' = (kaswi5+kaswi5'*Cdc14)*Swi5PP-(kiswi5+kiswi5'*Clb2)*Swi5P\
       -(kaswi5+kaswi5'*Cdc14)*Swi5P+(kiswi5+kiswi5'*Clb2)*Swi5
Swi5PP' = (kaswi5+kaswi5'*Cdc14)*(1-Swi5ac)-(kiswi5+kiswi5'*Clb2)*Swi5PP\
        - (kaswi5+kaswi5'*Cdc14)*Swi5PP+(kiswi5+kiswi5'*Clb2)*Swi5P
kscdh1' = 0
APC' = 0

Vdclb2 = kdclb2' + kdclb2*Cdh1m11*APC
Vdclb5 = kdclb5' + kdclb5*Cdh1m11*APC
```

```
Vdsic1 = kdsic1' + kdsic1"*Clb5 + kdsic1*Clb2
Clb2 = Clb2T - Trim2
aux Clb2 = Clb2T - Trim2
Clb5 = Clb5T - Trim5
aux Clb5 = Clb5T - Trim5
Swi5ac = Swi5 + Swi5P + Swi5PP
aux Swi5ac = Swi5ac
global +1 {t-depriv} {kscdh1=0}
global +1 {t-depriv2} {APC=cdc16}
# parameters
p ksclb2'=0.001, ksclb2=0.035, kdclb2'=0.03, kdclb2=0.5, kas2=20, kds2=0.01
p ksclb5=0.01, kdclb5'=0.02, kdclb5=0.05, kas5=20, kds5=0.01
p kssic1'=0.02, kssic1=0.3, kdsic1=2, kdsic1'=0.3, kdsic1"=0.05
p kamcm1'=0.01, kamcm1=5, kimcm1=1, kaswi5=0.01, kaswi5'=2, kiswi5=0.01
p kiswi5'=11, kdcdh1=0.02, Cdc14=0.02, depriv=400, depriv2=400, cdc16=0.02
done
```

C.2 WinPP file for phase plane analysis of Clb2T and Sic1T

```
# The phase plane for enuo_3p3 model (Clb2T vs Sic1T)
p Cdh1m11=0, Cdc14=0.02, APC=1, ksclb2'=0.001, ksclb2=0.035, kdclb2'=0.03
p kdclb2=0.5, kas2=20, kds2=0.01, ksclb5=0.01, kdclb5'=0.02, kdclb5=0.05
p kssic1'=0.02, kssic1=0.3, kdsic1=2, kdsic1'=0.3, kdsic1"=0.05, kamcm1'=0.01
p kamcm1=5, kimcm1=1, kaswi5=0.01, kaswi5'=2, kiswi5=0.01, kiswi5'=14

Sic1T' = kssic1' + kssic1*Swi5A - Vdsic1*Sic1T
Clb2T' = ksclb2' + ksclb2*Mcm1P - Vdclb2*Clb2T
Clb5T = ksclb5/(kdclb5' + kdclb5*Cdh1m11*APC)
Clb2 = Clb2T - Trim*Clb2T/CdkT
Clb5 = Clb5T - Trim*Clb5T/CdkT
Mcm1P = (kamcm1' + kamcm1*Clb2)/(kamcm1' + kamcm1*Clb2 + kimcm1)
VdSwi5 = kaswi5 + kaswi5'*Cdc14
VpSwi5 = kiswi5 + kiswi5'*Clb2
num = sum(0,2) of ((VpSwi5/VdSwi5)^i')
denum = sum (0,3) of ((VpSwi5/VdSwi5)^i')
Swi5A = num/denum
CdkT = Clb2T + Clb5T
BB = CdkT + Sic1T + kds2/kas2
Trim = 2*CdkT*Sic1T/(BB + sqrt(BB^2-4*CdkT*Sic1T))
Vdclb2 = kdclb2' + kdclb2*Cdh1m11*APC
Vdsic1 = kdsic1' + kdsic1"*Clb5 + kdsic1*Clb2
Done
```

C.3 Varied parameters for four different simulation conditions in budding yeast of mitotic exit

C.4 MATLAB code for stochastic model of mitotic exit in budding yeast

The stochastic model "multi_noCdh1_stoch_3p3.m", the corresponding stochastic simulations and analysis are using MATLAB and SimBiology toolbox (Chapter 3). The model and the analysis are written into different separate functions: The build-in function and commands can be found in the documentation of the SimBiology (http). The detailed explanation of the inputs and outputs variables for each individual function please see the comment in each code below.

	Irreversible Exit	Reversible Exit	Deleted Sic1	Overexpressed Sic1
kssic1'	0.02	0.02	0	0.08
kssic1	0.3	0.3	0	0.3
deprive	200	30	200	30
deprive2	60	50	60	50

Table 8.1: Varied parameters for four different simulation conditions in budding yeast of mitotic exit. $deprive$ is the time to turn off Cdh1m11 induction. $deprive2$ is the time to turn off APC meaning shut off the $\mathrm{APC}^{\mathrm{Cdh1m11}}$ dependent degradation of M-Cdk. Some experimental details are relevant here. López-Avilés et al. (2009) used a constitutively active form of Cdh1 (Cdh1m11) in which all Cdk1 phosphorylation sites are mutated to non-phosphorylatable amino acids. Because Clb2 cannot inhibit Cdh1m11, the constitutively active form of Cdh1 works like an exit protein rather than a feedback loop component. The yeast strain used in the experiment also carried a temperature-sensitive APC mutation, which allowed the experimenters to terminate $\mathrm{APC}^{\mathrm{Cdh1}}$ dependent cyclin degradation by inactivating the APC.

- **Demo.m**: the file that includes all the functions can be called and to display the figures or plots for the stochastic model in Chapter 6.
- **multi_noCdh1_stoch_3p3.m**: The stochastic model of mitotic exit in budding yeast including all the reactions, parameters and initial values that has been described in Chapter 6 Section 6.2. However no simulations and plots are included in this file.
- **plot_two_situation.m**: use to plot the figures for the reversible and the irreversible conditions (or Sic1Δ and Sic1 overexpression conditions)
- **set_configure.m**: function that used to set the configuration for the simulations (e.g. which species to plot and the simulation length)
- **all_simulation_figure.m**: function that used to plot the figures with subplot function plot all the results in one figure.
- **percentage_re_ir.m**: the function that used to calculate the percentage of the reversible and irreversible of situations in number of simulations.
- **distribution_3D.m**: calculate the distribution of each species in 3D dimensional pattern

C.4.1 Matlab file that calls all the function for simulation: Demo.m

```
%% read in the stochastic model
multi_noCdh1_stoch_3p3;

%% set the configure for the simulation
cs = set_configure(Model,{'Clb2','Mcm1p','Swi5','Cdh1m11','Sic1','Trim5',...
     'Swi5p','Swi5pp','Trim2'},'ssa',150, 100);

%% simulation for the single cases
simobj(1)=sbiosimulate(Model, cs, obj_irrever);
simobj(2)=sbiosimulate(Model, cs, obj_rever);
simobj(3)=sbiosimulate(Model, cs, obj_sic1_deleted);
simobj(4)=sbiosimulate(Model, cs, obj_sic1_over);
% plot the figures for stochasti simulation in a single cell level
plot_two_situation(simobj(1),simobj(2));
```

```
plot_two_situation(simobj(3),simobj(4));

%% Multiple stochastic ensemble runs of the model
simDataObj = sbioensemblerun(Model,100,cs,obj_rever,'linear');

%% calculate the percentage of the reversible and irreversible
[x_irr,x_re] = percentage_re_ir(simDataObj,100,2000,[5,6,9])

%% calculate the distribution for the species
distribution_3D(simDataObj,0:50:2000);

%% calculate the average trend for population of cells
average_population(simDataObj);

%% plot the many subplot for population of cells
all_simulation_figure(simDataObj,[10,10]);
```

C.4.2 multi_noCdh1_stoch_3p3.m

```
% stochastic version
% Give reasonable molecular number for each speices,
% Convert the determinstic rate constant into the stochastic rate constant
% Introduce scale parameters V, Mcm1T, Swi5T
% create the model and the compartment
Model = sbiomodel('mitotic_noCdh1');
compObj = addcompartment(Model,'cell');
V=2000;
Mcm1T=10;
Swi5T=0.7;
% add initial molecular number for the species to the model
addspecies(compObj,'Clb2',V);
addspecies(compObj,'Clb5',0.5*V);
addspecies(compObj,'Mcm1p',0.83*V*Mcm1T);
addspecies(compObj,'Mcm1',0.17*V*Mcm1T);
addspecies(compObj,'Cdc14',0.02*V,'ConstantAmount',true);
addspecies(compObj,'Swi5',0);
addspecies(compObj,'Swi5ppp',V*Swi5T);
% add parameters to the model
addparameter(Model,'kscdh1',0.02*V,'ConstantValue',false);
addparameter(Model,'ksclb22',0.001*V);
addparameter(Model,'ksclb5',0.01*V);
addparameter(Model,'kssic11',0.02*V);
% first order parameters, no need to change
addparameter(Model,'kamcm11',0.01);
addparameter(Model,'kimcm1',1);
addparameter(Model,'kdcdh1',0.02);
addparameter(Model,'kiswi5',0.01);
addparameter(Model,'kaswi5',0.01);
addparameter(Model,'kds5',0.01);
addparameter(Model,'ksclb2',0.035/Mcm1T);
addparameter(Model,'kdclb22',0.03);
addparameter(Model,'kdclb55',0.02);
addparameter(Model,'kdsic11',0.3);
addparameter(Model,'kssic1',0.3/Swi5T);
addparameter(Model,'kds2',0.01);
% second order parameters, Ks=Kd/V
addparameter(Model,'kamcm1',5/V);
addparameter(Model,'kiswi55',14/V);
addparameter(Model,'kaswi55',2/V);
```

```
addparameter(Model,'kas5',20/V);
addparameter(Model,'kdclb2',0.5/V,'ConstantValue',false);
addparameter(Model,'kdclb5',0.05/V,'ConstantValue',false);
addparameter(Model,'kas2',20/V);
addparameter(Model,'kdsic1',2/V);
addparameter(Model,'kdsic111',0.05/V);
% add parameters for simulation
turnoff_cdh1m11obj = addparameter(Model,'depriv',30);
turnoff_APCobj = addparameter(Model,'depriv2',50);

% ================Mcm1p================================
r1_mcm1p = addreaction(Model,'Mcm1 -> Mcm1p');
kr1_mcm1p = addkineticlaw(r1_mcm1p,'MassAction');
set (kr1_mcm1p,'ParameterVariableNames','kamcm11');
r2_mcm1p = addreaction(Model,'Mcm1 + Clb2 -> Mcm1p + Clb2');
kr2_mcm1p = addkineticlaw(r2_mcm1p,'MassAction');
set (kr2_mcm1p,'ParameterVariableNames','kamcm1');
r3_mcm1p = addreaction(Model,'Mcm1p -> Mcm1');
kr3_mcm1p = addkineticlaw(r3_mcm1p,'MassAction');
set (kr3_mcm1p,'ParameterVariableNames','kimcm1');

% ================Cdh1m11==============================
r1_cdh1m11 = addreaction(Model,'null -> Cdh1m11');
kr1_cdh1m11 = addkineticlaw(r1_cdh1m11,'MassAction');
set (kr1_cdh1m11,'ParameterVariableNames','kscdh1');
r2_cdh1m11 = addreaction(Model,'Cdh1m11 -> null');
kr2_cdh1m11 = addkineticlaw(r2_cdh1m11,'MassAction');
set (kr2_cdh1m11,'ParameterVariableNames','kdcdh1');

% ================Trim5================================
r1_trim5 = addreaction(Model,'Sic1 + Clb5 -> Trim5');
kr1_trim5 = addkineticlaw(r1_trim5,'MassAction');
set (kr1_trim5,'ParameterVariableNames','kas5');
r2_trim5 = addreaction(Model,'Trim5 -> Sic1 + Clb5');
kr2_trim5 = addkineticlaw(r2_trim5,'MassAction');
set (kr2_trim5,'ParameterVariableNames','kds5');
r3_trim5 = addreaction(Model,'Trim5 + Cdh1m11 -> Sic1 + Cdh1m11');
kr3_trim5 = addkineticlaw(r3_trim5,'MassAction');
set (kr3_trim5,'ParameterVariableNames','kdclb5');
r4_trim5 = addreaction(Model,'Trim5  -> Clb5');
kr4_trim5 = addkineticlaw(r4_trim5,'MassAction');
set (kr4_trim5,'ParameterVariableNames','kdsic11');
r5_trim5 = addreaction(Model,'Trim5 -> Sic1');
kr5_trim5 = addkineticlaw(r5_trim5,'MassAction');
set (kr5_trim5,'ParameterVariableNames','kdclb55');
r6_trim5 = addreaction(Model,'Trim5 + Clb5 -> 2 Clb5');
kr6_trim5 = addkineticlaw(r6_trim5,'MassAction');
set (kr6_trim5,'ParameterVariableNames','kdsic111');
r7_trim5 = addreaction(Model,'Trim5 + Clb2 ->  Clb2 + Clb5');
kr7_trim5 = addkineticlaw(r7_trim5,'MassAction');
set (kr7_trim5,'ParameterVariableNames','kdsic1');

% ================Clb2=================================
r1_clb2 = addreaction(Model,'null -> Clb2');
kr1_clb2 = addkineticlaw(r1_clb2,'MassAction');
set (kr1_clb2,'ParameterVariableNames','ksclb22');
r2_clb2 = addreaction(Model,'Mcm1p -> Mcm1p + Clb2');
kr2_clb2 = addkineticlaw(r2_clb2,'MassAction');
set (kr2_clb2,'ParameterVariableNames','ksclb2');
```

```
r3_clb2 = addreaction(Model,'Clb2 -> null');
kr3_clb2 = addkineticlaw(r3_clb2,'MassAction');
set (kr3_clb2,'ParameterVariableNames','kdclb22');
r4_clb2 = addreaction(Model,'Cdh1m11 + Clb2 -> Cdh1m11');
kr4_clb2 = addkineticlaw(r4_clb2,'MassAction');
set (kr4_clb2,'ParameterVariableNames','kdclb2');

% ===============Clb5================================
r1_clb5 = addreaction(Model,'null -> Clb5');
kr1_clb5 = addkineticlaw(r1_clb5,'MassAction');
set (kr1_clb5,'ParameterVariableNames','ksclb5');
r2_clb5 = addreaction(Model,'Clb5 -> null');
kr2_clb5 = addkineticlaw(r2_clb5,'MassAction');
set (kr2_clb5,'ParameterVariableNames','kdclb55');
r3_clb5 = addreaction(Model,'Cdh1m11 + Clb5 -> Cdh1m11');
kr3_clb5 = addkineticlaw(r3_clb5,'MassAction');
set (kr3_clb5,'ParameterVariableNames','kdclb5');

% ===============Sic1================================
r1_sic1 = addreaction(Model,'null -> Sic1');
kr1_sic1 = addkineticlaw(r1_sic1,'MassAction');
set (kr1_sic1,'ParameterVariableNames','kssic11');
r2_sic1 = addreaction(Model,'Sic1 -> null');
kr2_sic1 = addkineticlaw(r2_sic1,'MassAction');
set (kr2_sic1,'ParameterVariableNames','kdsic11');
r3_sic1 = addreaction(Model,'Swi5 -> Sic1 + Swi5');
kr3_sic1 = addkineticlaw(r3_sic1,'MassAction');
set (kr3_sic1,'ParameterVariableNames','kssic1');
r31_sic1 = addreaction(Model,'Swi5p -> Sic1 + Swi5p');
kr31_sic1 = addkineticlaw(r31_sic1,'MassAction');
set (kr31_sic1,'ParameterVariableNames','kssic1');
r32_sic1 = addreaction(Model,'Swi5pp -> Sic1 + Swi5pp');
kr32_sic1 = addkineticlaw(r32_sic1,'MassAction');
set (kr32_sic1,'ParameterVariableNames','kssic1');
r4_sic1 = addreaction(Model,'Sic1 + Clb5 -> Clb5');
kr4_sic1 = addkineticlaw(r4_sic1,'MassAction');
set (kr4_sic1,'ParameterVariableNames','kdsic111');
r5_sic1 = addreaction(Model,'Sic1 + Clb2 -> Clb2');
kr5_sic1 = addkineticlaw(r5_sic1,'MassAction');
set (kr5_sic1,'ParameterVariableNames','kdsic1');

% ===============Trim2================================
r1_trim2 = addreaction(Model,'Sic1 + Clb2 -> Trim2');
kr1_trim2 = addkineticlaw(r1_trim2,'MassAction');
set (kr1_trim2,'ParameterVariableNames','kas2');
r2_trim2 = addreaction(Model,'Trim2 -> Sic1 + Clb2');
kr2_trim2 = addkineticlaw(r2_trim2,'MassAction');
set (kr2_trim2,'ParameterVariableNames','kds2');
r3_trim2 = addreaction(Model,'Trim2 -> Sic1');
kr3_trim2 = addkineticlaw(r3_trim2,'MassAction');
set (kr3_trim2,'ParameterVariableNames','kdclb22');
r4_trim2 = addreaction(Model,'Trim2 -> Clb2');
kr4_trim2 = addkineticlaw(r4_trim2,'MassAction');
set (kr4_trim2,'ParameterVariableNames','kdsic11');
r5_trim2 = addreaction(Model,'Trim2 + Cdh1m11 -> Sic1 + Cdh1m11');
kr5_trim2 = addkineticlaw(r5_trim2,'MassAction');
set (kr5_trim2,'ParameterVariableNames','kdclb2');
r6_trim2 = addreaction(Model,'Trim2 + Clb5 -> Clb5 + Clb2');
kr6_trim2 = addkineticlaw(r6_trim2,'MassAction');
```

```
set (kr6_trim2,'ParameterVariableNames','kdsic111');
r7_trim2 = addreaction(Model,'Trim2 + Clb2 -> 2 Clb2');
kr7_trim2 = addkineticlaw(r7_trim2,'MassAction');
set (kr7_trim2,'ParameterVariableNames','kdsic1');

% ===============Swi5====================================
r1_swi5 = addreaction(Model,'Swi5 + Clb2 -> Swi5p + Clb2');
kr1_swi5 = addkineticlaw(r1_swi5,'MassAction');
set (kr1_swi5,'ParameterVariableNames','kiswi55');
r11_swi5 = addreaction(Model,'Swi5p + Clb2 -> Swi5pp + Clb2');
kr11_swi5 = addkineticlaw(r11_swi5,'MassAction');
set (kr11_swi5,'ParameterVariableNames','kiswi55');
r111_swi5 = addreaction(Model,'Swi5pp + Clb2 -> Swi5ppp + Clb2');
kr111_swi5 = addkineticlaw(r111_swi5,'MassAction');
set (kr111_swi5,'ParameterVariableNames','kiswi55');
r2_swi5 = addreaction(Model,'Swi5p + Cdc14 -> Swi5 + Cdc14');
kr2_swi5 = addkineticlaw(r2_swi5,'MassAction');
set (kr2_swi5,'ParameterVariableNames','kaswi55');
r22_swi5 = addreaction(Model,'Swi5pp + Cdc14 -> Swi5p + Cdc14');
kr22_swi5 = addkineticlaw(r22_swi5,'MassAction');
set (kr22_swi5,'ParameterVariableNames','kaswi55');
r222_swi5 = addreaction(Model,'Swi5ppp + Cdc14 -> Swi5pp + Cdc14');
kr222_swi5 = addkineticlaw(r222_swi5,'MassAction');
set (kr222_swi5,'ParameterVariableNames','kaswi55');
r3_swi5 = addreaction(Model,'Swi5 -> Swi5p');
kr3_swi5 = addkineticlaw(r3_swi5,'MassAction');
set (kr3_swi5,'ParameterVariableNames','kiswi5');
r33_swi5 = addreaction(Model,'Swi5p -> Swi5pp');
kr33_swi5 = addkineticlaw(r33_swi5,'MassAction');
set (kr33_swi5,'ParameterVariableNames','kiswi5');
r333_swi5 = addreaction(Model,'Swi5pp -> Swi5ppp');
kr333_swi5 = addkineticlaw(r333_swi5,'MassAction');
set (kr333_swi5,'ParameterVariableNames','kiswi5');
r4_swi5 = addreaction(Model,'Swi5p -> Swi5');
kr4_swi5 = addkineticlaw(r4_swi5,'MassAction');
set (kr4_swi5,'ParameterVariableNames','kaswi5');
r44_swi5 = addreaction(Model,'Swi5pp -> Swi5p');
kr44_swi5 = addkineticlaw(r44_swi5,'MassAction');
set (kr44_swi5,'ParameterVariableNames','kaswi5');
r444_swi5 = addreaction(Model,'Swi5ppp -> Swi5pp');
kr444_swi5 = addkineticlaw(r444_swi5,'MassAction');
set (kr444_swi5,'ParameterVariableNames','kaswi5');

% =============add Event=======================
% turn off cdh1m11 and APC
addevent(Model,'time>depriv','kscdh1=0');
addevent(Model,'time>depriv2',{'kdclb5 = kdclb5*0.02','kdclb2 = kdclb2*0.02'});

% ============add variants==========================
% for the model to simulation the model in the different situiation
obj_irrever = addvariant(Model,'turn off cdh1m11 at 200 and turn off APC at 60');
obj_rever = addvariant(Model,'turn off cdh1m11 at 30 and turn off APC at 50');
obj_sic1_deleted = addvariant(Model,'sic1_del');
obj_sic1_over = addvariant(Model,'sic1_ov');

% irreversible version
addcontent(obj_irrever,{'parameter','depriv','Value',200});
addcontent(obj_irrever,{'parameter','depriv2','Value',60});
% reversible version
```

```
addcontent(obj_rever,{'parameter','depriv','Value',30});
addcontent(obj_rever,{'parameter','depriv2','Value',50})
% sic1 deleted version
addcontent(obj_sic1_deleted,{'parameter','kssic1','Value',0});
addcontent(obj_sic1_deleted,{'parameter','kssic11','Value',0})
addcontent(obj_sic1_deleted,{'parameter','depriv','Value',200});
addcontent(obj_sic1_deleted,{'parameter','depriv2','Value',60});
% sic1 overexpressed version
addcontent(obj_sic1_over,{'parameter','kssic11','Value',0.08*V});
addcontent(obj_sic1_over,{'parameter','depriv','Value',30});
addcontent(obj_sic1_over,{'parameter','depriv2','Value',50});
```

C.4.3 set_configure.m

```
function y = set_configure(model_obj, species_name, solver_type,...
             stop_time, every_steps_record)
% e.g. y = set_configure(Model, {'Clb2','Sic1'}, 'ssa', 150, 100)
% species_name={'Clb2', 'Mcm1p', 'Swi5', 'Cdh1m11', 'Sic1', 'Trim5',...
%               'Swi5p', 'Swi5pp', 'Trim2'}
model=model_obj;
cs = getconfigset(model);
cs.StopTime = stop_time;
cs.SolverType = solver_type;
cs.SolverOptions.LogDecimation = every_steps_record;
% species need to record
num_species_total = length(model.Species);
for i = 1:num_species_total
    species_name_list{i} = model.Species(i).Name;
end
    num_spe_rec = length(species_name);
for i=1:num_spe_rec
    pos = find(ismember(species_name_list,char(species_name(i)))==1);
    rec(i)= model.Species(pos);
end
set (cs.RuntimeOptions, 'StatesToLog', rec);
set (cs.CompileOptions, 'DimensionalAnalysis', false);
y = cs;
end
```

C.4.4 plot_two_situation.m

```
function plot_two_situation(simObj_data1, simObj_data2)
% use to plot the figures for reversible and irreversible
% (or sic1 deleted and sic1 overexpressed) conditions
% e.g. plot_two_situation(simObj(1),simObj(2))
first_data = simObj_data1;
second_data = simObj_data2;
col_clb2 = 1;
col_mcm1p = 2;
col_swi5 = 3;
col_cdh1m11 = 4;
col_sic1 = 5;
col_trim5 = 6;
col_swi5p = 7;
col_swi5pp = 8;
col_trim2 = 9;

figure
```

```
subplot(1,2,1);
t_ode = first_data.Time;
x_ode = first_data.Data;
plot(t_ode,(x_ode(:,col_clb2)+ x_ode(:,col_trim2)),'y',...
     t_ode,x_ode(:,col_cdh1m11),'m',...
     t_ode,x_ode(:,col_sic1)+ x_ode(:,col_trim2)+ x_ode(:,col_trim5),'g',...
     t_ode,x_ode(:,col_swi5)+ x_ode(:,col_swi5p)+ x_ode(:,col_swi5pp),'b',...
     'LineWidth',2.5);
set(gca,'YLim',[0 2300]);
ax1 = gca;
ax2 = axes('Position',get(ax1,'Position'), 'YAxisLocation','right',...
           'Color','none', 'YColor','r');
hold on;
plot(t_ode,x_ode(:,col_mcm1p),'Color','r','Parent',ax2,'LineWidth',2.5);
set(ax1,'FontSize',11,'FontWeight','b');
set(ax2,'YLim',[0,20000],'FontSize',11,'FontWeight','b');
ylabel(ax2,'Mcm1p');

subplot(1,2,2);
t_ode = second_data.Time;
x_ode = second_data.Data;
plot(t_ode,(x_ode(:,col_clb2)+ x_ode(:,col_trim2)),'y',...
     t_ode,x_ode(:,col_cdh1m11),'m',...
     t_ode,x_ode(:,col_sic1)+ x_ode(:,col_trim2)+ x_ode(:,col_trim5),'g',...
     t_ode,x_ode(:,col_swi5)+ x_ode(:,col_swi5p)+ x_ode(:,col_swi5pp),'b',...
     'LineWidth',2.5);
set(gca,'YLim',[0 2000]);
set(gca,'YLim',[0 2300]);
ax1 = gca;
ax2 = axes('Position',get(ax1,'Position'),'YAxisLocation','right',...
           'Color','none','YColor','r');
hold on;
plot(t_ode,x_ode(:,col_mcm1p),'Color','r','Parent',ax2,'LineWidth',2.5);
set(ax1,'FontSize',11,'FontWeight','b');
set(ax2,'YLim',[0,20000],'FontSize',11,'FontWeight','b');
ylabel(ax2,'Mcm1p');
end
```

C.4.5 percentage_re_ir.m

```
function [x_irr,x_re] = percentage_re_ir(dataObj, num_sim, V, sic1T_pos)
% calculate % of reversible, irreversible of situations
% data_obj: is the ensemblerun simData object
% num_sim: number of simulations
% V: the cell volume used for the simulations
% sic1T_pos: integer array of colume positions for sic1, trim2, trim5 in data
% e.g. [x_irr,x_re,ir_x,re_x] = percentage_re_ir(simDataObj,100,2000,[5,6,9])
num_irr = 0;
num_re = 0;
thres = 0.5*V;
n = num_sim;
simD = dataObj;
pos = sic1T_pos;

for i=1:n
 if simD(i,1).Data(end,pos(1))+ simD(i,1).Data(end,pos(2))+...
    simD(i,1).Data(end,pos(3))>thres
    num_irr = num_irr+1;
  else
```

```
    num_re = num_re+1;
  end
end
x_irr = num_irr;
x_re = num_re;
end
```

C.4.6 distribution_3D.m

```
function distribution_3D(simu_dataObj, bin_interval)
% calculate the distribution of each species
% e.g distribution_3D(simDataObj,0:50:2000)
bin_inter = bin_interval;
sim_DataObj = simu_dataObj;
num_sim = length(sim_DataObj);
T_tag = sim_DataObj(1,1).Time;
n_tag_step = length(T_tag);

% find the colume number for the species in the original simDataobj().Data
col_clb2 = 1;
col_mcm1p = 2;
col_swi5 = 3;
col_cdh1m11 = 4;
col_sic1 = 5;
col_trim5 = 6;
col_swi5p = 7;
col_swi5pp = 8;
col_trim2 = 9;

% create n_tag_step*num_sim matrix for each species
clb2_matrix = (-100)*ones(n_tag_step,num_sim);
trim2_matrix = (-100)*ones(n_tag_step,num_sim);
mcm1p_matrix = (-100)*ones(n_tag_step,num_sim);
cdh1m11_matrix = (-100)*ones(n_tag_step,num_sim);
sic1_matrix = (-100)*ones(n_tag_step,num_sim);
trim5_matrix = (-100)*ones(n_tag_step,num_sim);
swi5_matrix = (-100)*ones(n_tag_step,num_sim);
swi5p_matrix = (-100)*ones(n_tag_step,num_sim);
swi5pp_matrix = (-100)*ones(n_tag_step,num_sim);

for i=1:num_sim
    clb2_matrix(:,i) = sim_DataObj(i,1).Data(:,col_clb2);
    trim2_matrix(:,i) = sim_DataObj(i,1).Data(:,col_trim2);
    mcm1p_matrix(:,i) = sim_DataObj(i,1).Data(:,col_mcm1p);
    cdh1m11_matrix(:,i) = sim_DataObj(i,1).Data(:,col_cdh1m11);
    sic1_matrix(:,i) = sim_DataObj(i,1).Data(:,col_sic1);
    trim5_matrix(:,i) = sim_DataObj(i,1).Data(:,col_trim5);
    swi5_matrix(:,i) = sim_DataObj(i,1).Data(:,col_swi5);
    swi5p_matrix(:,i) = sim_DataObj(i,1).Data(:,col_swi5p);
    swi5pp_matrix(:,i) = sim_DataObj(i,1).Data(:,col_swi5pp);
end

% initialized the frequency matrix
Clb2T_freq_matrix=(-100)*ones(n_tag_step,length(bin_inter));
Mcm1p_freq_matrix=(-100)*ones(n_tag_step,length(bin_inter));
Cdh1m11_freq_matrix=(-100)*ones(n_tag_step,length(bin_inter));
Sic1T_freq_matrix=(-100)*ones(n_tag_step,length(bin_inter));
Swi5ac_freq_matrix=(-100)*ones(n_tag_step,length(bin_inter));
```

```
% frequence matrix containing molecular number distribution at each time point
for i=1:n_tag_step
Clb2T_freq_matrix(i,:)=hist(clb2_matrix(i,:)+trim2_matrix(i,:),bin_interval);
Mcm1p_freq_matrix(i,:)=hist(mcm1p_matrix(i,:),bin_interval*10);
Cdh1m11_freq_matrix(i,:)=hist(cdh1m11_matrix(i,:),bin_interval);
Sic1T_freq_matrix(i,:)=hist(sic1_matrix(i,:)+trim2_matrix(i,:)+...
                       trim5_matrix(i,:),bin_interval);
Swi5ac_freq_matrix(i,:)=hist(swi5_matrix(i,:)+swi5p_matrix(i,:)+...
                        swi5pp_matrix(i,:),bin_interval);
end

figure
surf(T_tag,bin_interval,Clb2T_freq_matrix');
shading interp;
title('Clb2T Molecular Distribution');
xlabel('time (min)');
ylabel('number of molecules');
zlabel('number of simulations');
colormap hsv;
view(0,90);
figure
surf(T_tag,bin_interval,Sic1T_freq_matrix');
title('Sic1T Molecular Distribution');
xlabel('time (min)');
ylabel('number of molecules');
zlabel('number of simulations');
shading interp;
colormap hsv;
view(0,90);
end
```

C.4.7 average_population.m

```
function average_population(simu_dataObj)
% calculate the total trend of population of cells in the westblot in gel;
% the colume number of the specis has been fixed, if the simulation
% optionals are changed, the colume number of each species also need to change.

sim_DataObj = simu_dataObj;
num_sim = length(sim_DataObj);
T_tag = sim_DataObj(1,1).Time;
n_tag_step = length(T_tag);
% find the colume number for the species in the original simDataobj().Data
col_clb2 = 1;
col_mcm1p = 2;
col_swi5 = 3;
col_cdh1m11 = 4;
col_sic1 = 5;
col_trim5 = 6;
col_swi5p = 7;
col_swi5pp = 8;
col_trim2 = 9;

% create n_tag_step*num_sim matrix for each species
clb2_matrix = (-100)*ones(n_tag_step,num_sim);
trim2_matrix = (-100)*ones(n_tag_step,num_sim);
mcm1p_matrix = (-100)*ones(n_tag_step,num_sim);
cdh1m11_matrix = (-100)*ones(n_tag_step,num_sim);
sic1_matrix = (-100)*ones(n_tag_step,num_sim);
```

```
trim5_matrix = (-100)*ones(n_tag_step,num_sim);
swi5_matrix = (-100)*ones(n_tag_step,num_sim);
swi5p_matrix = (-100)*ones(n_tag_step,num_sim);
swi5pp_matrix = (-100)*ones(n_tag_step,num_sim);

for i=1:num_sim
    clb2_matrix(:,i) = sim_DataObj(i,1).Data(:,col_clb2);
    trim2_matrix(:,i) = sim_DataObj(i,1).Data(:,col_trim2);
    mcm1p_matrix(:,i) = sim_DataObj(i,1).Data(:,col_mcm1p);
    cdh1m11_matrix(:,i) = sim_DataObj(i,1).Data(:,col_cdh1m11);
    sic1_matrix(:,i) = sim_DataObj(i,1).Data(:,col_sic1);
    trim5_matrix(:,i) = sim_DataObj(i,1).Data(:,col_trim5);
    swi5_matrix(:,i) = sim_DataObj(i,1).Data(:,col_swi5);
    swi5p_matrix(:,i) = sim_DataObj(i,1).Data(:,col_swi5p);
    swi5pp_matrix(:,i) = sim_DataObj(i,1).Data(:,col_swi5pp);
end

% initialized the average array
Clb2T_ave=(-100)*ones(n_tag_step,1);
Mcm1p_ave=(-100)*ones(n_tag_step,1);
Cdh1m11_ave=(-100)*ones(n_tag_step,1);
Sic1T_ave=(-100)*ones(n_tag_step,1);
Swi5ac_ave=(-100)*ones(n_tag_step,1);

% construct the average array for the species at each time point
for i=1:n_tag_step
 Clb2T_ave(i) = mean(clb2_matrix(i,:)+trim2_matrix(i,:));
 Mcm1p_ave(i) = mean(mcm1p_matrix(i,:));
 Cdh1m11_ave(i) = mean(cdh1m11_matrix(i,:));
 Sic1T_ave(i) = mean(sic1_matrix(i,:)+ trim2_matrix(i,:)+ trim5_matrix (i,:));
 Swi5ac_ave(i) = mean(swi5_matrix(i,:)+ swi5p_matrix(i,:)+ swi5pp_matrix(i,:));
end

figure
plot(T_tag,Clb2T_ave,'y',T_tag,Cdh1m11_ave,'m',T_tag,Sic1T_ave,'g',...
     T_tag,Swi5ac_ave,'b','LineWidth',2.5);
set(gca,'YLim',[0 2000]);
set(gca,'XLim',[0 150],'FontSize',11,'FontWeight','b');
ylabel(gca,'Number of molecular number');
ax1 = gca;
ax2 = axes('Position',get(ax1,'Position'),'YAxisLocation','right',...
           'Color','none','YColor','r'); %[1,0.69,0.39]);
hold on;
plot(T_tag,Mcm1p_ave,'Color','r','Parent',ax2,'LineWidth',2.5); %[1,0.69,0.39]
set(ax2,'XLim',[0 150],'YLim',[0,20000],'FontSize',11,'FontWeight','b');
ylabel(ax2,'Mcm1p');
xlabel(ax2,'Time');
title('Simulate the Population of Cells');
end
```

C.4.8 all_simulation_figure.m

```
function all_simulation_figure(simDataObj,num_fig)
% e.g. all_simulation_figure(simDataObj,[10,10])
% plot the figures with subplot function
% num_fig: array about how many rows and how many columes you want to plot
sim_DataObj = simDataObj;
num = length(sim_DataObj);
size = num_fig;
```

```
row = size(1);
col = size(2);
% find the colume number for the species in the original simDataobj().Data
col_clb2 = 1;
col_mcm1p = 2;
col_swi5 = 3;
col_cdh1m11 = 4;
col_sic1 = 5;
col_trim5 = 6;
col_swi5p = 7;
col_swi5pp = 8;
col_trim2 = 9;
figure
title('Multiple simulations of population cells')
for i=1:num
subplot(row,col,i);
plot(simDataObj(i,1).Time,(simDataObj(i,1).Data(:,col_clb2)+...
    simDataObj(i,1).Data(:,col_trim2)),'b', simDataObj(i,1).Time,...
    simDataObj(i,1).Data(:,col_cdh1m11),'m', simDataObj(i,1).Time,...
   (simDataObj(i,1).Data(:,col_sic1)+ simDataObj(i,1).Data(:,col_trim2)+...
    simDataObj(i,1).Data(:,col_trim5)),'r', simDataObj(i,1).Time,...
    simDataObj(i,1).Data(:,col_swi5) + simDataObj(i,1).Data(:,col_swi5p)+...
    simDataObj(i,1).Data(:,col_swi5pp),'g','LineWidth',2);
set(gca,'YLim',[0 2000]);
set(gca,'XLim',[0 150]);
end
legend(gca,'Clb2T','Cdh1m11','Sic1T','Swi5\_ac','Location','EastOutside');
end
```

D Mitotic Exit in Mammalian Cells

D.1 XPP file for the CLE model

```
# this version is changed the noise term for each single reaction process
init MPFT=892.43, I0=10, I=0, PP=1.14, Wee=4.09, Cdc25=995.91, time=0
#  generating a series of normally distributed random numbers
wiener wm1, wm2, wm3, wm4, wp1, wp2, wp3, we1, we2, we3, wc1, wc2, wc3

F25a = k25'/V*(V - Cdc25)*pMPFT
F25b = k25"/V*Cdc25*pMPFT
Fweea = kwee'/V*(V - Wee) *MPFT
Fweeb = kwee"/V*Wee*MPFT
MPFT' = F25a+F25b-Fweea-Fweeb+(wm1*sqrt(F25a)+wm2*sqrt(F25b)\
        -wm3*sqrt(Fweea)-wm4*sqrt(Fweeb))
I0'= 0
I' = ktr*(V*I0 - I)
Fappa = kapp'/V*PP*(V - PP)
Fappb = kapp*(V - PP)
Fipp = kipp'/V*Mpf*PP
PP' = Fappa+Fappb-Fipp+(wp1*sqrt(Fappa)+wp2*sqrt(Fappb)-wp3*sqrt(Fipp))
Fawee = Vawee/V*PP*(V - wee)
Fiwea = Viwee*wee
Fiweb = Viwee'/V*Mpf*wee
wee' = Fawee-Fiwea-Fiweb+(we1*sqrt(Fawee)-we2*sqrt(Fiwea)-we3*sqrt(Fiweb))
Fa25a = Va25*(V - Cdc25)
Fa25b = Va25'/V*Mpf*(V - Cdc25)
Fi25 = Vi25/V*PP*Cdc25
```

```
Cdc25' = Fa25a+Fa25b-Fi25+(wc1*sqrt(Fa25a)+wc2*sqrt(Fa25b)-wc3*sqrt(Fi25))
time' = 1
MPF = MPFT*(Kd*V)/(Kd*V + I)
aux MPF = MPFT*(Kd*V)/(Kd*V + I)
pMPFT = V - MPFT
aux pMPFT = V - MPFT

global +1 {time-depriv} {I0=0}
global -1 {MPFT-0} {MPFT=1e-5*V}
global +1 {MPFT-V} {MPFT=(1-1e-5)*V}
global -1 {PP-0} {PP=1e-5*V}
global +1 {PP-V} {PP=(1-1e-5)*V}
global -1 {Wee-0} {Wee=1e-5*V}
global +1 {Wee-V} {Wee=(1-1e-5)*V}
global -1 {Cdc25-0} {Cdc25=1e-5*V}
global +1 {Cdc25-V} {Cdc25=(1-1e-5)*V}

p ktr=0.5, V=1000, Kd=1, kapp'=0.05, kapp=0.003, kipp'=3
p kwee'=0.5, kwee"=25, Vawee=1, Viwee=0.01, Viwee'=0.3
p k25'=0.03, k25"=5, Vi25=1, Va25=0.01, Va25'=0.3, depriv=30

@ TOTAL=120,METH=euler,XHI=120,YLO=0,YHI=1000,BOUND=1000000
@ seed=895643, maxstorage=1000000, dt=0.005
@ nplot=5,yp=MPF,yp2=pMPFT,yp3=wee,yp4=cdc25, yp5=PP
done
```

D.2 XPP file for plotting the bifurcation diagram in mammalian mitotic exit

```
Mpf' = k25*(CycT - Mpf - Trimi) - kwee*Mpf
I' = ktr*(I0 - I)
Trimi = CycT*I/(kdi/kai + I)
PP2' = (kapp2'*PP2 + kapp2)*(PP2T - PP2) - (kipp2'*Mpf + kipp2"*CycA)*PP2
Wee' = Vawee*PP2*(WeeT - Wee) - (Viwee + Viwee'*Mpf + Viwee"*CycA)*Wee
Cdc25' = (Va25 + Va25'*Mpf + Va25"*CycA)*(Cdc25T - Cdc25) - Vi25*PP2*Cdc25
k25 = k25'*(Cdc25T - Cdc25) + k25"*Cdc25
kwee = kwee'*(WeeT - Wee) + kwee"*Wee
p CycT=0, PP2T=1, weeT=1, Cdc25T=1, CycA=0, I0=0, ktr=0.5
p kapp2'=0.05, kapp2=0.003, kipp2'=3, kipp2"=1.5, kai=100, kdi=100
p kwee'=0.5, kwee"=25, Vawee=1, Viwee=0.01, Viwee'=0.3, Viwee"=0.25
p k25'=0.03, k25"=5, Vi25=1, Va25=0.01, Va25'=0.3, Va25"=0.25
done
```

D.3 The binding and unbinding reaction frequency between Mpf and I using the SSA

D.4 XPP file for the SSA model

```
init I0=10, I=0, tr=0
global 0 t {MpfT=flr(0.892*N);MpfpT=flr((1-0.892)*N);Wee1=flr(0.004*N)}
global 0 t {Wee1p=flr((1-0.004)*N); PP2Ai=flr((1-0.00114)*N)}
global 0 t {Cdc25=flr((1-0.995)*N);Cdc25p=flr(0.995*N);PP2Aa=flr(N*0.00114)}

p N=1000, Kd=1, kapp'=0.05, kapp=0.003, kipp'=3, kwee'=0.5, kwee"=25
p Vawee=1, Viwee=0.01, Viwee'=0.3, k25'=0.03, k25"=5, Vi25=1, Va25=0.01
p depriv=30, ktr=0.5, Va25'=0.3
```

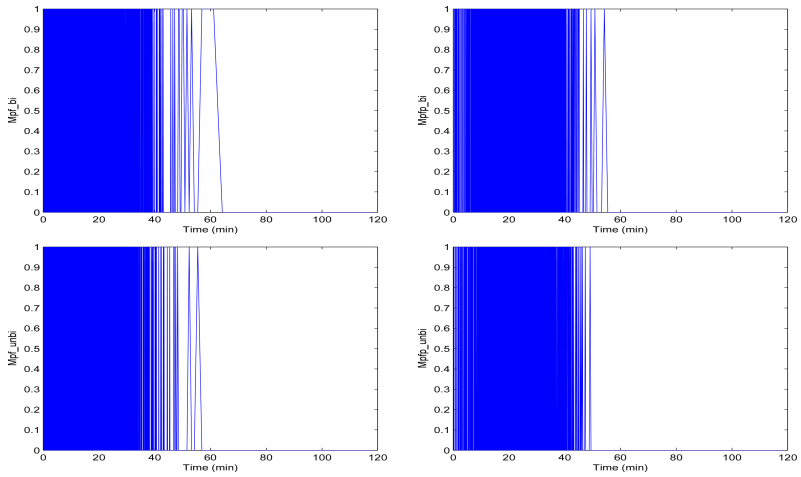

Figure 8.1: The binding and unbinding reaction frequencies between Mpf and I using the SSA approach without quasi-equilibrium assumption. Each vertical line presents each fired reaction once during the simulation. (A): frequency plot of binding reaction $Mpf + I \rightarrow IMpf$; (B): frequency plot of binding reaction $Mpfp + I \rightarrow IMpf$; (C): frequency plot of unbinding reaction $IMpf \rightarrow I + Mpf$; (D): frequency plot of unbinding reaction $IMpfp \rightarrow I + Mpfp$. The association and dissociation reactions between inhibitor and Mpf take place so frequently that they dramatically decrease the computational efficiency of the SSA simulation. Each binding or unbinding event is drawn as a vertical line along time series shown in a selected simulation example (Fig. 8.1). It is obvious from this figure that such association and dissociation reactions almost dominate all the fired reaction channels during first 40 minutes when inhibitor is present.

```
v1 = MpfT*Wee1*kwee"/N
v2 = v1 + MpfT*Wee1p*kwee'/N
v3 = v2 + MpfpT*Cdc25*k25'/N
v4 = v3 + MpfpT*Cdc25p*k25"/N
v5 = v4 + Cdc25*Mpf*Va25'/N
v6 = v5 + Cdc25*Va25
v7 = v6 + Cdc25p*PP2Aa*Vi25/N
v8 = v7 + Wee1*Mpf*Viwee'/N
v9 = v8 + Wee1*Viwee
v10 = v9 + Wee1p*PP2Aa*Vawee/N
v11 = v10 + PP2Ai*kapp
v12 = v11 + PP2Ai*PP2Aa*kapp'/N
v13 = v12 + PP2Aa*Mpf*kipp'/N
v14 = v13 + ktr*I0*N
v15 = v14 + I*ktr

s = ran(1)*v15
z1 = (s<v1)
z2 = (s<v2)&(s>=v1)
z3 = (s<v3)&(s>=v2)
z4 = (s<v4)&(s>=v3)
z5 = (s<v5)&(s>=v4)
z6 = (s<v6)&(s>=v5)
z7 = (s<v7)&(s>=v6)
z8 = (s<v8)&(s>=v7)
z9 = (s<v9)&(s>=v8)
z10 = (s<v10)&(s>=v9)
z11 = (s<v11)&(s>=v10)
z12 = (s<v12)&(s>=v11)
z13 = (s<v13)&(s>=v12)
```

```
z14 = (s<v14)&(s>=v13)
z15 = (s>v14)

I0' = I0
tr' = tr - log(ran(1))/v15
MpfT' = max(0, MpfT - z1 - z2 + z3 + z4)
MpfpT' = max(0, MpfpT + z1 + z2 - z3 - z4)
I' = max(0, I + z14 - z15)
Cdc25'= max(0, Cdc25 - z5 - z6 + z7)
Cdc25p'= max(0,Cdc25p + z5 + z6 - z7)
Wee1'= max(0,Wee1 - z8 - z9 + z10)
Wee1p'= max(0,Wee1p + z8 + z9 - z10)
PP2Aa'= max(0,PP2Aa + z11 + z12 - z13)
PP2Ai'= max(0,PP2Ai - z11 - z12 + z13)

Mpf = MpfT*(Kd*N)/(Kd*N + I)
aux Mpf_plot = flr(Mpf)
global 1 {tr-depriv} {I0=0; I=flr(I);MpfpT=flr(MpfpT);MpfT=flr(MpfT)}
global 1 {tr-depriv} {PP2Ai=flr(PP2Ai);Cdc25=flr(Cdc25);Cdc25p=flr(Cdc25p)}
global 1 {tr-depriv} {Wee1=flr(Wee1);Wee1p=flr(Wee1p);PP2Aa=flr(PP2Aa)}
global 1 {tr-121} {arret=1}

@ bound=100000000,meth=discrete,total=9000000,njmp=10000, seed=198676
@ nplot=5,xp=tr,yp=Mpf_plot,xp2=tr,yp2=MpfpT,xp3=tr,yp3=Wee1
@ xp4=tr,yp4=Cdc25p,xp5=tr,yp5=PP2Aa
@ xlo=0,ylo=0,xhi=120,yhi=1000,maxstor=100000
done
```

E Publications Related to the Subject of the D.Phil

- *Kapuy, O., He, E., López-Avilés, S., Uhlmann, F., Tyson, J. J., and Novák, B. (2009a). System-level feedbacks control cell cycle progression. FEBS Lett, 583 (24): 3992-3998.*

- *Kapuy, O., He, E., Uhlmann, F., and Novák, B. (2009b). Mitotic exit in mammalian cells. Mol Syst Biol, 5:324.*

- *He, E., Kapuy, O., Oliveira, R. A., Uhlmann, F., Tyson, J. J., and Novák, B. (2011). System-level feedbacks make the anaphase switch irreversible. Proc Natl Acad Sci U S A, 108 (24):10016-10021.*

Bibliography

Abrieu, A., Magnaghi-Jaulin, L., Kahana, J. A., Peter, M., Castro, A., Vigneron, S., Lorca, T., Cleveland, D. W., and Labb, J. C. (2001). Mps1 is a kinetochore-associated kinase essential for the vertebrate mitotic checkpoint. *Cell*, 106(1):83–93.

Alberghina, L., Hfer, T., and Vanoni, M. (2009). Molecular networks and system-level properties. *J Biotechnol*, 144(3):224–233.

Alberts, B., Johnson, A., Lewis, J., Raff, M., Roberts, K., and Walter, P. (2008). *Molecular Biology of the Cell (5th edition)*. Garland Science.

Alves, R., Antunes, F., and Salvador, A. (2006). Tools for kinetic modeling of biochemical networks. *Nat Biotechnol*, 24(6):667–672.

Antoni, A. D., Pearson, C. G., Cimini, D., Canman, J. C., Sala, V., Nezi, L., Mapelli, M., Sironi, L., Faretta, M., Salmon, E. D., and Musacchio, A. (2005). The Mad1/Mad2 complex as a template for Mad2 activation in the spindle assembly checkpoint. *Curr Biol*, 15(3):214–225.

Apweiler, R., Bairoch, A., Wu, C. H., Barker, W. C., Boeckmann, B., Ferro, S., Gasteiger, E., Huang, H., Lopez, R., Magrane, M., Martin, M. J., Natale, D. A., O'Donovan, C., Redaschi, N., and Yeh, L.-S. L. (2004). UniProt: the Universal Protein knowledgebase. *Nucleic Acids Res*, 32(Database issue):D115–D119.

Arkin, A., Ross, J., and McAdams, H. H. (1998). Stochastic kinetic analysis of developmental pathway bifurcation in phage lambda-infected Escherichia coli cells. *Genetics*, 149(4):1633–1648.

Ashburner, M., Ball, C. A., Blake, J. A., Botstein, D., Butler, H., Cherry, J. M., Davis, A. P., Dolinski, K., Dwight, S. S., Eppig, J. T., Harris, M. A., Hill, D. P., Issel-Tarver, L., Kasarskis, A., Lewis, S., Matese, J. C., Richardson, J. E., Ringwald, M., Rubin, G. M., and Sherlock, G. (2000). Gene ontology: tool for the unification of biology. The Gene Ontology Consortium. *Nat Genet*, 25(1):25–29.

Austin, D. W., Allen, M. S., McCollum, J. M., Dar, R. D., Wilgus, J. R., Sayler, G. S., Samatova, N. F., Cox, C. D., and Simpson, M. L. (2006). Gene network shaping of inherent noise spectra. *Nature*, 439(7076):608–611.

Balzsi, G., van Oudenaarden, A., and Collins, J. J. (2011). Cellular decision making and biological noise: from microbes to mammals. *Cell*, 144(6):910–925.

Beard, D. A. (2011). Simulation of cellular biochemical system kinetics. *Wiley Interdiscip Rev Syst Biol Med*, 3(2):136–146.

Becskei, A. and Serrano, L. (2000). Engineering stability in gene networks by autoregulation. *Nature*, 405(6786):590–593.

Becskei, A., Sraphin, B., and Serrano, L. (2001). Positive feedback in eukaryotic gene networks: cell differentiation by graded to binary response conversion. *EMBO J*, 20(10):2528–2535.

Blake, W. J., KAErn, M., Cantor, C. R., and Collins, J. J. (2003). Noise in eukaryotic gene expression. *Nature*, 422(6932):633–637.

Braunewell, S. and Bornholdt, S. (2007). Superstability of the yeast cell-cycle dynamics: ensuring causality in the presence of biochemical stochasticity. *J Theor Biol*, 245(4):638–643.

Brito, D. A. and Rieder, C. L. (2006). Mitotic checkpoint slippage in humans occurs via cyclin B destruction in the presence of an active checkpoint. *Curr Biol*, 16(12):1194–1200.

Brito, D. A., Yang, Z., and Rieder, C. L. (2008). Microtubules do not promote mitotic slippage when the spindle assembly checkpoint cannot be satisfied. *J Cell Biol*, 182(4):623–629.

Broek, D., Bartlett, R., Crawford, K., and Nurse, P. (1991). Involvement of p34cdc2 in establishing the dependency of S phase on mitosis. *Nature*, 349(6308):388–393.

Bruggeman, F. J., Blthgen, N., and Westerhoff, H. V. (2009). Noise management by molecular networks. *PLoS Comput Biol*, 5(9):e1000506.

Bruggeman, F. J., Hornberg, J. J., Boogerd, F. C., and Westerhoff, H. V. (2007). Introduction to systems biology. *EXS*, 97:1–19.

Cao, Y., Gillespie, D. T., and Petzold, L. R. (2005). Accelerated stochastic simulation of the stiff enzyme-substrate reaction. *J Chem Phys*, 123(14):144917.

Cao, Y., Gillespie, D. T., and Petzold, L. R. (2006). Efficient step size selection for the tau-leaping simulation method. *J Chem Phys*, 124(4):044109.

Chatterjee, A., Vlachos, D. G., and Katsoulakis, M. A. (2005). Binomial distribution based tau-leap accelerated stochastic simulation. *J Chem Phys*, 122(2):024112.

Cheeseman, I. M., Anderson, S., Jwa, M., Green, E. M., seog Kang, J., Yates, J. R., Chan, C. S. M., Drubin, D. G., and Barnes, G. (2002). Phospho-regulation of kinetochore-microtubule attachments by the Aurora kinase Ipl1p. *Cell*, 111(2):163–172.

Chen, K. C., Calzone, L., Csikasz-Nagy, A., Cross, F. R., Novák, B., and Tyson, J. J. (2004). Integrative analysis of cell cycle control in budding yeast. *Mol Biol Cell*, 15(8):3841–3862.

Cherry, J. M., Adler, C., Ball, C., Chervitz, S. A., Dwight, S. S., Hester, E. T., Jia, Y., Juvik, G., Roe, T., Schroeder, M., Weng, S., and Botstein, D. (1998). SGD: Saccharomyces Genome Database. *Nucleic Acids Res*, 26(1):73–79.

Cherry, J. M., Ball, C., Weng, S., Juvik, G., Schmidt, R., Adler, C., Dunn, B., Dwight, S., Riles, L., Mortimer, R. K., and Botstein, D. (1997). Genetic and physical maps of Saccharomyces cerevisiae. *Nature*, 387(6632 Suppl):67–73.

Ciliberto, A., Lukcs, A., Tth, A., Tyson, J. J., and Novk, B. (2005). Rewiring the exit from mitosis. *Cell Cycle*, 4(8):1107–1112.

Clarke, D. J. and Bachant, J. (2008). Kinetochore structure and spindle assembly checkpoint signaling in the budding yeast, Saccharomyces cerevisiae. *Front Biosci*, 13:6787–6819.

Clute, P. and Pines, J. (1999). Temporal and spatial control of cyclin B1 destruction in metaphase. *Nat Cell Biol*, 1(2):82–87.

Coffey, W., Kalmykov, Y. P., and Waldron, J. T. (2004). *The Langevin equation: with applications to stochastic problems in physics, chemistry, and electrical engineering (2nd Edition)*. World Scientific.

Cross, F. R., Archambault, V., Miller, M., and Klovstad, M. (2002). Testing a mathematical model of the yeast cell cycle. *Mol Biol Cell*, 13(1):52–70.

Csiksz-Nagy, A. and Mura, I. (2011). Role of mRNA Gestation and Senescence in Noise Reduction during the Cell Cycle. *Stud Health Technol Inform*, 162:236–243.

D'Angiolella, V., Mari, C., Nocera, D., Rametti, L., and Grieco, D. (2003). The spindle checkpoint requires cyclin-dependent kinase activity. *Genes Dev*, 17(20):2520–2525.

Davidson, C. J. and Surette, M. G. (2008). Individuality in bacteria. *Annu Rev Genet*, 42:253–268.

Degtyarenko, K., de Matos, P., Ennis, M., Hastings, J., Zbinden, M., McNaught, A., Alcntara, R., Darsow, M., Guedj, M., and Ashburner, M. (2008). ChEBI: a database and ontology for chemical entities of biological interest. *Nucleic Acids Res*, 36(Database issue):D344–D350.

Devault, A., Fesquet, D., Cavadore, J. C., Garrigues, A. M., Labb, J. C., Lorca, T., Picard, A., Philippe, M., and Dore, M. (1992). Cyclin A potentiates maturation-promoting factor activation in the early Xenopus embryo via inhibition of the tyrosine kinase that phosphorylates cdc2. *J Cell Biol*, 118(5):1109–1120.

Dirk P. Kroese, T. T. and Botev, Z. I. (2011). *Handbook of Monte Carlo Methods (Wiley Series in Probability and Statistics)*. Wiley; 1 edition.

Dobrzynski, M., Rodrguez, J. V., Kaandorp, J. A., and Blom, J. G. (2007). Computational methods for diffusion-influenced biochemical reactions. *Bioinformatics*, 23(15):1969–1977.

Doncic, A., Ben-Jacob, E., and Barkai, N. (2006). Noise resistance in the spindle assembly checkpoint. *Mol Syst Biol*, 2:2006.0027.

Doncic, A., Ben-Jacob, E., Einav, S., and Barkai, N. (2009). Reverse engineering of the spindle assembly checkpoint. *PLoS One*, 4(8):e6495.

Dunphy, W. G. (1994). The decision to enter mitosis. *Trends Cell Biol*, 4(6):202–207.

Elowitz, M. B., Levine, A. J., Siggia, E. D., and Swain, P. S. (2002). Stochastic gene expression in a single cell. *Science*, 297(5584):1183–1186.

Ermentrout, B. (2002). *Simulating, analyzing, and animating dynamical systems: a guide to XPPAUT for researchers and students*. Society for Industrial Mathematics; 1st edition.

Evans, T., Rosenthal, E. T., Youngblom, J., Distel, D., and Hunt, T. (1983). Cyclin: a protein specified by maternal mRNA in sea urchin eggs that is destroyed at each cleavage division. *Cell*, 33(2):389–396.

Fall, C. P., Eric S. Marland, J. M. W., and Tyson, J. J. (2002). *Computational cell biology*. Springer.

Fang, G. (2002). Checkpoint protein BubR1 acts synergistically with Mad2 to inhibit anaphase-promoting complex. *Mol Biol Cell*, 13(3):755–766.

Fang, G., Yu, H., and Kirschner, M. W. (1998). The checkpoint protein MAD2 and the mitotic regulator CDC20 form a ternary complex with the anaphase-promoting complex to control anaphase initiation. *Genes Dev*, 12(12):1871–1883.

Fang, X. and Zhang, P. (2011). Aneuploidy and tumorigenesis. *Semin Cell Dev Biol*, Mar 24:1–7.

Ferrell, J. E. (2002). Self-perpetuating states in signal transduction: positive feedback, double-negative feedback and bistability. *Curr Opin Cell Biol*, 14(2):140–148.

Ferrell, J. E. (2008). Feedback regulation of opposing enzymes generates robust, all-or-none bistable responses. *Curr Biol*, 18(6):R244–R245.

Foo, J., Leder, K., and Michor, F. (2011). Stochastic dynamics of cancer initiation. *Phys Biol*, 8(1):015002.

Frisa, P. S. and Jacobberger, J. W. (2009). Cell cycle-related cyclin b1 quantification. *PLoS One*, 4(9):e7064.

Fry, A. M. and Yamano, H. (2006). APC/C-mediated degradation in early mitosis: how to avoid spindle assembly checkpoint inhibition. *Cell Cycle*, 5(14):1487–1491.

Futcher, B. (1996). Cyclins and the wiring of the yeast cell cycle. *Yeast*, 12(16):1635–1646.

Futcher, B. (2002). Transcriptional regulatory networks and the yeast cell cycle. *Curr Opin Cell Biol*, 14(6):676–683.

Ghaemmaghami, S., Huh, W. K., Bower, K., Howson, R. W., Belle, A., Dephoure, N., O'Shea, E. K., and Weissman, J. S. (2003). Global analysis of protein expression in yeast. *Nature*, 425(6959):737–741.

Ghosh, B., Karmakar, R., and Bose, I. (2005). Noise characteristics of feed forward loops. *Phys Biol*, 2(1):36–45.

Gibson, M. A. and Bruck, J. (2000). Efficient Exact Stochastic Simulation of Chemical Systems with Many Species and Many Channels. *J. Phys. Chem. A*, 104 (9):pp 18761889.

Gillespie, D. T. (1976). A general method for numerically simulating the stochastic time evolution of coupled chemical reactions. *Journal of Computational Physics*, 22:403–434.

Gillespie, D. T. (1977). Exact stochastic simulation of coupled chemical reactions. *J phys.chem*, 81(25):23402361.

Gillespie, D. T. (1992). A rigorous derivation of the chemical master equation. *Physica A Statistical Mechanics and its Applications,*, Vol. 188:404–425.

Gillespie, D. T. (2000). The chemial Langevin equation. *Journal of chemical physics*, 113:297–306.

Gillespie, D. T. (2007). Stochastic simulation of chemical kinetics. *Annu Rev Phys Chem*, 58:35–55.

Gillespie, D. T. (2009). Deterministic Limit of Stochastic Chemical Kinetics. *J. Phys. Chem. B*, 113 (6):16401644.

Goldbeter, A. and Koshland, D. E. J. (1981). An amplified sensitivity arising from covalent modification in biological systems. *Proc Natl Acad Sci U S A*, 78(11):6840–6844.

Goss, P. J. and Peccoud, J. (1998). Quantitative modeling of stochastic systems in molecular biology by using stochastic Petri nets. *Proc Natl Acad Sci U S A*, 95(12):6750–6755.

Grima, R. and Schnell, S. (2008). Modelling reaction kinetics inside cells. *Essays Biochem*, 45:41–56.

Haas, P. J. (2010). *Stochastic Petri Nets: Modelling, Stability, Simulation (Springer Series in Operations Research and Financial Engineering)*. Springer.

Hagting, A., Elzen, N. D., Vodermaier, H. C., Waizenegger, I. C., Peters, J.-M., and Pines, J. (2002). Human securin proteolysis is controlled by the spindle checkpoint and reveals when the APC/C switches from activation by Cdc20 to Cdh1. *J Cell Biol*, 157(7):1125–1137.

Harper, J. W., Burton, J. L., and Solomon, M. J. (2002). The anaphase-promoting complex: it's not just for mitosis any more. *Genes Dev*, 16(17):2179–2206.

Hartwell, L. H. and Weinert, T. A. (1989). Checkpoints: controls that ensure the order of cell cycle events. *Science*, 246(4930):629–634.

Hasty, J., Pradines, J., Dolnik, M., and Collins, J. J. (2000). Noise-based switches and amplifiers for gene expression. *Proc Natl Acad Sci U S A*, 97(5):2075–2080.

He, E., Kapuy, O., Oliveira, R. A., Uhlmann, F., Tyson, J. J., and Novák, B. (2011). System-level feedbacks make the anaphase switch irreversible. *Proc Natl Acad Sci U S A*, 108(24):10016–10021.

Held, M., Schmitz, M. H. A., Fischer, B., Walter, T., Neumann, B., Olma, M. H., Peter, M., Ellenberg, J., and Gerlich, D. W. (2010). CellCognition: time-resolved phenotype annotation in high-throughput live cell imaging. *Nat Methods*, 7(9):747–754.

Herskowitz, I. (1988). Life cycle of the budding yeast Saccharomyces cerevisiae. *Microbiol Rev*, 52(4):536–553.

Holt, L. J., Krutchinsky, A. N., and Morgan, D. O. (2008). Positive feedback sharpens the anaphase switch. *Nature*, 454(7202):353–357.

Howell, B. J., Hoffman, D. B., Fang, G., Murray, A. W., and Salmon, E. D. (2000). Visualization of Mad2 dynamics at kinetochores, along spindle fibers, and at spindle poles in living cells. *J Cell Biol*, 150(6):1233–1250.

Huang, H.-C., Mitchison, T. J., and Shi, J. (2010). Stochastic competition between mechanistically independent slippage and death pathways determines cell fate during mitotic arrest. *PLoS One*, 5(12):e15724.

Huh, D. and Paulsson, J. (2011). Non-genetic heterogeneity from stochastic partitioning at cell division. *Nat Genet*, 43(2):95–100.

Iain M Cheeseman, D. G. D. and Barnes, G. (2002). Simple centromere, complex kinetochore: linking spindle microtubules and centromeric DNA in budding yeast. *J Cell Biol*, 157(2):199–203.

Ibrahim, B., Diekmann, S., Schmitt, E., and Dittrich, P. (2008). In-silico modeling of the mitotic spindle assembly checkpoint. *PLoS One*, 3(2):e1555.

Ibrahim, B., Dittrich, P., Diekmann, S., and Schmitt, E. (2007). Stochastic effects in a compartmental model for mitotic checkpoint regulation. *J. Integrative Bioinformatics*, 4(3):66.

Irniger, S. (2002). Cyclin destruction in mitosis: a crucial task of Cdc20. *FEBS Lett*, 532(1-2):7–11.

Jaspersen, S. L., Charles, J. F., and Morgan, D. O. (1999). Inhibitory phosphorylation of the APC regulator Hct1 is controlled by the kinase Cdc28 and the phosphatase Cdc14. *Curr Biol*, 9(5):227–236.

Jaspersen, S. L., Charles, J. F., Tinker-Kulberg, R. L., and Morgan, D. O. (1998). A late mitotic regulatory network controlling cyclin destruction in Saccharomyces cerevisiae. *Mol Biol Cell*, 9(10):2803–2817.

Johnson, K. A. and Goody, R. S. (2011). The original michaelis constant: translation of the 1913 michaelis-menten paper. *Biochemistry*, 50(39):8264–8269.

Jorgensen, P. and Tyers, M. (2004). How cells coordinate growth and division. *Curr Biol*, 14(23):R1014–R1027.

Kaern, M., Elston, T. C., Blake, W. J., and Collins, J. J. (2005). Stochasticity in gene expression: from theories to phenotypes. *Nat Rev Genet*, 6(6):451–464.

Kampen, N. V. (2007). *Stochastic Processes in Physics and Chemistry, Third Edition (North-Holland Personal Library)*. North Holland.

Kapuy, O., Barik, D., Sananes, M. R. D., Tyson, J. J., and Novk, B. (2009a). Bistability by multiple phosphorylation of regulatory proteins. *Prog Biophys Mol Biol*, 100(1-3):47–56.

Kapuy, O., He, E., López-Avilés, S., Uhlmann, F., Tyson, J. J., and Novák, B. (2009b). System-level feedbacks control cell cycle progression. *FEBS Lett*, 583(24):3992–3998.

Kapuy, O., He, E., Uhlmann, F., and Novák, B. (2009c). Mitotic exit in mammalian cells. *Mol Syst Biol*, 5:324.

Kar, S., Baumann, W. T., Paul, M. R., and Tyson, J. J. (2009). Special Feature: Exploring the roles of noise in the eukaryotic cell cycle. *Proc Natl Acad Sci U S A*, vol. 106(16):6471–6477.

Kienitz, A., Vogel, C., Morales, I., Mller, R., and Bastians, H. (2005). Partial downregulation of MAD1 causes spindle checkpoint inactivation and aneuploidy, but does not confer resistance towards taxol. *Oncogene*, 24(26):4301–4310.

Kops, G. J. P. L., Weaver, B. A. A., and Cleveland, D. W. (2005). On the road to cancer: aneuploidy and the mitotic checkpoint. *Nat Rev Cancer*, 5(10):773–785.

Kuthan, H. (2005). Temporal fluctuation of nuclear pore complex localization by single diffusing mRNP complexes. *J Theor Biol*, 236(3):256–262.

Lad, L., Lichtsteiner, S., Hartman, J. J., Wood, K. W., and Sakowicz, R. (2009). Kinetic analysis of Mad2-Cdc20 formation: conformational changes in Mad2 are catalyzed by a C-Mad2-ligand complex. *Biochemistry*, 48(40):9503–9515.

Lampson, M. A., Renduchitala, K., Khodjakov, A., and Kapoor, T. M. (2004). Correcting improper chromosome-spindle attachments during cell division. *Nat Cell Biol*, 6(3):232–237.

Lee, M. G. and Nurse, P. (1987). Complementation used to clone a human homologue of the fission yeast cell cycle control gene cdc2. *Nature*, 327(6117):31–35.

Lee, T. I., Rinaldi, N. J., Robert, F., Odom, D. T., Bar-Joseph, Z., Gerber, G. K., Hannett, N. M., Harbison, C. T., Thompson, C. M., Simon, I., Zeitlinger, J., Jennings, E. G., Murray, H. L., Gordon, D. B., Ren, B., Wyrick, J. J., Tagne, J.-B., Volkert, T. L., Fraenkel, E., Gifford, D. K., and Young, R. A. (2002). Transcriptional regulatory networks in Saccharomyces

cerevisiae. *Science*, 298(5594):799–804.

Lew, D. J. (2000). Cell-cycle checkpoints that ensure coordination between nuclear and cytoplasmic events in Saccharomyces cerevisiae. *Curr Opin Genet Dev*, 10(1):47–53.

Lew, D. J. and Burke, D. J. (2003). The spindle assembly and spindle position checkpoints. *Annu Rev Genet*, 37:251–282.

Li, F., Long, T., Lu, Y., Ouyang, Q., and Tang, C. (2004). The yeast cell-cycle network is robustly designed. *Proc Natl Acad Sci U S A*, 101(14):4781–4786.

Li, X. and Nicklas, R. B. (1995). Mitotic forces control a cell-cycle checkpoint. *Nature*, 373(6515):630–632.

Lodish, H., Berk, A., Zipursky, L., Matsudaira, P., Baltimore, D., and Darnell, J. (2004). *Molecular Cell Biology*. W.H. Freeman and Company (4th edition).

López-Avilés, S., Kapuy, O., Novák, B., and Uhlmann, F. (2009). Irreversibility of mitotic exit is the consequence of systems-level feedback. *Nature*, 459(7246):592–595.

Losick, R. and Desplan, C. (2008). Stochasticity and cell fate. *Science*, 320(5872):65–68.

Lukas, J., Lukas, C., and Bartek, J. (2004). Mammalian cell cycle checkpoints: signalling pathways and their organization in space and time. *DNA Repair (Amst)*, 3(8-9):997–1007.

Lund, E. W. (1965). Guldberg and Waage and the law of mass action. *J. Chem. Educ.*, 42 (10):548–550.

Luo, X., Tang, Z., Rizo, J., and Yu, H. (2002). The Mad2 spindle checkpoint protein undergoes similar major conformational changes upon binding to either Mad1 or Cdc20. *Mol Cell*, 9(1):59–71.

Luo, X., Tang, Z., Xia, G., Wassmann, K., Matsumoto, T., Rizo, J., and Yu, H. (2004). The Mad2 spindle checkpoint protein has two distinct natively folded states. *Nat Struct Mol Biol*, 11(4):338–345.

Lydall, D., Ammerer, G., and Nasmyth, K. (1991). A new role for MCM1 in yeast: cell cycle regulation of SW15 transcription. *Genes Dev*, 5(12B):2405–2419.

Macnamara, S., Bersani, A. M., Burrage, K., and Sidje, R. B. (2008). Stochastic chemical kinetics and the total quasi-steady-state assumption: application to the stochastic simulation algorithm and chemical master equation. *J Chem Phys*, 129(9):095105.

Maiato, H., DeLuca, J., Salmon, E. D., and Earnshaw, W. C. (2004). The dynamic kinetochore-microtubule interface. *J Cell Sci*, 117(Pt 23):5461–5477.

Mangan, S. and Alon, U. (2003). Structure and function of the feed-forward loop network motif. *Proc Natl Acad Sci U S A*, 100(21):11980–11985.

Mangan, S., Zaslaver, A., and Alon, U. (2003). The coherent feedforward loop serves as a sign-sensitive delay element in transcription networks. *J Mol Biol*, 334(2):197–204.

Mapelli, M., Massimiliano, L., Santaguida, S., and Musacchio, A. (2007). The Mad2 conformational dimer: structure and implications for the spindle assembly checkpoint. *Cell*, 131(4):730–743.

Marsan, M. A. (1989). Stochastic petri nets: An elementary introduction. In *In Advances in Petri Nets*, pages 1–29. Springer.

McAdams, H. H. and Arkin, A. (1999). It's a noisy business! Genetic regulation at the nanomolar scale. *Trends Genet*, 15(2):65–69.

McQuarrie, D. A. (1967). Stochastic Approach to Chemical Kinetics. *Journal of Applied Probability*, Vol. 4, No. 3:413–478.

Meraldi, P., Draviam, V. M., and Sorger, P. K. (2004). Timing and checkpoints in the regulation of mitotic progression. *Dev Cell*, 7(1):45–60.

Michaelis, L. and Menten, M. L. (1913). Die Kinetik der Invertinwirkung. *Biochemische Zeitschrift*, page 333 369.

Minshull, J., Pines, J., Golsteyn, R., Standart, N., Mackie, S., Colman, A., Blow, J., Ruderman, J. V., Wu, M., and Hunt, T. (1989). The role of cyclin synthesis, modification and destruction in the control of cell division. *J Cell Sci Suppl*, 12:77–97.

Mirchenko, L. and Uhlmann, F. (2010). Sli15(INCENP) dephosphorylation prevents mitotic checkpoint reengagement due to loss of tension at anaphase onset. *Curr Biol*, 20(15):1396–1401.

Mistry, H. B., MacCallum, D. E., Jackson, R. C., Chaplain, M. A. J., and Davidson, F. A. (2008). Modeling the temporal evolution of the spindle assembly checkpoint and role of Aurora B kinase. *Proc Natl Acad Sci U S A*, 105(51):20215–20220.

Mitrophanov, A. Y. and Groisman, E. A. (2008). Positive feedback in cellular control systems. *Bioessays*, 30(6):542–555.

Mochida, S. and Hunt, T. (2007). Calcineurin is required to release Xenopus egg extracts from meiotic M phase. *Nature*, 449(7160):336–340.

Mochida, S., Ikeo, S., Gannon, J., and Hunt, T. (2009). Regulated activity of PP2A-B55 delta is crucial for controlling entry into and exit from mitosis in Xenopus egg extracts. *EMBO J*, 28(18):2777–2785.

Moll, T., Tebb, G., Surana, U., Robitsch, H., and Nasmyth, K. (1991). The role of phosphorylation and the CDC28 protein kinase in cell cycle-regulated nuclear import of the S. cerevisiae transcription factor SWI5. *Cell*, 66(4):743–758.

Morgan, D. O. (1997). Cyclin-dependent kinases: engines, clocks, and microprocessors. *Annu Rev Cell Dev Biol*, 13:261–291.

Morgan, D. O. (2007). *The Cell Cycle: Principles of Control*. Oxford University Press and Sinauer Associates.

Mura, I. and Csiksz-Nagy, A. (2008). Stochastic Petri Net extension of a yeast cell cycle model. *J Theor Biol*, 254(4):850–860.

Murakami, H. and Nurse, P. (2000). DNA replication and damage checkpoints and meiotic cell cycle controls in the fission and budding yeasts. *Biochem J*, 349(Pt 1):1–12.

Murray, A. W. (1992). Creative blocks: cell-cycle checkpoints and feedback controls. *Nature*, 359(6396):599–604.

Musacchio, A. and Salmon, E. D. (2007). The spindle-assembly checkpoint in space and time. *Nat Rev Mol Cell Biol*, 8(5):379–393v.

Nasmyth, K. (1993). Control of the yeast cell cycle by the Cdc28 protein kinase. *Curr Opin Cell Biol*, 5(2):166–179.

Newman, J. R. S., Ghaemmaghami, S., Ihmels, J., Breslow, D. K., Noble, M., DeRisi, J. L., and Weissman, J. S. (2006). Single-cell proteomic analysis of S. cerevisiae reveals the architecture of biological noise. *Nature*, 441(7095):840–846.

Novák, B., Csikasz-Nagy, A., Gyorffy, B., Nasmyth, K., and Tyson, J. J. (1998). Model scenarios for evolution of the eukaryotic cell cycle. *Philos Trans R Soc Lond B Biol Sci*, 353(1378):2063–2076.

Novák, B. and Tyson, J. J. (1993). Numerical analysis of a comprehensive model of M-phase control in Xenopus oocyte extracts and intact embryos. *J Cell Sci*, 106 (Pt 4):1153–1168.

Novák, B. and Tyson, J. J. (1997). Modeling the control of DNA replication in fission yeast. *Proc Natl Acad Sci U S A*, 94(17):9147–9152.

Novák, B., Tyson, J. J., Gyorffy, B., and Csikasz-Nagy, A. (2007). Irreversible cell-cycle transitions are due to systems-level feedback. *Nat Cell Biol*, 9(7):724–728.

Novák, B., Vinod, P. K., Freire, P., and Kapuy, O. (2010). Systems-level feedback in cell-cycle control. *Biochem Soc Trans*, 38(5):1242–1246.

Novick, A. and Weiner, M. (1957). ENZYME INDUCTION AS AN ALL-OR-NONE PHENOMENON. *Proc Natl Acad Sci U S A*, 43(7):553–566.

Nurse, P. (1990). Universal control mechanism regulating onset of M-phase. *Nature*, 344(6266):503–508.

Okabe, Y. and Sasai, M. (2007). Stable stochastic dynamics in yeast cell cycle. *Biophys J*, 93(10):3451–3459.

Oksendal, B. (2007). *Stochastic Differential Equations: An Introduction with Applications*. Springer.

Oliveira, R. A., Hamilton, R. S., Pauli, A., Davis, I., and Nasmyth, K. (2010). Cohesin cleavage and Cdk inhibition trigger formation of daughter nuclei. *Nat Cell Biol*, 12(2):185–192.

Parry, D. H., Hickson, G. R. X., and O'Farrell, P. H. (2003). Cyclin B destruction triggers changes in kinetochore behavior essential for successful anaphase. *Curr Biol*, 13(8):647–653.

Paulsson, J. (2004). Summing up the noise in gene networks. *Nature*, 427(6973):415–418.

Pedraza, J. M. and Paulsson, J. (2008). Effects of molecular memory and bursting on fluctuations in gene expression. *Science*, 319(5861):339–343.

Pines, J. (2011). Cubism and the cell cycle: the many faces of the APC/C. *Nat Rev Mol Cell Biol*, 12(7):427–438.

Pomerening, J. R. (2008). Uncovering mechanisms of bistability in biological systems. *Curr Opin Biotechnol*, 19(4):381–388.

Pomerening, J. R. (2009). Positive-feedback loops in cell cycle progression. *FEBS Lett*, 583(21):3388–3396.

Pomerening, J. R., Kim, S. Y., and Ferrell, J. E. (2005). Systems-level dissection of the cell-cycle oscillator: bypassing positive feedback produces damped oscillations. *Cell*, 122(4):565–578.

Pomerening, J. R., Sontag, E. D., and Ferrell, J. E. (2003). Building a cell cycle oscillator: hysteresis and bistability in the activation of Cdc2. *Nat Cell Biol*, 5(4):346–351.

Potapova, T. A., Daum, J. R., Byrd, K. S., and Gorbsky, G. J. (2009). Fine tuning the cell cycle: activation of the Cdk1 inhibitory phosphorylation pathway during mitotic exit. *Mol Biol Cell*, 20(6):1737–1748.

Potapova, T. A., Daum, J. R., Pittman, B. D., Hudson, J. R., Jones, T. N., Satinover, D. L., Stukenberg, P. T., and Gorbsky, G. J. (2006). The reversibility of mitotic exit in vertebrate cells. *Nature*, 440(7086):954–958.

Queralt, E., Lehane, C., Novák, B., and Uhlmann, F. (2006). Downregulation of PP2A(Cdc55) phosphatase by separase initiates mitotic exit in budding yeast. *Cell*, 125(4):719–732.

Rao, C. V., Wolf, D. M., and Arkin, A. P. (2002). Control, exploitation and tolerance of intracellular noise. *Nature*, 420(6912):231–237.

Raser, J. M. and O'Shea, E. K. (2004). Control of stochasticity in eukaryotic gene expression. *Science*, 304(5678):1811–1814.

Raser, J. M. and O'Shea, E. K. (2005). Noise in gene expression: origins, consequences, and control. *Science*, 309(5743):2010–2013.

Reddy, G. P. (1994). Cell cycle: regulatory events in G1–¿S transition of mammalian cells. *J Cell Biochem*, 54(4):379–386.

Reddy, S. K., Rape, M., Margansky, W. A., and Kirschner, M. W. (2007). Ubiquitination by the anaphase-promoting complex drives spindle checkpoint inactivation. *Nature*, 446(7138):921–925.

Resat, H., Petzold, L., and Pettigrew, M. F. (2009). Kinetic modeling of biological systems. *Methods Mol Biol*, 541:311–335.

Rieder, C. L. (2010). Mitosis in vertebrates: the G2/M and M/A transitions and their associated checkpoints. *Chromosome Res*, 19:291–306.

Rieder, C. L., Cole, R. W., Khodjakov, A., and Sluder, G. (1995). The checkpoint delaying anaphase in response to chromosome monoorientation is mediated by an inhibitory signal produced by unattached kinetochores. *J Cell Biol*, 130(4):941–948.

Rieder, C. L., Schultz, A., Cole, R., and Sluder, G. (1994). Anaphase onset in vertebrate somatic cells is controlled by a checkpoint that monitors sister kinetochore attachment to the spindle. *J Cell Biol*, 127(5):1301–1310.

Robinson, J. C. (2004). *An Introduction to Ordinary Differential Equations*. Cambridge University Press.

Salis, H. and Kaznessis, Y. (2005). Accurate hybrid stochastic simulation of a system of coupled chemical or biochemical reactions. *J Chem Phys*, 122(5):54103.

Salwinski, L. and Eisenberg, D. (2004). In silico simulation of biological network dynamics. *Nat Biotechnol*, 22(8):1017–1019.

Sauro, H. M. (2009). Network dynamics. *Methods Mol Biol*, 541:269.

Schafer, K. A. (1998). The cell cycle: a review. *Vet Pathol*, 35(6):461–478.

Schwob, E. and Nasmyth, K. (1993). CLB5 and CLB6, a new pair of B cyclins involved in DNA replication in Saccharomyces cerevisiae. *Genes Dev*, 7(7A):1160–1175.

Sear, R. P. and Howard, M. (2006). Modeling dual pathways for the metazoan spindle assembly checkpoint. *Proc Natl Acad Sci U S A*, 103(45):16758–16763.

Sha, W., Moore, J., Chen, K., Lassaletta, A. D., Yi, C.-S., Tyson, J. J., and Sible, J. C. (2003). Hysteresis drives cell-cycle transitions in Xenopus laevis egg extracts. *Proc Natl Acad Sci U S A*, 100(3):975–980.

Shanbhag, D. N. and Rao, C. R., editors (2003). *Stochastic processes: modelling and simulation*. Elsevier Science Ltd.

Sherr, C. J. and Roberts, J. M. (1999). CDK inhibitors: positive and negative regulators of G1-phase progression. *Genes Dev*, 13(12):1501–1512.

Shmulevich, I., Dougherty, E. R., Kim, S., and Zhang, W. (2002). Probabilistic Boolean Networks: a rule-based uncertainty model for gene regulatory networks. *Bioinformatics*, 18(2):261–274.

Sible, J. C. and Tyson, J. J. (2007). Mathematical modeling as a tool for investigating cell cycle control networks. *Methods*, 41(2):238–247.

Simonetta, M., Manzoni, R., Mosca, R., Mapelli, M., Massimiliano, L., Vink, M., Novák, B., Musacchio, A., and Ciliberto, A. (2009). The influence of catalysis on mad2 activation dynamics. *PLoS Biol*, 7(1):e10.

Simpson, M. L., Cox, C. D., Allen, M. S., McCollum, J. M., Dar, R. D., Karig, D. K., and Cooke, J. F. (2009). Noise in biological circuits. *Wiley Interdiscip Rev Nanomed Nanobiotechnol*, 1(2):214–225.

Sironi, L., Mapelli, M., Knapp, S., Antoni, A. D., Jeang, K.-T., and Musacchio, A. (2002). Crystal structure of the tetrameric Mad1-Mad2 core complex: implications of a 'safety belt' binding mechanism for the spindle checkpoint. *EMBO J*, 21(10):2496–2506.

Sironi, L., Melixetian, M., Faretta, M., Prosperini, E., Helin, K., and Musacchio, A. (2001). Mad2 binding to Mad1 and Cdc20, rather than oligomerization, is required for the spindle checkpoint. *EMBO J*, 20(22):6371–6382.

Skommer, J., Raychaudhuri, S., and Wlodkowic, D. (2011). Timing is everything: stochastic origins of cell-to-cell variability in cancer cell death. *Front Biosci*, 16:307–314.

Smith, J. A. and Martin, L. (1973). Do cells cycle? *Proc Natl Acad Sci U S A*, 70(4):1263–1267.

Smith, J. R. and Whitney, R. G. (1980). Intraclonal variation in proliferative potential of human diploid fibroblasts: stochastic mechanism for cellular aging. *Science*, 207(4426):82–84.

Solomon, M. J., Glotzer, M., Lee, T. H., Philippe, M., and Kirschner, M. W. (1990). Cyclin activation of p34cdc2. *Cell*, 63(5):1013–1024.

Sotillo, R., Hernando, E., Daz-Rodrguez, E., Teruya-Feldstein, J., Cordn-Cardo, C., Lowe, S. W., and Benezra, R. (2007). Mad2 overexpression promotes aneuploidy and tumorigenesis in mice. *Cancer Cell*, 11(1):9–23.

Spellman, P. T., Sherlock, G., Zhang, M. Q., Iyer, V. R., Anders, K., Eisen, M. B., Brown, P. O., Botstein, D., and Futcher, B. (1998). Comprehensive identification of cell cycle-regulated genes of the yeast Saccharomyces cerevisiae by microarray hybridization. *Mol Biol Cell*, 9(12):3273–3297.

Stemmann, O., Zou, H., Gerber, S. A., Gygi, S. P., and Kirschner, M. W. (2001). Dual inhibition of sister chromatid separation at metaphase. *Cell*, 107(6):715–726.

Steuer, R. (2004). Effects of stochasticity in models of the cell cycle: from quantized cycle times to noise-induced oscillations. *J Theor Biol*, 228(3):293–301.

Strogatz, S. H. (1994). *Nonlinear dynamics and chaos: with applications to physics, biology, chemistry, and engineering*. Perseus Books Publishiing LLC.

Sullivan, M. and Morgan, D. O. (2007). Finishing mitosis, one step at a time. *Nat Rev Mol Cell Biol*, 8(11):894–903.

Sullivan, M. and Uhlmann, F. (2003). A non-proteolytic function of separase links the onset of anaphase to mitotic exit. *Nat Cell Biol*, 5(3):249–254.

Sveiczer, A., Novák, B., and Mitchison, J. M. (1996). The size control of fission yeast revisited. *J Cell Sci*, 109 (Pt 12):2947–2957.

Swain, P. S., Elowitz, M. B., and Siggia, E. D. (2002). Intrinsic and extrinsic contributions to stochasticity in gene expression. *Proc Natl Acad Sci U S A*, 99(20):12795–12800.

Takahashi, K., Tanase-Nicola, S., and ten Wolde, P. R. (2010). Spatio-temporal correlations can drastically change the response of a MAPK pathway. *Proc Natl Acad Sci U S A*, 107(6):2473–2478.

Tanaka, T. U. (2010). Kinetochore-microtubule interactions: steps towards bi-orientation. *EMBO J*, 29(24):4070–4082.

Tang, Z., Bharadwaj, R., Li, B., and Yu, H. (2001). Mad2-Independent inhibition of APCCdc20 by the mitotic checkpoint protein BubR1. *Dev Cell*, 1(2):227–237.

Tighe, A., Johnson, V. L., Albertella, M., and Taylor, S. S. (2001). Aneuploid colon cancer cells have a robust spindle checkpoint. *EMBO Rep*, 2(7):609–614.

Tom, E. and Schulman, K. A. (1997). Mathematical models in decision analysis. *Infect Control Hosp Epidemiol*, 18(1):65–73.

Toni, T., Jovanovic, G., Huvet, M., Buck, M., and Stumpf, M. P. H. (2011). From qualitative data to quantitative models: analysis of the phage shock protein stress response in Escherichia coli. *BMC Syst Biol*, 5:69.

Tyson, J. J., Chen, K., and Novák, B. (2001). Network dynamics and cell physiology. *Nat Rev Mol Cell Biol*, 2(12):908–916.

Tyson, J. J., Chen, K. C., and Novák, B. (2003). Sniffers, buzzers, toggles and blinkers: dynamics of regulatory and signaling pathways in the cell. *Curr Opin Cell Biol*, 15(2):221–231.

Tyson, J. J. and Novák, B. (2001). Regulation of the eukaryotic cell cycle: molecular antagonism, hysteresis, and irreversible transitions. *J Theor Biol*, 210(2):249–263.

Tyson, J. J. and Novák, B. (2008). Temporal organization of the cell cycle. *Curr Biol*, 18(17):R759–R768.

Tyson, J. J., Novák, B., Chen, K., and Val, J. (1995). Checkpoints in the cell cycle from a modeler's perspective. *Prog Cell Cycle Res*, 1:1–8.

Ullah, M., Schmidt, H., Cho, K. H., and Wolkenhauer, O. (2006). Deterministic modelling and stochastic simulation of

biochemical pathways using MATLAB. *Syst Biol (Stevenage)*, 153(2):53–60.

Vader, G., Maia, A. F., and Lens, S. M. (2008). The chromosomal passenger complex and the spindle assembly checkpoint: kinetochore-microtubule error correction and beyond. *Cell Div*, 3:10.

van Leuken, R., Clijsters, L., and Wolthuis, R. (2008). To cell cycle, swing the APC/C. *Biochim Biophys Acta*, 1786(1):49–59.

van Zon, W. and Wolthuis, R. M. F. (2010). Cyclin A and Nek2A: APC/C-Cdc20 substrates invisible to the mitotic spindle checkpoint. *Biochem Soc Trans*, 38(Pt 1):72–77.

Vázquez-Novelle, M. D. and Petronczki, M. (2010). Relocation of the chromosomal passenger complex prevents mitotic checkpoint engagement at anaphase. *Curr Biol*, 20(15):1402–1407.

Veening, J.-W., Smits, W. K., and Kuipers, O. P. (2008). Bistability, epigenetics, and bet-hedging in bacteria. *Annu Rev Microbiol*, 62:193–210.

Verma, R., Annan, R. S., Huddleston, M. J., Carr, S. A., Reynard, G., and Deshaies, R. J. (1997). Phosphorylation of Sic1p by G1 Cdk required for its degradation and entry into S phase. *Science*, 278(5337):455–460.

Visintin, R., Craig, K., Hwang, E. S., Prinz, S., Tyers, M., and Amon, A. (1998). The phosphatase Cdc14 triggers mitotic exit by reversal of Cdk-dependent phosphorylation. *Mol Cell*, 2(6):709–718.

Visintin, R., Hwang, E. S., and Amon, A. (1999). Cfi1 prevents premature exit from mitosis by anchoring Cdc14 phosphatase in the nucleolus. *Nature*, 398(6730):818–823.

Walczak, C. E., Cai, S., and Khodjakov, A. (2010). Mechanisms of chromosome behaviour during mitosis. *Nat Rev Mol Cell Biol*, 11(2):91–102.

Waltermann, C. and Klipp, E. (2011). Information theory based approaches to cellular signaling. *Biochim Biophys Acta*.

Westermann, S., Avila-Sakar, A., Wang, H.-W., Niederstrasser, H., Wong, J., Drubin, D. G., Nogales, E., and Barnes, G. (2005). Formation of a dynamic kinetochore- microtubule interface through assembly of the Dam1 ring complex. *Mol Cell*, 17(2):277–290.

Westermann, S., Wang, H.-W., Avila-Sakar, A., Drubin, D. G., Nogales, E., and Barnes, G. (2006). The Dam1 kinetochore ring complex moves processively on depolymerizing microtubule ends. *Nature*, 440(7083):565–569.

Wilkinson., D. J. (2006). *Stochastic Modelling for Systems Biology, Chapman and Hall/CRC mathematical & computational biology series Volume 0 of Mathematical and Computational Biology Series*. Taylor & Francis.

Wilkinson, D. J. (2009). Stochastic modelling for quantitative description of heterogeneous biological systems. *Nat Rev Genet*, 10(2):122–133.

Wu, J. Q., Guo, J. Y., Tang, W., Yang, C.-S., Freel, C. D., Chen, C., Nairn, A. C., and Kornbluth, S. (2009). PP1-mediated dephosphorylation of phosphoproteins at mitotic exit is controlled by inhibitor-1 and PP1 phosphorylation. *Nat Cell Biol*, 11(5):644–651.

Yang, Z., Kenny, A. E., Brito, D. A., and Rieder, C. L. (2009). Cells satisfy the mitotic checkpoint in Taxol, and do so faster in concentrations that stabilize syntelic attachments. *J Cell Biol*, 186(5):675–684.

Yu, R. C., Pesce, C. G., Colman-Lerner, A., Lok, L., Pincus, D., Serra, E., Holl, M., Benjamin, K., Gordon, A., and Brent, R. (2008). Negative feedback that improves information transmission in yeast signalling. *Nature*, 456(7223):755–761.

Yuping, Z., Minping, Q., Ouyang Qi, Deng Minghua, L. F., and Chao, T. (2006). Stochastic model of yeast cell-cycle network. *Physica D: Nonlinear Phenomena*, Volume 219:35–39.

Zachariae, W., Schwab, M., Nasmyth, K., and Seufert, W. (1998). Control of cyclin ubiquitination by CDK-regulated binding of Hct1 to the anaphase promoting complex. *Science*, 282(5394):1721–1724.

Zhang, S.-Q., Ching, W.-K., Ng, M. K., and Akutsu, T. (2007). Simulation study in Probabilistic Boolean Network models for genetic regulatory networks. *Int J Data Min Bioinform*, 1(3):217–240.

Zhao, Y. and Chen, R.-H. (2006). Mps1 phosphorylation by MAP kinase is required for kinetochore localization of spindle-checkpoint proteins. *Curr Biol*, 16(17):1764–1769.